

UC Santa Barbara

UC Santa Barbara Electronic Theses and Dissertations

Title

Exploring the Early-time Evolution of Rare and Extreme Supernovae with Las Cumbres Observatory

Permalink

<https://escholarship.org/uc/item/6cv9z0nj>

Author

Pellegrino, Craig Michael

Publication Date

2023

Peer reviewed|Thesis/dissertation

University of California
Santa Barbara

Exploring the Early-time Evolution of Rare and Extreme Supernovae with Las Cumbres Observatory

A dissertation submitted in partial satisfaction
of the requirements for the degree

Doctor of Philosophy
in
Physics

by

Craig M. Pellegrino

Committee in charge:

Professor D. Andrew Howell, Co-Chair
Professor Lars Bildsten, Co-Chair
Professor Crystal Martin

June 2023

The dissertation of Craig M. Pellegrino is approved.

Professor Crystal Martin

Professor Lars Bildsten, Committee Co-Chair

Professor D. Andrew Howell, Committee Co-Chair

June 2023

Exploring the Early-time Evolution of Rare and Extreme Supernovae with Las
Cumbres Observatory

Copyright © 2023

by

Craig M. Pellegrino

“To follow knowledge like a sinking star,
Beyond the utmost bound of human thought.”

(*Ulysses*, 31-32)

Acknowledgements

First and foremost, I'd like to thank everyone who made this research possible: my advisor, Dr. Andy Howell, for scientific guidance and support (both moral and financial); Dr. Curtis McCully, for teaching me how to code and, more importantly, how to navigate software development as an astronomer; Dr. Iair Arcavi, for providing me with guidance and The Supernova Exchange, a website which I've only been partially successful in emulating; Dr. Giacomo Terreran, for helpful discussions (both about science and football); all my fellow graduate students in the group, past and former, including Dr. Daichi Hiramatsu, Dr. Jamie Burke, Este Padilla Gonzalez, Megan Newsome, and Joseph Farah, for teaching me all the intricacies of running a global observatory and how to have fun while doing it; all the members of the Global Supernova Project around the world, who helped gather all the data and refine the science that I present in this dissertation; the members of Las Cumbres Observatory, who created a welcoming work environment and run a fantastic telescope network; and the NSF and NASA, for supporting this work.

On a personal note, I'd like to thank my family, especially my parents and brother, who didn't try to stop me when I told them I wanted to live on the other side of the country and pursue this crazy dream for five years. A special thanks for all the late-night airport pick-ups, early-morning drop-offs, and for all your kindness, empathy, and patience during this very transformative time in my life. I'd also like to thank all my friends at UCSB, including Sean, Molly, Matt, Alex, Joel, and Jenny, for making Santa Barbara an especially great place to spend five years.

And finally, I wouldn't be anywhere near where I am today without Sarina. Thank you for being my rock through all the ups and downs of the last three years—I couldn't have done it without you.

Curriculum Vitæ

Craig M. Pellegrino

EDUCATION

- University of California, Santa Barbara** September 2018 – June 2023
Ph.D. Physics, Astrophysics Emphasis, June 2023
M.A. Physics, Astrophysics Emphasis, June 2021
Advisor: Professor D. Andrew Howell
- Vassar College** August 2014 – May 2018
B.A. Physics and Astronomy, Mathematics Minor

RESEARCH

- University of Virginia** starting July 2023
Postdoctoral Research Associate
Modjaz Explosions and Transient Astronomy Lab (METAL)
- Las Cumbres Observatory** August 2018 – June 2023
Graduate Student Researcher
Global Supernova Project
- Vassar College** August 2017 – May 2018
Undergraduate Researcher
Measurements of radial extents of high-redshift galaxies in the Hubble Frontier Field Parallel images
- Texas A&M University** June 2017 – August 2017
NSF REU Fellow
Stellar kinematics of ultra-faint dwarf satellite galaxies

OBSERVING

- Las Cumbres Observatory** August 2018 – Present
Imaging with SBIG, Sinistro, and Spectral cameras
Spectroscopy with FLOYDS spectrographs
- Southern Astrophysical Research Telescope** January 2022 – Present
Spectroscopy with the Goodman High Throughput Spectrograph
- Neil Gehrels *Swift* Observatory** January 2021 – Present
Imaging with the Ultraviolet/Optical Telescope
and with the X-Ray Telescope

TEACHING

University of California, Santa Barbara September 2018 – June 2019
Teaching Assistant
ASTRO 1 – Basic Astronomy
ASTRO 2 – History of the Universe

Vassar College August 2017 – May 2018
Senior Astronomy Intern

OUTREACH

Astronomy on Tap Santa Barbara September 2018 – Present
Coordinator and co-host of public astronomy-themed public lecture series

Photometric Pipeline Teaching Assistant November 2021 – Present
Assist users of the Las Cumbres photometric data reduction pipeline

Graduate Student Life Representative September 2019 – June 2020
Representative of the Physics department to the UCSB Graduate Student Association

AWARDS & HONORS

Sigma Xi Spring 2018 – Present
Research Society – Vassar College

NSF REU Fellow Summer 2017
Texas A&M University

SOFTWARE

snex2 github.com/LCOGT/snex2
Target and Observation Manager to store and visualize data for the
Global Supernova Project, a collaboration of over 200 astronomers

lcogtsnpipeline github.com/LCOGT/lcogtsnpipeline
Reduces photometry with images obtained using Las Cumbres Observatory telescopes

floyds_pipeline github.com/LCOGT/floyds_pipeline
Reduces spectra from the Las Cumbres Observatory FLOYDS spectrographs

PRESENTATIONS

6. MIAPbP Interacting Supernovae Workshop, Garching, Germany February 2023
“The Diverse Properties of Type Icn Supernovae”
5. Astronomy Seminar Series, University of California, Santa Barbara January 2023
“Exploring the Parameter Space of Rapidly-evolving Supernovae with Las Cumbres Observatory”

4. CIERA Observer’s Group Meeting, Chicago, IL, USA January 2023
“Exploring the Parameter Space of Rapidly-evolving Supernovae with Las Cumbres Observatory”
3. SuperVirtual 2022 (virtual) November 2022
“Evidence for Multiple Progenitor Channels of Type Icn Supernovae”
2. American Astronomical Society 240, Pasadena, CA, USA June 2022
“Exploring the Possible Progenitors of Type Icn Supernovae”
1. Astronomy Seminar Series, University of California, Santa Barbara November 2019
“Constraining the Source of the High-velocity Ejecta in Type Ia SN 2019ein”

PUBLICATIONS

Lead Author

4. **Pellegrino, C.**, Hiramatsu, D., Arcavi, I., Howell, D. A., Bostroem, K. A., et al., *“SN 2020bio: A Double-peaked Type IIb Supernova with Evidence of Early-time Circumstellar Interaction,”* 2023, under review, [arXiv:2301.04662](https://arxiv.org/abs/2301.04662)
3. **Pellegrino, C.**, Howell, D. A., Terreran, G., Arcavi, I., Bostroem, K. A., et al., *“The Diverse Properties of Type Icn Supernovae Point to Multiple Progenitor Channels,”* 2022, [ApJ](https://doi.org/10.1086/9711), **938**, 73
2. **Pellegrino, C.**, Howell, D. A., Vinkó, J., Gangopadhyay, A., Xiang, D., et al., *“Circumstellar Interaction Powers the Light Curves of Luminous Rapidly Evolving Optical Transients,”* 2022, [ApJ](https://doi.org/10.1086/9711), **926**, 125
1. **Pellegrino, C.**, Howell, D. A., Sarbadhicary, S. K., Burke, J., Hiramatsu, D., et al., *“Constraining the Source of the High-velocity Ejecta in Type Ia SN 2019ein,”* 2020, [ApJ](https://doi.org/10.1086/9367), **897**, 159

Major Contribution

4. Gangopadhyay, A., Misra, K., Hosseinzadeh, G., Arcavi, I., **Pellegrino, C.**, et al., *“Evolution of a Peculiar Type Ibn Supernova SN 2019wep,”* 2022, [ApJ](https://doi.org/10.1086/9711), **930**, 127
3. Sand, D. J., Sarbadhicary, S. K., **Pellegrino, C.**, Misra, K., Dastidar, R., et al., *“Circumstellar Medium Constraints on the Environment of Two Nearby Type Ia Supernovae: SN 2017cbv and SN 2020nlb,”* 2021, [ApJ](https://doi.org/10.1086/9711), **922**, 21
2. Rho, J., Evans, A., Geballe, T. R., Banerjee, D. P. K., Hoefflich, P., et al. (incl. **Pellegrino, C.**), *“Near-infrared and Optical Observations of Type Ic SN 2020oi and Broad-lined Type Ic SN 2020bvc: Carbon Monoxide, Dust, and High-velocity Supernova Ejecta,”* 2021, [ApJ](https://doi.org/10.1086/9711), **908**, 232
1. Gangopadhyay, A., Misra, K., Hiramatsu, D., Wang, S. Q., Hosseinzadeh, G., et al. (incl. **Pellegrino, C.**), *“Flash Ionization Signatures in the Type Ibn Supernova SN 2019uo,”* 2020, [ApJ](https://doi.org/10.1086/9367), **889**, 170

Collaboration

33. A. Ravi et al., “Near-Infrared and Optical Observations of Type Ic SN 2021krf: Luminous Late-time Emission and Dust Formation,” 2023, [ApJ](#), *accepted*, [arXiv:2211.00205](#)
32. M. Deckers et al., “Photometric study of the late-time near-infrared plateau in Type Ia supernovae,” 2023, [MNRAS](#), **521**, 4414
31. M. Shrestha et al., “Limit on Supernova Emission in the Brightest Gamma-Ray Burst, GRB 221009A,” 2023, [ApJL](#), **946**, L25.
30. T. Ben-Ami et al., “The Type Ibn Supernova 2019kjb: Indications for Diversity in Type Ibn Supernova Progenitors,” 2023, [ApJ](#), **946**, 30.
29. A. Pastorello et al., “Forbidden hugs in pandemic times. IV. Panchromatic evolution of three luminous red novae,” 2023, [A&A](#), **671**, A158.
28. Y. Yang et al., “The Interaction of Supernova 2018evt with a Substantial Amount of Circumstellar Matter – An SN 1997cy-like Event,” 2022, [MNRAS](#), **519**, 1618.
27. B. Ailawadhi et al., “Photometric and spectroscopic analysis of the Type II SN 2020jfo with a short plateau,” 2022, [MNRAS](#), **519**, 248.
26. Q. Wang et al., “Revealing the Progenitor of SN 2021zby through Analysis of the TESS Shock-cooling Light Curve,” 2023, [ApJL](#), **943**, L15.
25. G. Hosseinzadeh et al., “JWST Imaging of the Cartwheel Galaxy Reveals Dust Associated with SN 2021afdx,” 2023, [ApJL](#), **942**, L18.
24. M. Williamson et al., “SN 2019ewu: A Peculiar Supernova with Early Strong Carbon and Weak Oxygen Features from a New Sample of Young SN Ic Spectra,” 2023, [ApJL](#), **944**, L49.
23. M. Singh et al., “Optical studies of a bright Type Iax supernova SN 2020rea,” 2022, [MNRAS](#), **517**, 5617.
22. G. Zeltyn et al., “A Transient “Changing-look” Active Galactic Nucleus Resolved on Month Timescales from First-year Sloan Digital Sky Survey V Data,” 2022, [ApJL](#), **939**, L16
21. J. Yang et al., “Using 1991T/1999aa-like Type Ia Supernovae as Standardizable Candles,” 2022, [ApJ](#), **938**, 83.
20. J.E. Andrews et al., “High-Cadence TESS and Ground-based Data of SN 2019esa, the Less Energetic Sibling of SN 2006gy,” 2022, [ApJ](#), **938**, 19.
19. G. Hosseinzadeh et al., “Weak Mass Loss from the Red Supergiant Progenitor of the Type II SN 2021yja,” 2022, [ApJ](#), **935**, 31
18. K. Medler et al., “SN 2020acat: an energetic fast rising Type IIb supernova,” 2022, [MNRAS](#), **513**, 5540

17. G. Valerin et al., “Low luminosity Type II supernovae—IV. SN 2020cxd and SN 2021aai, at the edges of the sub-luminous supernovae class,” 2022, [MNRAS](#), **513**, 4893
16. G. Hosseinzadeh et al., “Constraining the Progenitor System of the Type Ia Supernova 2021aefx,” 2022, [ApJL](#), **933**, 45
15. A. Fiore et al., “Close, bright, and boxy: the superluminous SN 2018hti,” 2022, [MNRAS](#), **512**, 3
14. I. Irani et al., “Less than 1% of Core-Collapse Supernovae in the local universe occur in elliptical galaxies,” 2022, [ApJ](#), **927**, 10
13. E. Parrag et al., “SN 2019hcc: a Type II supernova displaying early O II lines,” 2021, [MNRAS](#), **506**, 4
12. J.E. Jencson et al., “AT 2019qyl in NGC 300: Internal Collisions in the Early Outflow from a Very Fast Nova in a Symbiotic Binary,” 2021, [ApJ](#), **920**, 127
11. J. Burke et al., “A Bright Ultraviolet Excess in the Transitional O2es-like Type Ia Supernova 2019yvq,” 2021, [ApJ](#), **919**, 142
10. K. Medler et al., “SN 2020cpg: an energetic link between Type IIb and Ib supernovae,” 2021, [MNRAS](#), **506**, 183
9. X. Zeng et al., “SN 2017fgc: A fast-expanding type Ia supernova exploded in massive shell galaxy NGC 474,” 2021, [ApJ](#), **919**, 49
8. C.P. Gutierrez et al., “The double-peaked Type Ic supernova 2019cad: another SN 2005bf-like object,” 2021, [MNRAS](#), **504**, 4
7. C. Baltay et al., “Low-redshift Type Ia Supernova from the LSQ&LCO Collaboration,” 2021, [PASP](#), **133**, 1022
6. X. Zeng et al., “SN 2017hpa: A Nearby Carbon-rich Type Ia Supernova with a Large Velocity Gradient,” 2021, [ApJ](#), **909**, 176
5. B. Barna et al., “SN 2019muj—a well-observed Type Iax supernova that bridges the luminosity gap of the class,” 2021, [MNRAS](#), **501**, 1
4. S.J. Prentice et al., “SN 2018gjx reveals that some SNe Ibn are SNe IIb exploding in dense circumstellar material,” 2020, [MNRAS](#), **499**, 1450
3. M. Nicholl et al., “An outflow powers the optical rise of the nearby, fast-evolving tidal disruption event AT2019qiz,” 2020, [MNRAS](#), **499**, 482
2. W.V. Jacobson-Galán et al., “SN 2019ehk: A Double-peaked Ca-rich Transient with Luminous X-Ray Emission and Shock-ionized Spectral Features,” 2020, [ApJ](#), **898**, 166
1. D.Q. Nagasawa et al., “Chemical abundance analysis of three α -poor, metal-poor stars in the ultrafaint dwarf galaxy Horologium I,” 2018, [ApJ](#), **852**, 99

Submitted

2. K. Davis et al., “SN 2022ann: A type Icn supernova from a dwarf galaxy that reveals helium in its circumstellar environment,” 2022, [MNRAS](#), [submitted](#), [arXiv:2211.05134](#)
1. J. Burke et al., “Early Lightcurves of Type Ia Supernovae are Consistent with Nondegenerate Progenitor Companions,” 2022, [ApJ](#), [submitted](#), [arXiv:2207.07681](#)

Astronomical Circulars

[243](#) transient classifications and circulars ([39](#) as lead author).

Abstract

Exploring the Early-time Evolution of Rare and Extreme Supernovae with Las
Cumbres Observatory

by

Craig M. Pellegrino

The advent of wide-field surveys has led to an exponential increase in the number of supernovae discovered each year. As the sample sizes of these objects have grown, we have discovered supernovae that show greater diversity within their spectroscopic classes than expected, as well as objects that do not fit into traditional classification schemes altogether. Studying these “extreme” supernovae in greater detail is crucial to understanding the poorly-understood end stages of stars’ lives; early-time observations within hours of the supernova explosion probe the progenitor star’s stellar structure as well as its circumstellar environment, which can be used to test current theories of stellar evolution.

Here I present studies utilizing photometric and spectroscopic observations, primarily taken by Las Cumbres Observatory, of supernovae that occupy poorly-understood or unpopulated regions of parameter space. First, I examine an object with extreme ejecta velocities. Observations of this Type Ia supernova, SN 2019ein, within days of explosion show some of the fastest-moving ejecta of any supernova. The potential sources of this high-velocity ejecta in the context of the poorly-understood progenitor channels and explosion mechanisms of Type Ia supernovae are explored.

Next, I investigate the powering mechanisms and progenitor systems of supernovae with rapidly-evolving luminosities. High-cadence observations of objects within this region of supernova phase space reveal significant diversity in their circumstellar environ-

ments and powering mechanisms. In particular, I show evidence connecting luminous, rapidly-evolving unclassified transients with supernovae powered by interaction with circumstellar material. I also present the first sample study of a new class of supernovae, Type Icn supernovae, with rapidly-evolving light curves powered by interaction with circumstellar material that is both hydrogen- and helium-poor. Studying these unique and rare objects reveals that some are likely the explosions of stars less massive than expected from our current understanding of mass-loss in massive stars. Finally, I present evidence of diversity in the powering mechanisms and progenitors of the well-understood class of Type IIb supernovae. Each of these major findings challenges our understanding of supernova physics as well as theories of mass loss during the final stages of stellar evolution.

Contents

Curriculum Vitae	vi
Abstract	xii
1 Introduction	1
1.1 A Brief Overview of Supernovae	1
1.2 Las Cumbres Observatory	8
1.3 The Extremes of “Normal” Supernovae	11
2 Constraining the Source of the High-velocity Ejecta in SN 2019ein	13
2.1 Introduction	13
2.2 Observations	16
2.3 Photometric Results	21
2.4 Spectroscopic Analysis	25
2.5 Progenitor Constraints from Radio Observations	34
2.6 Mixing and Optical Depth Effects	42
2.7 Summary	49
3 The Phase Space of Rapidly-evolving Supernovae	52
3.1 Supernova Powering Mechanisms	52
3.2 Supernova Phase Space	56
4 Circumstellar Interaction and Luminous, Rapidly-evolving Transients	60
4.1 Introduction	62
4.2 Observations and Sample Description	65
4.3 Data Analysis	72
4.4 Circumstellar-interaction Models	78
4.5 Discussion	88
4.6 Conclusions	96

5	Type Icn Supernovae: A New Class of Rapidly-Evolving Supernovae with Multiple Progenitor Channels	98
5.1	Introduction	100
5.2	Sample Description and Observations	103
5.3	Photometric Properties	108
5.4	Spectroscopic Features	114
5.5	Progenitor Analysis	118
5.6	Discussion	128
5.7	Conclusions	138
6	SN 2020bio: Diversity in the Class of Double-peaked Type IIb Supernovae	141
6.1	Introduction	142
6.2	Discovery and Data Description	145
6.3	Photometric and Spectral Analysis	148
6.4	Light-curve Modeling and Progenitor Inference	157
6.5	Discussion and Conclusions	167
7	Conclusions and Future Outlook	171
	Bibliography	175

Chapter 1

Introduction

1.1 A Brief Overview of Supernovae

1.1.1 Observational Characteristics of Supernovae

Supernovae are the explosive ends of stars' lives. Despite this seemingly simple definition, supernovae play integral roles in the evolution of the universe. They mark the ends of millions to billions of years of stellar evolution in a fraction of a second, spewing more mass than that of the Sun outwards at speeds approaching 10% of the speed of light, enriching the interstellar and circumgalactic media with fresh fuel with which to continue the stellar life cycle. The kinetic energy of their ejecta as well as the thermal energy from the radioactive decay of unstable isotopes produced in their explosions powers luminous emission that outshines their entire host galaxies for rest-frame weeks to years. Observing supernovae out to billions of parsecs has allowed astronomers to map the expansion of the universe, revealing unknown physics in the form of dark energy. Finally, supernovae carry imprints of their progenitor stars in their very early-time and late-time emission. The cosmic "crime scenes" of these explosions are the only environments in which astronomers can directly probe the size, structure, and composition of a star in its final moments.

More technically, supernovae consist of the thermonuclear explosions of white dwarfs and the core-collapses of evolved stars with zero-age main sequence masses $\gtrsim 8 M_{\odot}$. Like most classification schemes in astronomy, the taxonomy of supernovae is rooted in history. Supernovae are typically divided into observational subtypes based on the features in their spectra (Filippenko 1997). Broadly, supernovae that do not show signatures of hydrogen in their ejecta are classified as Type I, whereas those that do are classified as Type II. These two broad groups are subdivided even further based on additional spectroscopic characteristics: supernovae without hydrogen but with strong helium are classified as Type Ib, those without both hydrogen and helium as well as weak silicon are classified as Type Ic, and those without hydrogen and helium but with strong silicon are Type Ia. To add to the confusion, new subgroups are discovered and defined seemingly every year.

The spectral lines used for classification are formed in the expanding layers of the progenitor star that are ejected by the supernova explosion. Luminosity inputs, normally from the supernova shock at early times and radioactive decay of unstable iron-group element isotopes at later times, provide high-energy photons that heat and ionize the freely-expanding ejecta. Emission is produced by the recombination of electrons and ions within this hot gas and the subsequent spectral lines are Doppler broadened by the ejecta velocity (typically on the order of $10,000 \text{ km s}^{-1}$).

An example of a spectroscopic time series is shown in Figure 1.1. At early times, hours to several days after the explosion, the supernova ejecta remains hot and ionized. Due to electron scattering in this ionized medium the photosphere lies in the outermost ejecta. At these phases optical supernova spectra may be blue and relatively featureless, as shown in the top spectrum of Figure 1.1. Any lines at these times must form from the material in the very outer layers of the progenitor star or in the surrounding circumstellar medium.

As the ejecta expands and cools with time, the photosphere recedes in mass coordi-

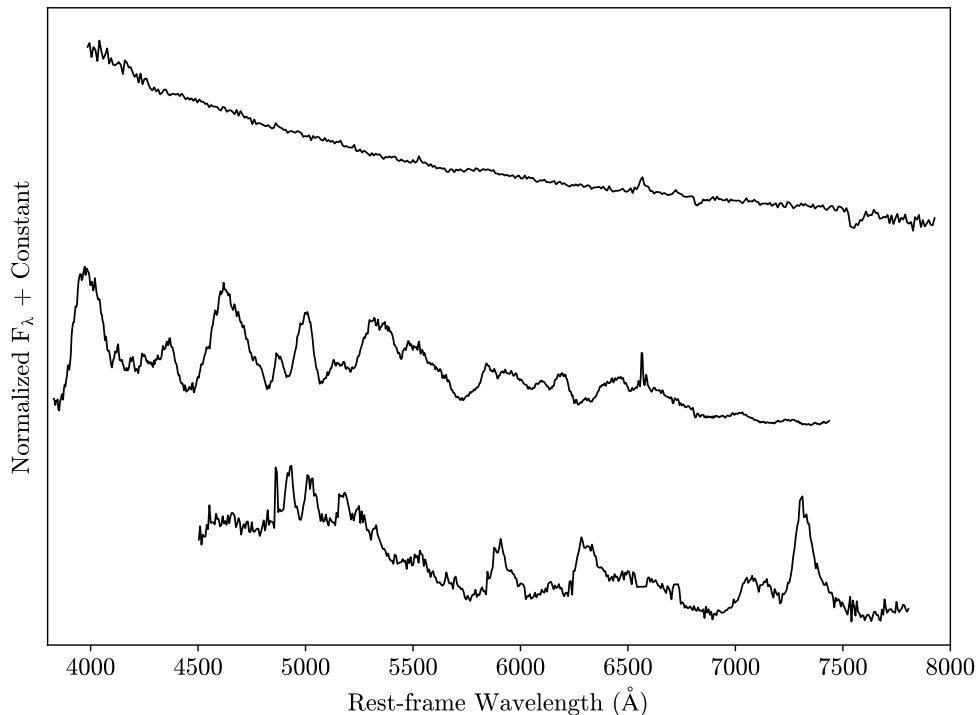


Figure 1.1: An example of spectral evolution over 200 days after explosion using spectra of the Type IIb supernova SN 2020bio (see Chapter 6). Early-time- (top), photospheric- (middle), and nebular- (bottom) phase spectra are shown.

nates and more lines formed from deeper within the ejecta are visible to the observer. These features are often P Cygni profiles in which emission and absorption for each line are simultaneously visible. Emission features form from photons created by the recombination of free electrons and ions which are subsequently Doppler broadened by the isotropic motion of the expanding ejecta, whereas absorption features are formed along the observer line-of-sight by material at higher velocities (Figure 1.1, middle).

Approximately 100 – 200 days after the explosion, the ejecta has expanded and cooled enough that the photosphere completely recedes to the center of the ejected material. This marks the beginning of the nebular phase (see, e.g., [Jerkstrand 2017](#) for a review). At these phases the ejecta densities and temperatures are low enough that the observed lines are forbidden or semi-forbidden transitions produced by collisional excitation and

and de-excitation. The supernova spectra transitions from continuum- and absorption-dominated to emission-dominated. An example spectrum is shown in Figure 1.1 (bottom). While their emission is intrinsically faint, nearby supernovae are still bright enough to be observed in this phase. The strengths and line profiles of these nebular features provides information about the material produced at the core of the progenitor star.

Much of the above discussion has implicitly focused on optical observations of supernovae. Optical observations are the *de facto* observations because they are easily obtained from ground-based instruments and the spectral energy distribution of most supernovae peaks in the optical throughout most of their evolution. However, complementary and often crucial information can be gained from observations in other wavelength regimes:

- γ -ray observations have connected gamma-ray bursts—some of the most energetic events in the universe—to Type Ic supernovae with unique explosion mechanisms (e.g., [Modjaz et al. 2016](#));
- X-ray and radio observations probe interaction between the supernova ejecta and material in the surrounding circumstellar environment, allowing astronomers to map out the mass-loss history of the progenitor star ([Chevalier 1982](#); [Chevalier & Fransson 1994](#));
- Ultraviolet observations are crucial for core-collapse supernovae within days of explosion, when their spectra resemble hot blackbodies that peak in the ultraviolet, and have serendipitously observed the supernova shock as it reaches the surface of the progenitor star ([Modjaz et al. 2009](#));
- Infrared observations are necessary to observe supernovae in high-extinction environments, which reddens their spectral energy distributions, as well as to search for dust produced in their ejecta (e.g., [Todini & Ferrara 2001](#); [Gall et al. 2014](#)).

Studying supernovae in each of these wavelength regimes is worthy of multiple dissertations each. For this one, we will focus on optical observations. However, in several of the discussed works ultraviolet observations were crucial to constructing bolometric light curves by accurately probing the supernova spectral energy distribution over a wider wavelength range. These observations were obtained by the Neil Gehrels *Swift* satellite (Gehrels et al. 2004) which has proven to be an essential resource for supernova science.

1.1.2 Physical Characteristics of Supernovae

While observational characteristics are an important tool to understand supernovae, it is becoming abundantly clear that classifying supernovae based on these observational features is not an adequate system to accurately describe the physical properties of their progenitor stars nor of the explosion mechanisms that produce them (Gal-Yam 2017a). Therefore, one of the primary goals of studying supernovae (and indeed, the goal that motivates this dissertation) is mapping the observational characteristics of different types of supernovae to their progenitor stars. This is accomplished in multiple ways—through comparisons between theoretical models of stellar evolution and the chemical abundances inferred from supernova spectroscopy, direct progenitor detection in pre-explosion images, model fits to their luminosity evolution to infer explosion energies and ejecta masses, explosion site analyses, and studying their progenitor structure and surrounding environment via very early-time supernova observations. Here are the broad conclusions from these areas of research for the three main spectroscopic subtypes:

Type Ia supernovae have spectra that lack hydrogen and helium and are dominated by intermediate mass elements such as silicon, calcium, and sulfur. Their light curves are relatively standard, rising to peak brightness $-20 \lesssim M \lesssim -19$ in 15 – 22 days (Yao et al. 2019; Miller et al. 2020). Their standardizable light curves as well as their com-

mon spectral features point to uniform progenitors with similar masses and/or explosion mechanisms. A theoretical progenitor system that matches all their observed characteristics is the complete disruption of a white dwarf star (Maoz et al. 2014). This has been confirmed in multiple ways. First, very early-time observations of SN 2011fe, one of the closest Type Ia supernovae to date, allowed for strict limits on the radius of its progenitor star which excludes virtually any astrophysical object besides a white dwarf (Bloom et al. 2012). Additionally, theoretical models of nuclear burning in white dwarfs closely matches the chemical abundances observed from spectra of Type Ia supernovae (Khokhlov 1991; Seitenzahl et al. 2013). Their uniform light curves and spectra imply a white dwarf progenitor that explodes at or near the Chandrasekhar mass. However, the mechanism by which the star explodes and the system by which it gains mass remain debated (see Section 1.3 for further discussion).

Type II supernovae have hydrogen-rich spectra that point to a progenitor that has retained significant amounts of its hydrogen envelope at the time of explosion. Direct progenitor detections in pre-explosion images from *Hubble Space Telescope* have revealed these supernovae to be the explosions of red supergiant stars with zero-age main sequence masses $8 M_{\odot} \lesssim M_{\text{ZAMS}} \lesssim 20 M_{\odot}$ (e.g., Van Dyk et al. 2003; Van Dyk 2017). In many ways, Type II supernovae have the best-understood progenitors. Even so, the upper limit to their potential progenitor masses remains a mystery, with theory and observation in somewhat considerable tension (Smartt 2009).

Finally, supernovae without hydrogen and strong silicon are classified as either Type Ib or Type Ic, depending on the presence of helium in their spectra. These supernovae are known as stripped-envelope supernovae due to their progenitors' apparent lack of a hydrogen envelope before exploding. In many ways the physical properties of their progenitors are the least well-understood. While there is consensus they are the core-collapse of stars initially more massive than $8 M_{\odot}$, their exact progenitor channels are

debated. Observationally, stars with initial masses $M_{\text{ZAMS}} \geq 25 M_{\odot}$ are observed to lose their entire hydrogen envelope during their Wolf-Rayet phase (Crowther 2007). However, such massive progenitors are in tension with many observational characteristics of stripped-envelope supernovae. For example, the mass of their ejecta inferred from their light curves are well below the pre-supernova mass of a Wolf-Rayet star (e.g., Lyman et al. 2016). Additionally, searches for progenitors in pre-explosion images have had mixed results, with many candidates being consistent with lower-mass stars in binary systems (Bersten et al. 2014; Kilpatrick et al. 2021). Therefore, the initial masses of their progenitors and the mechanisms by which they lose their hydrogen and even helium layers are still poorly understood.

1.1.3 Supernovae in the Era of Time-domain Surveys

Studying ensembles of supernovae is how astronomers, within the last century, have been able to determine the explosive fates of stars whose lifetimes of billions of years far exceed our own. Within this short period of time our growing understanding of supernovae and their physics, in turn, has revolutionized our theories of stellar evolution. Many of these research advances are fueled by the exponentially-increasing number of supernovae discovered each year. The acceleration in discovery rates is due to the advent of wide-field and all-sky surveys which have proved to be efficient discovery engines for time-variable astronomical sources. Surveys such as the Palomar Transient Factory (PTF; Law et al. 2009), All-Sky Automated Survey for Supernovae (ASAS-SN; Shappee et al. 2014), Zwicky Transient Facility (ZTF; Bellm et al. 2019; Graham et al. 2019), Asteroid Terrestrial-impact Last Alert System (ATLAS Tonry et al. 2018), and others have discovered tens of thousands of supernovae and supernovae candidates each year, while within the next several years the Legacy Survey of Space and Time (LSST) at the

Rubin Observatory is expected to issue millions of alerts each *night* (Ivezić et al. 2019). These ever-increasing volumes of data have in turn led to robust samples of different types of supernovae.

However, with these large samples of supernovae have also come an increasing number of individual objects that are outliers with respect to their classmates, or with respect to any class altogether. Many of these discoveries have been made due to high-cadence surveys which catch supernovae within hours of their explosions. These early-time observations, along with high-cadence follow-up observations across the electromagnetic spectrum, have revealed objects with distinct photometric and spectroscopic features that challenge our understanding of their explosion mechanisms and their progenitor stars. This dissertation focuses on understanding well-observed examples of these “extreme” supernovae that have been discovered within the last five years.

1.2 Las Cumbres Observatory

The discovery surveys introduced in Section 1.1 are efficient engines for finding new supernovae. However, to study them in greater detail, it is necessary to obtain higher-cadence follow-up observations across the electromagnetic spectrum as rapidly as possible. Rapidly following young supernovae is important because at early times, the progenitor star’s circumstellar environment and the structure of its outer envelope can be inferred from photometric and spectroscopic observations in the ultraviolet, optical, and infrared. Additionally, supernovae of all types have shown surprising deviations from their expected behavior at early times. Whether these deviations are caused by pre-existing circumstellar material, the presence of a companion star, unusual progenitor structure, or different explosion mechanisms are all areas of great interest.

In order to maximize the scientific impact from the discovery of young supernovae

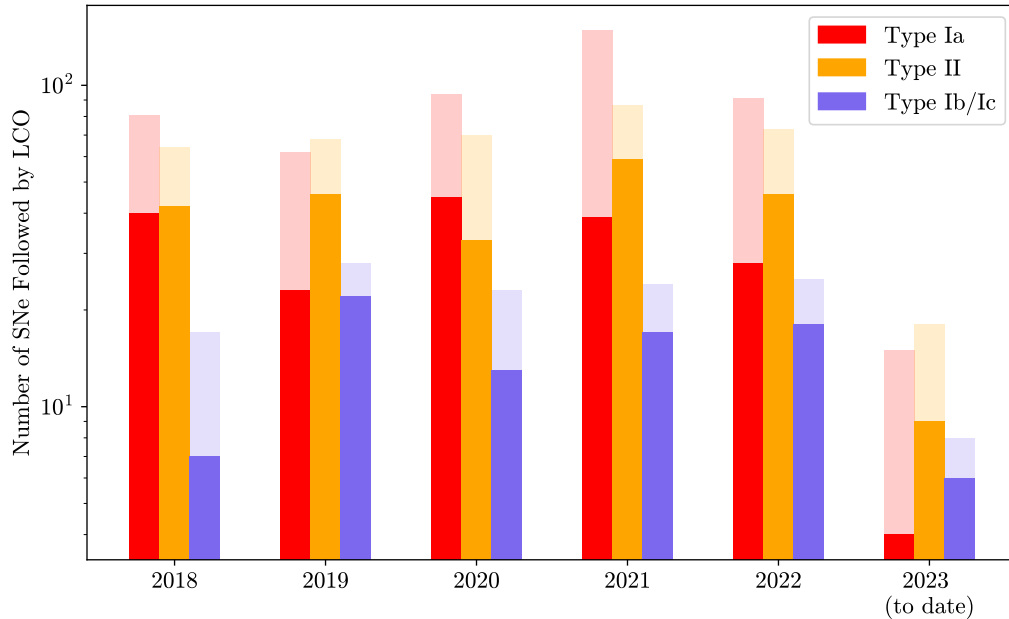


Figure 1.2: A histogram showing the supernovae observed by the GSP using LCO since 2018. The sample is divided by spectroscopic subtype. Lower-opacity bars show the full number of each class that LCO began following that year, while shaded bars show the subset of objects with more than 100 data points each.

within hours of their explosion, the alerts from time-domain surveys must be disseminated, ingested, and follow-up observations scheduled programmatically. At the intersection of these technical and scientific challenges is Las Cumbres Observatory (LCO; [Brown et al. 2013](#)). LCO is a network of 25 robotic telescopes spread across the globe at 7 sites, designed so that at any time of the day there are telescopes in the dark, capable of observing an astronomical transient in a matter of minutes. Observations on LCO telescopes are scheduled dynamically using a programmatic scheduler, which balances requests from different time-domain collaborations to build each site’s observation schedule in real time. 40 cm and 1 m telescopes are used for photometric observations while 2 m telescopes primarily obtain spectra using the FLOYDS spectrographs. Additionally, observations can be requested at partner facilities within the AEON network, including

Gemini and the Southern Astrophysical Research (SOAR) telescope.

LCO has served as the main source of the data presented throughout this dissertation. These data were primarily obtained by the Global Supernova Project (GSP), an LCO key project led by LCO time-domain astronomers. The GSP is a global collaboration of over 200 supernova researchers that share data and observational resources to obtain high-quality photometric and spectroscopic observations of hundreds of supernovae. Figure 1.2 shows the distribution of the common spectroscopic subtypes of supernovae observed by the GSP since 2018. Since its inception the GSP has observed over 2250 supernovae, and since 2018 over 500 individual supernovae have more than 100 data points each.

Graduate students at LCO are integral to the day-to-day functioning of the GSP as well as the observatory as a whole. Students monitor the data intake of the observatory, adjusting observation requests as needed to obtain more data for young or interesting supernovae while canceling follow-up of objects that are old or no longer interesting. Data that LCO obtains are processed and reduced, often by hand, by the same students before being shared with the broader GSP collaboration. Students also lead software development projects to build data reduction pipelines and Target and Observation Managers for the GSP, managing thousands of targets and hundreds of thousands of data points altogether. In return, students are invited to join papers using observations they scheduled or reduced as well as lead projects of their choosing.

In addition to the resources available to LCO and the broader AEON network, GSP collaborators have access to extensive follow-up resources across the electromagnetic spectrum. Members have institutional access to 6m-, 8m-, and 10m-class telescopes including MMT, the Magellan telescopes, and Keck. Many have guest investigator programs on telescopes such as *Swift* and *Chandra*. Additionally, the GSP collaborates with the Keck Infrared Transient Survey to obtain and analyze infrared spectra of interesting targets of opportunity. These additional resources are integral to much of the work presented

throughout this dissertation.

1.3 The Extremes of “Normal” Supernovae

Within the large samples of supernovae extensively studied by the GSP using the LCO network, we have discovered examples of “extreme” objects that challenge our understanding of their progenitor stars and the physics that produce them. These “extreme” examples of more normal supernovae include objects with ejecta velocities much higher than expected, objects with peculiar light curves indicating different powering mechanisms, and objects with observables that map to progenitors that challenge our understanding of massive star evolution.

This dissertation focuses particularly on the extremes of two observables—ejecta velocities and light-curve timescale. Critically, both these quantities are probed via very early-time observations. Due to the homologous expansion of the supernova ejecta (where the expansion rate of the ejecta is proportional to its distance from the center of the explosion, $v_{\text{ej}} \propto R_{\text{ej}}$), the fastest-moving ejecta is observed at the earliest times, before the photosphere recedes deeper into the expanding material. Similarly, in the last several years supernovae have been discovered that rise and fade to the detection limit of wide-field surveys in a matter of days. Studying the full evolution of these objects is only possible with observations taken soon after explosion.

One example of diversity within a well-understood class that was only discovered via early-time LCO follow-up is in Type Ia supernovae. Observationally, Type Ia supernovae have been identified as the thermonuclear detonations and/or deflagrations of white dwarfs. The thermonuclear runaway, caused by a detonation wave that sweeps across the surface of the star (Shen & Bildsten 2009) or by reaching a critical density in

the core (Khokhlov 1991), completely unbinds and almost entirely burns the progenitor¹. The high densities and availability of intermediate mass elements leads to the production of $\approx 0.5 M_{\odot}$ of unstable ^{56}Ni . The decay of this isotope, with a half-life of ≈ 6.1 days (Arnett 1982), powers their light curves which rise to a peak luminosity in two to three rest-frame weeks.

It is important to understand Type Ia supernovae, especially their diversity, in greater detail because of their use as standardizable candles for cosmological measurements. Due to a correlation between their peak luminosities and light-curve decline rate, known as the Phillips relation (Phillips 1993), Type Ia supernovae are an important rung in the cosmological distance ladder. Their use in this way revealed the accelerated expansion of the universe and the existence of dark energy (Riess et al. 1998; Schmidt et al. 1998; Perlmutter et al. 1999). However, it is clear that a sizeable minority of Type Ia supernovae exist outside of the Phillips relation (Taubenberger 2017). Understanding the cause of this diversity is paramount to refining their use as distance indicators. It is possible that different progenitor channels—whether the progenitor white dwarf accretes material from a nondegenerate companion star, a degenerate helium star, or another white dwarf—or different explosion mechanisms can produce some of the observed diversity. However, to test these theories, observations of peculiar and extreme Type Ia supernovae are needed throughout their full evolution.

The following chapter presents the first finding of this dissertation. It details the discovery and analysis of SN 2019ein, a Type Ia supernova with some of the highest ejecta velocities measured to date. These extreme ejecta velocities as a result of different potential progenitor channels and explosion mechanisms of Type Ia supernovae is examined.

¹Some peculiar objects that appear related to Type Ia supernovae may be the result of a partial deflagration that does not completely unbind the progenitor (Foley et al. 2013). We do not consider these “Type Iax” supernovae in this work.

Chapter 2

Constraining the Source of the High-velocity Ejecta in SN 2019ein

This chapter was reproduced from [Pellegriano et al. \(2020\)](#) with only minor changes to fit the formatting of this dissertation. I'd like to thank my coauthors, without whom this work would not have been possible: D. A. Howell, S. K. Sarbadhicary, J. Burke, D. Hiramatsu, C. McCully, P. A. Milne, J. E. Andrews, P. Brown, L. Chomiuk, E. Y. Hsiao, D. J. Sand, M. Shahbandeh, N. Smith, S. Valenti, J. Vinkó, J. C. Wheeler, S. Wyatt, and Y. Yang.

2.1 Introduction

Supernovae Ia (SNe Ia) are thermonuclear explosions involving at least one white dwarf (WD) progenitor star ([Bloom et al. 2012](#)). A unique characteristic of SNe Ia is that they show a relationship between their peak luminosity and the width of their light curve, known as the Phillips relation ([Phillips 1993](#)). This correlation allows the calibration of absolute brightness by light curve shape, which enables the determination of distances on cosmological scales. As standardizable candles, observations of SNe Ia have revealed the existence of dark energy (e.g. [Riess et al. 1998](#); [Schmidt et al. 1998](#); [Perlmutter et al. 1999](#)) and allow for a low-redshift measurement of the Hubble constant (e.g. [Riess et al.](#)

2019). A better understanding of their progenitor systems, explosion mechanisms, and observational characteristics is important to mitigate systematic uncertainties in order to use these objects for cosmological measurements.

Over the last several decades, sky surveys and deep imaging have led to the discovery of thousands of SNe Ia (e.g. [Guy et al. 2010](#); [Lusso et al. 2012](#); [Macaulay et al. 2019](#)). Large samples have shown that significant diversity exists within the population of SNe Ia (e.g. [Parrent et al. 2014](#)). Obtaining detailed observations of SNe Ia is important for understanding the sources of this diversity. While the majority of SNe Ia are “normal” and obey the Phillips relation, a sizeable minority of peculiar objects tends to show varied photometric and spectral evolution around peak brightness (e.g. [Filippenko et al. 1992a, b](#); [Phillips et al. 1992](#)), suggesting that fundamental differences beyond luminosity exist in the population of SNe Ia.

Models of progenitor systems and explosion mechanisms have attempted to explain the observed photometric and spectroscopic heterogeneity. Most SN Ia progenitor systems are modeled by accretion onto a degenerate WD from a nondegenerate companion (the single-degenerate scenario, e.g. [Whelan & Iben 1973](#)) or by the accretion or merger of two degenerate WDs (the double-degenerate scenario, e.g. [Iben & Tutukov 1984](#)). In addition, a variety of theoretical explosion models have been able to reproduce observed characteristics of SNe Ia. One such model is a delayed-detonation explosion, where a (subsonic) deflagration flame transitions to a (supersonic) detonation at some transition density ([Iwamoto et al. 1999](#); [Nomoto et al. 2013](#)). Delayed-detonation simulations are able to reproduce a wide variety of light-curve widths, ^{56}Ni masses, ejecta compositions, and ejecta velocities in Chandrasekhar-mass progenitor WDs ([Khokhlov 1991](#); [Seitenzahl et al. 2013](#)). Another popular model is the double-detonation explosion, in which a detonation of helium accreted onto the surface of a WD leads to a second detonation at the core of the star ([Fink et al. 2010](#); [Kromer et al. 2010](#); [Woosley & Kasen 2011](#)).

Several observational classification schemes have been proposed that may indirectly probe these different physical models. [Branch et al. \(2006\)](#) propose one such scheme, in which SNe Ia are classified by the strength of their Si II absorption features at maximum light. Additionally, [Wang et al. \(2009\)](#) sort SNe Ia by their Si II velocities, measured from the minimum of the absorption trough at B -band maximum light, into two classes: a high-velocity (HV) class, with $v_{\text{Si II}} \gtrsim 12,000 \text{ km s}^{-1}$, and a normal class, with $v_{\text{Si II}} \lesssim 12,000 \text{ km s}^{-1}$. After maximum light, SNe Ia can be classified as either high-velocity gradient (HVG) or low-velocity gradient (LVG) if the measured Si II velocity gradient is above or below $70 \text{ km s}^{-1} \text{ day}^{-1}$, respectively ([Benetti et al. 2005](#)).

This diversity in velocity may arise from different distributions of Si in the outer layers of the ejecta, which in turn depend on the explosion mechanism. For instance, [Mazzali et al. \(2005\)](#) studied the Si II and Ca II absorption features in the Type Ia SN 1999ee and found that two separate components, separated by over $7,000 \text{ km s}^{-1}$, were visible in the spectra before B -band maximum light. The authors described these as high-velocity features (HVF) and photospheric velocity features (PVF) and suggested they could be the result of additional mass at HVs. Other studies have attributed HVFs, particularly of the Ca II NIR feature, to interactions between the SN shock wave and a shell of circumstellar material formed from the SN progenitor system (e.g. [Gerardy et al. 2004](#); [Mulligan & Wheeler 2018, 2017](#)).

One distinguishing feature between explosion mechanisms is the symmetry of the ejecta. [Woosley et al. \(2007\)](#) modeled spectroscopically normal SNe Ia and found that in asymmetric explosions, the color evolution and Si II 6355 Å velocity evolution exhibit significant viewing-angle dependence. Additionally, [Maund et al. \(2010\)](#) found an empirical relation between the Si II 6355 Å velocity gradient, as originally defined by [Benetti et al. \(2005\)](#), and the polarization across the same line, which traces the degree of the Si asymmetry in the ejecta (see, e.g., [Wang & Wheeler 2008](#) for a review). Therefore, a

better understanding of the spectroscopic differences of SNe Ia is crucial to constraining their explosion mechanisms and ejecta geometries.

In this paper we present observations of SN 2019ein, an extreme HV SN Ia. Our early-time observations, beginning two weeks before maximum light, make SN 2019ein one of the best-studied HV SN Ia. The earliest spectral data at 14 days before B -band maximum light reveal some of the highest ejecta velocities ever measured. Perhaps more interestingly, the emission features in the P Cygni profile of SN 2019ein are blueshifted with respect to the redshift of its host galaxy. This systematic offset is greatest at very early times (several days after explosion) and gradually decreases as the SN evolves. Such a large emission shift sets SN 2019ein apart from other SNe Ia and hints at a puzzling explosion mechanism and ejecta geometry.

In Section 2.2, we detail our data acquisition, reduction, and analysis procedure. In Section 2.3, we present comprehensive early-time light curves from the near-ultraviolet (NUV) to the near-infrared (NIR), along with model fits and fitted parameters. In Section 2.4, we present spectra, measure velocities of absorption features, and compare observations with a delayed-detonation explosion model. In Section 2.5, we place limits on the nature of the progenitor system and the source of HV ejecta using early-time radio observations. In Section 2.6 we offer several possible explanations for the HV ejecta and blueshifted emission features exhibited by SN 2019ein. Finally, we conclude in Section 2.7.

2.2 Observations

SN 2019ein was discovered on MJD 58604.47 (2019 May 1.47) by the ATLAS survey at magnitude 18.194 in their cyan filter (Heinze et al. 2019). The last nondetection of the transient was by the Zwicky Transient Facility (Bellm et al. 2019) in r band at a

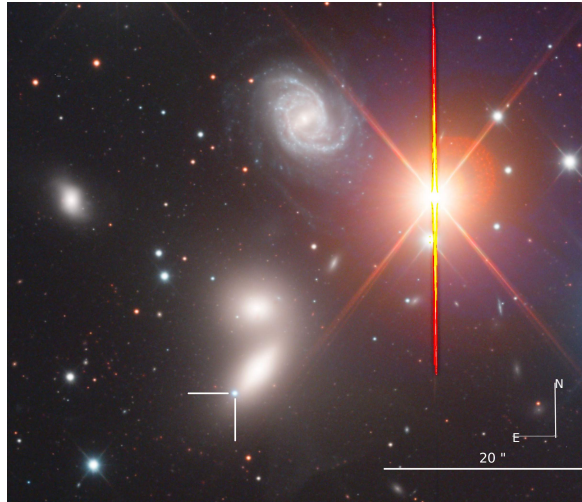


Figure 2.1: An RGB-color image of SN 2019ein (shown in the white crosshairs) in NGC 5353 along with its surrounding environment. A scale bar is shown in the bottom right corner. The image was produced using LCO 1m data files courtesy of Peter Iláš.

limit of 19.72 mag on MJD 58602.27 (2019 April 29.27), implying that SN 2019ein was discovered within two days after explosion. SN 2019ein exploded in the outskirts of NGC 5353, a lenticular galaxy in a nearby galaxy group. An image of NGC 5353 along with SN 2019ein is shown in Figure 2.1. Using surface brightness fluctuation measurements, J. Jensen et al. (2020, in preparation) measure the distance to NGC 5353 to be 32.96 ± 1.68 Mpc, and the redshift taken from the NASA/IPAC Extragalactic Database¹ is 0.00775.

We began daily photometric and spectroscopic follow-up observations of SN 2019ein starting on 2019 May 2 with the Global Supernova Project using Las Cumbres Observatory (LCO; Brown et al. 2013). Our first spectrum, obtained with the FLOYDS spectrograph on the 2m telescope at Haleakalā, allowed LCO to classify SN 2019ein as a young SN Ia (Burke et al. 2019). *UBgVri*-band data were obtained with the SBIG, Sinistro, and Spectral cameras on 0.4m, 1m, and 2m telescopes, respectively. With the PyRAF-based photometric reduction pipeline *lcogtsnpipe* (Valenti et al. 2016), PSF fitting was

¹<https://ned.ipac.caltech.edu>

performed (Stetson 1987). *UBV*-band photometry was calibrated to Vega magnitudes using Landolt standard fields (Landolt 1992), while *gri*-band photometry were calibrated to AB magnitudes using the Sloan Digital Sky Survey (SDSS; Albareti et al. 2017). Additionally, magnitudes were corrected for color terms using these standards. Because the SN was offset from the host galaxy, image subtraction was not necessary.

We obtained four epochs of NIR photometry in *JHK_s* filters with the 2MASS camera on the Minnesota-60" telescope on Mt. Lemmon, AZ, as part of the Arizona Transient Exploration and Characterization (AZTEC) program. The data were reduced and stacked with the IRAF² `-xdimsum` package. Aperture photometry was obtained with IRAF and calibrated to 20 local standards from the 2MASS catalog (Skrutskie et al. 2006).

We requested observations from the Ultraviolet and Optical Telescope (UVOT) on the Neil Gehrels Swift Observatory (Gehrels et al. 2004) after the detection of SN 2019ein. The first epoch of Swift data was obtained on MJD 58605.404 (2019 May 2.4), coincident with the first LCO photometric and spectroscopic epochs. Data were obtained in *uvw2*, *uvm2*, *uvw1*, *u*, *b*, and *v* filters and reduced using the data-reduction pipeline for the Swift Optical/Ultraviolet Supernova Archive (SOUSA; Brown et al. 2014), including applying aperture corrections and zero-points from Breeveld et al. (2011). Galaxy subtraction was not performed.

14 LCO spectra were obtained using the FLOYDS instruments on LCO 2m telescopes at Siding Springs and Haleakalā between -14 days to 60 days with respect to *B*-band maximum. Our spectra cover approximately the entire optical range from 3500 to 10000 Å at resolution $R \approx 300$ -600. Data were reduced using the `floydsspec` custom pipeline, which performs flux and wavelength calibration, cosmic-ray removal, and spectrum ex-

²IRAF is distributed by the National Optical Astronomy Observatories, which are operated by the Association of Universities for Research in Astronomy, Inc., under cooperative agreement with the National Science Foundation.

traction³. In addition, we obtained several spectra in the optical and NIR using the B&C Spectrograph on the Bok 90" telescope, the Blue Channel Spectrograph on the MMT at the Fred Lawrence Whipple Observatory, and the SpeX spectrograph (Rayner et al. 2003) in PRISM mode with a $0.5 \times 15''$ slit on the NASA Infrared Telescope Facility, which was obtained and reduced following the methods in Hsiao et al. (2019). These data are presented in Section 2.4.

2.2.1 Radio Observations

Radio observations of SN 2019ein were obtained with the Karl G. Jansky Very Large Array (VLA) on 2019 May 3 within two days of discovery. Two follow-up observations about a week apart were subsequently obtained. Each observation was 1 hr long, with 37.6 minutes time on source per block for SN 2019ein. All observations were taken in *C* band (4-8 GHz) in the *B* configuration (program: 19A-010, PI: L. Chomiuk). The observations were obtained in wide-band continuum mode, yielding 4 GHz of bandwidth sampled by 32 spectral windows, each 64 MHz wide sampled by 2 MHz wide channels. We used 3C286 as our flux and bandpass calibrator, and J1419+3821 as our phase calibrator.

We obtained the data sets processed by the VLA CASA calibration pipeline, run on CASA version 5.4.1.⁴ The pipeline consists of a collection of algorithms that automatically loads the raw data into a CASA measurement set (MS) format, flags corrupted data (e.g. due to antenna shadowing, channel edges, and radio frequency interference or RFI), applies various corrections (e.g. antenna position and atmospheric opacity) and derives delay, flux-scale, bandpass, and phase calibrations that are applied to the data.

For each epoch, the *C*-band data were split into 4-6 GHz and 6-8 GHz data sets, and each one was imaged using the CASA routine `tclean`. We use Briggs weighting

³https://github.com/svalenti/FLOYDS_pipeline/blob/master/bin/floydsspec

⁴<https://science.nrao.edu/facilities/vla/data-processing/pipeline>

of the data with a `robust=0.7` to provide reasonable balance of angular resolution and source sensitivity. We used multiterm, multifrequency synthesis as our deconvolution algorithm (set with `deconvolver='mtmfs'` in `tclean`), which performs deconvolution on a Taylor-series expansion of the wide-band spectral data in order to minimize frequency-dependent artifacts (Rau & Cornwell 2011). We set `nterms=2` which uses the first two Taylor terms to create images of intensity and spectral index. Multiple bright radio sources appear off-center in the 8.4' field of view, so we use “w-projection” (applied with `gridder='wproject'` in `tclean`) to account for non-coplanar effects when deconvolving these sources (Cornwell 2008). The radio nucleus of the host galaxy is the brightest radio source in the field (peak flux ~ 25 mJy) and forms artifacts near the site of the SN, so we performed a phase-only self-calibration with a solution interval of 2 minutes to further clean and reduce the RMS noise in the image. The cleaned and self-calibrated 6-8 GHz image was then convolved to the resolution of the 4-6 GHz image using `CONVL` in AIPS. Both images were then combined using `COMB` in AIPS, weighted by their respective RMS noise, to create the final *C*-band image (central frequency of 6 GHz) of the SN 2019ein field.

No radio source was detected at the site of SN 2019ein in any of the cleaned deconvolved images down to 3σ limits of $\sim 18 \mu\text{Jy}$ in the first image, and 25 and 23 μJy in the subsequent images. We discuss the constraints on progenitor models set by these limits in Section 2.5.

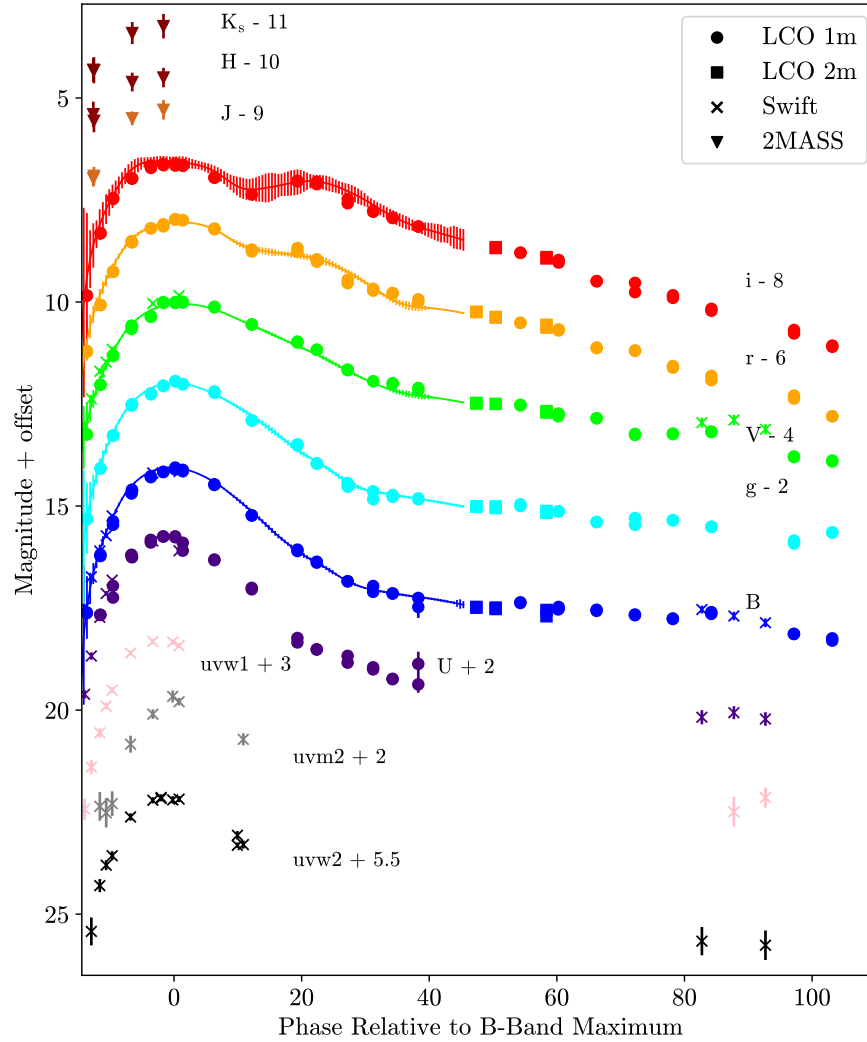


Figure 2.2: The NUV, optical, and NIR light curves of SN 2019ein, along with SALT2 fits and error bars to LCO data in $BgVri$ filters (solid lines). The LCO $UBgVri$ photometry is available as Data behind the Figure.

2.3 Photometric Results

2.3.1 Light Curves of SN 2019ein

Swift $uvw2$, $uvm2$, $uvw1$, Johnson-Cousins UBV , SDSS gri , and 2MASS JHK_s light curves are shown in Figure 2.2, along with SALT2 (Guy et al. 2007) fits to $BgVri$ data between -14 days and 40 days with respect to B -band maximum light. Our high-cadence

observations make the rise of this light curve extremely well-sampled. Because SN 2019ein was discovered quite early, we are able to tightly constrain the rise time and explosion time. Given the SALT2 fits to the light curve, we find the B -band maximum occurred at $\text{MJD } 58619.45 \pm 0.03$ (2019 May 16.5), which implies a rise time of ≈ 14 days since the beginning of observations and a maximum of 17 days since explosion (all phases hereafter are given in terms of B -band maximum light). Using an expanding fireball model, Kawabata et al. (2020) estimated the explosion time of SN 2019ein to be $\text{MJD } 58602.87 \pm 0.55$, giving a B -band rise time of ≈ 16.5 days, which is consistent with our estimates. This fast rise supports the suggestion that HV SNe tend to have shorter B -band rise times (Ganeshalingam et al. 2011).

SALT2 fitted parameters, corrected for host galaxy reddening by adopting the value presented in Kawabata et al. (2020), who estimate the host extinction as $E(B - V)_{\text{host}} = 0.09 \pm 0.02$ mag, are used to calculate a distance modulus of $\mu = 32.60 \pm 0.07$ (Betoule et al. 2014), which matches our measured distance modulus from J. Jensen et al. (2020, in preparation). Overall, the fitted parameters show that SN 2019ein is a photometrically normal SN Ia, albeit with a slightly lower absolute magnitude at peak brightness ($M_{B_{\text{max}}} = -18.81 \pm 0.059$) than expected. For a decline rate of $\Delta m_{15}(B) = 1.40 \pm 0.004$, SNe Ia have on average $M_{B_{\text{max}}} \approx -19$ (Hamuy et al. 1996). Therefore SN 2019ein falls slightly below the average, even with the modest reddening correction. We find good agreement between our estimated parameters and those derived in Kawabata et al. (2020), although our peak B -band absolute magnitude is fainter than their estimates, perhaps due to our use of a different distance modulus.

2.3.2 Color

The $B-V$ color evolution of SN 2019ein is plotted in Figure 2.3, along with the color curve of the delayed-detonation explosion model of Blondin et al. (2015), hereafter the B15 model. The model broadly matches the data at all phases, particularly around B -band maximum, although it tends to predict a bluer color at later phases. Similar trends can be seen in comparisons of other HV SNe with both the B15 model (Gutiérrez et al. 2016) and NV SNe (Wang et al. 2009). At early times, the $B-V$ color evolution matches the red group of Stritzinger et al. (2018), although among this sample SN 2019ein has a unique Branch classification in this sample (Branch et al. 2006), as described in Section 2.4.1. After correcting for host reddening, the $B-V$ color of SN 2019ein is 0.08 ± 0.04 around B -band maximum. This value falls in the overlap between the Normal and HV subsamples of Foley & Kasen (2011).

Additionally, we measure the NUV-optical colors using our Swift photometry. The $uvw1-v$ and $u-v$ colors one day after B -band maximum are 1.58 ± 0.08 and 0.25 ± 0.06 , respectively. These colors place SN 2019ein in the NUVR group of Milne et al. (2013), which is the group of most normal SNe Ia with $u-v < -0.4$ at maximum light. This is consistent with results that show HV and HVG SNe are all members of the NUVR group (Milne et al. 2013; Loyd et al. 2018). Given our velocity measurements discussed in Section 2.4, the colors of SN 2019ein fit those of other HV SNe well.

2.3.3 Bolometric Luminosity and ^{56}Ni Mass

Using our maximum-light photometry, we estimate the bolometric maximum luminosity and the corresponding ^{56}Ni mass. We follow the methods outlined in Howell et al. (2009): first, the measured flux at B -band maximum is calculated by integrating the magnitudes in U , g , r , and i filters to ensure optimal wavelength coverage of the opti-

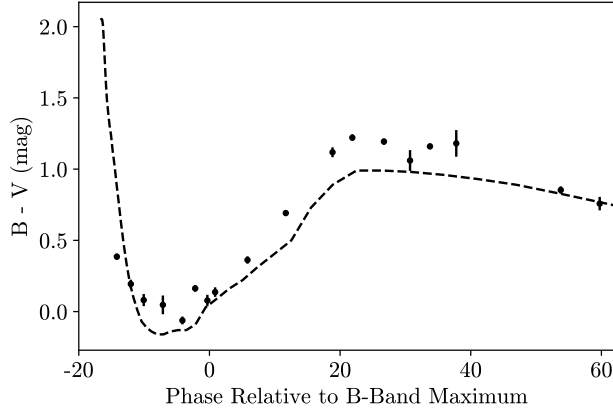


Figure 2.3: $B - V$ color data of SN 2019ein compared with the color curve of the B15 model of Blondin et al. (2015) for the HV SN 2002bo (dashed line). Only LCO 1m photometry data obtained before +60 days are presented. For clarity, observations taken on the same day have been median combined. The data have been corrected for Milky Way extinction; neither the data nor the model have been corrected for host galaxy extinction.

cal region. In order to calculate the flux across the rest of the spectrum, we adopted the synthetic spectrum produced by the B15 model. As we show in Section 2.4.3, this model produces close fits to the spectrum of SN 2019ein at maximum light. We scale the B15 spectrum flux to match the distance of SN 2019ein. Next we scale the flux of the synthetic spectrum within our filter wavelength ranges to match the observed flux. We then divide this “warped” flux by the ratio of the measured flux to the total flux in the synthetic spectrum, and define this quantity to be the bolometric flux.

Following this procedure, we find a maximum bolometric luminosity of $L \sim 7.28 \times 10^{42}$ erg s⁻¹. Using the relationship for the luminosity per ⁵⁶Ni mass \dot{S} from Howell et al. (2009),

$$\dot{S} = 6.31 \times 10^{43} e^{t_r/8.8} + 1.43 \times 10^{43} e^{t_r/111} \text{ erg s}^{-1} M_{\odot}^{-1} \quad (2.1)$$

which is based on Arnett’s rule (Arnett 1979), we calculate a ⁵⁶Ni mass of $\sim 0.33 M_{\odot}$ assuming a rise time of ≈ 16.5 days. This mass is on the low end for SNe Ia (Stritzinger et al. 2006), but is supported by the analytic relationship found in Könyves-Tóth et al.

(2020) between light-curve width and ^{56}Ni mass. Because SN 2019ein is a relatively fast decliner with $\Delta m_{15}(B) = 1.40$ and is slightly subluminous ($M_B = -18.81$), we conclude that this ^{56}Ni mass is a reasonable estimate.

2.4 Spectroscopic Analysis

Figure 2.4 (left) shows the spectral evolution of SN 2019ein, from -14 to 60 rest-frame days with respect to B -band maximum light. In our earliest spectrum (Figure 2.4, top right) the most striking features include the broad absorption trough centered at approximately 7500 \AA , which is most likely the result of blended Ca II and O I absorption at HVs ($> 30,000 \text{ km s}^{-1}$), as well as the broad Si II absorption centered at a wavelength less than 6000 \AA . The Si II absorption minimum corresponds to a velocity of approximately $24,000 \text{ km s}^{-1}$, which is one of the highest velocities ever measured in a SN Ia (Gutiérrez et al. 2016). Additionally, the Ca II H&K absorption feature is not well defined in this spectrum. This could be due to blending with other absorption lines, or it may be that the line is blueshifted outside of the sensitivity of our spectrograph, although such a blueshift would correspond to a seemingly unphysical velocity of $\sim 45,000 \text{ km s}^{-1}$. At this phase, the entire spectrum of SN 2019ein is noticeably blueshifted with respect to that of SN 2011fe. Before maximum light the blueshifts of the emission peaks remain prominent; the shifts are greatest in our first epoch, where both the Si II 6355 \AA and Ca II NIR components are displaced with velocities upward of $10,000 \text{ km s}^{-1}$ (Figure 2.4, bottom right).

Also seen in the earliest spectrum is a small absorption notch, denoted with a black arrow, at a rest-frame wavelength of approximately 6150 \AA . This feature is most likely C II 6580 \AA at $\approx 20,000 \text{ km s}^{-1}$, as there is also a possible absorption feature from the C II 7235 \AA line at the same velocity. Unburnt carbon in early-time spectra of SNe Ia is not

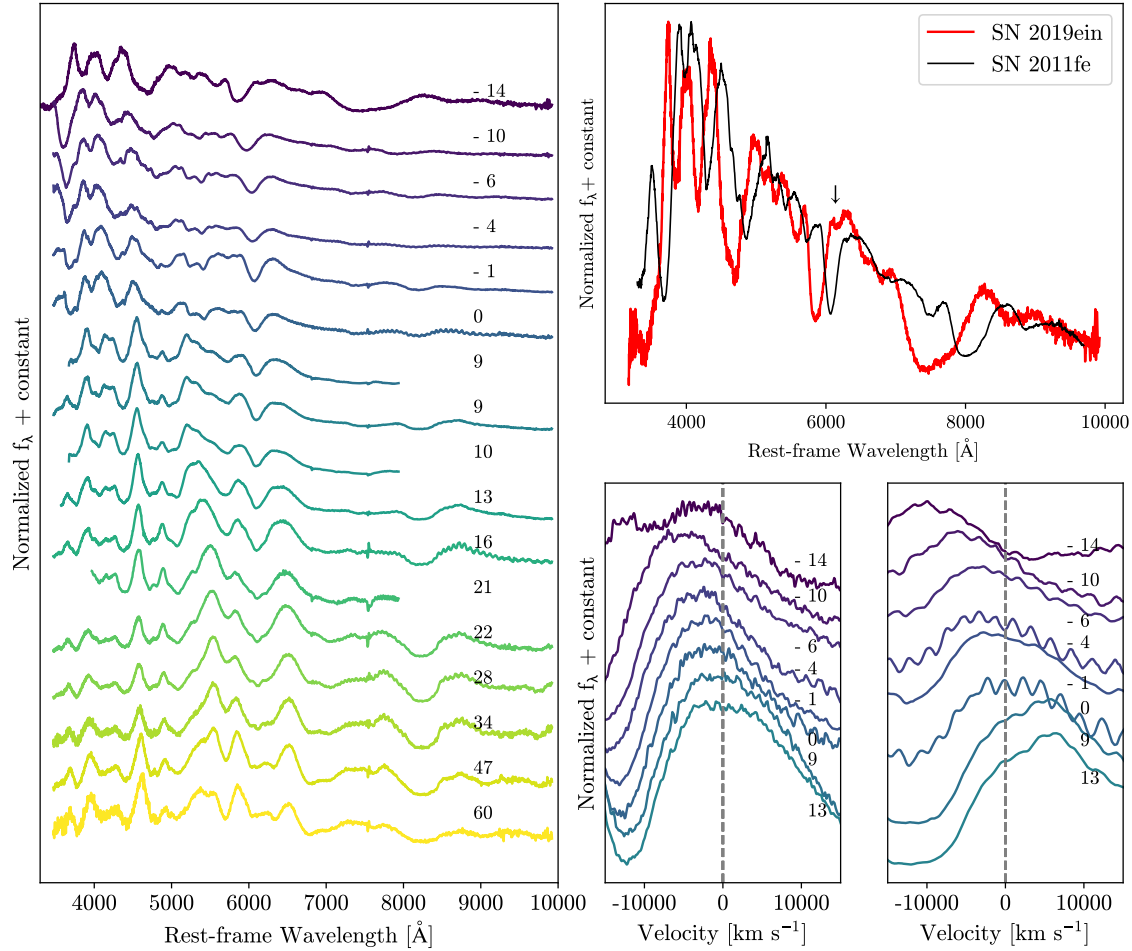


Figure 2.4: Left: the spectral evolution of SN 2019ein, from discovery 14 days before B -band maximum light until 60 days after B maximum. The phase with respect to B -band maximum is shown to the right of each spectrum. All fluxes are plotted on a linear scale. These spectra are available as Data behind the Figure. Top right: the spectrum of SN 2019ein at -14 days (red) compared with that of SN 2011fe at the same phase (black). A downward arrow denotes C II absorption in the spectrum of SN 2019ein. Bottom right: the emission components of the Si II 6355 \AA (left) and Ca II NIR (right) P Cygni profiles from -14 days to 13 days with respect to B -band maximum light. The rest wavelengths of these features are shown with dashed lines. We caution that the apparent redshift of the Ca II NIR emission component after maximum light is most likely due to line overlap.

unusual (e.g. Parrent et al. 2011; Blondin et al. 2012; Folatelli et al. 2012; Lusso et al. 2012; Maguire et al. 2014); however, few SNe Ia show Si II 6355 Å absorption velocities higher than C II 6580 Å absorption velocities at early times (Parrent et al. 2011; Folatelli et al. 2012; Lusso et al. 2012), with a notable exception being SN 2011fe (Parrent et al. 2012; Pereira et al. 2013). The fact that SN 2019ein shows the opposite trend at this phase may shed light on the explosion mechanism and ejecta geometry. Parrent et al. (2011) note that $v_{\text{C II}}/v_{\text{Si II}} < 1$ if the C II feature comes from an asymmetric ejecta distribution viewed at an angle with respect to the observer’s line of sight.

Close to *B*-band maximum, we note a possible HVF in the Ca II H&K line, as a weaker, lower velocity component becomes visible at roughly -4 days. However, HVFs usually develop at earlier phases, and this feature we observe is equally well fit by Si II absorption, making identification of HVFs at this phase difficult. Except for this exception, we do not find evidence for HVFs in the spectra of SN 2019ein, and all the velocities we report here are measured from the center of the dominant absorption feature for each line. The lack of two distinct absorption components sets SN 2019ein apart from most other HV SNe Ia. We discuss possible reasons for this difference in Section 2.6.

Using the MMT Observatory, we obtained a medium-resolution ($R \approx 3900$) spectrum centered on the Si II 6355 Å absorption feature at +18 days with respect to *B*-band maximum (Figure 2.5). At this phase, the feature takes on an unusual asymmetric appearance. In particular, there appear to be multiple overlapping absorption troughs, each with a different line strength and Doppler shift. This may be caused by significant Si II mixing at this epoch, in which different distributions of Si II are moving at different velocities. This possibility is explored further in Section 2.6.

By approximately three weeks after maximum light, the Si II feature begins to blend with iron-group element (IGE) lines that dominate the spectrum. These IGE features, marked with black arrows, are most easily seen in the NIR spectrum obtained 32 days

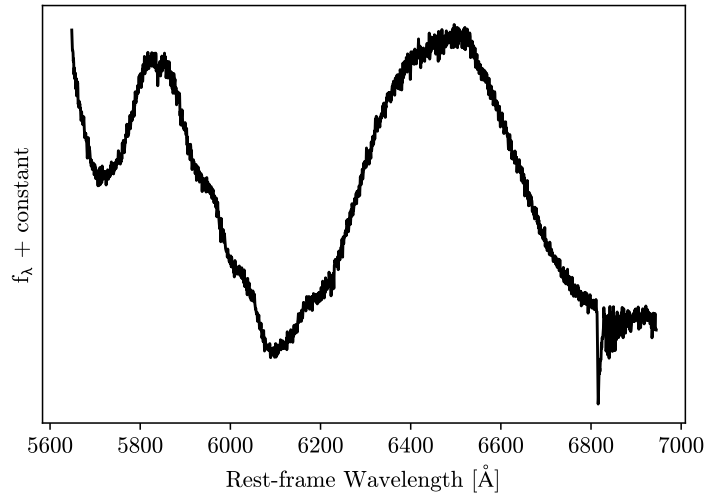


Figure 2.5: A medium-resolution spectrum of SN 2019ein, obtained with the MMT spectrograph at +18 days with respect to B -band maximum light, centered on the Si II 6355 Å absorption feature. Wavelengths have been shifted to the rest frame.

after B -band maximum, shown in Figure 2.6. Line blanketing from IGEs are seen in between the two telluric regions and at wavelengths greater than $2.0 \mu\text{m}$. At this later phase, most C I and intermediate-mass element (IME) lines, usually seen around maximum light (e.g. Hsiao et al. 2013, 2015), have disappeared from the NIR spectrum.

2.4.1 Branch Classification

Branch et al. (2006) showed that the ratio of the pseudo-equivalent width (pEW) of the Si II 6355 Å absorption line to that of the Si II 5972 Å line can be used as a spectroscopic classification of SNe Ia. Here we classify SN 2019ein in the same way. We measure the pEWs with the following procedure: first, the spectrum is smoothed with a Savitzky-Golay filter to reduce the effects of noise. Next, the absorption feature of interest is defined and maxima blueward and redward of the absorption minimum along the continuum are found. We define the pseudo-continuum as simply the linear curve connecting the two maxima, so long as the curve does not intersect the spectral feature.

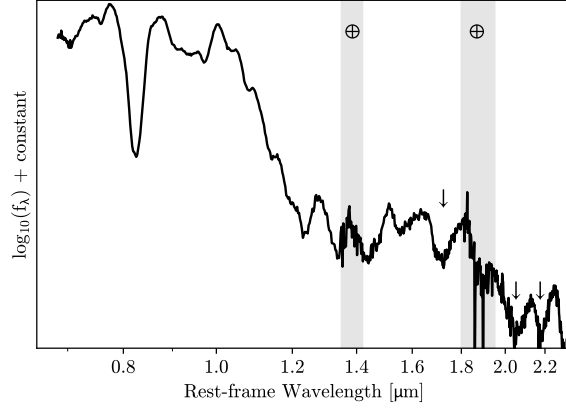


Figure 2.6: An NIR spectrum of SN 2019ein, obtained with the SpeX spectrograph via low-resolution PRISM mode on the NASA Infrared Telescope Facility at +32 days with respect to B -band maximum light. Wavelengths have been shifted to the rest frame and fluxes have been plotted in logarithmic units. The gray shaded regions denote wavelengths with strong telluric features, while black arrows denote possible IGE absorption features.

Finally, the pEW is calculated using the formula (e.g. [Garavini et al. 2007](#))

$$\text{pEW} = \sum_{i=0}^{N-1} \Delta\lambda_i \left(\frac{f_c(\lambda_i) - f(\lambda_i)}{f_c(\lambda_i)} \right) \quad (2.2)$$

, where $f(\lambda_i)$ is the measured flux, $f_c(\lambda_i)$ is the flux of the pseudo-continuum, and $\Delta\lambda_i = \lambda_{i+1} - \lambda_i$ is the size of the wavelength bin at each wavelength interval λ_i .

At maximum light, we find that the pEW of Si II 6355 is $125 \pm 2.1 \text{ \AA}$ and the pEW of Si II 5972 is $22.5 \pm 2.8 \text{ \AA}$. The corresponding Branch diagram is plotted in [Figure 2.7](#). Compared to the sample from [Blondin et al. \(2012\)](#), SN 2019ein falls within the broad-line (BL) region of parameter space. This classification agrees with that presented in [Kawabata et al. \(2020\)](#). The right side of [Figure 2.7](#) shows the pEW of Si II 6355 \AA versus the velocity of the Si II 6355 \AA absorption feature at maximum light, labeled by spectroscopic subtype. Here SN 2019ein lies within the population of HV SNe. [Blondin et al. \(2012\)](#) find a correlation between BL SNe and HV SNe, according to the [Wang et al. \(2009\)](#) classification scheme.

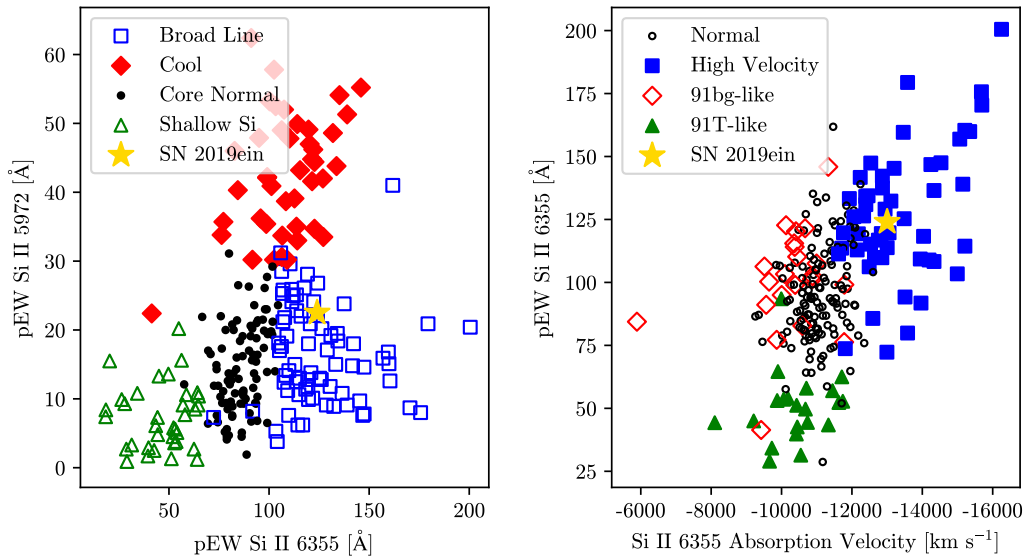


Figure 2.7: Left: pEW of Si II 5972 Å plotted against the pEW of Si II 6355 Å at B -band maximum light, according to Branch et al. (2006). Different Branch classifications are given by different colored symbols. SN 2019ein is shown with a gold star. Right: pEW of Si II 6355 Å versus Si II 6355 Å absorption velocity at B -band maximum light. Here different symbols correspond to different spectral subclasses of SNe Ia. Sample data are obtained from Blondin et al. (2012).

2.4.2 Absorption Velocities

SN 2019ein shows some of the highest expansion velocities of any SNe Ia in its early-time spectra. Velocities were calculated following the method outlined in Childress et al. (2014): first we select the absorption line of interest and define a pseudo-continuum by fitting a linear curve to the continuum maxima on both sides of the absorption trough. We normalize the flux with respect to this pseudo-continuum before fitting a Gaussian to the normalized absorption line. The minimum of the Gaussian is taken to be the Doppler-shifted observed wavelength, and the expansion velocity is calculated by comparing this measured absorption minimum to the known rest value of the line.

Figure 2.8 compares the Si II 6355 Å and Ca II H&K absorption velocity evolution of SN 2019ein to several other HV SNe Ia from Gutiérrez et al. (2016). These objects

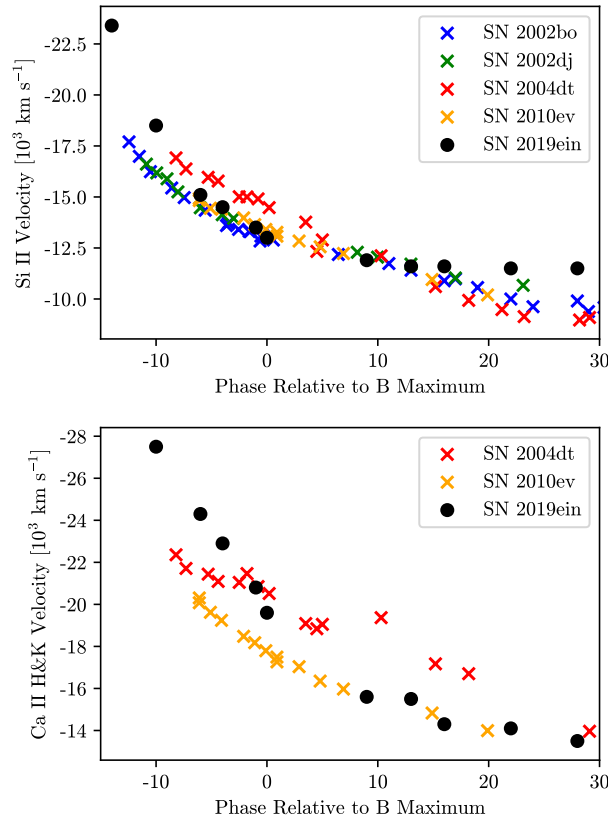


Figure 2.8: The Si II 6355 Å (top) and Ca II H&K (bottom) absorption velocity evolution from -14 days to 30 days for SN 2019ein, compared to a sample of other HV SNe (from Gutiérrez et al. 2016).

all show similar spectral features (Figure 2.9), including strong Ca II NIR absorption at early times, broad Si II 6355 Å absorption at maximum light, and HV Si II and Ca II before maximum. We do not report a Ca II H&K velocity -14 days with respect to *B*-band maximum light because at this epoch, no clear absorption minimum is identified within the wavelength range of our spectrograph.

The velocity evolution of all lines is rapid. The first epoch, corresponding to 14 days before maximum light and at most 3 days after explosion, shows the highest Si II velocity in this sample. By maximum light, the ejecta velocity remains high, yet falls within the range of the other HV SNe. After maximum light, we measure a velocity gradient to the

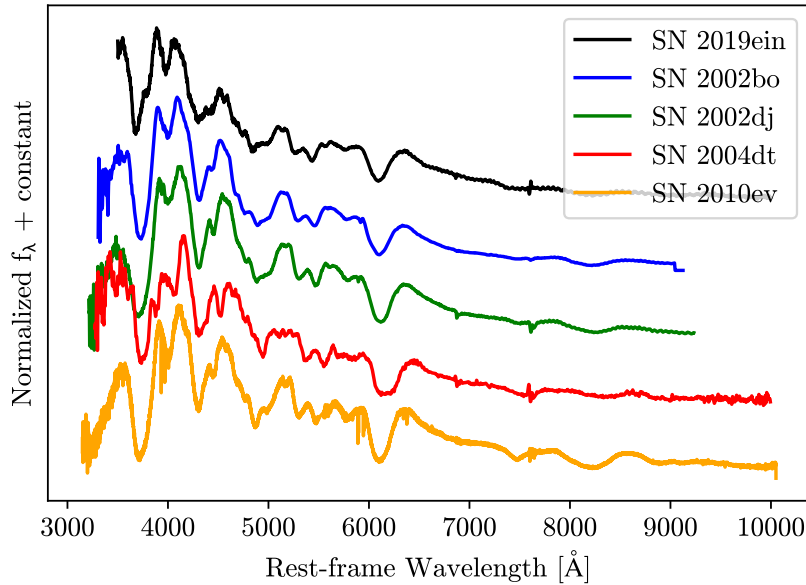


Figure 2.9: Spectra of SN 2019ein and four other HV SNe at -4 days with respect to B -band maximum light (from [Gutiérrez et al. 2016](#) and [Altavilla et al. 2007](#)).

Si II velocity following the example of [Blondin et al. \(2012\)](#), who found that measuring the change in Si II velocity between maximum light and 10 ± 2 days after maximum gives the most consistent result. Using this method, we calculate a Si II velocity gradient $\dot{v} = 122 \pm 25 \text{ km s}^{-1} \text{ day}^{-1}$, placing SN 2019ein in the HVG class ([Benetti et al. 2005](#)).

2.4.3 Comparison to a Delayed-detonation Explosion Model

[Dessart et al. \(2014\)](#) found that delayed-detonation explosions best model BL HVG SNe Ia. Additionally, [Kawabata et al. \(2020\)](#) found that the observed properties of SN 2019ein match those seen in the delayed-detonation models of [Iwamoto et al. \(1999\)](#). Figure 2.10 compares the spectra of SN 2019ein at various phases to delayed-detonation model spectra produced by [Blondin et al. \(2015\)](#). The B15 model simulates the spherically symmetric delayed-detonation of a Chandrasekhar-mass WD, imposed with radial mixing to match abundance stratifications observed in SNe ejecta, particularly those of

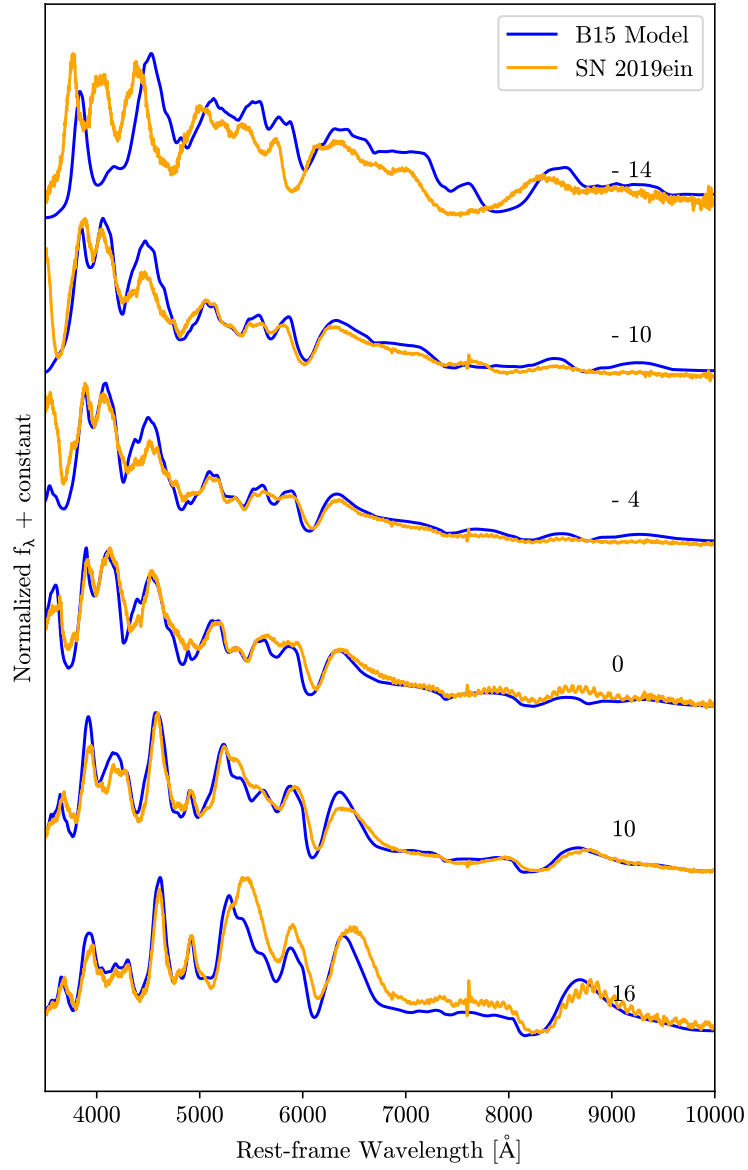


Figure 2.10: Spectra of SN 2019ein (orange) compared with the B15 synthetic spectra (blue; [Blondin et al. 2015](#)). Shown at the top right of every spectrum is the corresponding phase with respect to B -band maximum light.

IMEs and IGEs. Synthetic spectra from explosion to nearly 100 days after maximum light are produced.

Beginning 10 days before B -band maximum, the synthetic spectra match the strengths and velocities of most of the absorption features, including the Si II 6355 Å and Ca II NIR and H&K troughs. However, at our earliest epoch of -14 days, the spectrum of SN 2019ein significantly deviates from the B15 model spectrum at the same phase. The model fails to reproduce the extremely high absorption velocities, the broad mix of O I and Ca II NIR absorption, and the overall blueshift of the emission features with respect to the rest frame of the galaxy. The authors found similar discrepancies when they compared the earliest model spectra to the early-time spectra of SN 2002bo, and suggested that this may be due to underestimated outward mixing or a more complicated explosion than their one-dimensional, spherically symmetric model. Observational evidence for this enhancement of IMEs in the outer layers of the ejecta, possibly due to an extended burning front or significant mixing, was also found for SN 2002bo (Benetti et al. 2004) and the HV SN 2004dt (Altavilla et al. 2007).

In order to investigate the cause of this discrepancy, we now explore possible sources of the HV ejecta in SN 2019ein, including interaction with a circumstellar shell of material from the progenitor system or mixing and optical depth effects in the ejecta.

2.5 Progenitor Constraints from Radio Observations

Radio emission is a sensitive probe of the progenitor environment (which we will refer to as circumstellar medium, or CSM). The CSM is modified by mass loss from the progenitor in the pre-SN stage, and interaction of the SN ejecta with this CSM accelerates electrons to relativistic energies and amplifies the ambient magnetic field, producing synchrotron radio emission (Chevalier 1982, 1984, 1998). Simple models of radio emis-

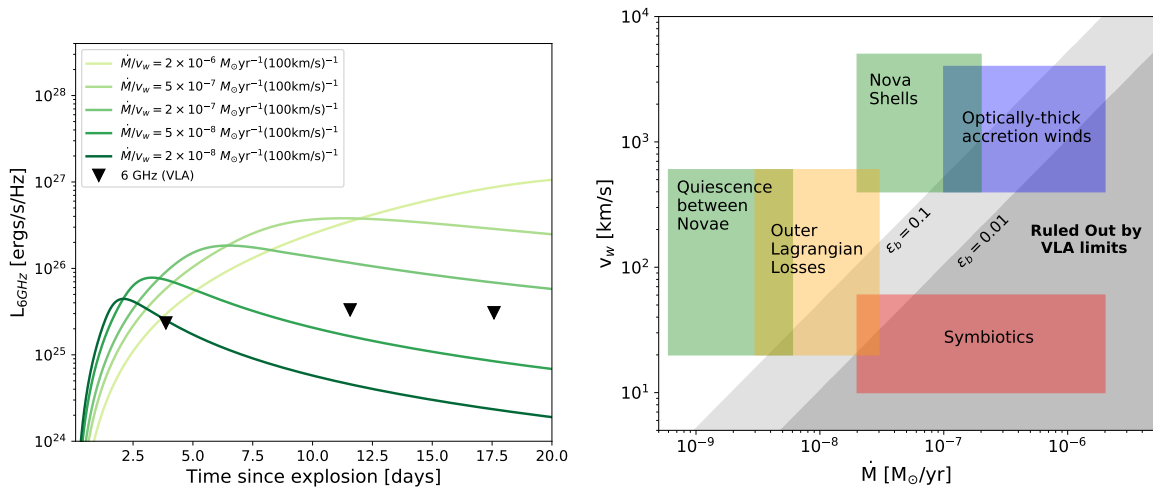


Figure 2.11: (a) 6 GHz radio light curves from the r^{-2} wind model (Section 2.5.1) for different ratios of constant mass-loss rates (\dot{M}) and wind velocities (v_w). The 3σ 6GHz VLA upper limits are shown as black triangles. (b) The parameter space of $\dot{M}-v_w$. The colored regions show approximate parameter spaces expected for different single-degenerate progenitor models as defined in Figure 3 of Chomiuk et al. (2012). The light and dark gray regions represent the parameter space of the r^{-2} model that is ruled out by our VLA upper limits. These regions are defined by $\dot{M}/v_w > 1.9 \times 10^{-10} M_\odot \text{yr}^{-1} (\text{km s}^{-1})^{-1}$ assuming $\epsilon_b = 0.1$, and $\dot{M}/v_w > 9.5 \times 10^{-10} M_\odot \text{yr}^{-1} (\text{km s}^{-1})^{-1}$ assuming $\epsilon_b = 0.01$ (see Section 2.5.1 for details)

sion have provided constraints on the CSM environment and progenitor properties for both core-collapse (e.g. [Ryder et al. 2004](#); [Chevalier & Fransson 2006](#); [Soderberg et al. 2006](#); [Weiler et al. 2007](#); [Salas et al. 2013](#)) and SNe Ia ([Panagia et al. 2006](#); [Chomiuk et al. 2016](#)). Radio emission is yet to be detected from a SN Ia, but nondetections have provided stringent constraints on progenitor scenarios ([Chomiuk et al. 2016](#)), particularly for nearby events such as SN 2011fe ([Horesh et al. 2012](#); [Chomiuk et al. 2012](#)) and SN 2014J ([Pérez-Torres et al. 2014](#)). We can similarly interpret possible progenitor scenarios of SN 2019ein by comparing our VLA observations with models of radio emission from circumstellar interaction.

2.5.1 Wind Model ($\propto r^{-2}$)

For single-degenerate progenitors, a fraction of the mass, transferred via accretion from a nondegenerate companion, is expected to be lost in the form of a wind. [Chevalier \(1982\)](#) created a simple parametric model of such a wind, characterized by a constant mass-loss rate (\dot{M}) and wind velocity (v_w), which leads to a CSM whose density (ρ) varies with radius (r) as

$$\rho = \frac{1}{4\pi r^2} \left(\frac{\dot{M}}{v_w} \right) \tag{2.3}$$

The synchrotron radio light curve from a shock propagating through such a CSM is described in [Chevalier \(1982\)](#) and [Chevalier \(1998\)](#). In this work, we follow the formalism of [Chomiuk et al. \(2016\)](#) (hereafter C16), who adopted the self-similar solutions of [Chevalier \(1982\)](#) for radio observations of SNe Ia. We assume a Chandrasekhar-mass WD progenitor that exploded with 10^{51} erg of kinetic energy, consistent with our optical observations, and a steep outer ejecta profile of $\rho_{ej} \sim v_{ej}^{-10}$ interacting with the above CSM. Electrons are accelerated to a power-law spectrum ($\sim E^{-p}$, with $p = 3$). The average fraction of the shock energy shared by the cosmic-ray electrons and the amplified

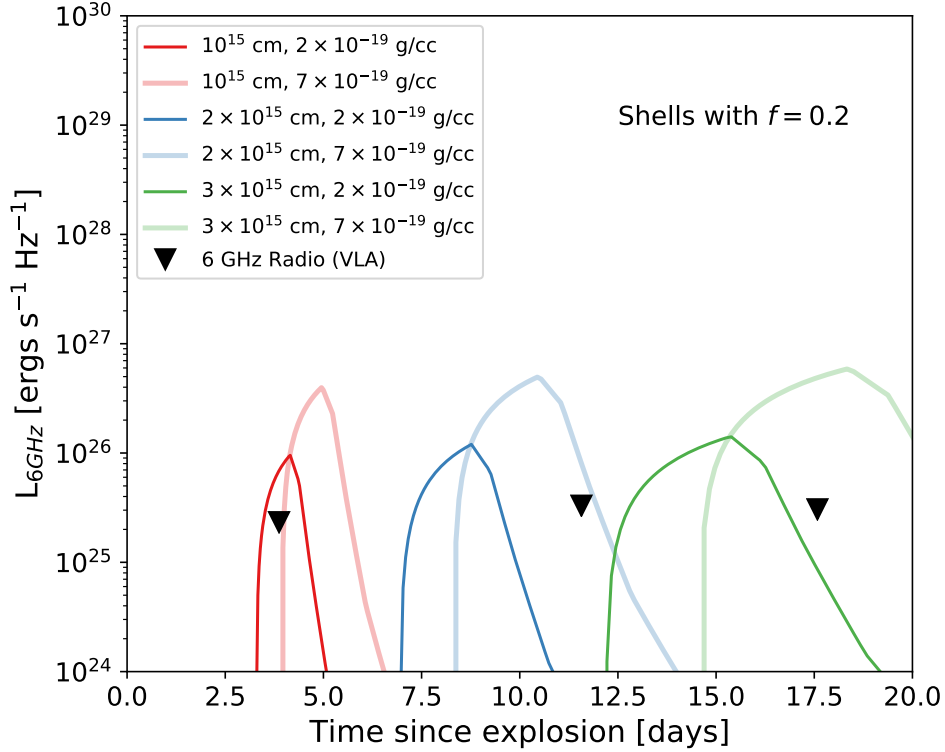


Figure 2.12: Light curves from the shell model of H16 for a shell of fractional width, $f = 0.2$. The colors are for different shell radii, and the different shades are for different densities. The black triangles show the 3σ upper limits from our VLA observations.

magnetic field in the shock vicinity is parameterized as ϵ_e and ϵ_b respectively. As in Chomiuk et al. (2012) and Chomiuk et al. (2016), we set $\epsilon_e = 0.1$ and $\epsilon_b = [0.1, 0.01]$, consistent with values expected in Type Ib/c SNe (Chevalier & Fransson 2006; Sironi & Spitkovsky 2011; Soderberg et al. 2012).

The light-curve models for different values of the free parameters \dot{M} and v_w are shown in Figure 2.11(a). The rising part of the light curves corresponds to the regime where the ejecta are still optically thick to synchrotron self-absorption at 5 GHz. When the ejecta are optically thin, the light curve declines. Higher ratios of \dot{M}/v_w correspond to denser outflows, which leads to brighter light curves and a delayed transition to the optically thin stage, which explains why the peaks are shifted to later epochs.

Figure 2.11(b) shows our constraints on the \dot{M}/v_w parameter space from the VLA

upper limits in Section 2.2.1. We are able to rule out the parameter space for $\dot{M}/v_w > 1.9 \times 10^{-10} M_\odot \text{ yr}^{-1} (\text{km s}^{-1})^{-1}$ for $\epsilon_e = \epsilon_b = 0.1$. For $\epsilon_e = 0.1$ and $\epsilon_b = 0.01$, we find that $\dot{M}/v_w > 9.5 \times 10^{-10} M_\odot \text{ yr}^{-1} (\text{km s}^{-1})^{-1}$.

The above constraints on \dot{M}/v_w can provide some insight into possible single-degenerate progenitor models for SN 2019ein by comparing with typical values of \dot{M} and v_w expected in these models as compiled in Chomiuk et al. (2012). Our observations are sensitive enough to rule out symbiotic progenitors, i.e. a WD that accretes from the wind of a giant companion, which is generally characterized by $\dot{M} > 10^{-8} M_\odot \text{ yr}^{-1}$ and $v_w \approx 30 \text{ km s}^{-1}$ (Seaquist & Taylor 1990; Chen et al. 2011; Patat et al. 2011). A symbiotic channel was also deemed unlikely for the nearest events SN 2011fe and SN 2014J, and was found to contribute no more than 16% of a sample of 85 SNe Ia with available radio observations studied by (Chomiuk et al. 2016). For $\epsilon_e = 0.1$ and $\epsilon_b = 0.01$, our increased upper limit of $\dot{M}/v_w > 9.5 \times 10^{-10} M_\odot \text{ yr}^{-1} (\text{km s}^{-1})^{-1}$ still excludes the majority of symbiotic progenitors observed in the Galaxy (Seaquist et al. 1993; Chomiuk et al. 2016).

White dwarfs can also be in single-degenerate systems with a main-sequence or a slightly evolved companion undergoing mass transfer via Roche-lobe overflow. For mass accretion rates $\gtrsim 3 \times 10^{-7} M_\odot \text{ yr}^{-1}$, steady nuclear burning occurs on the surface of the WD, and about $\sim 1\%$ of the mass is lost from the outer Lagrangian point with velocities of about a few 100 km s^{-1} (Shen & Bildsten 2007). The expected \dot{M}/v_w in such a scenario falls within our VLA limits, and therefore such a progenitor channel cannot be ruled out for SN 2019ein from our radio observations alone. With increasing accretion rate, however, the nuclear burning shell will drive fast optically thick winds with $v_w \approx \text{few} \times 1000 \text{ km s}^{-1}$ (Hachisu et al. 1999), and some part of this parameter space is ruled out by our VLA upper limits. For accretion rates $\approx (1 - 3) \times 10^{-7} M_\odot \text{ yr}^{-1}$, the steady burning will be interrupted by recurrent nova flashes. Novae with short recurrence time will likely create a series of dense shells with which the SN shock will

interact, and such shells typically have values of \dot{M} and v_w as shown in Figure 2.11(b). For longer recurrence times, the SN shock is more likely to interact with CSM created with a steady wind with $\dot{M} \approx 10^{-9} - 10^{-8} M_\odot \text{ yr}^{-1}$ in between distant novae shells (Wood-Vasey & Sokoloski 2006). Both these cases are allowed within our upper limits in the context of the r^{-2} model, but we will also analyze the presence of nova shells with a more appropriate shell-interaction model in Section 2.5.2.

We note here the importance of radio observations taken soon after explosion or discovery for SNe Ia. The first observation, which was triggered < 2 days of discovery and $\lesssim 4$ days of explosion, provided a constraint that is almost a factor of five deeper on \dot{M}/v_w than the observation a week later (Figure 2.11(a)). This is because lower \dot{M}/v_w shifts the peak of the radio light curve to earlier times, as seen in Figure 2.11(a). The prompt observation resulted in more stringent constraints on Type Ia progenitor models involving symbiotic systems and optically thick winds.

2.5.2 Shell Interaction Model

Interaction and acceleration of material in solar-composition CSM shells has been proposed as a way to explain HVEs in Type Ia spectra (Gerardy et al. 2004; Mulligan & Wheeler 2018, 2017). Such shells can be expected in WD progenitors that undergo nova outbursts. Shells can consist of recently ejected material or of swept-up material from previous outbursts. Shock interaction with such a shell can produce detectable radio emission, and radio light curves for such a CSM created by discrete mass-loss events cannot be appropriately described by a continuous mass-loss model.

We therefore use the models described in Nayeri et al. (2016), hereafter H16, for radio emission from a CSM shell interacting with SN ejecta. H16 performed hydrodynamical simulations of a $\rho_{ej} \sim v_{ej}^{-10}$ ejecta profile interacting with a single, solar-metallicity, fully

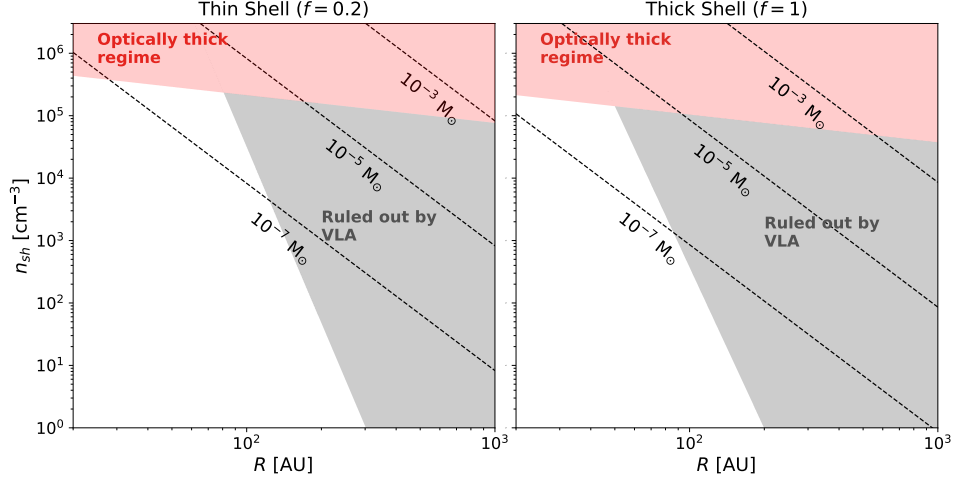


Figure 2.13: Parameter space of the CSM shell radii R versus shell density $n_h = \rho_{sh}/\mu m_p$, where ρ_{sh} is the density in units of g cm^{-3} , $\mu = 1.4$, and $m_p = 1.67 \times 10^{-24}$ g. Dashed lines in both panels correspond to lines of constant shell mass $M_{sh} = 4/3\pi\rho_{sh}R^3[(1+f)^3 - 1]$. The left panel corresponds to a thin shell, while the right panel corresponds to a thick shell. The gray shaded region is the parameter space where the H16 light curves are inconsistent with the constraints described in Section 2.5.2. The red shaded region is where optical depth due to synchrotron self-absorption is > 1 and the optically thin ejecta assumption of H16 is no longer valid.

ionized shell defined by an inner radius R , fractional width $f = \Delta R/R$, and constant shell density ρ_{sh} . Interaction creates a forward shock in the shell and a reverse shock in the ejecta, but the dynamics do not reach self similarity, unlike in the [Chevalier \(1982\)](#) case. The forward shock subsequently accelerates the CSM and sets it in free expansion.

In the optically thin approximation, the H16 light-curve model can be analytically expressed in terms of f , ρ_{sh} and R (see Eqs. 5-13 in H16). Figure 2.12 shows example light curves from the H16 model. The light curves are characterized by a rapid brightening at the beginning of the interaction, reaching a peak luminosity when the forward shock reaches the outer edge of the CSM shell, and a steep decline once the shock breaks out.⁵ For larger f , the light curves peak at later times because the shock takes longer to reach

⁵The model assumes a vacuum outside the shell region. The decline phase will therefore likely be modified when there is a progenitor wind present beyond the shell (C. E. Harris et al. 2020, in preparation).

the CSM outer edge. For larger R , the light curves begin at a later time, and larger ρ_{sh} produces brighter light curves.

Similar to the analysis in [Cendes et al. \(2020\)](#), we explore the parameter space of R - ρ_{sh} for a given f that produces light curves within our VLA upper limits at the observed epochs. We explore two cases of shells: a thin shell ($f = 0.2$) characteristic of shells expected in nova eruptions, and a thick shell ($f = 1$) to show the effects of increasing shell width. Similar to the wind model, the shell models assume a standard Chandrasekhar-mass WD explosion with 10^{51} erg of kinetic energy, and $\epsilon_e = \epsilon_b = 0.1$. We also use an additional constraint: the peak of the light curve must occur before the first epoch (i.e. at 3.87 days after explosion). This is because any shell interaction leading to HV absorption features must have occurred before the first spectral observation (i.e. after the shell has been accelerated by the forward shock, [Gerardy et al. 2004](#)).

Figure 2.13 shows the result of applying the H16 shell models to our VLA observations. For our fiducial model parameters in both the thin and thick shell cases, the VLA limits only allow CSM shells $\lesssim 10^{-6} M_{\odot}$ within radii < 100 AU. In comparison, CSM masses $\sim 10^{-3} - 10^{-2} M_{\odot}$ are generally required to explain HVFs observed in SNe Ia ([Gerardy et al. 2004](#)). We note that this conclusion remains unchanged even when we assume $\epsilon_b = 0.01$ because the shaded region in Figure 2.13 is determined primarily by the condition that the peak of the light curve must occur before the first epoch, as mentioned previously. As explained in H16, the light curve peaks when the shock reaches the outer edge of the shell and is thus mainly a hydrodynamical timescale, which is independent of the parameter ϵ_b that affects only the radio emission.

A caveat, however, is that the H16 model approximates the radio emission as optically thin, whereas at densities $> 10^5 \text{ cm}^{-3}$ for the radii explored here, effects such as synchrotron self-absorption, free-free absorption, and radiative cooling of the shock gas will become important. Light-curve models in this optically thick regime would require a

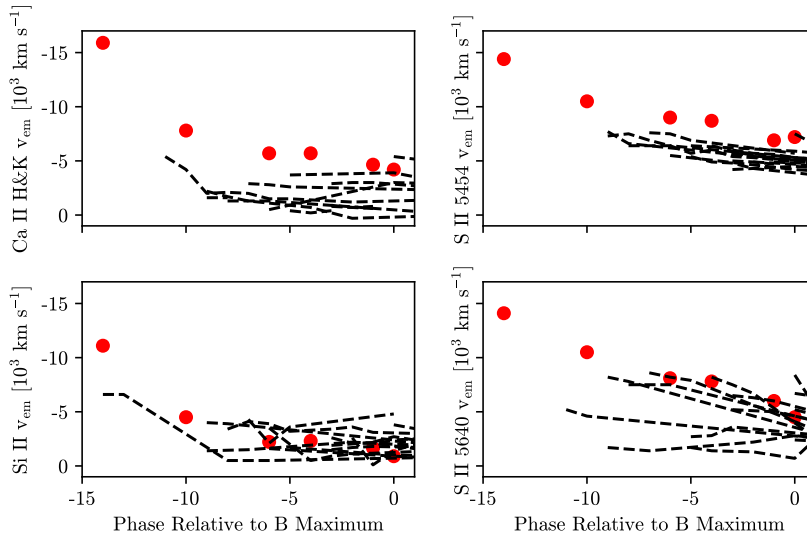


Figure 2.14: The emission peak Ca II H&K (top left), Si II 6355 Å (bottom left), S II 5454 Å (top right), and S II 5640 Å (bottom right) velocities of SN 2019ein, shown in red, compared against the low-redshift sample from Blondin et al. (2006), shown in dashed black, from -14 days to 0 days with respect to B -band maximum light.

formal solution of the radiative transfer equation, which will be explored in an upcoming paper (C. E. Harris et al. 2020, in preparation), and will help provide more accurate constraints on the presence of dense and massive CSM shells.

2.6 Mixing and Optical Depth Effects

The high emission velocities before maximum light make SN 2019ein unusual, even among HV SNe Ia. More specifically, although P Cygni emission blueshifts have been theoretically predicted and observed in Type II SNe (Dessart & Hillier 2005) and were discussed by Blondin et al. (2006) in a sample of low-redshift SNe Ia, the emission velocities seen in the spectra of SN 2019ein are the highest ever measured. Figure 2.14 shows the evolution of the emission velocities for four lines in the spectra of SN 2019ein compared to the sample from Blondin et al. (2006). It is clear that at early times, the emission peaks in SN 2019ein are substantially more blueshifted than in any of the objects

in the comparison sample. This extreme behavior is most clearly seen in the plots of the Ca II H&K and S II emission velocities, where the emission velocities at -14 days with respect to B -band maximum are $\approx 15,000 \text{ km s}^{-1}$. At the same phase, the Si II emission component of the P Cygni profile is blueshifted by $\approx 10,000 \text{ km s}^{-1}$. Even around maximum light, the velocities of these lines are among the highest ever measured. After maximum, the emission peaks are either no longer resolvable or become distorted due to line overlap, possibly of multiple Doppler-shifted emission features (see Figure 2.5). Here we only present emission velocities up to B -band maximum, where we trust our measurements have not been biased.

In order to investigate whether specific ejecta compositions or abundance enhancements could cause both the high absorption and emission velocities at early times, we compare SYN++ (Thomas et al. 2011) model spectra to our spectrum of SN 2019ein at -10 days. In particular, we focus on the Si II 6355 Å feature and test whether multiple components of the ejecta, such as a HV component with a velocity above the photospheric velocity (PV), can reproduce the measured Doppler shifts.

Our synthetic spectrum is shown in Figure 2.15 compared to our spectrum of SN 2019ein at -10 days. We find that an ejecta with only a HV Si II component offset from the PV by several thousand km s^{-1} provides the best fit to our data. This matches the lack of separate HVFs and PVFs, particularly in the Si II and Ca II lines, at early times in our observed spectra, as well as the analysis of our radio observations, which places stringent constraints on the mass of a CSM shell, which has been proposed to produce HVFs. Altogether, this indicates that only a HV Si II component is present in the ejecta of SN 2019ein. We attempt to explain the existence of this HV component as being due to ejecta mixing from an asymmetric explosion or being caused by optical depth effects in the outer layers of the ejecta.

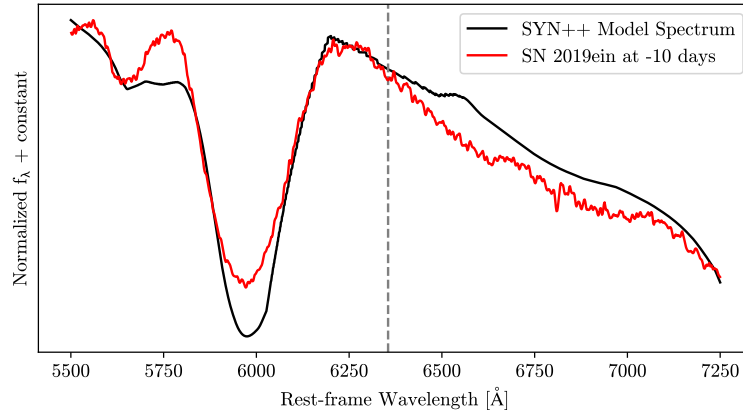


Figure 2.15: SYN++ synthetic spectrum (black) of the Si II 6355 Å feature at -10 days with respect to *B*-band maximum, compared to the spectrum of SN 2019ein at the same epoch (red). Our synthetic spectrum contains only a HV Si II component offset from the photospheric velocity by 2,500 km s⁻¹. The rest wavelength of the Si II emission peak is represented by a dashed vertical line.

2.6.1 Evidence for Asymmetries

In Section 2.4.3 we discuss that objects similar to SN 2019ein exhibit significant mixing of their IMEs to higher velocities. This may be evidence of an aspherical ejecta distribution due to an asymmetric explosion, in which clumps of IMEs are mixed to higher velocities along the observer’s line of sight, producing HV absorption and emission features. Similar clumps are produced in models of off-center delayed-detonation explosions (Seitenzahl et al. 2013). The connection between mixing and asymmetries has observational support. Polarization measurements show that HVFs in SNe ejecta are more polarized than PVFs, indicating that HV ejecta have more asymmetric distributions (Maund et al. 2013; Bulla et al. 2016). Additionally, Nagao et al. (2019) observed high polarization alongside a blueshift of the H α line during the photospheric phase of the Type II SN 2017gmr.

There is evidence for such an aspherical ejecta distribution in the spectra of SN 2019ein; in the early-time spectra of SN 2019ein, we see Si II with a higher absorption velocity than

C II at -14 days, whereas the opposite relation is true at this phase for the SNe studied by [Parrent et al. \(2011\)](#). In a spherically symmetric model of a Type Ia explosion, the inner burning regions are surrounded by a shell of unburnt material comprised mostly of C and O. However, an asymmetric explosion with strong outward mixing could force IMEs produced in the nuclear burning to higher velocities. In addition, our medium-resolution spectrum obtained 18 days after *B*-band maximum light reveals multiple overlapping Si II absorption features, with each absorption minimum offset by several thousand km s⁻¹. This may be evidence of significant mixing of the Si II ejecta to lower and higher velocities, rather than the stratified shell-like structure proposed in studies of other SNe Ia ([Cain et al. 2018](#)).

Studying the nebular-phase spectroscopy of SNe Ia, [Maeda et al. \(2010\)](#) found a relationship between the Doppler shift of the nebular-phase emission features and the Si II velocity gradient at early times, whereby HVG SNe exhibit redshifted nebular-phase emission lines and LVG SNe show blueshifted nebular emission lines. This correlation is suggested to detail information about the symmetry of the explosion because the nebular-phase emission features trace the deflagration ash in the core of the progenitor WD. In this model, HVG SNe are viewed from the direction opposite to the initial deflagration.

Finally, [Maund et al. \(2010\)](#) and [Cikota et al. \(2019\)](#) found correlations between the Si II line polarization and velocity evolution around maximum, with more polarized SNe belonging to the HV and HVG classes. [Maund et al. \(2010\)](#) argue that this relationship implies the existence of global asymmetries in the ejecta, which, along with the correlation between velocity evolution and nebular-phase velocity shifts ([Maeda et al. 2010](#)), connects early- and late-time velocity behavior to the three-dimensional geometry of the explosion. It is possible that the high absorption and emission velocities seen in the spectra of SN 2019ein are signatures of IMEs in the ejecta that were outwardly mixed in an off-center explosion.

2.6.2 Optical Depth Effects

Blueshifted emission features have been suggested to be caused by optical depth effects in Type II SNe (e.g. [Dessart & Hillier 2005, 2011](#); [Anderson et al. 2014](#)). These features arise from steep density profiles in the expanding ejecta (see Figure 16 in [Dessart & Hillier 2005](#)). [Blondin et al. \(2006\)](#) were the first to model these features in SNe Ia. Using the radiative transfer code `CMFGEN` ([Hillier & Miller 1998](#)), the authors found that differences in optical depths of Si II and S II lines resulted in overall blueshifted emission peaks when the flux was integrated over a range of impact parameters.

In this picture, contours of constant optical depth in the photosphere trace out a variable amount of the emitting ejecta, where the amount of emission from the ejecta above the photosphere depends on the optical depth of the line being considered. In the classical P Cygni profile, the flux from the ejecta moving perpendicular to the observer's line of sight makes up the majority of the emission, resulting in an emission peak centered on the rest wavelength of the line. However, when lines with low optical depth are considered, there is little to no emission from the ejecta at large impact parameters because the density gradient in the outer ejecta layers is steep. Instead, the flux is dominated by ejecta moving toward the observer even if the ejecta is distributed more or less spherically. The result is an overall blueshift of the emission peak, proportional to the ejecta velocity. Because the authors modeled individual lines, the emission blueshifts cannot be the result of line overlap.

As seen in Figure 2.14, SN 2019ein has some of the highest emission peak velocities at early times compared to the sample from [Blondin et al. \(2006\)](#). This extreme behavior can be understood in the context of the above explanation: because blueshifted emission is dominated by flux from the ejecta moving toward the observer, we would expect that the emission velocity is correlated with the absorption velocity. [Blondin et al. \(2006\)](#)

found that this trend exists, with the ratio of v_{peak} to v_{abs} approaching 0.6 around -10 days relative to B -band maximum for the Si II 5454 Å line. Over time, the photosphere quickly recedes from the low-density material and the emitting region becomes more spherical, causing this ratio to approach 0 around B -band maximum light. However, at early times the photosphere is very far out in the ejecta, so the emitting ejecta we observe must be at HVs, leading to a greater emission peak blueshift. Our SYN++ spectrum supports this picture; the blueshift of the Si II 6355 Å emission peak is proportional to the Si II ejecta velocity. Because SN 2019ein has some of the highest absorption velocities measured at its earliest phases, the emission velocities of those lines are among the highest as well.

2.6.3 Discussion

We find that the high absorption and emission velocities at early times can be explained by an HV-only ejecta component, possibly due to mixing in an asymmetric explosion or optical depth effects in the outer layers of the ejecta. It is possible that both effects are at play; the models of [Maeda et al. \(2010\)](#) predict that the outer regions of the SN ejecta on the side opposite from an off-center ignition are less dense and produce HVG SNe. It could be that in this lower density environment, the ejecta is optically thinner, leading to a majority of the flux stemming from material moving along the observer’s line of sight and producing blueshifted emission features.

Another nearby SN Ia with a well-studied density structure is SN 2012fr ([Childress et al. 2013](#); [Maund et al. 2013](#); [Contreras et al. 2018](#)). [Cain et al. \(2018\)](#) found that SN 2012fr showed signs of a shell-like density enhancement at low velocities, which could explain the unusual Si II velocity evolution as well as the presence of separate HV and PV features. However, SN 2012fr and similar SNe Ia tend to be slow decliners ($\Delta m_{15} \lesssim 1$), HV yet LVG, and fall outside the BL region of the Branch diagram ([Contreras et al.](#)

2018). These classifications are at odds with those we present for SN 2019ein. Therefore we suggest that SN 2019ein most likely has a different density enhancement than the shell-like structure of SN 2012fr.

One potential bias in our measurements is line blanketing. Line blanketing can warp the shape of the emission peaks, potentially biasing measurements of the peak wavelength. As noted by Branch et al. (2007), synthetic spectra rarely if ever produce the significant emission peak Doppler shifts around maximum light observed by Blondin et al. (2006) and again here in SN 2019ein. However, synthetic spectra also rarely produce only HV ejecta components, as we have done in our SYN++ model. Furthermore, the observed emission shifts are not seen in just one line but globally, and seem to follow a similar evolution over time. This can be seen in the comparison between the B15 model spectra and the real data in the earliest epoch (Figure 2.10). Therefore we conclude that line blanketing is unlikely able to reproduce the peculiar emission blueshifts at all wavelengths and phases.

Future observations will be necessary to provide more conclusive results on the geometry of the ejecta. For example, measuring a Doppler shift of the nebular-phase emission peaks could support the argument that SN 2019ein has signatures of an aspherical explosion. In addition, early-time polarimetry data would provide an additional measurement of the asymmetries in both specific spectral features, such as the Si II absorption line, and globally via the continuum polarization. However, as discussed by Dessart & Hillier (2011) and Woosley et al. (2007), low continuum polarization does not necessarily imply that the explosion was spherically symmetric; both authors find that even in models with significant asphericity, the line and continuum polarization could be low due to density and ionization effects. In the case of some geometries presented in Dessart & Hillier (2011) both an emission blueshift and a low polarization signal are produced, regardless of the underlying symmetry of the ejecta.

It is reasonable to question why SN 2019ein is so unusual, even in a sample of other BL HV SNe. One possible explanation is early-time observations; it is possible that SN 2019ein was first observed mere hours after explosion, allowing us to see the extremely high absorption and emission velocities at an earlier phase than other HV SNe. Another explanation is that SN 2019ein was observed from a rare viewing angle, as would be the case if the explosion were strongly asymmetric. Either way, the analysis of early-time photometry and spectroscopy presented here demonstrates the importance of finding and observing SNe Ia quickly after explosion.

2.7 Summary

We have presented photometric and spectroscopic observations of SN 2019ein, a SN Ia with some of the highest early-time ejecta velocities ever measured. We observe a Si II 6355 Å absorption velocity of 24,000 km s⁻¹ 14 days before *B*-band maximum light. In addition, the early-time emission components of the P Cygni profiles appear blueshifted with respect to the host galaxy redshift, with emission peaks of Si II, Ca II, and S II moving at velocities up to or above 10,000 km s⁻¹. This emission blueshift is also among the highest ever measured, making SN 2019ein an outlier even among other HV SNe.

Radio observations taken as early as <4 days after explosion provide insight into the progenitor system of SN 2019ein as well as the source of the HV ejecta. Our 3 σ VLA upper limits of 18, 25, and 23 μ Jy at 3.87, 11.57, and 17.58 days after explosion are sensitive enough to rule out symbiotic progenitors for SN 2019ein. We also rule out part of the parameter space of a single-degenerate model involving accretion from a main-sequence or slightly evolved companion at accretion rates $> 3 \times 10^{-7} M_{\odot} \text{ yr}^{-1}$, because the resulting fast optically thick winds would likely have created detectable circumstellar material. Such progenitor scenarios were also ruled out for the nearest and best-studied

SNe Ia 2011fe and 2014J. Our upper limits cannot rule out models of a WD accreting at lower rates $\sim (1 - 3) \times 10^{-7} M_{\odot}$ from a main-sequence or slightly evolved companion via winds that are sometimes interrupted by recurrent nova flashes. With our shell-interaction model (Nayyeri et al. 2016) we can rule out the presence of optically thin shells, which have been theoretically predicted to source HV ejecta, of masses $> 10^{-6} M_{\odot}$ at distances < 100 AU from the progenitor. However, denser or more massive shells in the optically thick regime cannot be ruled out by the current model, and will be revisited in the future with a more sophisticated shell model that takes synchrotron self-absorption and radiative losses into account.

We find that SN 2019ein is well fit by a delayed-detonation explosion model (Blondin et al. 2015) except at early times, where our measured ejecta velocities are even higher than those predicted. By modeling the early spectra of SN 2019ein, we find that both the high absorption and emission velocities may be due to a HV component of the ejecta that is detached from the photosphere. This detached component of the ejecta may be evidence of an aspherical distribution of intermediate-mass elements, perhaps due to mixing in an asymmetric explosion (Seitenzahl et al. 2013). Additionally, optical depth effects in the very outer layers of the ejecta may lead to an overall blueshift in the spectrum, as the majority of the flux observed comes from material moving along the observer’s line of sight. These results highlight the need for more detailed modeling of SN ejecta, especially at early times.

By studying a larger sample of HV SNe Ia, we can begin to probe the overlap between explosion models, asymmetries, and ejecta velocities. Results from such a sample would have implications on theories of Type Ia progenitor systems and explosion mechanisms. It is possible that a united picture will emerge, one in which the ejecta geometry and the viewing angle to a SN affect observables such as color, velocity, and light-curve width. A similar intrinsic difference has already been noted in the colors and host environments of

HV and Normal SNe ([Chang et al. 2013](#); [Zheng et al. 2018](#)), and may be used to reduce uncertainties in Type Ia distances, improving the precision of cosmological measurements.

Chapter 3

The Phase Space of Rapidly-evolving Supernovae

3.1 Supernova Powering Mechanisms

Chapter 2 focuses on the extremes of one observable—ejecta velocity—explored via early-time observations. The remaining chapters of this work focus on the extremes of another observable—light-curve duration. Even more than ejecta velocity, the parameter space of light-curve duration has been opened up owing to the influx of data from high-cadence time-domain surveys. Surveys such as ZTF, ATLAS, and ASAS-SN, which scan the same region of the sky or the entire sky with a cadence of 2-3 days, have discovered objects that rise and decline in brightness faster than other known classes of supernovae.

Most Type I supernovae have light curves that are powered by the radioactive decay of ^{56}Ni and ^{56}Co , which have e-folding times of 8.8 and 111.3 days, respectively (Arnett 1979). The timescale on which their light curves rise to peak brightness is set by the time for photons produced via radioactive decay to diffuse out of the expanding ejecta. This relatively straightforward relationship gives a range of predicted light-curve rise times for an ordinary range of ejecta masses, explosion energies, and ^{56}Ni masses. For example, Type Ia supernovae eject roughly a Chandrasekhar mass and produce ≈ 0.5

M_{\odot} of ^{56}Ni ; thus they have a small variance in their light-curve timescales. Even Type Ib and Ic supernovae, with greater diversity in their ejecta and ^{56}Ni masses than Type Ia supernovae, have a relatively narrow range of light-curve rise and decline times.

While not powered by radioactive decay at early times, H-rich (Type II) supernovae also have well-understood powering mechanisms. Their early-time light curves are powered by the energy deposition of the supernova shock into the outer layers of the ejecta. This shock ionizes the progenitor’s hydrogen-rich material. As the ejecta cools the hydrogen recombines, providing a constant source of photons with energies corresponding to the hydrogen recombination temperature. In many Type II supernovae this receding recombination front within the ejecta creates a light curve plateau. The duration of this plateau is sensitive to the mass of the hydrogen-rich material (Hiramatsu et al. 2021b).

On the other hand, a growing number of supernovae discovered by current time-domain surveys have light-curve timescales that are in conflict with these commonly-assumed powering mechanisms. For example, a rare class of objects we will refer to as “fast transients” (but are also called fast-blue optical transients (FBOTs), rapidly-evolving transients, and rapidly-rising luminous transients in the literature) have light curves that are too short and luminous to be powered by the radioactive decay of ^{56}Ni alone—the ^{56}Ni masses inferred from simple analytical model fits are unphysically larger than their inferred ejecta masses (Drout et al. 2014; Pursiainen et al. 2018). Instead, other physical mechanisms are needed to power their emission, particularly at early times.

To explain their luminosity evolution, we investigate alternative powering mechanisms. One such mechanism is interaction with circumstellar material (typically the material lost by the progenitor star before exploding) that is confined to distances $R_{\text{CSM}} \lesssim 10^{17}$ cm. The progenitor star can shed material through several potential channels, including non-conservative mass transfer with a binary companion, stellar winds, and eruptive mass-loss episodes (see e.g., Smith 2014 for a review). Each of these mechanisms

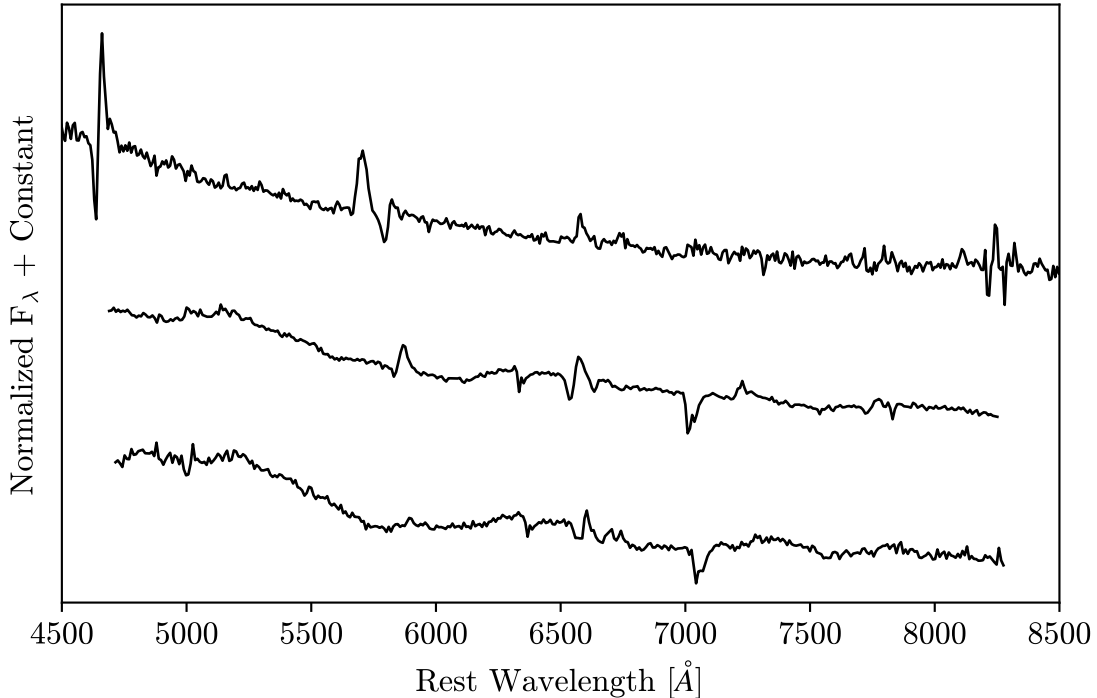


Figure 3.1: Spectral evolution of the interaction-powered SN 2021csp (from [Pellegrino et al. 2022d](#), see Chapter 5)). At early times (top) the spectrum is blue and dominated by narrow emission and P Cygni features from ionized circumstellar material. As the photosphere recedes intermediate-width features from the swept-up ejecta and circumstellar material are seen (middle). Finally, as the interaction ceases broad ejecta features become visible (bottom).

is poorly understood, and observing supernovae interacting with pre-existing circumstellar material allows us to study and test these theories of stellar evolution. In fact, it is becoming evident that a significant fraction of, if not all, massive stars undergo some degree of mass loss before exploding ([Bruch et al. 2021](#); [Strotjohann et al. 2021](#)), and the amount of mass they lose is challenging to explain within current paradigms.

For an extensive overview of interaction-powered supernovae, see [Smith \(2017\)](#). Here we briefly summarize points of interest. As the ejecta collides with the circumstellar material forward- and reverse-traveling shocks are produced that traverse the circumstellar medium and supernova ejecta, respectively. High-energy photons propagate before the

shock at early times, ionizing the external unshocked circumstellar material. This flash ionization causes narrow emission or P Cygni lines to be visible in spectra for hours to several days. These narrow lines, superimposed on a blue continuum produced by the optically thick shocked gas, have Gaussian widths set by the velocity of the circumstellar material and broader Lorentzian wings caused by electron scattering in this ionized medium (see Figure 3.1).

Material swept up by the forward and reverse shocks accumulates in a cold dense shell between both shocked regions. X-ray and ultraviolet photons produced by the high temperatures of the shocks (10^5 K) provides a consistent source of luminosity that excites electron transitions in the swept-up material. As the photosphere recedes in mass coordinate over time, the emission from this material is visible to the observer as intermediate-width P Cygni features with velocities set by the velocity of this shell. Emission from this region persists as long as the interaction is ongoing to provide a source of high-energy photons. This shock duration is a function of the circumstellar density profile, radial extent, shock velocity, and circumstellar medium and ejecta masses. The result is luminosity inputs that can last from hours to years.

After the interaction has ceased, the photosphere recedes into the expanding supernova ejecta. At these phases the spectra appear like “normal” non-interacting supernova spectra, with Doppler-broadened features set by the velocity of the ejecta. However, by the time the interaction has stopped, these features may be too faint to observe. This is because interaction is an efficient means of producing luminous emission from an otherwise weak explosion. The typical kinetic energy of the supernova ejecta is on the order of 10^{51} erg (Sukhbold et al. 2016); therefore, converting even a small fraction of this energy to thermal emission can increase the luminosity of the supernova by many factors.

Another mechanism that can power short-lived, luminous emission is the deposition of energy as the supernova shock breaks out from the outer layers of the progenitor.

Theory predicts that as the shock reaches an optical depth $\tau \approx \frac{c}{v}$, where v is the speed of sound in the material, photons will diffuse out of the expanding outer progenitor layers (e.g., [Nakar & Sari 2010](#)). This “shock breakout” can be observed as a brief but luminous burst of energy, particularly in the ultraviolet and X-ray ([Chevalier & Fransson 2008](#); [Modjaz et al. 2009](#)).

Subsequently the expanding outer layers of the progenitor (now the supernova ejecta) that were heated by the shock will radiate and cool. Depending on the density structure of this material, this “shock cooling” emission can be observed from hours to days after shock breakout ([Rabinak & Waxman 2011](#); [Piro 2015](#); [Sapir & Waxman 2017](#)). Optical surveys with high cadences will observe the shock cooling emission as a rapidly-declining light curve that can last up to a week. In many cases, objects that have observed shock cooling emission are Type IIb supernovae (see [Chapter 6](#)) due to the unique envelope structure of their progenitors—they have partially-stripped, low-mass, extended envelopes which allows for this shock cooling emission to be visible over days, rather than hours.

3.2 Supernova Phase Space

One metric by which supernovae can be roughly sorted is by comparing their peak luminosities with some characteristic light-curve timescale. A commonly-used characteristic timescale in the literature is $t_{1/2}$, the rest-frame time over which the transient has a luminosity \geq half its peak luminosity. In this “supernova phase space,” shown in [Figure 3.2](#), a large fraction of spectroscopically-similar supernovae are grouped together. For example, Type II supernovae with light-curve plateaus have $t_{1/2} \approx 70 - 100$ days and Type Ia supernovae are clustered in an area representing the Phillips relation ([Phillips 1993](#)). The fast transients introduced in [Section 3.1](#) fall on the extreme edge of this

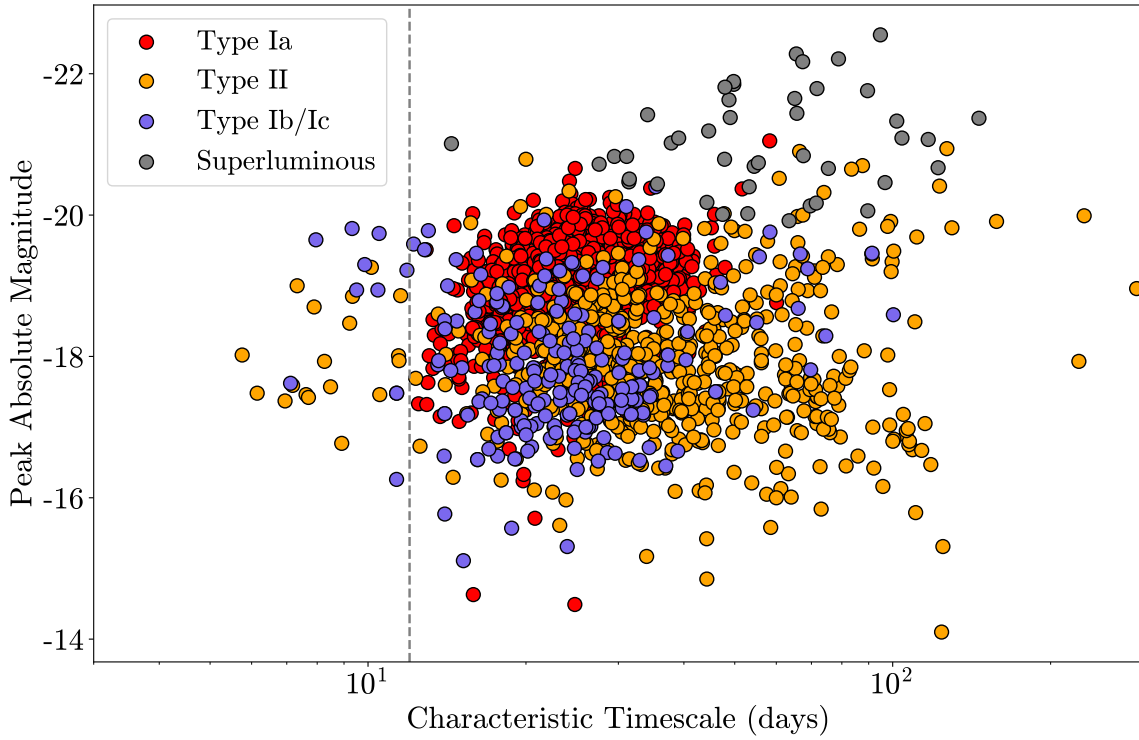


Figure 3.2: The current sample of spectroscopically-classified supernovae from the ZTF Bright Transient Survey. Broad supernova classifications (Type Ia, Type II, etc.) are shown in different colors. Objects left of the dashed vertical line are classified as “fast transients,” with $t_{1/2} \leq 12$ days.

phase space. Historically, they have been quantitatively defined as having $t_{1/2} \leq 12$ days (Drout et al. 2014; Ho et al. 2021).

Such rapid evolution makes obtaining well-sampled, multi-band photometric and spectroscopic coverage of these objects a challenge for most follow-up facilities. These events must be flagged early as having peculiar evolution to alert the community that further follow-up is needed. However, often these transients are found in archival data searches rather than in real-time. For example, many fast transients from surveys such as the Pan-STARRS1 Medium-Deep Survey evolved too quickly or were too faint to obtain spectroscopic classifications (Drout et al. 2014). Even those with spectroscopic observations often have spectra that are blue and featureless, making classification dif-

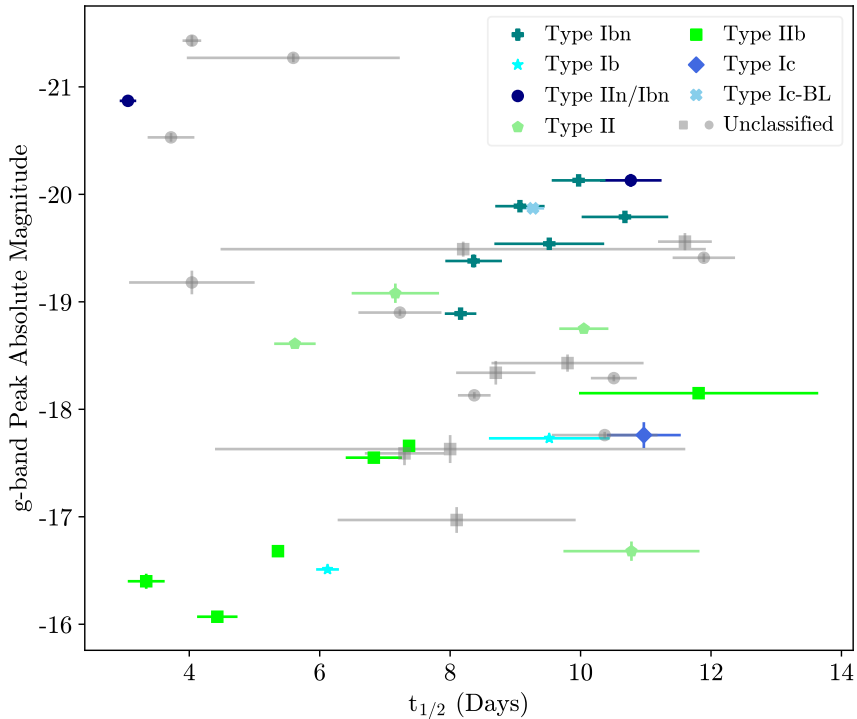


Figure 3.3: Spectroscopically-classified (colored symbols) and unclassified (gray circles) fast transients from [Ho et al. \(2021\)](#). Gray squares are spectroscopically-unclassified transients from [Drout et al. \(2014\)](#).

difficult ([Drout et al. 2014](#); [Arcavi et al. 2016](#); [Pursiainen et al. 2018](#)). However, with the advent of robotically-controlled queue-based telescopes as well as spectroscopically-complete surveys such as the ZTF Bright Transient Survey (BTS; [Fremming et al. 2020](#); [Perley et al. 2020](#)), more objects within this fast-evolving region of parameter space have been spectroscopically classified. The current ZTF BTS sample is shown in Figure 3.2. It is spectroscopically complete for objects with peak brightnesses ≤ 18.5 mag. Therefore, it consists of both nearby, fainter sources as well as brighter and more distant objects.

The fast-evolving objects in this sample, which are shown left of the vertical dashed line, are relatively heterogeneous in their spectroscopic classifications and peak brightnesses. These objects are shown in more detail in Figure 3.3. To help elucidate their powering mechanisms and progenitors, their spectroscopic classifications are broken down

into further subtypes for comparison. The classified objects are all core-collapse supernovae of various types. However, several commonalities between them can be found, including common mechanisms that power their light curves. In particular, radioactive decay is not their sole powering mechanism. Instead, many classes of supernovae powered by circumstellar interaction, such as Type IIn and Type Ibn supernovae (shown in dark blue and teal, respectively), are found in the more luminous region of this phase space. The less-luminous half is dominated by Type IIb supernovae that have early-time light curves powered by shock cooling emission.

The remainder of this dissertation details efforts to map out objects and classes in this region of phase space. The main goal of these efforts is to test our understanding of stellar evolution and the physics that power supernovae in this extreme regime. As a result, we have made several advances in our understanding of these objects: i) we have connected luminous, fast-evolving objects to known classes of supernovae powered by interaction with hydrogen-poor circumstellar material (Chapter 4); ii) we have analyzed the first sample of a new, rare class of supernovae produced by stars that have undergone the most extreme mass-loss observed (Chapter 5); and iii) we have revealed new diversity in the progenitors of known classes of stripped-envelope and interaction-powered supernovae (Chapter 6). These findings have proven to be transformative to our understanding of the supernovae that occupy the fast-evolving region of supernova phase space.

Chapter 4

Circumstellar Interaction and Luminous, Rapidly-evolving Transients

This chapter investigates the powering mechanisms and progenitors of rapidly-evolving supernovae that lie on the upper half of fast transient phase space—that is, objects with peak absolute magnitudes $\lesssim -17.5$. Even though they fade in a matter of days, these objects are more easily identified than their less-luminous counterparts due to their bright multi-wavelength emission, allowing them to be observed at relatively higher redshifts. Even so, these objects are exceedingly rare; Figure 3.2 shows that only tens occupy this region of phase space in a sample of several thousand supernovae. Due to this rarity, the nature of their light-curve powering mechanisms and their progenitor stars have been intensely debated (see Section 4.5).

The work presented in this chapter is one of the first to connect luminous fast transients with more well-understood supernovae powered by circumstellar interaction. In particular, this is the first systematic study of similarities between unclassified fast transients from the literature and Type Ibn supernovae—supernovae powered by interaction with hydrogen-poor, helium-rich circumstellar material. Type Ibn supernovae are rare, with only ≈ 50 discovered to date. However, samples of well-studied Type Ibn super-

novae show intriguing characteristics. First, their light curves are relatively homogeneous, rising to peak absolute magnitudes $-19 \lesssim M \lesssim -18$ in about a week and subsequently fading by 0.1 mag day^{-1} (Hosseinzadeh et al. 2017b). On the other hand, their spectra show more evidence for diversity—some have narrow P Cygni helium features from circumstellar interaction whereas others only show helium in emission (Hosseinzadeh et al. 2017b); some show flash features, indicating an extended circumstellar medium rich in carbon, nitrogen, and hydrogen (Gangopadhyay et al. 2020, 2022); and some show transitional spectra with narrow features of both hydrogen and helium, potentially indicating a progenitor that underwent less extensive mass loss (e.g., Pastorello et al. 2015). They are almost exclusively found in star-forming galaxies (Hosseinzadeh et al. 2019), and a precursor event observed at the location of the archetypal Type Ibn SN 2006jc two years before the terminal explosion has been used to tie these objects to massive stars in their Wolf-Rayet phase (Pastorello et al. 2007).

While previous studies have suggested a connection between fast transients and circumstellar interaction (e.g., Drout et al. 2014; Rest et al. 2018; Fox & Smith 2019; Xiang et al. 2021), this is the first study to show that observational characteristics of both unclassified fast transients and Type Ibn supernovae can be reproduced with simple semi-analytical models. This connection has subsequently been a matter of debate in the literature since (e.g., Maeda & Moriya 2022; Khatami & Kasen 2023). However, it is becoming clear that circumstellar interaction must play a key role in the luminosity evolution of a large fraction of the objects that occupy this region of phase space. As a result, this chapter is an important piece in our evolving understanding of the extremes of luminous, rapidly-evolving supernovae.

This chapter was reproduced from Pellegrino et al. (2022c) with only minor changes to fit the formatting of this dissertation. I'd like to thank my coauthors, without whom this work would not have been possible: D. A. Howell, J. Vinkó, A. Gangopadhyay, D.

Xiang, I. Arcavi, P. Brown, J. Burke, D. Hiramatsu, G. Hosseinzadeh, Z. Li, C. McCully, K. Misra, M. Newsome, E. Padilla Gonzalez, T. A. Pritchard, S. Valenti, X. Wang, and T. Zhang.

4.1 Introduction

Over the last several years time-domain surveys, including Panoramic Survey Telescope and Rapid Response System, Pan-STARRS1 (PS1; [Kaiser et al. 2010](#)), the Dark Energy Survey (DES; [Flaugher 2005](#)), and the Zwicky Transient Facility (ZTF; [Bellm et al. 2019](#); [Graham et al. 2019](#)), have led to the discovery of thousands of astronomical transients. Among these discoveries have been objects that are more luminous and evolve more rapidly than other known classes of supernovae (SNe). Samples of these rapidly evolving (hereafter “fast”) transients have been identified in PS1 ([Drout et al. 2014](#) hereafter D14), the Supernova Legacy Survey ([Arcavi et al. 2016](#)), DES ([Pursiainen et al. 2018](#)), the Kepler mission ([Rest et al. 2018](#)), and ZTF ([Ho et al. 2021](#)), among others. Although their exact classification has varied, broadly they display rises to peak brightness in fewer than five days and declines from peak to half-peak brightness in fewer than ten days. D14 was one of the first to identify a large sample of fast transients that had a time above half their maximum brightness, $t_{1/2}$, of $\lesssim 12$ days and absolute magnitude $-16.5 \lesssim M \lesssim -20$.

Most of the fast transients identified to date have been found at cosmological distances, i.e. $d_L \gtrsim 200$ Mpc, making full multiband studies of these objects difficult. This changed with the discovery of AT 2018cow, a fast transient identified at a redshift $z = 0.014$ ([Benetti et al. 2018](#)), or luminosity distance $d_L = 60$ Mpc ([Prentice et al. 2018](#)). AT 2018cow presented the first opportunity for a true multiband study, from radio to γ ray, of a nearby fast transient. Observations of strong X-ray emission ([Margutti et al.](#)

2019), an initially hot and featureless spectrum (Prentice et al. 2018), and a receding photosphere (Perley et al. 2019) all affected the physical interpretation of the progenitor system of this fast transient. Since the discovery of AT 2018cow other similar transients have been discovered at higher redshifts (Coppejans et al. 2020; Ho et al. 2020; Perley et al. 2021).

Due to their high peak luminosities and rapid evolution, modeling the powering mechanism of these fast transients has proven difficult. A ^{56}Ni -decay powering source is impossible to reconcile with both the peak luminosities and rapid evolution of these objects. Other possible powering sources include the thermonuclear explosion of a white dwarf within an H-rich envelope (Arcavi et al. 2016), magnetar spin-down (Prentice et al. 2018), a tidal disruption event by an intermediate-mass black hole (Perley et al. 2019), and interaction with circumstellar material (CSM; Drout et al. 2014; Rivera Sandoval et al. 2018). These various models each have their advantages and drawbacks when compared to the complex temporal evolution of AT 2018cow.

More recently, similar characteristics have been noticed between certain fast transients, specifically AT 2018cow, and Type Ibn supernovae (SNe Ibn; Fox & Smith 2019; Xiang et al. 2021). SNe Ibn are rare but well studied (Pastorello et al. 2008; Hosseinzadeh et al. 2017b hereafter H17). There is evidence that their progenitor systems are high-mass stars, such as Wolf-Rayet (WR) stars, that undergo significant mass loss in a short period of time before explosion (Smith & Owocki 2006; Foley et al. 2007; Smith et al. 2012 but see also Hosseinzadeh et al. 2019). In many cases their early-time spectra show hot blue continua superimposed with emission lines of He I and He II, indicating interaction with a CSM composed of material possibly stripped from a massive star. In particular, SNe Ibn show similar rise times, peak luminosities, and decline times when compared with fast transients (Fox & Smith 2019; Clark et al. 2020; Xiang et al. 2021), hinting that some SNe Ibn may be included in samples of photometrically identified fast

transients.

In one of the largest samples of fast transients to date, [Ho et al. \(2021\)](#) published observations of 42 objects discovered during Phase I of ZTF, some of which were observed by the Bright Transient Survey ([Fremling et al. 2020](#); [Perley et al. 2020](#)), with times above half the maximum brightness of fewer than 12 days. Of these objects, 20 were spectroscopically classified. The objects with spectra in the sample primarily consist of core-collapse SNe such as Type IIb SNe (SNe IIb) that are powered by shock-cooling emission at early times, interaction-powered objects mainly classified as SNe Ibn, and more extreme objects such as AT2018cow. This study—one of the first to present a large sample of spectroscopically classified fast-evolving transients—points toward fast transients being a heterogeneous class of objects, with many powered by CSM interaction. However, many other objects in this sample, including the most luminous and fastest-evolving transients similar to AT2018cow, remain spectroscopically unclassified, and their powering mechanisms are uncertain.

As time-domain surveys discover more SN candidates than can be spectroscopically classified, it is important to investigate whether a single progenitor system and powering mechanism can explain the observed properties of objects in different regions of the fast transient parameter space. In this work, we compare photometry and spectra between SNe Ibn and other photometrically classified fast transients in literature (i.e. $t_{1/2} \lesssim 12$ days) in order to explore a common progenitor system for these objects. We identify four fast-evolving SNe Ibn with Las Cumbres Observatory (LCO; [Brown et al. 2013](#)) observations and compare these SNe with a sample of fast transients from D14 and AT2018cow. As CSM interaction at early times and ^{56}Ni decay at late times are the proposed powering sources of SNe Ibn, we investigate whether they can reproduce the light curves of other fast transients, as well. We model the bolometric luminosities of the objects in our sample with inputs from CSM interaction plus ^{56}Ni decay. We calculate

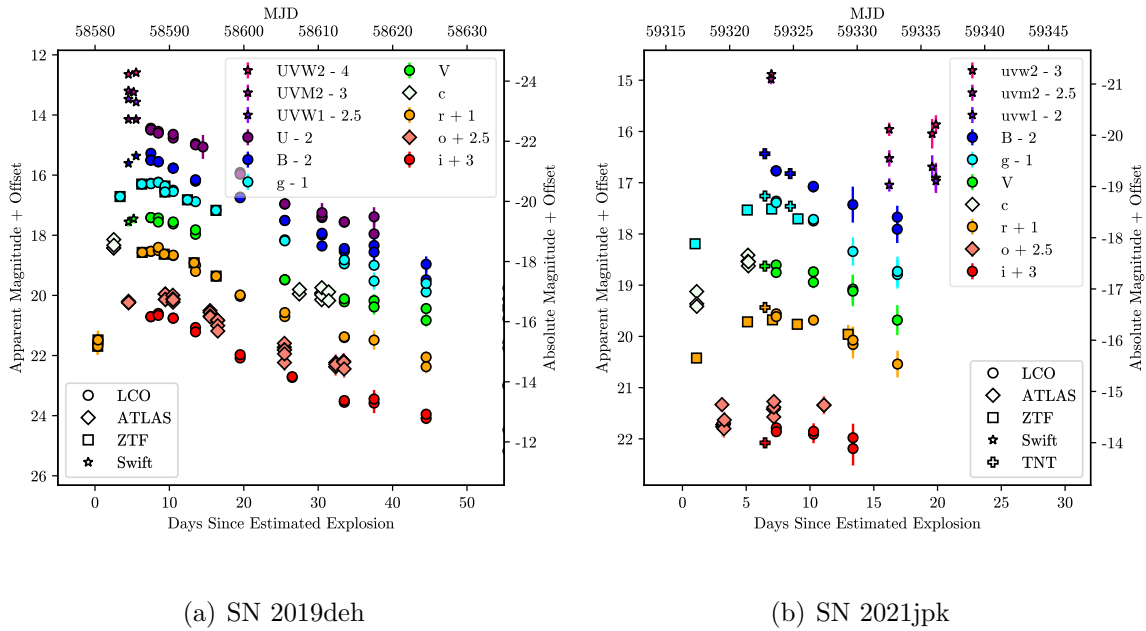


Figure 4.1: Observed UV and optical light curves of the Type Ib (a) SN 2019deh and (b) SN 2021jpk from LCO (circles), ATLAS (diamonds), ZTF (squares), Swift (stars), and TNT (plus signs). All photometry have been corrected for MW extinction.

rise times, peak luminosities, and decline times for these models and compare them with light-curve parameters for SNe Ib and other photometrically classified fast transients.

This paper is organized as follows. In Section 4.2 we discuss the objects and data in our sample of fast transients and SNe Ib. In Section 4.3 we detail the photometric and spectroscopic analysis of these objects. We describe our model light curves and compare them to data in Section 4.4. We discuss a possible common progenitor system between SNe Ib and some fast transients in Section 4.5. Finally, we conclude in Section 4.6.

4.2 Observations and Sample Description

Throughout this work we compare a sample of SNe Ib observed by LCO with fast transients from D14 as well as AT 2018cow. Details of each sample, including selection

criteria for our SNe Ibn, are presented below.

4.2.1 Fast-evolving SNe Ibn

We begin by identifying four fast-evolving SNe Ibn observed by LCO through the Global Supernova Project (GSP). These objects were chosen because they all have optical and ultraviolet (UV) observations beginning at or before maximum light, spectra obtained within a few days of maximum light, and g -band decline rates greater than 0.1 mag day^{-1} , which is the average decline rate for SNe Ibn (Hosseinzadeh et al. 2017b). Because of their faster-than-average evolution, we classify these objects as fast-evolving SNe Ibn. Two (SN 2019uo and SN 2019wep) have LCO observations and data-reduction details presented in other works (Gangopadhyay et al. 2020 Gangopadhyay 2021, in preparation). In this work we present LCO photometry and spectra of SN 2019deh and SN 2021jpk, two additional fast-evolving SNe Ibn. ZTF observations of SN 2019deh were discussed in Ho et al. (2021) while SN 2021jpk has no published data thus far.

SN 2019deh and SN 2021jpk were discovered by ZTF on MJD 58580.36 (2019 April 7.36 UT) and MJD 59317.29 (2021 April 13.29) at r -band magnitude 20.75 ± 0.28 and g -band magnitude 19.26 ± 0.09 , respectively. Assuming a standard cosmology with $H_0 = 73 \text{ km s}^{-1} \text{ Mpc}^{-1}$, $\Omega_m = 0.27$, and $\Omega_\Lambda = 0.73$, the luminosity distances we use for SN 2019deh and SN 2021jpk are 237 Mpc and 164 Mpc, respectively (Beers et al. 1995; Adelman-McCarthy et al. 2007). Due to the rapid evolution of these objects, the first LCO observations were not obtained until around the time of maximum brightness and continued for the next several weeks.

LCO light curves for both objects along with detections from ZTF, the Asteroid Terrestrial-impact Last Alert System (ATLAS; Tonry et al. 2018), Swift, and the Tsinghua NAOC Telescope (TNT; Huang et al. 2012) are shown in Figure 4.1. We cor-

rect the photometry for Milky Way (MW) dust extinction assuming $A_V = 0.0772$ and $A_V = 0.0555$ from the dust maps of [Schlafly & Finkbeiner \(2011\)](#) for SN 2019deh and SN 2021jpk, respectively. Due to the relatively large offset between SN 2019deh and its host galaxy, we assume a negligible host-galaxy extinction. For SN 2021jpk, we attempt to estimate the host-galaxy extinction by comparing its $B - V$ colors to those of Type Ibn SN 2010al, which is spectroscopically similar to SN 2021jpk ([Taubenberger et al. 2021](#)). After correcting for MW extinction the colors of both objects are consistent. Additionally, the spectrum of SN 2021jpk shows no host Na ID absorption; therefore we assume negligible host extinction. To estimate the time of explosion and time of maximum light for SN 2019deh we fit a second-order polynomial to the ATLAS fluxes in o -band during the first 15 days of observations. The estimated explosion time, t_{exp} , is MJD 58579.99 ± 0.25 and time of maximum brightness, t_{peak} , is MJD 58588.5 ± 0.65 . Due to the sparse light-curve sampling at early times we take the average of the last nondetection and first ZTF detection of SN 2021jpk as a conservative estimate of its explosion date, $t_{exp} = \text{MJD } 59316.3 \pm 0.99$. From fitting a second-order polynomial to the peak of the light curve we estimate $t_{peak} = \text{MJD } 59324.10 \pm 0.45$.

Optical Photometry

LCO $UBgVri$ -band data were obtained with the Sinistro camera on LCO 1m telescopes. Using the `lcogtsnpipe` photometric data-reduction pipeline ([Valenti et al. 2016](#)) point-spread function (PSF) fitting was performed on LCO images to extract PSF magnitudes ([Stetson 1987](#)). The UBV -band photometry was calibrated to Vega magnitudes using Landolt standard fields ([Landolt 1992](#)), while gri -band photometry was calibrated to AB magnitudes using the Sloan Digital Sky Survey ([Smith et al. 2002](#)). Color terms for each epoch were computed using these standards. Background subtraction was performed on four of the objects (SN 2019uo, SN 2019wep, AT 2018cow, and SN 2021jpk)

due to their proximity to their host galaxies. Template images were obtained after the SNe had faded and subtraction was performed using PyZOGY (Guevel & Hosseinzadeh 2017), an implementation of the algorithm described in Zackay et al. (2016).

We also obtained two epochs of *BgVri*-band photometry of SN 2021jpk using the 0.8 m TNT. All images were processed using standard IRAF¹ techniques. PSF photometry was calibrated to standard stars and converted to *BgVri* magnitudes. Because the SN signal was strong at the time of observation, background subtraction was not performed.

Swift Photometry

We also present UV observations obtained with the Ultraviolet and Optical Telescope (UVOT; Roming et al. 2005) on the Neil Gehrels Swift Observatory (Gehrels et al. 2004) for SN 2021jpk. Images were obtained in the *uvw2*, *uvm2*, and *uvw1* filters beginning MJD 59323.3, coincident with the time of maximum light. The data were reduced using the data-reduction pipeline of the Swift Ultraviolet/Optical Supernova Archive (Brown et al. 2014) using the aperture corrections and zero-points of Breeveld et al. (2011). Galaxy subtraction was not performed.

Optical Spectra

LCO spectra covering the optical range from 3500 to 10,000 Å at a resolution $R \approx 300$ -600 were obtained with the Folded Low Order whYte-pupil Double-dispersed Spectrograph (FLOYDS) spectrographs on the Faulkes Telescope North and Faulkes Telescope South through the GSP. Data were reduced using the `floydsspec` custom pipeline, which performs flux and wavelength calibration, cosmic-ray removal, and spectrum extraction².

¹IRAF is distributed by the National Optical Astronomy Observatories, which are operated by the Association of Universities for Research in Astronomy, Inc., under cooperative agreement with the National Science Foundation (NSF).

²https://github.com/svalenti/FLOYDS_pipeline/

Details of the spectra shown in this work and a discussion of their features used for classification are given in Section 4.3.3.

4.2.2 D14 Fast Transients

Throughout this work we compare our fast-evolving SNe Ibn sample to the gold and silver samples of rapidly evolving transients presented in D14 from the PS1 Median Deep Survey. These ten objects were confirmed to be extragalactic in origin and satisfied three criteria: (1) they rose $\gtrsim 1.5$ mag in the previous nine days before maximum light; (2) they declined $\gtrsim 1.5$ mag in the 25 days after maximum light; and (3) they appeared in at least three consecutive observations. These criteria were selected in order to exclude the most common SNe subtypes.

The objects in the gold and silver samples have $t_{1/2} \lesssim 12$ days, a median redshift of $z = 0.275$ and a median of 19 photometric detections across the optical region of the electromagnetic spectrum. Five have spectroscopic observations within several days of maximum light. All were observed in the $g_{P1}r_{P1}i_{P1}z_{P1}$ filters. Additional observations for several objects were obtained with the Gemini GMOS (Hook et al. 2004) and Magellan IMACS (Dressler et al. 2006) instruments in ri -band. Data were reduced as described in D14.

We correct photometry for MW extinction using the $E(B-V)$ values listed in Table 1 of D14. We also use the D14 luminosity distances when calculating the bolometric luminosities of these objects. Since PS1 does not observe in all filters every night, we follow the process described in D14 to interpolate photometric observations to a common epoch. Due to the rapid evolution of these objects, we only interpolate observations that were taken within a day of a g_{P1} -band detection. For each common epoch with observations in at least three filters, we fit a blackbody spectral energy distribution

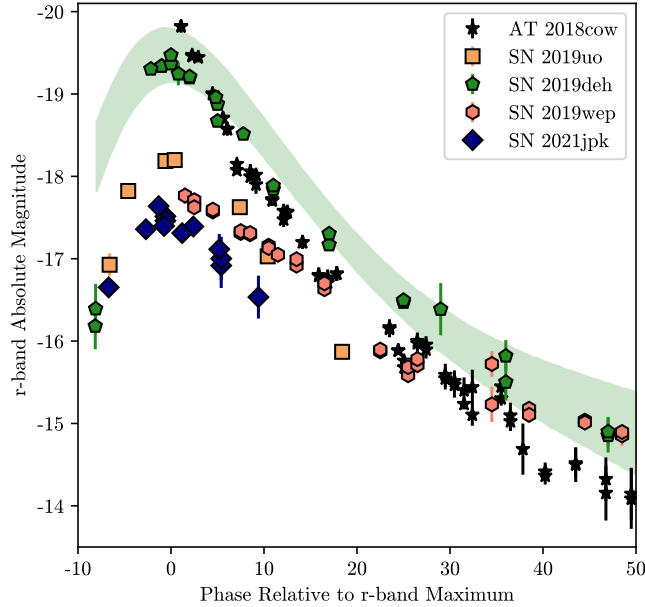


Figure 4.2: r -band absolute magnitude light curves for the fast-evolving SNe Ibn as well as AT 2018cow. All photometry have been corrected for MW extinction. The shaded region is the R -band SNe Ibn template from H17. The objects presented here tend to evolve more rapidly, and have a wider range of peak luminosities, than the H17 template.

(SED) to the rest-frame fluxes in order to calculate bolometric luminosities. The results from our best-fit blackbody SEDs are consistent with those presented in D14.

4.2.3 AT 2018cow

We also compare the SNe Ibn and D14 fast transients to LCO observations of AT 2018cow. AT 2018cow was discovered by ATLAS on MJD 58285.44 in CGCG 137-068 at a redshift of $z = 0.014145$ (Prentice et al. 2018). Due to its high luminosity and recent nondetection about four days prior, AT 2018cow was quickly identified as an unusual transient (Smartt et al. 2018). Rapid follow-up across the electromagnetic spectrum began soon after discovery (Prentice et al. 2018; Rivera Sandoval et al. 2018; Margutti et al. 2019;

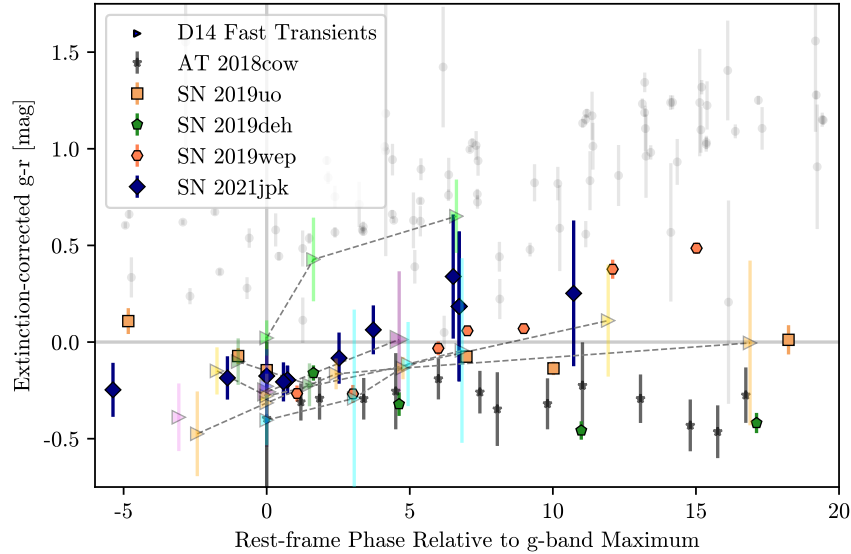


Figure 4.3: $g-r$ colors of the fast transients from D14 (triangles) compared with colors of fast-evolving SNe Ibn (colored shapes), AT 2018cow (black stars), and a sample of SNe Ibc (Taddia et al. 2015; Sako et al. 2018 gray points). Colors have been corrected for MW extinction. PS1 fast transient colors are connected with dashed lines. The fast transients and SNe Ibn have colors that are mostly bluer than those of the comparison objects, particularly at later times.

Perley et al. 2019; Xiang et al. 2021), making it the best-observed fast transient to date.

LCO began observing AT 2018cow on MJD 58288.07 with daily photometric and spectroscopic cadences. $UBgVri$ -band images and optical spectra were taken nearly continuously for the first two months of the object’s evolution before it became too faint to observe. LCO data of AT 2018cow, as well as a description of the data-reduction process, are presented in Xiang et al. (2021). Throughout this paper we use the bolometric luminosities calculated in Xiang et al. (2021) as well as the rise time, decline time, and peak absolute magnitudes presented in Prentice et al. (2018) and Perley et al. (2019).

4.3 Data Analysis

4.3.1 Photometric Properties

The r -band absolute magnitude light curves for the objects described in Sections 4.2.1 and 4.2.3 are shown in Figure 4.2. Also included as the green-shaded region is the SN Ibn light-curve template presented in H17. Our objects show a wider range of peak luminosities and evolution timescales than the H17 template. For instance, SN 2019uo has a lower peak absolute magnitudes and faster rise time than the template. However, Hosseinzadeh et al. (2017b) state that because nondetections were not included in the fitting process, the template is biased to a brighter and shallower evolution at early times by SNe Ibn with longer rise times. AT 2018cow is similar to the template in terms of peak r -band absolute magnitude (-19.82 ± 0.06 and -19.46 ± 0.32 mag, respectively) and decline rate (≈ 0.2 mag day $^{-1}$ and 0.1 mag day $^{-1}$, respectively), and is a closer match to SN 2019deh, but it displays a brighter peak absolute magnitude by almost two magnitudes and a faster decline than the other SNe Ibn. These objects show that some SNe Ibn have rise times and decline rates that are more similar to those of luminous fast transients such as AT 2018cow than other SNe Ibn, indicating that objects like AT 2018cow may lie at the extreme end of a distribution of SNe Ibn.

In Figure 4.3 we show the $g-r$ color evolution of these objects as well as that of the fast transients from D14. The colors of all the transients are presented in the observer frame. Although many of the D14 objects are at high redshifts, where K -corrections become important, Figure 9 of D14 shows that K -corrections do not greatly change the maximum light $g-r$ colors. Therefore we expect that K -corrections will not significantly affect our conclusions here. In order to compare these colors with those of other types of SNe, we also plot the $g-r$ colors of a sample of Type Ib and Ic SNe (SNe Ibc; Taddia et al. 2015).

Before maximum light both the SNe Ibn and fast transients have consistently blue colors. After maximum light, some of these objects evolve to slightly redder colors. However, two objects—SN 2019deh and AT 2018cow—stand out as having little redward evolution when compared with the other objects. These extreme blue colors are rare, even among our sample of fast-evolving objects, and are evidence for photospheric temperatures that remain high throughout the evolution of these objects (Drout et al. 2014; Perley et al. 2019). More broadly, compared to the sample of SNe Ibc, the SNe Ibn and fast transient colors are mostly bluer at all times. One fast transient—PS1-12bb—is significantly redder than the other sample objects. However, as discussed in Section 4.4 PS1-12bb also has a different luminosity evolution than other fast transients and therefore may be an unrelated object.

4.3.2 Blackbody Radius Measurements

Given our multiband follow-up we are able to construct bolometric light curves for our sample of fast-declining SNe Ibn. For objects with no bolometric luminosity measurements published we fit a blackbody SED to our multiband photometry using the code `Superbol` (Nicholl 2018). After correcting for MW extinction and shifting to the rest frame, we interpolate our observations to common epochs and fit for bolometric luminosities and blackbody radii and temperatures. We believe a blackbody approximation is valid as the spectra of the objects we consider are well modeled by blackbodies throughout their evolution. In order to ensure sufficient coverage in the UV, where the SEDs of these objects peak (Drout et al. 2014), we take care to measure luminosities only at epochs close to those with Swift observations. In the case of SN 2019deh, only two UV observations were obtained, both around maximum light. In order to calculate the bolometric luminosity at later times we estimate magnitudes in the Swift UVOT

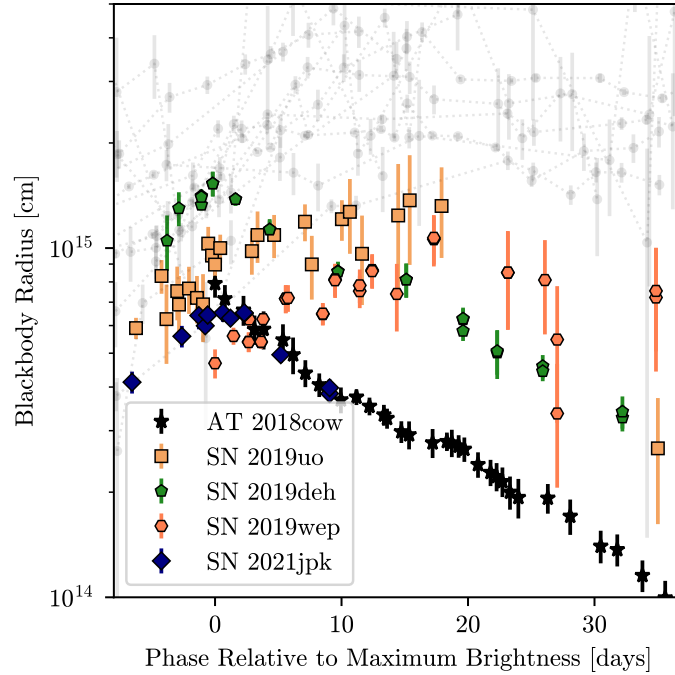


Figure 4.4: Blackbody radius measurements for our fast-evolving SNe Ibn as well as AT 2018cow (from [Perley et al. 2019](#)) compared to estimates from a sample of SNe Ibc ([Taddia et al. 2015](#) gray points). The SNe Ibn and AT 2018cow have smaller blackbody radii at all epochs than the comparison objects, with a different evolution: our sample shows constant or decreasing blackbody radii after maximum light, whereas the others have constant or increasing radii.

filters by interpolating our LCO U -band measurements onto a grid of $uvw2-U$, $uvm2-U$, and $uvw1-U$ colors from the archetypal Type Ibn SN 2006jc ([Pastorello et al. 2007](#); [Bianco et al. 2014](#); [Brown et al. 2014](#)). Although an approximation, this method avoids the assumption of constant UV colors at later times which may lead to overestimated luminosities.

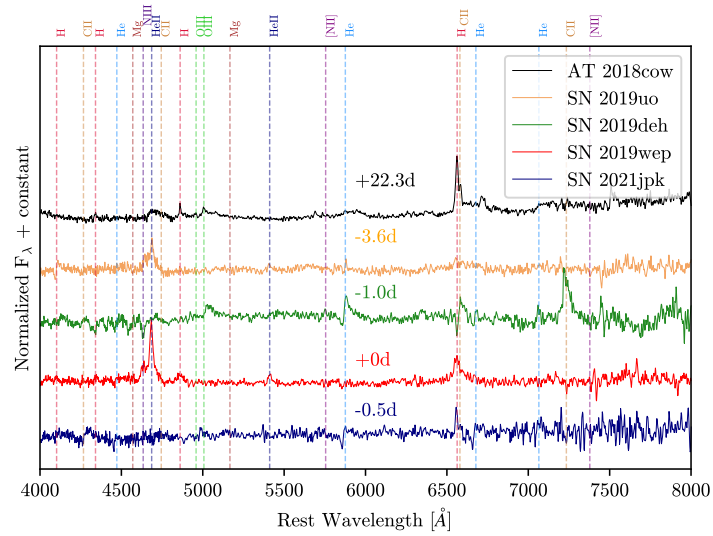
The blackbody radius evolution for our fast-evolving SNe Ibn and AT 2018cow are shown in Figure 4.4. For comparison, we plot blackbody radii estimates from a sample of SNe Ibc ([Taddia et al. 2015](#); [Sako et al. 2018](#)). [Ho et al. \(2021\)](#) notice that AT 2018cow and some SNe Ibn are distinct from other transients in that their blackbody radii decrease over time. We find a similar trend for most of our objects. All have blackbody radii of \approx

10^{14} – 10^{15} cm that tend to plateau or decrease after maximum light. The faster-evolving objects tend to have decreasing radii, whereas the radii of the slower-evolving SNe are more constant. These properties are distinct when compared to the SNe Ibc, which display larger radii that remain constant or increase after maximum light. AT 2018cow is somewhat unique as it has a smaller peak blackbody radius than the SNe Ibn, with the exception of SN 2021jpk. This may be evidence of a more confined CSM, as discussed in Section 4.5.

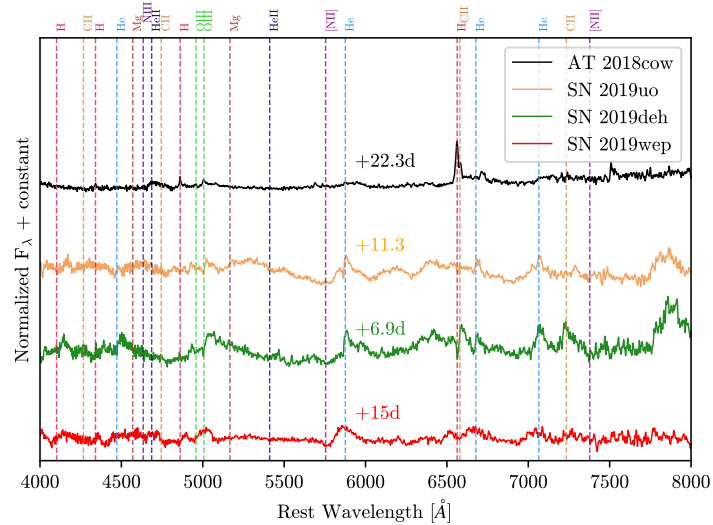
4.3.3 Spectroscopic Evolution

A defining characteristic of fast transients is their featureless blue continua, which makes spectroscopic classification difficult (Drout et al. 2014). AT 2018cow is one such object, with featureless spectra closely approximating a blackbody for the first ≈ 20 days of its evolution (Prentice et al. 2018). Blue, featureless continua are often found in young core-collapse SNe, in which the expanding ejecta is still hot and optically thick, preventing the formation of P-Cygni features (e.g., Hosseinzadeh et al. 2017b). A constant featureless continuum is evidence for a sustained powering mechanism such as shock cooling or CSM interaction.

Similarly, at early times SNe Ibn have spectra that show hot blue continua superimposed with narrow lines of He and other elements. These narrow lines originate from highly ionized species in a nearby CSM shell or wind and disappear once this material recombines or is swept up by the SN explosion, providing direct observable evidence for CSM interaction in SNe Ibn. It has been noted that AT 2018cow shows similar signs of interaction with a He-rich CSM. Fox & Smith (2019) find that the spectra of AT 2018cow are qualitatively similar to those of SNe Ibn convolved with a hot ($\sim 10^4$ K) blackbody. Additionally, similar spectral features, including narrow- and intermediate-width



(a)



(b)

Figure 4.5: (a) A comparison of the early-time spectra of the fast-evolving SNe Ibn to that of AT 2018cow at a later phase. All spectra have been continuum subtracted. Phases with respect to g -band peak brightness are labeled for each spectrum and spectral features are marked with dotted lines. The SNe Ibn spectra are similar to that of AT 2018cow, hinting that SNe Ibn-like spectral features in AT 2018cow may be hidden at earlier times. (b) Same as above, but here the spectra of the SNe Ibn are one to two weeks past maximum. At this stage the features of the SNe Ibn are more developed than those of AT 2018cow. SN 2021jpk is not included as spectra were only obtained at maximum light.

He emission lines from pre- and post-shocked CSM, are seen in both the late-time spectra of AT 2018cow and in spectra of SNe Ibn (Fox & Smith 2019; Xiang et al. 2021).

Figure 4.5 compares an LCO spectrum of AT 2018cow to LCO spectra of fast-evolving SNe Ibn at both early (top) and late (bottom) times. The spectra have been normalized as follows: from each spectrum we subtract the flux from its best-fit blackbody and divide by the median of the remaining flux. We find that a blackbody fits the continua well for all phases we consider here. When comparing a later spectrum of AT 2018cow with spectra of SNe Ibn around maximum light, the objects show qualitative similarities. All the objects show hot blue continua before normalization with emission lines of He, including a He II emission line in the spectrum of AT 2018cow that is broader than the same line in the spectra of SN 2019uo and SN 2019wep. Additionally, at early times SN 2019uo and SN 2019wep show flash features of C III and N III (Gangopadhyay et al. 2020 Gangopadhyay 2021, in preparation). However, at about two weeks after maximum the spectra of SNe Ibn show more developed emission and P-Cygni features of He I, C II, and O III than AT 2018cow, which still resembles a hot blackbody with few narrow emission lines. This consistently high photospheric temperature may be evidence of a long-lasting powering source for AT 2018cow, such as sustained CSM interaction, which can mask the underlying spectrum (Fox & Smith 2019).

Despite their different evolution at later times, the similar spectral features between AT 2018cow and the SNe Ibn, including a strong blue continuum and emission lines of He I and He II, hint at a common progenitor system. In particular, narrow emission lines with WR-like features are evidence for CSM interaction (Taddia et al. 2013; Gal-Yam et al. 2014a), pointing to a common circumstellar environment. In the case of SNe Ibn, it is unclear if the CSM has a shell-like density profile due to a preexplosion outburst in the months or years before explosion (e.g., Smith et al. 2008) or a wind-like profile from a WR stellar wind (see e.g., Crowther 2007 for a review). AT 2018cow shows more

peculiarities than SNe Ibn, such as He I emission features in the late-time spectra that are redshifted by several thousand km s^{-1} (Benetti et al. 2018). This redshift may be explained by asymmetries in a CSM shell (Margutti et al. 2019), which may be common in interaction-powered SNe (Soumagnac et al. 2020). Additionally, the emission features are broader and do not appear until much later than in SNe Ibn. This different evolution at later times may be the case if the CSM is closer to the progenitor star and is quickly overrun by the optically thick ejecta at early times (Fox & Smith 2019). Once the ejecta has expanded and cooled, the optical depth will drop and broadened emission lines from continued interaction with post-shocked CSM can be observed (Fox & Smith 2019). This may imply that the CSM is much more confined in radius in the case of AT 2018cow than in SNe Ibn. A discussion of the CSM properties of these objects is given in Section 4.4.2.

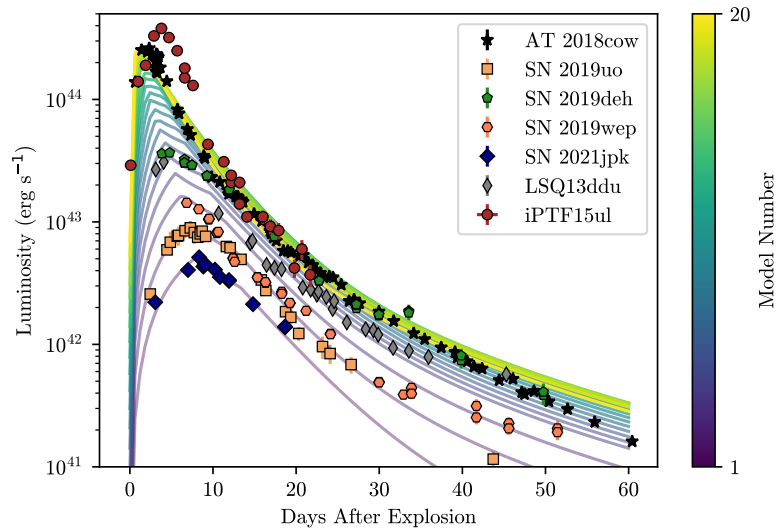
4.4 Circumstellar-interaction Models

4.4.1 Model Description

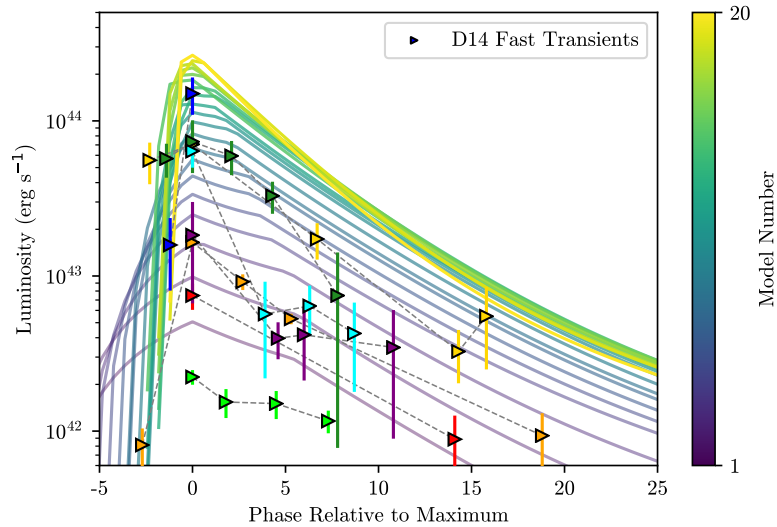
Modeling the energy source powering the light curves of SNe Ibn and other fast transients is necessary to understanding their progenitor systems. Due to their similar colors, photometric evolution, and spectral features, it is plausible that photometrically classified fast transients have a similar powering mechanism and progenitor environment to SNe Ibn. In SNe Ibn, the combination of narrow emission lines seen in spectra at early times and the fast rise to peak luminosity point to CSM interaction as a primary power source. Modeling the light curves of SNe Ibn has shown that either a combination of CSM interaction and ^{56}Ni decay (Clark et al. 2020; Wang & Li 2020; Wang et al. 2021) or CSM interaction alone (Karamahmetoglu et al. 2021) can sufficiently reproduce their luminosity evolution.

Due to their rarity ($\approx 0.1\%$ of the core-collapse SNe rate for AT 2018cow-like transients; [Ho et al. 2021](#)) and rapid evolution, the mechanisms powering the light curves of fast transients have not been as well studied. However, radioactive decay cannot be the sole powering mechanism, as the amount of radioactive Ni needed to reach high peak luminosities in only a few days often exceeds the total ejecta mass by an order of magnitude ([Drout et al. 2014](#); [Arcavi et al. 2016](#); [Pursiainen et al. 2018](#); [Rest et al. 2018](#)). Multiple physical interpretations of AT 2018cow have been suggested, including powering due to a central engine ([Prentice et al. 2018](#); [Margutti et al. 2019](#)), shock breakout from an optically thick shell of CSM ([Rivera Sandoval et al. 2018](#)), and the tidal disruption event of a white dwarf ([Perley et al. 2019](#)). More recently, [Xiang et al. \(2021\)](#) modeled the bolometric light curve of AT 2018cow with CSM interaction and ^{56}Ni decay. This choice is physically motivated by the similar luminosity evolution between AT 2018cow and SNe Ibn as well as the narrow emission lines of He and C seen in its spectra, as described in [Section 4.3](#). They found that the light curve of AT 2018cow can be reasonably explained by an energetic explosion with a small amount of ejected mass within an optically thick CSM shell or wind of small inner radius.

To explore whether the same powering source can sufficiently reproduce the light-curve evolution of both SNe Ibn and other fast transients, we construct a grid of CSM interaction plus ^{56}Ni decay models. We begin with the code presented in [Jiang et al. \(2020\)](#), which finds self-similar solutions to the interaction between expanding SN ejecta and a stationary CSM as first presented by [Chevalier \(1982\)](#) and [Chevalier & Fransson \(1994\)](#). This model assumes a two-zone SN ejecta: an inner region with a shallow density profile, $\rho \propto r^{-\delta}$, and an outer region with a much steeper profile, $\rho \propto r^{-n}$. The CSM density is parametrized as $\rho \propto r^{-s}$, with $s = 0$ being a shell-like CSM and $r = 2$ being a wind-like CSM. To this solution we also add the analytic formalism for ^{56}Ni decay with diffusion as presented in [Chatzopoulos et al. \(2012\)](#).



(a)



(b)

Figure 4.6: (a) Model light curves powered by CSM interaction and ^{56}Ni decay (solid curves) compared with bolometric luminosities of fast-evolving SNe Ibn (colored points) and the fast transient AT 2018cow (black stars). The model light curves span the range of luminosities between the faint, fast-evolving SNe Ibn and AT 2018cow. (b) Same as the top figure, but comparing the model light curves to the fast transients from D14. Again the models replicate the luminosity evolution of many of the objects. Note here that phase is plotted with respect to the time of g -band maximum.

Because this CSM interaction plus ^{56}Ni decay model has the potential for degeneracy between its many input parameters, we first focus on qualitatively reproducing the observed evolution of the SNe Ibn and fast transient light curves in order to gain a better understanding of the progenitors of these objects. To do so, the model is fit to the bolometric light curves, calculated from our UV and optical photometry, of our faintest objects (SN 2021jpk and SN 2019uo) and our brightest (AT 2018cow) using the Markov Chain Monte Carlo routine `emcee` (Foreman-Mackey et al. 2013). This is done in order to obtain initial model parameters that reproduce the light curves of both the faint, slower-evolving and bright, fast-evolving objects. These initial parameters are compared with best-fit values published for the objects in our sample (Gangopadhyay et al. 2020; Xiang et al. 2021) as well as other SNe Ibn and fast transients (e.g., Karamahmetoglu et al. 2021; Clark et al. 2020). We find reasonable qualitative agreement between our values and those published in the literature. In order to reproduce the light curves of all the objects in our sample, we smoothly vary the model parameters between the initial values of the faint, slow-evolving objects and the bright, fast-evolving ones. The following parameters are varied:

1. v_{ej} , the ejecta velocity;
2. M_{ej} , the ejecta mass;
3. M_{CSM} , the CSM mass;
4. R_0 , the inner radius of the CSM;
5. ρ_0 , the density of the CSM at the inner radius;
6. ϵ , the radiation efficiency;
7. κ_γ , the gamma ray opacity; and

8. M_{Ni} , the mass of ^{56}Ni produced.

For all the models we set $n = 10$, $\delta = 1$, $s = 0$, and the optical opacity $\kappa_{\text{opt}} = 0.1 \text{ cm}^2 \text{ g}^{-1}$. We caution that allowing these parameters to vary as well may also provide good fits to the data. This model grid is not meant to produce best fits to the data (for our efforts to find best fits, see Section 4.4.3). Instead, it is simply meant to illustrate similarities between the progenitor environments of SNe Ibn and fast transients and show that a continuous range of initial conditions can reproduce the behavior of both classes of objects.

4.4.2 Comparison to Observations

Our model light curves are shown in Figure 4.6. Different colors correspond to different models. The top panel compares the models to fast-evolving SNe Ibn as well as AT 2018cow. We have supplemented our sample of SNe Ibn with published data of LSQ13ddu (Clark et al. 2020) and iPTF15ul (Hosseinzadeh et al. 2017b). The models span over 1.5 orders of magnitude between the faintest object (SN 2021jpk) and the most luminous (iPTF15ul). Additionally, they reproduce the observed rise and decline times of these objects, including the rapid evolution of AT 2018cow, as well as the luminosity evolution of most of the objects out to ~ 60 days after explosion.

The bottom panel of Figure 4.6 compares the same models with the fast transients in D14. The range of luminosities is again reproduced by the models. Due to the small number of observations at similar epochs, the light curves of the objects are more sparsely populated, which makes comparing their late-time evolution to the models difficult. At least some of the objects have similar rise times and decline rates as the models, whereas others show different evolution. However, several factors make comparing this sample to the CSM models difficult. First, the PS1 objects have poorly constrained phases and

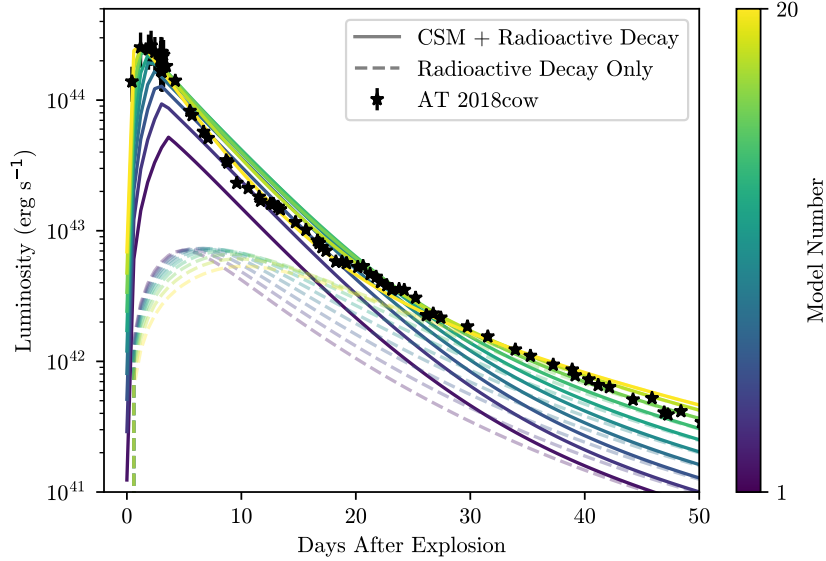


Figure 4.7: Model light curves with fixed ejecta parameter values but varying CSM parameter values. Plotted for comparison is the bolometric light curve of AT 2018cow. The radioactive decay component of each light curve is plotted with a dashed line.

late-time evolution due to their sparse light-curve sampling. Additionally, several of the objects show a tentative increase in the bolometric luminosity roughly ten days after maximum light. [Ho et al. \(2021\)](#) suggest these objects may be Type IIb SNe. In these cases, the observed rapid decline may be caused by shock-cooling emission, while a low ^{56}Ni mass may produce a weak secondary peak that went unobserved. Besides these cases, however, the broad agreement between the luminosities and decline rates of our models and the PS1 fast transients suggests that some of these objects may be powered by CSM interaction.

To test the effect the CSM parameters have on the models, we construct a separate grid with the same M_{ej} , v_{ej} , κ_{γ} , and M_{Ni} values as our model that best matches AT 2018cow, but with CSM parameters that are varied over the full range of values. The results are shown in Figure 4.7. We find that models with smaller and denser CSM shells power light curves that evolve faster and reach higher peak luminosities. The radiation

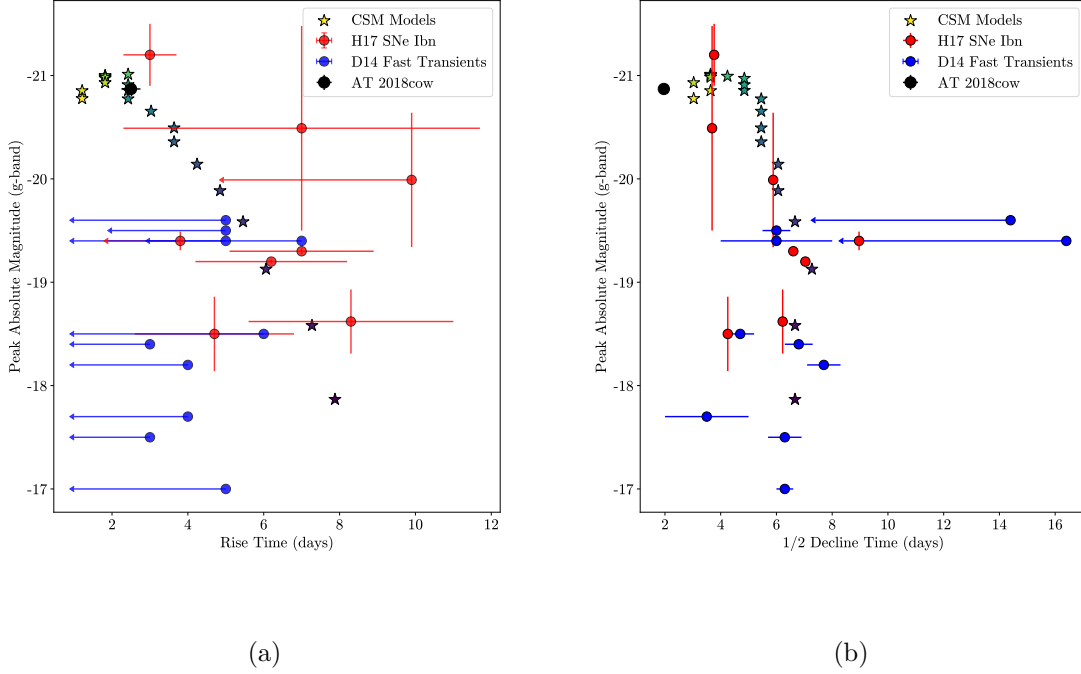


Figure 4.8: (a) Rest-frame g -band peak absolute magnitude versus rise time for our model light curves (colored stars) compared to SNe Ibn from H17 (red points), fast transients from D14 (blue points), and AT 2018cow (black point). The color map is the same as in Figure 4.6. The models span the parameter space between the fast-evolving SNe Ibn and the luminous fast transients. The fast transients not matched by these models are discussed in Section 4.5.1. (b) Peak absolute magnitude versus time to decline by half the peak luminosity for the same objects. Again, the models span the parameter space between SNe Ibn and fast transients.

diffusion timescale is also significantly impacted by the choice of CSM parameters. For AT 2018cow, this leads to a transition from CSM interaction to radioactive decay as the primary powering mechanism at ≈ 20 days after peak, as noted previously (Xiang et al. 2021).

In order to compare these models with the larger sample of objects in a different parameter space, in Figure 4.8 we plot the rest-frame peak g -band absolute magnitudes versus rise times and decline times of the models, several of the SNe Ibn in H17, the fast transients in D14, and AT 2018cow. To estimate peak absolute magnitudes of the model

light curves, we find the flux within the g -band assuming a blackbody SED given by the photospheric radius and temperature of each model.

In this phase space the model light curves exist on the boundary between the D14 fast transient and SNe Ibn populations. Additionally, the more luminous models evolve the fastest, which is key to replicating the behavior of the brightest, fastest-evolving transients such as AT 2018cow. Although there are still objects in this parameter space that are not matched by the models, we have reproduced the range of light-curve behaviors of the more luminous fast-evolving objects, including SNe Ibn, many of the fast transients in D14, and more extreme objects such as AT 2018cow. This shows that SNe Ibn and some other fast transients may share a common powering source, rather than having distinct physical mechanisms.

4.4.3 Comparison with Other Model Results

In order to test the model dependency of these results, we fit the bolometric light curves of all the objects shown in Figure 4.6 utilizing the `Minim` code and applying the `hybrid` model presented in Chatzopoulos et al. (2013). This model assumes the interaction between an optically thick CSM and an expanding SN ejecta, using the self-similar solution of Chevalier (1982) for the calculation of the expansion of the forward and reverse shocks, as the main powering mechanism. The shock heating efficiency, ϵ , is assumed to be 100%. While this may not be fully true in reality, this assumption provides a useful lower limit for the strength of the CSM interaction without introducing an additional (poorly constrained) parameter for the shock heating efficiency. In addition, the usual radioactive Ni-Co-Fe decay is used as the heating source of the SN ejecta. The CSM is modeled as a simple, constant-density shell with an inner radius of R_{ej} and an outer radius specified by its mass (M_{CSM}) and density (ρ_{CSM}). As earlier, the density

structure of the SN ejecta is assumed as an outer power law, this time having $n = 12$ (a built-in value in the `hybrid` model) and an inner, flat region within $r_0 = 0.1R_{\text{ej}}$. Note that instead of the CSM density, the formal mass-loss rate $\dot{M} = 4\pi R_{\text{ej}}^2 \rho_{\text{CSM}} v_w$ with $v_w = 10 \text{ km s}^{-1}$ is used in the `hybrid` model as a fitting parameter, even though it has no direct physical meaning in the context of a constant-density CSM cloud. After the forward and reverse shock passes through the CSM shell and the ejecta, the shock-heated material radiates out its thermal energy via radiative diffusion. The `hybrid` model applies the usual constant-opacity approximation. We set the optical opacity as $\kappa_{\text{opt}} = 0.1 \text{ cm}^2 \text{ g}^{-1}$ and the gamma-ray opacity as $\kappa_\gamma = 0.03 \text{ cm}^2 \text{ g}^{-1}$.

The best-fit models are selected based on χ^2 minimization by applying the Price algorithm, which samples the parameter space with a controlled random-search method (see [Chatzopoulos et al. 2013](#) for more details). The parameters from these fits are in reasonable (order-of-magnitude) agreement with those from our model grid, despite the different assumptions made between the two models (including different ejecta power-law indices and efficiency values) and the fact that the CSM models presented earlier were produced to qualitatively match the range of observed light curves properties without performing rigorous best-fit routines. This agreement supports the insight our model grid gives into the progenitor systems of these fast-evolving objects.

Our calculations using the `Minim` code reveal that due to the rapid light-curve evolution of these transients, both the forward and reverse shocks sweep up the CSM and the SN ejecta by approximately the time of maximum light. After maximum, the decline of the light curve can be explained by the cooling of a shock-heated ejecta and CSM. This behavior is different from what is observed in other interacting (Type IIIn) SNe, where the shocks live much longer and the CSM cloud stays optically thick on a longer timescale.

Our best-fit `Minim` light curves are shown in [Figure 4.9](#). We find that the `Minim` models provide almost perfect fitting to the data of the SNe Ibn, assuming both CSM interaction

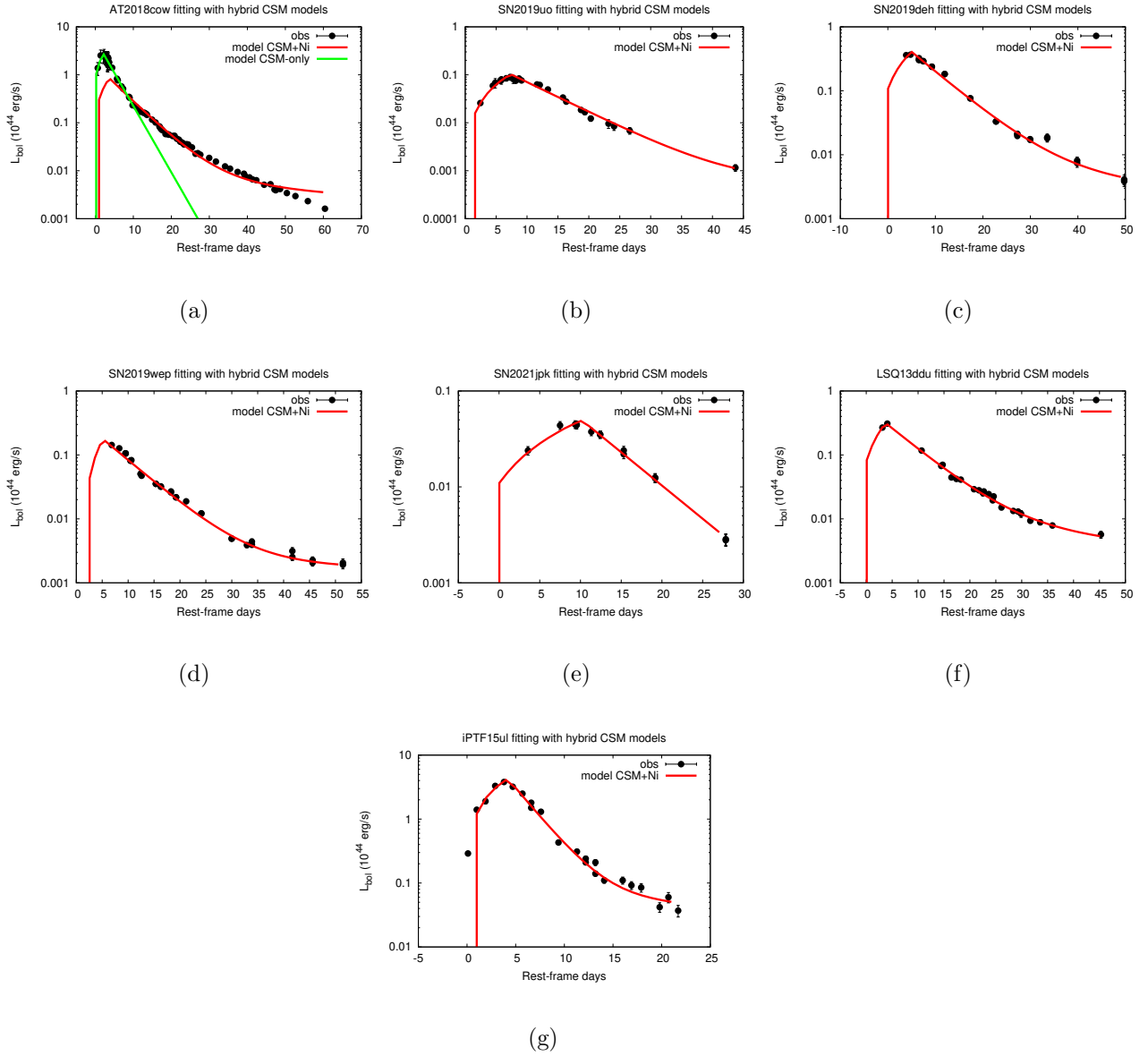


Figure 4.9: Best-fit Minim models to the bolometric light curves of (a) AT 2018cow, (b) SN 2019uo, (c) SN 2019deh, (d) SN 2019wep, (e) SN 2021jpk, (f) LSQ13ddu, and (g) iPTF15ul assuming luminosity contributions from CSM interaction and ^{56}Ni decay.

and Ni-Co decay as coexisting heating sources; without the radioactive energy input, the CSM-only light curves are not compatible with the observations. On the other hand, AT 2018cow is peculiar because its long-lasting quick decline rate is not well described by the predicted Ni-Co decay rate at late phases. For this object the CSM-only model can fit the peak of the light curve, but then the model light curve declines too fast, which suggests the presence of an additional heating source. Because the `hybrid` model in `Minim` assumes full trapping of the γ rays from Ni-Co decay, it is possible that γ -ray leaking (possibly caused by noncentral Ni distribution or a nonspherical ejecta geometry) may explain the unusual decline of AT 2018cow. We further discuss the possibility of an asymmetric ejecta for AT 2018cow in Section 4.5.1.

4.5 Discussion

4.5.1 Is CSM Interaction Sufficient to Model Fast Transients?

Based on the similarities discussed in Section 4.3, we are motivated to consider a common powering source and progenitor system between SNe Ibn and some fast transients. These observational similarities include the following:

1. a similar color evolution, with colors that are consistently bluer than other SNe Ibn;
2. similar blackbody radius evolution, with both classes of objects exhibiting receding photospheres after peak brightness; and
3. similar spectral features, such as a hot blue continuum superimposed with narrow He lines as well as occasional flash features of He, C, O, and other highly ionized elements.

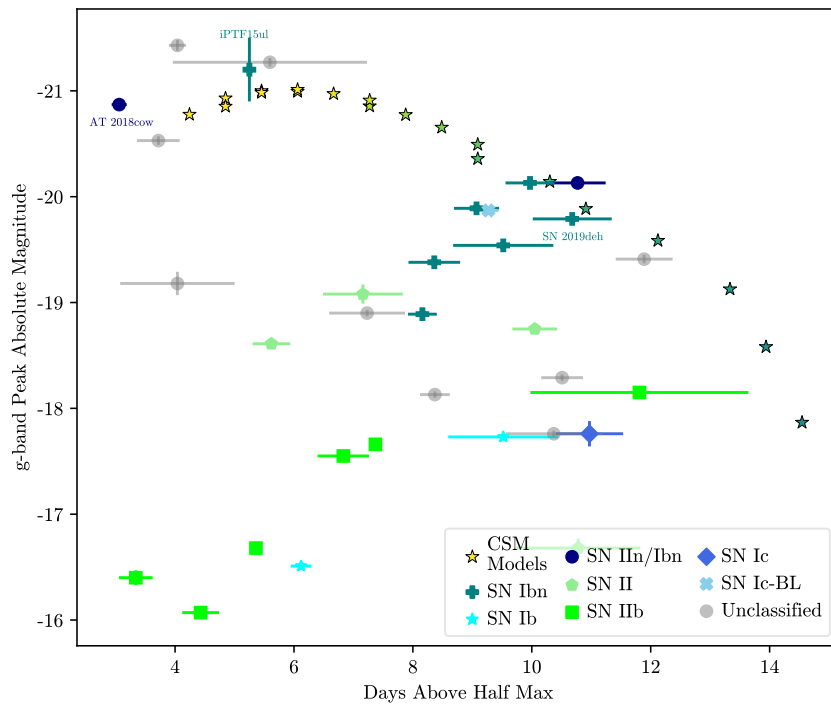


Figure 4.10: Rest-frame g -band absolute magnitude versus time above half-maximum of our CSM models (colored stars) compared to that of several of the objects presented in Ho et al. (2021) other symbols). Spectroscopically classified transients are plotted as colored symbols and three objects from Ho et al. (2021) that we discuss in this work are labeled.

These common characteristics can all be explained by interaction between CSM and the SN ejecta. Modeling this interaction as the primary powering source of these objects at early times, along with a ^{56}Ni decay component, we are able to reproduce the range of rise times, peak luminosities, and decline rates in our sample of SNe Ibn, some fast transients from D14, and AT 2018cow.

However, these CSM interaction models do not match the observed light-curve properties of all the fast transients reported in D14. In particular, the model parameters we consider here are unable to reproduce the fainter fast-rising objects. [Ho et al. \(2021\)](#) studied a large sample of spectroscopically classified fast transients in ZTF Phase I and found that objects in this region of parameter space (i.e. $t_{\text{rise}} \lesssim 5$ days and peak $M_g \gtrsim -18$) were mainly SNe IIb. It is more likely, therefore, that the faint and fast-rising transients in D14 are observed shock-cooling light curves from SNe IIb, and therefore are physically distinct from those powered by CSM interaction.

It is also possible that other powering mechanisms, such as a central engine, are needed to reproduce some observed features of fast transients, such as the high ejecta velocities and X-ray luminosities seen in AT 2018cow and other similar transients ([Coppejans et al. 2020](#); [Ho et al. 2020](#); [Perley et al. 2021](#)). [Ho et al. \(2021\)](#) argue that the high radio and X-ray luminosity of AT 2018cow and several other spectroscopically unclassified fast transients set them apart from other objects with rapid evolution, including luminous SNe Ibn. On the one hand, X-ray and radio emission can arise from CSM interaction ([Chevalier 1982](#); [Chevalier & Fransson 1994](#)). [Rivera Sandoval et al. \(2018\)](#) initially use the variable X-ray luminosity of AT 2018cow as evidence of CSM interaction powering the light curve. Their estimated CSM radii ($\approx 100 - 200$ au) and masses ($\gtrsim 0.08 M_{\odot}$), inferred from the X-ray emission are qualitatively similar to our model parameters. On the other hand, [Margutti et al. \(2019\)](#) argue against an external CSM shock as the primary power source for AT 2018cow. Observations of the early X-ray luminosity of AT 2018cow disfavor

an external shock as the source of the X-ray emission and instead show the need for a central source of high-energy photons (Margutti et al. 2019). Similar X-ray luminous and/or radio-loud fast transients have recently been discovered at cosmological distances (Coppejans et al. 2020; Ho et al. 2020; Perley et al. 2021). If these transients have the same physical mechanism as AT 2018cow, the central X-ray source must be physically distinct from the external interaction powering the luminous radio emission (Ho et al. 2019a).

However, Margutti et al. (2019) show that interior shocks originating from ejecta interacting with a dense equatorial CSM ring may be sufficient to power the X-ray luminosity observed in AT 2018cow. A highly asymmetric CSM has been attributed to other astrophysical phenomena, including luminous red novae (Metzger & Pejcha 2017) and SNe such as iPTF14hls (Andrews & Smith 2018), and may arise naturally from binary interaction (Sana et al. 2012) or explosive mass loss (Smith & Arnett 2014). Asymmetries in the CSM may explain some of the other unusual features of this object. Most of the ejecta will be able to freely expand past the CSM. However, at regions of high CSM densities the ejecta will be decelerated by the circumstellar interaction. The result is that the interaction beneath the photosphere will continue to be the primary power source of the luminosity, but the spectral signatures of this interaction would be hidden until the photosphere has time to recede (Andrews & Smith 2018). This may also explain the featureless blue continuum at early times that gives way to redshifted and broadened He features at later times as the photosphere recedes. The varying X-ray emission around 20 days past peak occurs at roughly the same time as the onset of these spectral features, which again may indicate that the photosphere has receded enough for X-rays generated by the CSM interaction to escape the ejecta (Margutti et al. 2019). It is interesting to note that at this phase Perley et al. (2019) estimate a blackbody radius of ≈ 18.5 au, in very close agreement with the CSM inner radius of the model light curve from our grid

that best matches the evolution of AT 2018cow.

4.5.2 Comparison with ZTF Rapidly Evolving Transient Sample

Ho et al. (2021) constructed one of the largest samples of fast-evolving transients to date, with 22 spectroscopically classified objects in addition to 20 nonclassified ones. They found that fast-evolving transients can be split into three groups: faint and fast-evolving objects tend to be the initial shock-cooling phase seen in SNe IIb without the accompanying ^{56}Ni -powered secondary peak, more luminous and slower-evolving objects tend to be interaction-powered SNe such as SNe Ibn and IIn, and the most luminous and fastest-evolving objects are radio-loud and X-ray luminous objects such as AT 2018cow. In Figure 4.10 we compare our CSM model grid with the gold and silver samples from ZTF. Our models agree with their conclusions that the luminous and slower-evolving fast transients are dominated by interaction-powered SNe. However, we again show that our models reach even the most luminous and fast-evolving objects, including the parameter space of AT 2018cow-like transients, implying a common origin between these objects and SNe Ibn.

Several of the SNe we compare with our models in Figure 4.6 are included in either the ZTF spectroscopically classified sample or objects Ho et al. (2021) identify from literature as being fast transients. We have labeled these objects in Figure 4.10. In this plot iPTF15ul stands out as being the fastest-evolving and most luminous spectroscopically classified object, besides AT 2018cow. iPTF15ul was classified by Hosseinzadeh et al. (2017b) as a probable SN Ibn and is one of the most luminous SNe Ibn reported to date. In Figure 4.11 we compare a dereddened spectrum³ of iPTF15ul around peak brightness

³Using the extinction law of Cardelli et al. (1989) and the estimated A_V value from Hosseinzadeh et al. (2017b)

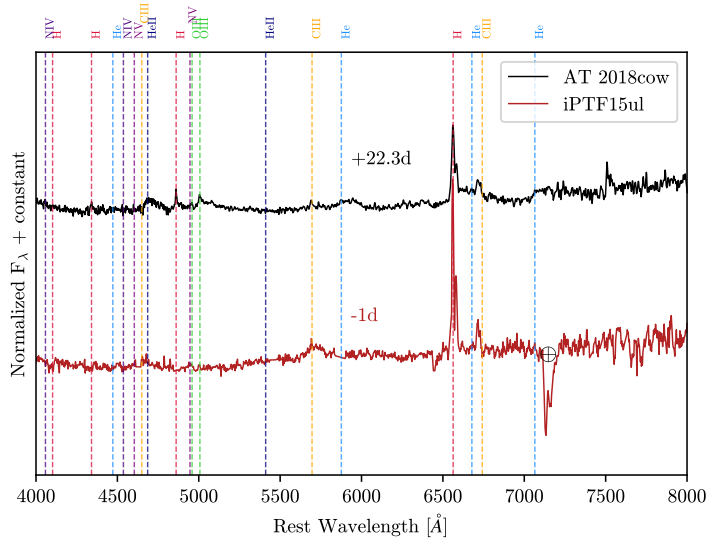


Figure 4.11: A dereddened rest-frame spectrum of the probable Type Ibn iPTF15ul around maximum light compared to a spectrum of AT 2018cow about three weeks after maximum light. Phases relative to g -band maximum light are denoted above each spectrum and some spectral features are marked with dashed colored lines. Telluric absorption is marked with a \oplus symbol. Both objects display similar features, including highly ionized C and weak He lines, which set them apart from the other objects considered in this work. The spectrum of iPTF15ul was obtained from WISeREP (Yaron & Gal-Yam 2012).

to the spectrum of AT 2018cow three weeks after peak. Similar features are seen between the two spectra, including C III emission lines and weak He I features, the latter of which is rare in SNe Ibn spectra at maximum light (Hosseinzadeh et al. 2017b; Gangopadhyay et al. 2020). The spectra of these two objects appear more similar to each other than to any of the spectra shown in Figure 4.5.

Based on the similar light-curve properties and spectral features, iPTF15ul may be a transitional object between SNe Ibn and AT 2018cow-like fast transients. However, several differences set iPTF15ul apart from AT 2018cow-like objects. First, an X-ray search from the Swift X-ray Telescope (Burrows et al. 2005) only yielded nondetections with an upper limit of 1.6×10^{-2} counts s^{-1} at maximum light. This may indicate some of the physical processes powering the high-energy emission seen in AT 2018cow

are missing in the case of iPTF15ul. Furthermore, its extremely high peak luminosity may be affected by host reddening estimates, which are highly uncertain (Hosseinzadeh et al. 2017b). If the reddening estimate is correct, though, iPTF15ul shows that some SNe Ibn without luminous X-ray emission may still occupy the same region of parameter space as AT 2018cow-like transients, even if the latter do have a distinct source of X-ray and radio emission. This is particularly important as future time-domain surveys will photometrically classify more objects across different regions of fast transient parameter space. Our model grid shows that these objects can be explained entirely by CSM interaction and radioactive decay on the basis of their light curves alone.

4.5.3 Common Progenitor Scenarios

The host galaxies of fast transients and SNe Ibn have been extensively studied (Drout et al. 2014; Hosseinzadeh et al. 2019; Lyman et al. 2020; Wiseman et al. 2020; Ho et al. 2021). The majority of spectroscopically classified fast transients from Ho et al. (2021) and the fast transients from D14 were found in star-forming galaxies. This indicates that the progenitors of most fast transients are massive stars. The range of parameters in both our model grid and the best-fit `Minim` models can tell us more about the progenitor systems of these transients. We note a general trend in which fainter, slower-evolving, interaction-driven SNe have lower explosion energies (governed by M_{ej} and v_{ej}) and less ^{56}Ni produced. On the other hand, the models that best reproduce the observed behavior of the fastest and most luminous transients have fast ejecta, relatively low masses of both ejecta and CSM, and produce more ^{56}Ni . The small ejecta mass ($\approx 1 M_{\odot}$) perhaps could indicate much of the progenitor star’s mass remains gravitationally bound to a compact remnant, as has been proposed for other fast-evolving transients (Dexter & Kasen 2013).

To gain a qualitative understanding of the proposed progenitor systems of fast tran-

sients and SNe Ibn, we compare our best-fit model parameters to the CSM properties inferred from observation. Signatures of mass loss in the months to years leading up to explosion have been observed for several SNe Ibn. In the first case, a preexplosion outburst was observed at the position of SN 2006jc two years before explosion (Foley et al. 2007; Pastorello et al. 2007; Smith et al. 2008). However, the rise of SN 2006jc was not well constrained, and from X-ray data we can infer that the shock did not reach the CSM until several weeks after explosion (Immler et al. 2008). SN 2019uo also has precursor emission observed approximately a year before explosion (Strotjohann et al. 2021). The light curve from our model grid that best matches SN 2019uo has an inner CSM radius $R_0=65$ au, similar to estimates derived from light-curve fits (Gangopadhyay et al. 2020) and preexplosion mass loss (Strotjohann et al. 2021).

All of our models require a significant CSM mass relatively close to the progenitor star, indicating a large rate of mass loss shortly before explosion. An increase in mass-loss rates may be common in the years prior to interaction-driven SNe (Ofek et al. 2014; Bruch et al. 2021; Strotjohann et al. 2021), including eruptive mass-loss events (Wang & Li 2020). A proposed progenitor of SNe Ibn are WR stars (Foley et al. 2007; Smith et al. 2012), yet they have not been observed to undergo violent luminous blue variable-like eruptions. However, if such events occur during the nuclear burning stages within the last months to years of a WR star’s lifetime (Shiode & Quataert 2014), they would not be observable in the Galactic WR population. On a qualitative level our model parameters agree with those from simulations of exploding WR stars, including low M_{ej} and M_{Ni} (Dessart & Hillier 2011). This may indicate that a WR-like progenitor to SNe Ibn and some fast transients is plausible.

Our model grid and the `Minim` models predict different relationships between the properties of the CSM and the peak luminosities of the transients. This disagreement may be due to different assumptions made between the models: for instance, the different

ejecta power-law indices or the use of a mass-loss rate to derive the CSM densities in the case of the `Minim` models. For the model grid, the fact that more luminous models have smaller CSM radii may help to explain the peculiar features of AT 2018cow-like transients, including the X-ray and radio emission and the delayed emergence of spectral features. These unusual features may be explained if the CSM is very close to the progenitor star and is quickly enveloped by the expanding ejecta. If this is the case, then the spectral features will not emerge until the photosphere recedes back past the CSM shell. This also explains the increased variability in the X-ray luminosity of AT 2018cow beginning at the same phase, as once the photosphere recedes past the location of the shock within the CSM fewer X-rays are reprocessed by the ejecta.

4.6 Conclusions

We present one of the first investigations into a common powering mechanism between a sample of Type Ibn SNe and other photometrically classified fast optical transients. We are motivated to consider interaction with CSM as a powering mechanism for these two samples based on their similar light-curve properties and spectral features. We identify several fast-evolving Type Ibn SNe with well-sampled multiband light curves using data from LCO and Swift. We notice many similarities when comparing the light curves, colors, blackbody radii, and spectra of these Type Ibn SNe with those of fast transients such as AT 2018cow. Modeling their light curves with luminosity inputs from circumstellar interaction and ^{56}Ni decay reproduces the observed range of peak luminosities, rise times, and decline times of the objects in our sample, suggesting that these transients may have similar progenitor environments with significant mass-loss rates prior to explosion.

These results are in agreement with recent studies (e.g., [Ho et al. 2021](#)) which have found that fast transients are a heterogeneous class of objects, some of which show

signatures of circumstellar interaction. Additionally, our models show that circumstellar interaction can reproduce the evolution of even the fastest-evolving and most luminous transients. The model parameters presented in this work demonstrate that relatively little ejecta mass and CSM ($\lesssim 4 M_{\odot}$ total) are needed to reproduce the properties of fast transients, arguing against the need for exotic progenitor systems or powering sources to explain these objects. Additionally, models with faster-evolving light curves tend to have denser and more confined CSM, possibly indicating large-scale mass-loss events prior to explosion. However, it remains to be seen whether fast transients with luminous X-ray and radio emission, such as AT 2018cow, can also be explained by circumstellar interaction, or if additional powering sources are needed to reproduce these features.

The analytical circumstellar-interaction models used in this work make several simplifying assumptions, such as a stationary photosphere and spherical symmetry, that are likely unrealistic. In the future, further work should be done in modeling circumstellar interaction with an asymmetric distribution of material, as this is both a more realistic physical scenario (Smith & Arnett 2014) and will have important effects on observation (Smith 2017). It is possible that an asymmetric CSM may be able to reproduce the full range of observed features of AT 2018cow-like fast transients, but more work must be done to test this hypothesis.

This study demonstrates the importance of circumstellar interaction in understanding the properties of core-collapse SNe. It is likely that the majority of massive stars undergo enhanced mass loss at the ends of their lifetimes (Ofek et al. 2014; Bruch et al. 2021; Strotjohann et al. 2021), suggesting that circumstellar interaction in core-collapse SNe to some degree may be ubiquitous. This points to the growing need for more rapid spectroscopic follow-up of transients, especially fast-evolving objects at cosmological distances, in order to better understand the overlap between fast transients and interaction-powered classes of SNe.

Chapter 5

Type Icn Supernovae: A New Class of Rapidly-Evolving Supernovae with Multiple Progenitor Channels

Due to an increasing desire to spectroscopically classify more objects in the rapidly-evolving region of phase space (as well as intense competition to do so), a new class—Type Icn supernovae—was discovered in 2021¹ (Gal-Yam et al. 2021). Type Icn supernovae are defined by signatures of interaction with circumstellar material that is both hydrogen- and helium-poor. The lack of both these elements in their spectra, as well as the identification of elements such as carbon and neon, indicate that the progenitor stars of these supernovae lost an extraordinary amount of material before exploding—the nucleosynthetic products in their spectra indicate they were stripped down to their carbon-burning layers before exploding. Such extensive mass-loss is difficult to reconcile with current theory. As a result, these supernovae offer a new window into stellar evolution.

Much of the mystery surrounding these objects is exacerbated by their rapid evolution—they fall firmly within the phase space of fast-evolving transients (Figure 5.9), making them difficult to discover and spectroscopically classify. This work is the first to study the entire sample of Type Icn supernovae (4 objects) at the time the writing began.

¹As this chapter shows, the first supernovae unambiguously classified as Type Icn were discovered in 2019. However, this class was not defined until 2021.

By comparing these objects to one another, significant diversity was found in their light-curve properties, spectroscopic features, and host galaxies. The evidence favors multiple progenitor channels, such as a helium star progenitor with a pre-explosion mass of $\approx 3 - 4 M_{\odot}$, for these objects. This is a novel conclusion in contrast with the literature consensus that interacting stripped-envelope supernovae are the explosions of the most massive Wolf-Rayet type stars (e.g., [Foley et al. 2007](#); [Pastorello et al. 2008](#)). However, an outpouring of subsequent work in the past year alone has supported the picture that lower-mass binaries are a possible, and potentially necessary, channel to produce these objects (e.g., [Davis et al. 2022](#); [Dessart et al. 2022](#); [Wu & Fuller 2022](#); [Sun et al. 2023](#)). As a result, this work has helped reshape the community’s consensus on the causes of such extreme mass-loss and the fates of the most massive stars.

Since this work was published, several new Type Icn supernovae have been discovered ([Pellegrino et al. 2022b, 2023a](#)). They continue to show considerable diversity in their observational properties, as well as more significant overlap with their Type Ibn cousins. This overlap suggests a spectrum of mass-loss histories and progenitor properties between these two classes. In the future, observations of transitional Type Ibn/Icn supernovae will potentially reveal new evidence as to their possible progenitor channels.

This chapter was reproduced from [Pellegrino et al. \(2022d\)](#) with only minor changes to fit the formatting of this dissertation. I’d like to thank my coauthors, without whom this work would not have been possible: D. A. Howell, G. Terreran, I. Arcavi, K. A. Bostroem, P. J. Brown, J. Burke, Y. Dong, A. Gilkis, D. Hiramatsu, G. Hosseinzadeh, C. McCully, M. Modjaz, M. Newsome, E. Padilla Gonzalez, T. A. Pritchard, D. J. Sand, S. Valenti, and M. Williamson.

5.1 Introduction

Stars with initial masses $\gtrsim 8 M_{\odot}$ end their lives as core-collapse supernovae (SNe; e.g., [Janka 2012](#)). While single stars in the mass range $8 \lesssim M_{\text{ZAMS}} \lesssim 25 M_{\odot}$ are thought to explode as Type II SNe ([Smartt 2009](#)), the fate of stars more massive than $\approx 25 M_{\odot}$ is uncertain ([Smartt 2015](#)). These stars are expected to lose their outer H envelopes, either through line-driven stellar winds ([Castor et al. 1975](#); [Abbott 1982](#); [Vink et al. 2000](#)) or stripping due to binary companion interaction ([Yoon et al. 2010](#); [Sana et al. 2012](#)), and appear as Wolf-Rayet (W-R) stars ([Crowther 2007](#)). W-R stars may explode as stripped-envelope SNe (SESNe) of Types Ib and Ic (SNe Ibc; [Sukhbold et al. 2016](#)), or the most massive may collapse directly to a black hole, producing little or no optical emission ([MacFadyen & Woosley 1999](#)).

However, recent evidence has suggested that W-R stars are unlikely to be the progenitors of all SNe Ibc. Searches for W-R stars at the locations of SNe Ibc in pre-explosion images have had mixed success ([Cao et al. 2013](#); [Eldridge et al. 2013](#); [Kilpatrick et al. 2021](#)), and ejecta masses estimated from SNe Ibc light curves are well below the pre-SN masses of W-R stars (e.g., [Lyman et al. 2016](#); [Taddia et al. 2018](#)). Instead, it is possible that less massive stars undergoing binary interaction may lose their H envelopes and explode as SESNe ([Podsiadlowski et al. 1992](#)). Some SNe that show signs of extreme binary interaction have been discovered ([Drout et al. 2013](#); [De et al. 2018](#); [Yao et al. 2020](#)). Classified as ultra-stripped SNe (USSNe), these objects show diverse photometric and spectral evolution. Some may have powering sources such as shock-cooling emission ([Kleiser & Kasen 2014](#)) instead of or in addition to radioactive decay of ^{56}Ni at early times. Many are located in regions devoid of star formation within their host galaxies (e.g., [Drout et al. 2013](#); [De et al. 2018](#)). Spectroscopically they resemble SNe Ibc but have lower explosion energies and ejecta masses and produce less ^{56}Ni . Based on their

small ejecta and ^{56}Ni masses, as well as their local environments, they are thought to originate from stars with initial masses of 8–20 M_{\odot} that have undergone extensive binary companion stripping and explode as bare, low-mass ($\approx 1\text{--}3 M_{\odot}$, [Tauris et al. 2015](#)) cores.

Occasionally, SESNe show evidence for circumstellar interaction (CSI) between the SN ejecta and circumstellar material (CSM), consisting of the stripped outer layers of the progenitor. Quickly after explosion, the CSI drives forward and reverse shocks into the CSM and ejecta, which converts some of the kinetic energy of the explosion to thermal energy and leads to a rapid rise in luminosity. As the CSM cools, it emits narrow emission lines of highly ionized species. SNe that interact with H-poor, He-rich CSM have spectra dominated by narrow He lines and are classified as Type Ibn SNe (SNe Ibn; [Pastorello et al. 2007](#)). CSI powers their early-time light curves, which rise and decline in luminosity much faster than those of other SN classes. Because of this rapid evolution, SNe Ibn make up part of the “fast transient” population ([Ho et al. 2021](#); [Pellegrino et al. 2022c](#)). W-R stars are commonly proposed as the progenitors to SNe Ibn ([Pastorello et al. 2007](#); [Foley et al. 2007](#)), but some evidence shows that these objects may not all be the explosions of massive stars ([Hosseinzadeh et al. 2019](#)). Highly efficient W-R winds, eruptive mass-loss episodes, and binary interaction have all been proposed as mechanisms to strip the progenitor stars of their H and He layers.

Recently, an even more extreme subtype of interacting SESN has been discovered. These objects are classified as Type Icn SNe (SNe Icn) owing to their narrow spectral lines indicative of interaction with a H- and He-poor CSM. Despite being theoretically predicted ([Smith 2017](#); [Woosley 2017](#)), only two such objects have been published in the literature to date ([Fraser et al. 2021](#); [Gal-Yam et al. 2022](#); [Perley et al. 2022](#)). Their early-time spectra are blue with narrow emission lines, similar to those of SNe Ibn, but the features are produced by highly ionized C and O, rather than He. Their light curves rise rapidly to peak luminosities comparable to those of most SNe Ibn ($M \approx -19$). After

maximum, as the SN ejecta becomes optically thin, their spectra appear more similar to normal SNe Ibc or SNe Ibn (Gal-Yam et al. 2022; Perley et al. 2022).

The overall photometric and spectroscopic similarities between SNe Ibn and SNe Icn suggest that their progenitors may be similar. It has been proposed that both SNe Ibn and SNe Icn are the explosions of W-R stars, with different spectral features due to different W-R star subtype progenitors, different amounts of mass loss, or both (Gal-Yam et al. 2022; Perley et al. 2022). On the other hand, their progenitors or explosion mechanisms may differ. It is not clear whether the core collapse of a W-R star should completely eject the entirety of the stellar material or if a substantial fraction may fall back onto the compact remnant (e.g., MacFadyen & Woosley 1999), perhaps driven by a strong reverse shock generated by CSI (Chevalier 1989; Kleiser et al. 2018). Furthermore, even if these two classes have different explosion or progenitor properties, the observable signatures of these differences may be masked by the dominant CSI at early times. Therefore, it is crucial to study a collection of these objects throughout their evolution in order to better understand their inherent differences.

In this work, we analyze a sample of four SNe Icn—SN 2019jc, SN 2019hgp, SN 2021ckj, and SN 2021csp. This sample adds two new SNe Icn to those already published in the literature. These SNe were all extensively observed photometrically and spectroscopically with Las Cumbres Observatory (LCO; Brown et al. 2013) through the Global Supernova Project. The SNe Icn display a range of peak luminosities, light-curve properties, and late-time spectral evolution. In an effort to better understand their progenitor channels, explosion mechanisms, and relationships to other SESNe, we model their bolometric light curves with luminosity inputs from CSI and ^{56}Ni decay (Chatzopoulos et al. 2012). We also examine the host galaxy properties at the explosion site of the closest SN Icn, SN 2019jc, in order to constrain its progenitor mass.

This paper is organized as follows. In Section 5.2, we describe the objects in our

sample and the process of collecting and reducing our data. In Section 5.3, we analyze the light-curve and blackbody properties of these objects. We discuss their prominent spectral features and spectral evolution in Section 5.4. In Section 5.5, we attempt to fit their bolometric light curves with CSI and ^{56}Ni decay models and study their host galaxies. We discuss possible progenitor systems and explosion mechanisms in Section 2.6, and we conclude in Section 5.7.

5.2 Sample Description and Observations

In this work we present and analyze observations of four SNe Icn. Because the sample size of these objects is still small, with only a handful classified to date, any data are crucial to better understanding their progenitor systems and explosion mechanisms. Two objects in our sample—SN 2019hgp and SN 2021csp—have been closely studied in previous works (Fraser et al. 2021; Gal-Yam et al. 2022; Perley et al. 2022). We add observations of two other SNe Icn, primarily obtained with LCO. One of the objects (SN 2021ckj) was classified on the Transient Name Server² as an SN Icn (Pastorello et al. 2021), while the other (SN 2019jc) was identified as an SN Icn during a retroactive search of our archival data after this subclass was more rigorously defined (Gal-Yam et al. 2021; Pellegrino et al. 2022a).

5.2.1 SN Icn Sample Description

SN 2019jc was discovered by the Asteroid Terrestrial-impact Last Alert System (ATLAS; Tonry et al. 2018) in UGC 11849 on MJD 58491.21 (UTC 2019 January 8; Heinze et al. 2019) with a 2-day nondetection before the first detection. SN 2019hgp, SN 2021ckj, and SN 2021csp were discovered by the Zwicky Transient Facility (ZTF; Bellm et al. 2019;

²<https://www.wis-tns.org/>

Graham et al. 2019) on MJD 58642.24 (UTC 2019 June 8; Gal-Yam et al. 2022), MJD 59254.29 (UTC 2021 February 9; Forster et al. 2021) and MJD 59256.48 (UTC 2021 February 11; Perley et al. 2022) with nondetections approximately 1, 2, and 2 days prior, respectively. We assume a cosmology with $H_0 = 73 \text{ km s}^{-1} \text{ Mpc}^{-1}$, $\Omega_m = 0.27$, and $\Omega_\Lambda = 0.73$ to derive luminosity distances. We use the dust maps of Schlafly & Finkbeiner (2011) to estimate Galactic reddening. We assume no host galaxy extinction for SN 2019hgp and SN 2021csp to be consistent with the analyses of Fraser et al. (2021), Gal-Yam et al. (2022), and Perley et al. (2022). We also assume negligible host extinction for SN 2019jc owing to its large projected offset from its host galaxy and for SN 2021ckj owing to its early-time colors that are similar to the other SNe Icn (Figure 5.3).

LCO follow-up observations commenced soon after the discovery of each of these objects. Early observations have proved to be crucial in studying SNe Icn, as a rapid rise to peak brightness is a signature of these objects (Fraser et al. 2021; Gal-Yam et al. 2022; Perley et al. 2022). We fit a quadratic spline to the early-time g -band data for each object in order to measure $t_{1/2, \text{rise}}$, the time to rise from half the peak luminosity to peak, the time of g -band peak brightness $t_{\text{max}, g}$, the g -band peak absolute magnitude $M_{\text{peak}, g}$, and the time to decline from peak to half the peak brightness, $t_{1/2, \text{decl}}$. When possible, we fit the LCO data combined with those from the literature. All values are given in the observer frame.

5.2.2 Optical Photometry

LCO $UBgVri$ -band images were obtained using the SBIG and Sinistro cameras on LCO 0.4m and 1.0m telescopes, respectively. Data reduction was performed using the `lcogtsnpipe` pipeline (Valenti et al. 2016), which extracts point-spread function magnitudes after calculating zero-points and color terms (Stetson 1987). UBV -band photome-

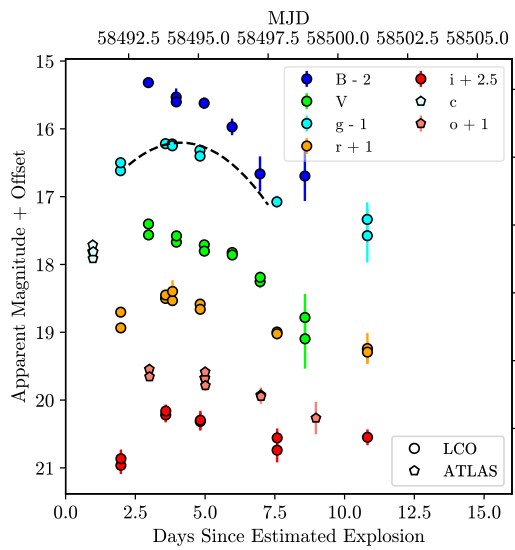
try was calibrated to Vega magnitudes using Landolt standard fields (Landolt 1992) and *gri*-band photometry was calibrated to AB magnitudes (Smith et al. 2002) using Sloan Digital Sky Survey (SDSS) catalogs. Three of the SNe Icn (SN 2019hgp, SN 2021ckj, and SN 2021csp) were contaminated by host galaxy light; therefore, background subtraction was performed using the HOTPANTS (Becker 2015) image subtraction algorithm with template images obtained after the SNe had faded.

We also include publicly available ATLAS and ZTF photometry in our analyses, when possible. ATLAS photometry was obtained from the forced photometry server for SN 2019jc and ZTF alert photometry was obtained for SN 2019hgp, SN 2021ckj, and SN 2021csp. These data were not processed further.

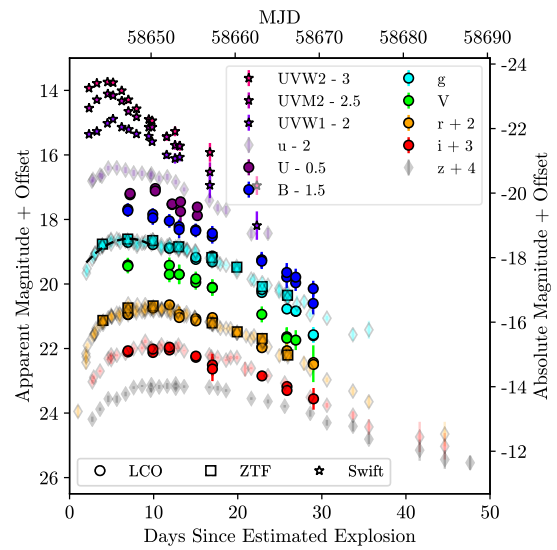
5.2.3 Ultraviolet Photometry

Ultraviolet (UV) and optical photometry was obtained with the Ultraviolet and Optical Telescope (UVOT; Roming et al. 2005) on the Neil Gehrels Swift Observatory (Gehrels et al. 2004). Swift photometry for SN 2019hgp and SN 2021csp has already been published (Fraser et al. 2021; Gal-Yam et al. 2022; Perley et al. 2022). We use those data throughout this paper, calibrated to Vega magnitudes. Data were reduced using the Swift Optical/Ultraviolet Supernova Archive (Brown et al. 2014) pipeline with the most recent calibration files and the zero-points of Breeveld et al. (2011). In both cases images from the final epochs were used to background-subtract the host galaxy light. Although Swift also observed SN 2021ckj, only nonconstraining upper limits on the flux at each epoch were recoverable during the data reduction process. Therefore, we do not include these data in our analysis. UV follow-up was not triggered for SN 2019jc.

5.2.4 Spectroscopy



(a) SN 2019jc



(b) SN 2019hgp

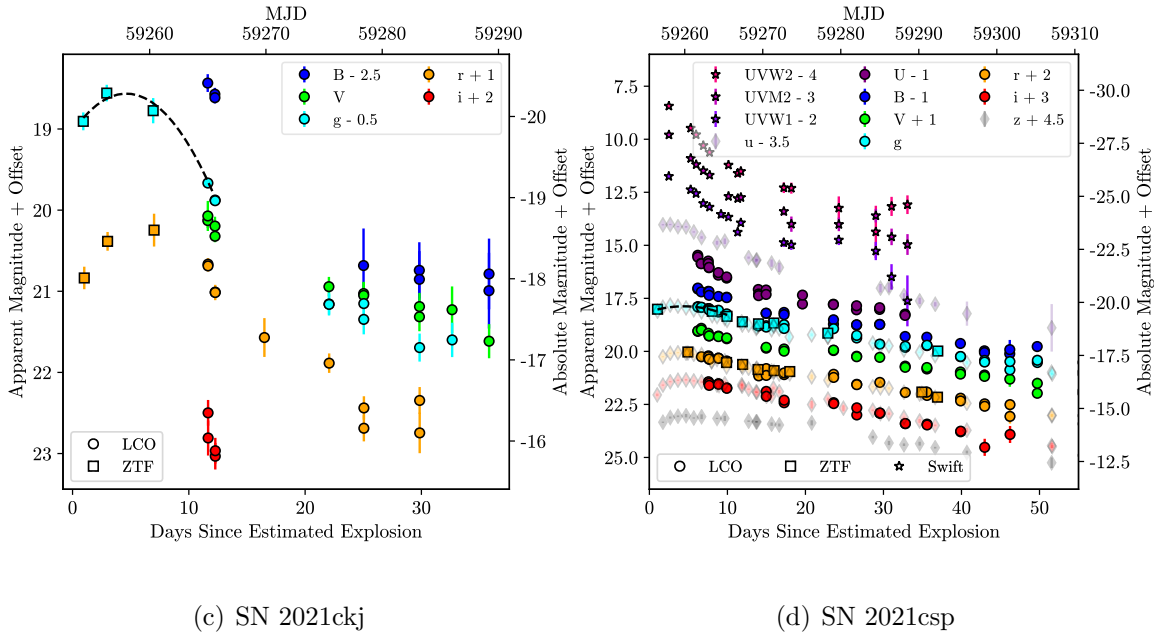


Figure 5.1: Multiband light curves of four SNe Icn. MJD and phases with respect to the estimated explosion dates are given, and photometry is given in apparent and absolute magnitudes. $uvw2-$, $uvm2-$, $uvw1-$, $U-$, $B-$, and $V-$ band photometry is calibrated to Vega magnitudes, while other bands are calibrated to AB magnitudes. LCO photometry is marked by circles, ZTF photometry by squares, ATLAS photometry by pentagons, and Swift photometry by stars. For comparison, $ugriz$ -band photometry from Gal-Yam et al. (2022) and Perley et al. (2022) is shown in lighter shaded diamonds. The photometry of all the objects except SN 2019jc has been template subtracted; as SN 2019jc is at the outskirts of its host galaxy, it should not suffer from significant host contamination. Dashed lines show the quadratic splines used to estimate the rise times and peak magnitudes of SN 2019jc, SN 2019hgp, and SN 2021ckj.

LCO spectra were obtained using the FLOYDS spectrographs on the 2.0m Faulkes Telescope North and Faulkes Telescope South. Spectra cover a wavelength range of 3500–10000 Å at a resolution $R \approx 300$ -600. Data were reduced using the `floydsspec` pipeline³, which performs cosmic-ray removal, spectrum extraction, and wavelength and flux calibration.

A spectrum of SN 2019jc around maximum light was obtained using the blue and red arms of the Low Resolution Imaging Spectrometer on the Keck I 10m telescope (Oke

³https://github.com/svalenti/FLOYDS_pipeline/

et al. 1995) using the 600/4000 grism and 400/8500 grating. Data cover the wavelength range 3200–10000 Å. The spectrum was observed with a 1''5 long slit at the parallactic angle and reduced in a standard way using the LPIPE pipeline (Perley 2019). Additionally, spectra of SN 2021ckj and SN 2021csp were obtained using the Goodman High Throughput Spectrograph on the Southern Astrophysical Research (SOAR) 4.1m telescope. All data were taken with the red camera covering the wavelength range 5000–9000 Å using a 1'' slit and the 400 mm⁻¹ line grating. Reductions were performed via the Goodman Spectroscopic Data Reduction Pipeline⁴, which performs bias and flat corrections, cosmic-ray removal, spectrum extraction, and wavelength calibration. Fluxes were calibrated to a standard star observed on the same nights with the same instrumental setup.

5.3 Photometric Properties

The UV and optical light curves of the four SNe Icn are shown in Figure 5.1. All objects besides SN 2019jc have been template corrected to subtract background galaxy light. SN 2019jc, on the other hand, exploded at the outskirts of its host galaxy and therefore should not suffer from significant host contamination. All data have been corrected for Galactic extinction. We also plot the *ugriz*-band data sets from Gal-Yam et al. (2022) and Perley et al. (2022) for SN 2019hgp and SN 2021csp, respectively, for completeness. Early-time LCO photometric coverage is most extensive for SN 2019jc and SN 2019hgp, with multiple observations occurring before maximum light. All the objects rise to maximum brightness within a week of the estimated explosion date. The rise time of SN 2021csp is the most extreme, reaching its peak luminosity in fewer than 3 days.

This rapid rise to peak brightness is also seen in other interaction-powered SESNe

⁴https://github.com/soar-telescope/goodman_pipeline

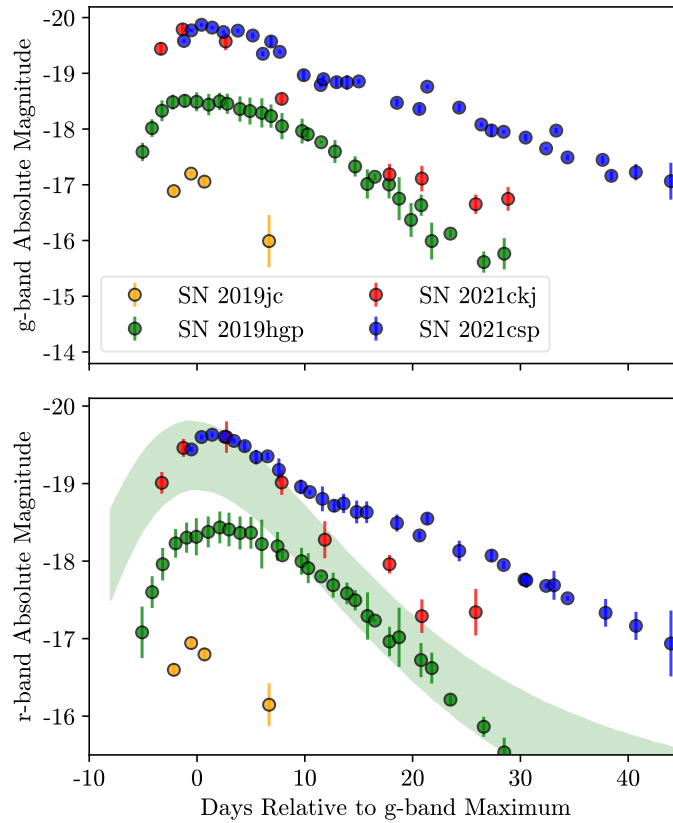


Figure 5.2: Extinction-corrected g -band (top) and r -band (bottom) absolute magnitudes of the four SNe Icn. Time is given relative to g -band maximum light. We also include the R -band SN Ibn light-curve template from Hosseinzadeh et al. (2017) (shaded green region). Solid lines show weighted-average magnitudes at each epoch. The SNe Icn display a range of peak luminosities, rise times, and decline rates.

such as SNe Ibn, which have some of the fastest-evolving light curves of any SN subtype (Ho et al. 2021). Interaction-powered objects also tend to be UV-bright at early times, as shown by the light curves of SN 2019hgp and SN 2021csp for which there was extensive Swift coverage of the light-curve peak. Both the fast rise and luminous UV emission are characteristic of CSI, which can generate a rapid rise in luminosity as the SN shocks sweep up the CSM and ejecta. Early-time multiband observations of these objects are crucial to capturing the rapidly evolving CSI-powered emission.

The g - and r -band absolute magnitude light curves from Perley et al. (2022), Gal-

Yam et al. (2022), and this work are shown in Figure 5.2. Overlaid is the R -band SN Ibn light-curve template from Hosseinzadeh et al. (2017b). There is a wide range ($\gtrsim 3$ mag) in the peak absolute magnitudes, with the g -band brightness of SN 2021csp approaching that of superluminous SNe (see, e.g., Howell 2017 for a review). On the other hand, SN 2019jc is faint relative to both the other SNe Icn and a sample of SNe Ibn (Hosseinzadeh et al. 2017b). The overall light-curve shapes are comparable to the SN Ibn light-curve template. Although the SN Icn absolute magnitudes have a greater spread than the template, Hosseinzadeh et al. (2017b) note that the template is biased by brighter, longer-rising objects and therefore does not replicate well the fainter, faster-evolving objects.

We plot the $g-r$ color evolution of the SNe Icn using the full data sets shown in Figure 5.1 compared with the colors of a sample of SNe Ibc (Taddia et al. 2015) and SNe Ibn (Pellegrino et al. 2022c) in Figure 5.3. The photometry of all the SNe Icn except SN 2019jc has been K -corrected owing to the high redshifts of these objects. For each object we calculate K -corrections using spectra roughly coeval with the photometry (Hogg et al. 2002). In most cases we find that this correction is small ($\lesssim 0.1$ mag). The SN Ibc and SN Ibn colors have not been K -corrected owing to their low average redshift. We find that the colors of the SNe Icn are bluer on average than those of the SNe Ibc at the same phase. This is not surprising, as the spectral energy distribution (SED) of other objects powered by CSI tends to peak at bluer wavelengths (Ho et al. 2021). Roughly 10 days after g -band maximum the SN Icn colors evolve redward, with the exception of SN 2019hgp and SN 2021csp, which maintain a constant blue color throughout their evolution. This constant color evolution is also seen among SNe Ibn and other fast transients from Ho et al. (2021), which may be indicative of a long-lasting CSI powering source (e.g., Ho et al. 2021; Fraser et al. 2021; Pellegrino et al. 2022c; Perley et al. 2022).

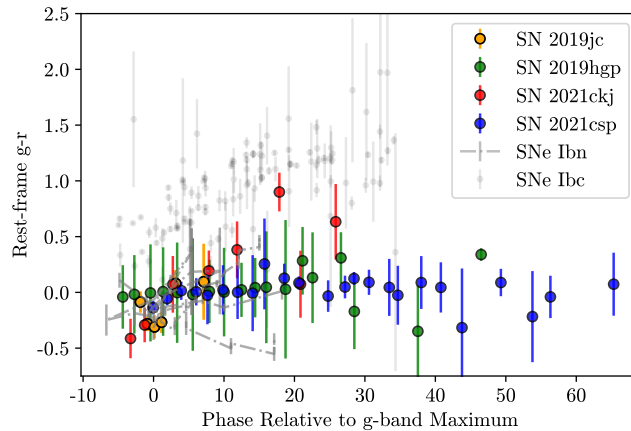


Figure 5.3: $g-r$ colors of the four SNe Icn compared to those of SNe Ibn (Pellegrino et al. 2022c) and a sample of ordinary SNe Ibc (Taddia et al. 2015). The colors of the SNe Icn except for SN 2019jc have been K -corrected owing to their high redshifts.

5.3.1 Blackbody Fits

For our objects with extensive multiband coverage we are able to estimate bolometric luminosities and blackbody properties. As the spectra of these objects appear blue and mostly featureless (besides the narrow emission lines), their SEDs are well fit by a blackbody function. The bolometric luminosities we estimate from our blackbody fits are used to model the mechanisms powering the light curves of these objects in Section 5.5. Because the SEDs of these objects peak in the UV at early times, full multiwavelength observations are crucial for well-estimated bolometric light curves. SN 2019hgp and SN 2021csp have well-sampled UV light curves from Swift (Fraser et al. 2021; Gal-Yam et al. 2022; Perley et al. 2022). For these objects, we use the full, Galactic-extinction-corrected data sets shown in Figure 5.1 to estimate bolometric luminosities. Epochs with photometry obtained in at least three filters are fit with a blackbody SED to the available UV and optical data, with bolometric luminosities calculated by integrating over the full UV, optical, and infrared wavelength ranges.

However, SN 2019jc was only observed in the optical bands. In order to estimate

its full bolometric luminosity evolution from optical-only data, we calculate bolometric corrections using the data of SN 2019hgp and SN 2021csp. For epochs with both Swift and optical coverage, we fit the full multiwavelength data set assuming a blackbody SED and compare this “true” bolometric luminosity (integrated over the full UV, optical, and infrared wavelength ranges) to that calculated from fits to only the optical data set. This gives the following time-dependent bolometric correction, valid up to ≈ 25 days after peak:

$$BC = 1.6 \times 10^{-5}t^3 - 1.3 \times 10^{-3}t^2 + 3.8 \times 10^{-2}t + 0.30 \quad (5.1)$$

where t is the phase relative to g -band maximum light and the bolometric correction BC is the ratio between the luminosities calculated from the optical-only and the full data sets.

These bolometric corrections are applied to all luminosities calculated from photometric epochs of SN 2019jc, SN 2019hgp, and SN 2021csp with data in only optical filters in order to estimate true bolometric luminosities. These results are presented and discussed in Section 5.5. Since multiband data are missing during the rising part of the light curve of SN 2021ckj, we do not attempt to fit a blackbody to its photometry.

The blackbody radius and temperature evolutions of each object we fit are shown in Figure 5.4. Only epochs with Swift data are shown for SN 2019hgp and SN 2021csp. For SN 2019jc, which lacks UV data, the blackbody parameters are inferred from fits to the optical data, leading to larger error bars. In almost all cases the values reported here are broadly consistent with those reported in Gal-Yam et al. (2022) and Perley et al. (2022). Also shown are the radii and temperatures of a sample of SNe Ibn (Pellegrino et al. 2022c) and the fast transient AT 2018cow (Perley et al. 2019; Margutti et al. 2019). We choose these objects for comparison because they also have well-studied multiband light curves, are classified as fast transients, and may represent exotic core-collapse sce-

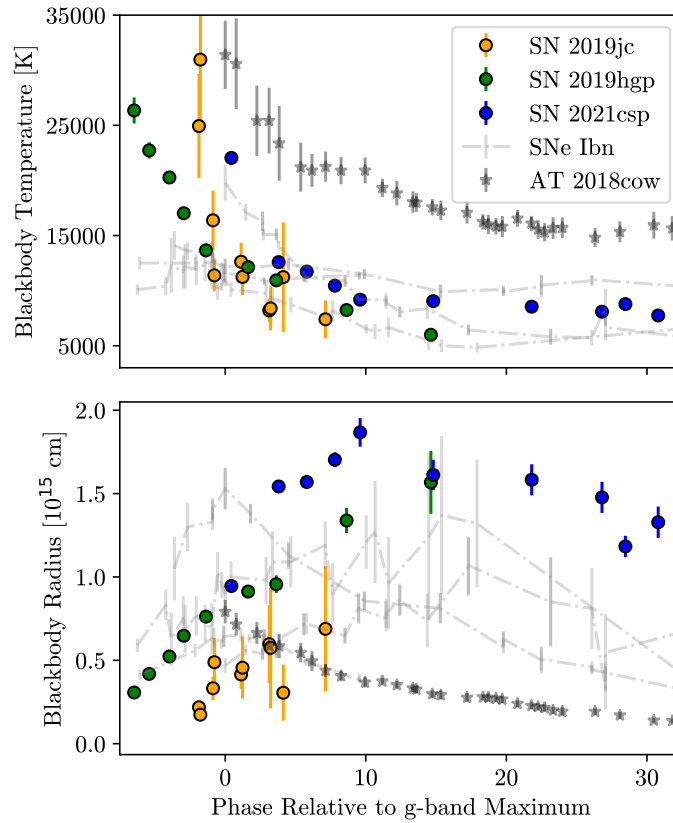


Figure 5.4: A comparison of the estimated blackbody temperatures (top) and radii (bottom) of the SNe Icn, a sample of SNe Ibn (Pellegrino et al. 2022c), and the fast transient AT 2018cow (Perley et al. 2019). The radius and temperature evolutions of the SNe Icn follow those of the SNe Ibn but are different from those of AT 2018cow.

narios of massive stars. The temperature and radius evolutions of the SNe Icn closely match those of the SNe Ibn. We find similar early-time temperatures between the two classes of objects. Both also have expanding blackbody radii until roughly a week after maximum, after which the radii stay constant or recede. AT 2018cow, on the other hand, has a much higher early-time temperature and a blackbody radius that begins to recede earlier than the other objects. This may suggest that the ejecta composition and circumstellar environment of the SNe Icn and SNe Ibn are more similar to each other than to AT 2018cow.

5.4 Spectroscopic Features

Spectroscopic observations of the SNe Icn obtained with the Global Supernova Project range from several days before maximum to over 3 weeks after maximum, allowing us to observe the evolution of these objects over a variety of phases. The spectra of all the objects in our sample, in order of phase, are shown in Figure 5.5. For completeness, we also include the publicly available classification spectrum of SN 2021ckj (Pastorello et al. 2021) obtained 4.4 days after g -band maximum light. Our spectroscopic observations of SN 2019jc all occurred before maximum light. Such early observations are difficult to obtain for this fast-evolving class of objects and allow us to study their spectral features close to the time of explosion in greater detail.

Before maximum (Figure 5.5 (a)), the SN Icn spectra are blue and superimposed with strong, narrow lines of C III and C IV. These spectra are distinct from any other class of SNe. They are qualitatively closest in appearance to the early-time spectra of SNe Ibn, which have narrow emission lines of He that are photoionized by the radiation from the forward shock (Smith 2017), but the narrow lines in the SNe Icn are stronger than those seen in SNe Ibn. Several of the lines, including C IV λ 5812 and C III λ 4650, show narrow absorption components in addition to the strong emission lines. A closer look at some of these narrow features is given in Figure 5.6. The emission peaks have maxima that are slightly blueshifted or redshifted relative to their rest wavelengths. Additionally, the absorption components have minima that are blueshifted by ≈ 500 — 2000 km s $^{-1}$ from their rest-frame values. The blue edge of this absorption relative to rest, marked by ticks in Figure 5.6, varies from ≈ -1500 km s $^{-1}$ in the case of SN 2019jc to ≈ -3000 km s $^{-1}$ for SN 2021csp. These values are consistent with those reported by Gal-Yam et al. (2022) and Perley et al. (2022). These absorption features measure the velocity of the preshocked CSM. If we assume that this velocity corresponds to the wind velocity of

the progenitor star, then high wind velocities $\gtrsim 1000 \text{ km s}^{-1}$ can constrain the possible progenitor channels of these events to luminous blue variables, W-R stars, and stripped low-mass He stars (Crowther 2007; Vink 2017), as previously noted by Fraser et al. (2021); Gal-Yam et al. (2022); Perley et al. (2022).

Several days before maximum light the spectra of SN 2019jc and SN 2019hgp display a forest of narrow P Cygni features blueward of 5000 \AA . Our Keck spectrum of SN 2019jc allows us to study these lines in greater detail. A closer look at this spectrum is shown in Figure 5.5 (d). We follow the process outlined in Gal-Yam (2019) to identify the most notable features. We find that the strongest features can be reproduced by a blend of highly ionized species of elements, including C I, C III, C IV, He II, O II, Ne I, and Ne II. Of particular interest is the He II $\lambda 4686$ feature, which suggests that the CSM surrounding SN 2019jc is not completely devoid of He. Previous studies have noted that the spectra of SN 2019hgp and SN 2021csp closely match the H- and N-depleted spectra of the WC-subtype of W-R stars (Gal-Yam et al. 2022; Perley et al. 2022). We also do not identify any H or N lines in the SN 2019jc spectrum; an emission line close to 4600 \AA could be N V $\lambda 4604$, but we do not detect other N lines. It is more likely that this emission line can be attributed to Ne II $\lambda 4607$. Several other Ne I and Ne II P Cygni features are identified in the spectrum with comparable line widths and velocities. Ne is rarely, if ever, seen in the spectra of core-collapse SNe, yet both SN 2019jc and SN 2019hgp (Gal-Yam et al. 2022) have early-time spectra with considerable Ne features. This Ne likely formed during C burning and therefore was stripped from the inner layers of the progenitor star. The observed Ne abundance in the CSM may help place constraints on potential progenitor channels, as Ne emission is weak in the spectra of WC-type W-R stars (Crowther 2007). A more thorough discussion of a W-R progenitor of these objects is given in Section 5.6.1.

After maximum, the strong C III and C IV emission lines that dominated the spectra

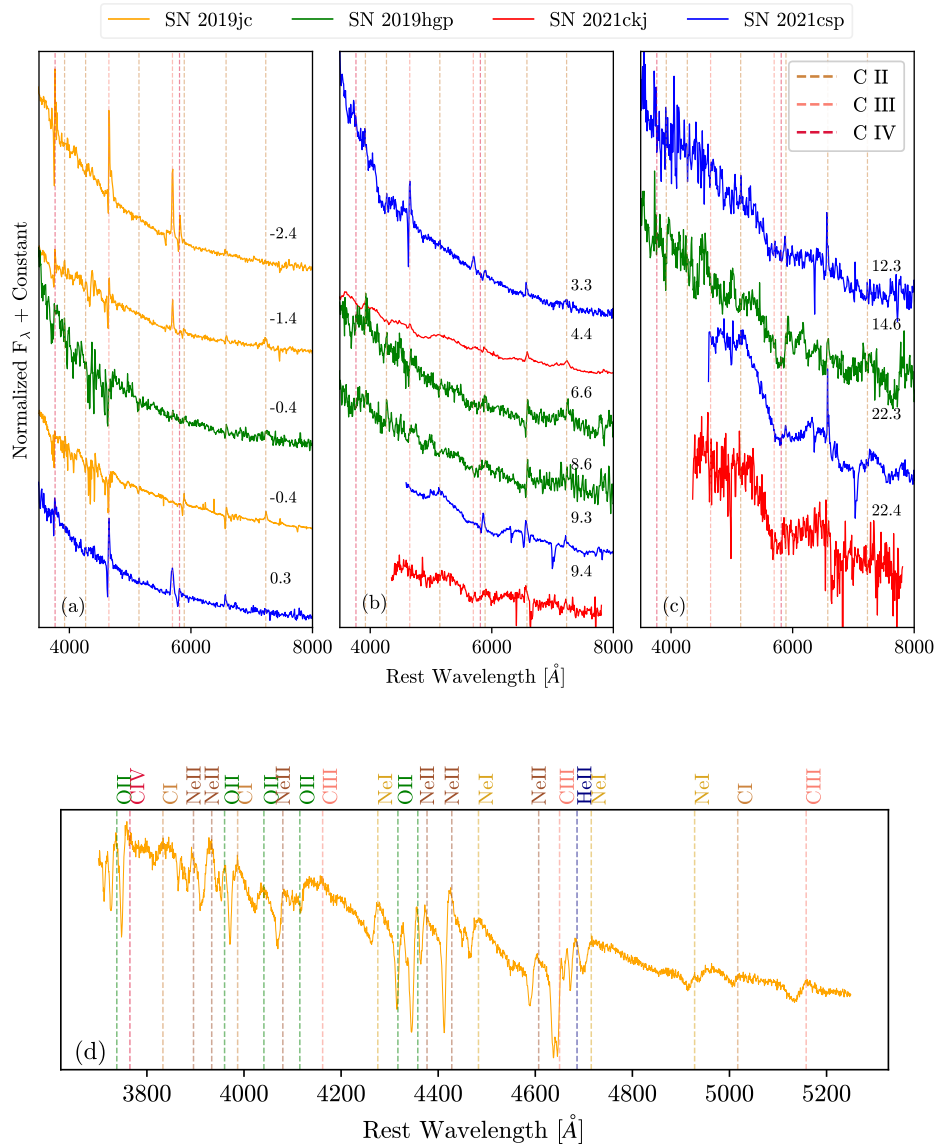


Figure 5.5: The spectral evolution of the four SNe Icn (a) before maximum light, (b) up to ten days after maximum, and (c) roughly 3 weeks after maximum. All wavelengths have been shifted to the rest frame, and fluxes have been normalized and shifted for display. Prominent absorption and emission features of ionized C have been marked by vertical dashed lines. (d) The Keck LRIS spectrum of SN 2019jc at maximum light in the region blueward of 5300 \AA . A number of narrow absorption and emission features have been identified.

fade. They are replaced by weaker emission and P Cygni lines of C II and O III. The spectra all maintain their blue continua until roughly 10 days after peak brightness. At this phase, their characteristics begin to diverge. A break in the continuum develops blueward of 6000 Å in the spectra of the luminous SNe Icn SN 2021ckj and SN 2021csp. This sharp rise in the continua has been attributed to Fe II fluorescence due to ongoing CSI (Perley et al. 2022). By 3 weeks after maximum light the narrow lines have mostly faded and broad features have developed in the spectra of these objects. For example, we note a broad feature consistent with the Ca II near-IR triplet in our latest spectrum of SN 2021csp. The maximum blueshifted velocity of this feature is 10,000 km s⁻¹, consistent with Perley et al. (2022). On the other hand, SN 2019hgp retains its P Cygni features for a longer time. At this phase SN 2019hgp more closely resembles more normal SNe Ic (Gal-Yam et al. 2022).

A possible explanation for the differences in late-time spectral features observed in the SN Icn sample is if SN 2021ckj and SN 2021csp had a strong asymmetric outflow, possibly caused by a jet or an aspherical CSM, in which a fraction of the ejecta expanded at high velocities. An asymmetric, high-velocity outflow could create the broad features seen in the spectra of these objects. Fraser et al. (2021) notice similarities between the late-time spectra of SN 2021csp and those of peculiar SNe Ic-BL such as iPTF16asu (Whitesides et al. 2017; Wang et al. 2021) and SN 2018gep (Ho et al. 2019b; Pritchard et al. 2021; Leung et al. 2021), both of which were fast evolving and had evidence for CSI at early times. However, Perley et al. (2022) find that the late-time spectra of SN 2021csp are more similar to those of SNe Ibn in terms of their shape and color. Additionally, their light-curve fits rule out a normal SN Ic-BL explosion powering SN 2021csp. In either case, it may be that the differences between the late-time SN Icn spectra reflect a difference in explosion mechanisms or in viewing angles. A more thorough discussion of these differences is given in Section 5.6.

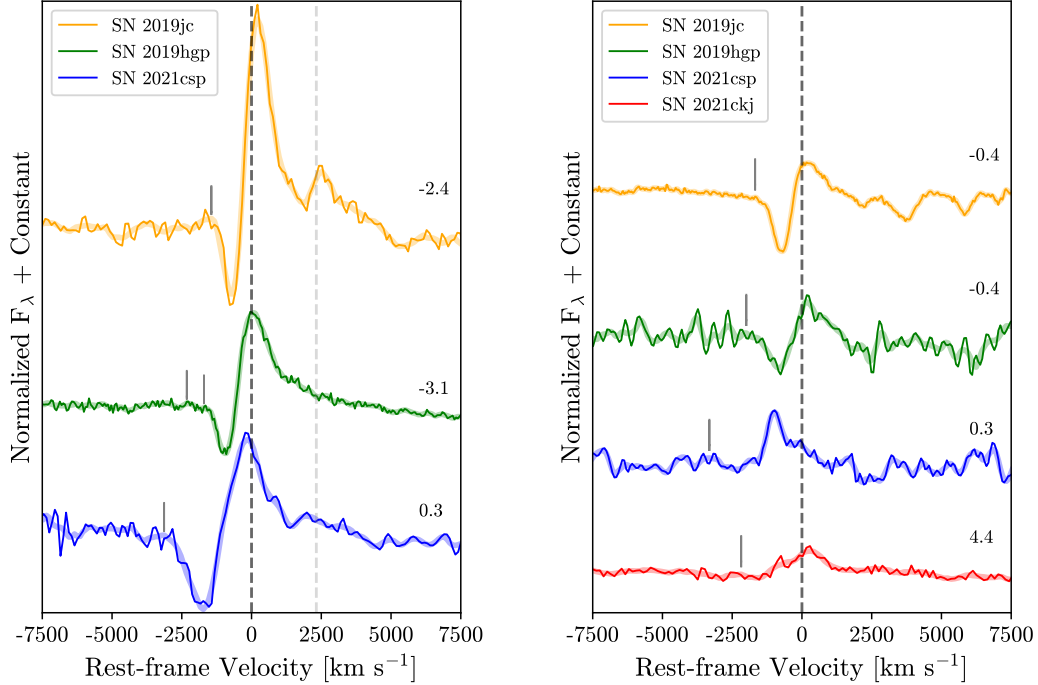


Figure 5.6: Left: the early-time profiles of the C III $\lambda 4650$ line. Spectra smoothed with a Savitzky-Golay filter are shown by the lightly shaded curves. The rest velocity is indicated by the dashed black line, while the nearby He II $\lambda 4686$ line is marked by the dashed gray line. Estimated maximum wind velocities are indicated by the tick marks to the left of each absorption feature. For SN 2019hgp, two potential maxima are identified. Phases relative to g -band peak are given to the right of each spectrum. Right: same as the left panel, but for the C II $\lambda 6580$ line around maximum light. The spectrum of SN 2021ckj and the earlier spectrum of SN 2019hgp were obtained from WiseRep (Yaron & Gal-Yam 2012).

5.5 Progenitor Analysis

5.5.1 Circumstellar Interaction Models

Their rapid evolution, high peak luminosities, blue colors, and narrow spectral features indicate that SNe Icn are primarily powered by CSI at early times. In order to estimate the physical parameters of the SN ejecta and CSM, we attempt to fit the bolometric light curves of our SN Icn sample using a CSI model (Chatzopoulos et al. 2012).

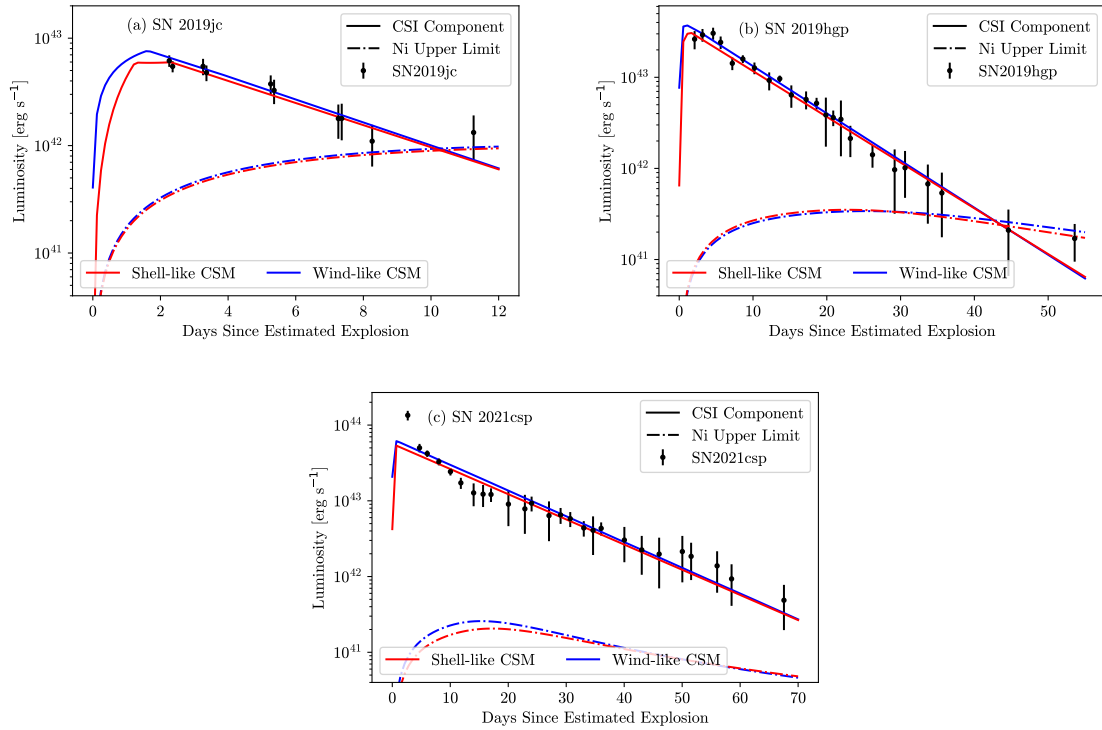


Figure 5.7: Model CSI and ^{56}Ni decay light curves compared to the bolometric light curves of (a) SN 2019jc, (b) SN 2019hgp, and (c) SN 2021csp. The CSI components are shown with a solid line, and the radioactive decay components are shown with a dashed-dotted line. Different fits assuming a shell-like and wind-like CSM are shown in red and blue, respectively. We find few differences between the different CSM structures. The ^{56}Ni decay component is estimated assuming that the latest photometric epoch for each object is powered solely by radioactive decay. Our early-time observations of each object are compatible with only a CSI component, with conservative upper limits on the ^{56}Ni mass from late-time photometry ($M_{\text{Ni}} \leq 0.04 M_{\odot}$).

CSI can reproduce the optical behavior of many different fast-evolving SNe (e.g., [Rest et al. 2018](#); [Pritchard et al. 2021](#); [Xiang et al. 2021](#)) at early phases, while radioactive decay of ^{56}Ni is often needed to match the late-time light-curve evolution. The model, which uses the semianalytical formalism described in [Chevalier \(1982\)](#) and [Chevalier & Fransson \(1994\)](#), has already been used to fit the light curves of interaction-powered SNe ([Jiang et al. 2020](#)), including SNe Ibn and other fast transients ([Pellegrino et al. 2022c](#)). Although this analytical modeling makes several simplifying assumptions, such as spherical symmetry and a centrally located powering source, it is a useful tool for obtaining rough estimates of the explosion and progenitor properties.

CSI drives forward and reverse shocks into the CSM and SN ejecta, respectively, which sweeps up the material and converts kinetic energy into radiation. To calculate the luminosity input from these shocks, the model assumes that the CSM begins directly outside the progenitor radius. The SN ejecta distribution is modeled with a steeper density gradient in the outer ejecta ($\rho \propto r^{-n}$) and a shallower gradient in the inner ejecta ($\rho \propto r^{-\delta}$). We assume as fixed parameters the ejecta density power laws, $n = 10$ and $\delta = 1$, as well as the optical opacity, $\kappa_{\text{opt}} = 0.04 \text{ g cm}^{-2}$, appropriate for mixtures of C and O ([Rabinak & Waxman 2011](#)). We test both a shell-like ($\rho_{\text{CSM}} \propto \text{constant}$) and wind-like ($\rho_{\text{CSM}} \propto r^{-2}$) CSM distribution. We then fit for the remaining ejecta and CSM parameters:

1. M_{ej} , the ejecta mass;
2. v_{ej} , the ejecta velocity;
3. M_{CSM} , the CSM mass;
4. R_0 , the inner CSM radius;
5. ρ_0 , the CSM density at R_0 ; and

6. ϵ , the efficiency in converting kinetic to thermal energy.

Best-fit model light curves compared with measured bolometric luminosities (described in Section 5.3.1) are shown in Figure 5.7. We find that both a CSM shell and wind fit all the objects well. Therefore, we are unable to make conclusions about the structure of the CSM. For all our objects we find that CSI alone reproduces the early-time luminosity evolution, with very little ejecta ($M_{\text{ej}} \lesssim 2 M_{\odot}$) needed to reproduce the light curves. The mass of ^{56}Ni produced in the explosion, M_{Ni} , is not well constrained by our early-time data, particularly for the luminous SN 2021csp. To find a conservative upper limit on the M_{Ni} for each object, we assume that the entirety of the luminosity at the latest photometric epoch is due to radioactive decay and calculate the necessary M_{Ni} using our best-fit ejecta masses and velocities. For SN 2019hgp, we use late-time (50 days after peak) photometry from Gal-Yam et al. (2022) to estimate the bolometric luminosity at this epoch. Because SN 2019jc was only observed up to ≈ 10 days after explosion, when CSI is almost certainly still the dominant powering mechanism, our M_{Ni} upper limit is particularly conservative for this object.

A similar procedure was performed by Perley et al. (2022), who use late-time nondetections of SN 2021csp to put limits on the amount of ^{56}Ni synthesized in the explosion. From their nondetection roughly 80 days after maximum, they estimate $L < 6 \times 10^{40}$ erg s $^{-1}$ at this phase. To estimate M_{Ni} using this late-time luminosity upper limit, we follow the formalism of Hamuy (2003) and account for varying gamma-ray optical depth (Clocchiatti & Wheeler 1997; Sollerman et al. 1998). We use our best-fit M_{ej} and v_{ej} values to estimate an explosion energy and assume a gamma-ray opacity $\kappa_{\gamma} = 0.08$ cm 2 g $^{-1}$ (varying this parameter has a negligible effect on our estimates). From this procedure we find that $M_{\text{Ni}} \leq 0.03 M_{\odot}$ is permitted by the late-time photometry of SN 2021csp (Perley et al. 2022). Following a similar procedure, we find comparable upper limits for

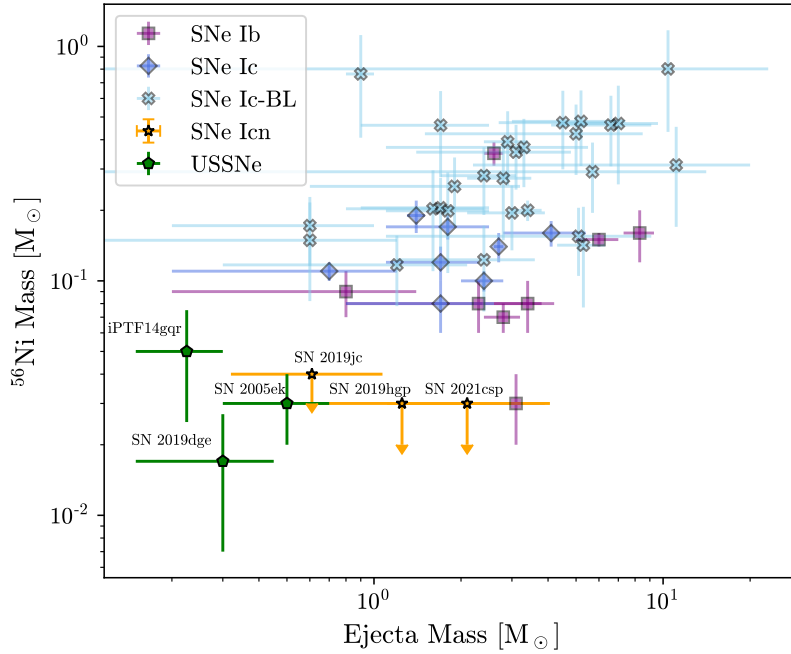


Figure 5.8: The ^{56}Ni mass vs. the ejecta mass of the SNe Icn (orange) fit with a CSI model, assuming a shell-like CSM structure. For comparison we plot ejecta and radioactive mass values from a sample of SESNe (Taddia et al. 2018, 2019 blue and purple) and USSNe from the literature (Drouot et al. 2013; De et al. 2018; Yao et al. 2020 green). The SN Icn ^{56}Ni masses are upper limits derived from late-time photometry; even so, they are at odds with estimates of the SESNe but are in agreement with some USSNe.

SN 2019jc ($M_{\text{Ni}} \leq 0.04 M_{\odot}$) and SN 2019hgp ($M_{\text{Ni}} \leq 0.03 M_{\odot}$) from the last photometric epochs of these objects.

Figure 5.8 compares the ejecta and ^{56}Ni mass parameters for our SN Icn sample to those of SNe Ibc and SNe Ic-BL in literature (Taddia et al. 2018, 2019). We find that the ejecta and ^{56}Ni masses of the SNe Icn differ by a factor of several from those of the SESNe. Most striking is the differences in estimated ^{56}Ni masses between the SNe Icn and the SNe Ic-BL, which are off by an order of magnitude in many cases. These discrepancies suggest that normal SN Ibc or SN Ic-BL explosions within a dense CSM cannot be the underlying explosion mechanisms powering SNe Icn, as also noted by Perley et al. (2022).

Additionally, the best-fit ejecta mass estimates are in conflict with the pre-SN masses

of observed WC-type W-R stars, which are $\gtrsim 10 M_{\odot}$ (e.g., [Crowther et al. 2002](#); [Sander et al. 2019](#)). This assumes that the entirety of the star’s mass is ejected during the explosion; if, instead, a significant portion of the star’s mass directly collapses to a black hole or falls back onto the newly formed compact object, this could alleviate some of the discrepancy ([Moriya et al. 2010](#)). Another possible explanation for the discrepancy could be if a significant fraction of the ejecta is “dark” and does not interact with the CSM, in which case the ejecta mass estimates from our light-curve fitting would be an underestimate of the true mass ([Gal-Yam et al. 2022](#)). On the other hand, the combination of best-fit ejecta and ^{56}Ni masses is more consistent with USSNe such as iPTF14gqr ([De et al. 2018](#)), SN 2005ek ([Drout et al. 2013](#)), and SN 2019dge ([Yao et al. 2020](#)). These objects are plotted with green symbols in Figure 5.8. In particular, the ejecta and ^{56}Ni masses of SN 2019jc fall in the same region of parameter space as the USSN candidates.

In Figure 5.9 we plot the g -band absolute magnitude versus time above half the maximum luminosity of our SN Icn sample compared with the fast transient samples from [Drout et al. \(2014\)](#) and [Ho et al. \(2021\)](#). [Ho et al. \(2021\)](#) found that the luminous fast transients are primarily SNe powered by CSI. Three of the SNe Icn (SN 2019hgp, SN 2021ckj, and SN 2021csp) also fall within the same region of parameter space as SNe Ibn. SN 2019jc, on the other hand, is unique in that it is the least luminous and fastest-evolving SN Icn, occupying the same region of parameter space as SNe IIb with light curves that are dominated by rapidly evolving shock-cooling emission. Despite its location in this phase space, we instead favor circumstellar interaction as the primary mechanism powering the light curve of SN 2019jc owing to its early-time spectral features. We also note that the USSN SN 2019dge has a similar light-curve timescale and peak luminosity to SN 2019jc. We explore other similarities between SNe Icn and USSNe in Section 5.6.1.

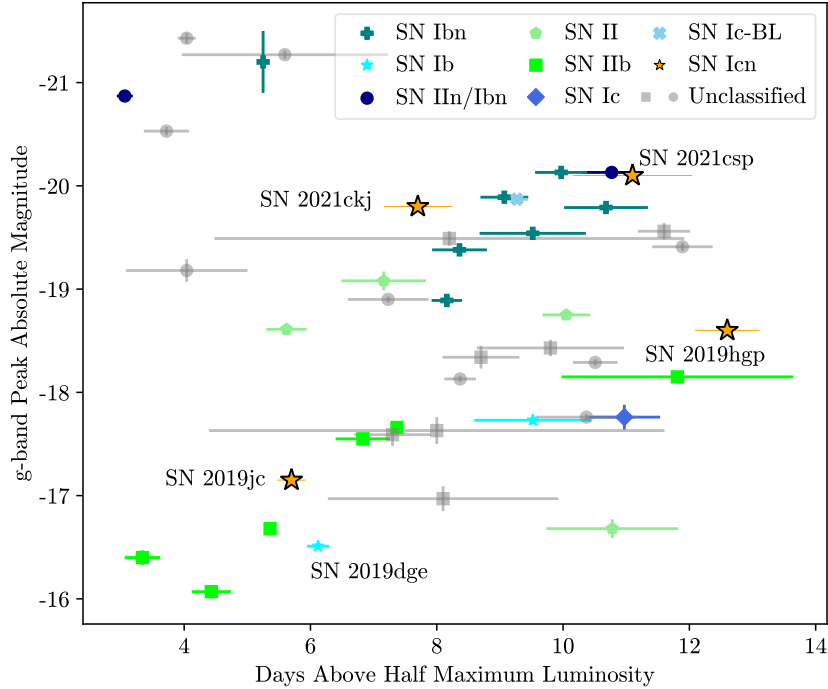


Figure 5.9: The g -band peak absolute magnitude vs. time above half the peak luminosity of the SNe Icn compared with the fast transient gold samples from [Drout et al. \(2014\)](#) (gray squares) and [Ho et al. \(2021\)](#) (other symbols). The SNe Icn, as well as the ultra-stripped Type Ib SN 2019dge ([Yao et al. 2020](#)), are labeled. SN 2019hgp, SN 2021ckj, and SN 2021csp occupy similar regions of parameter space as rapidly evolving SNe Ibn, but SN 2019jc is remarkably fainter and faster evolving.

5.5.2 Host Galaxy Analysis

The host galaxies of SN 2019hgp and SN 2021csp have previously been studied ([Gal-Yam et al. 2022](#); [Perley et al. 2022](#)). Their hosts were found to be similar in star formation rate (SFR) and stellar mass to hosts of normal SNe Ibn and SNe Ibc (see, e.g., Figure 18 of [Perley et al. 2022](#)). This implies a similar progenitor environment between these classes of objects, as SESNe are more frequently associated with regions of higher star formation that produce high-mass stars ([Anderson et al. 2012](#)).

The SNe Icn studied in the literature have been at higher redshifts, which makes

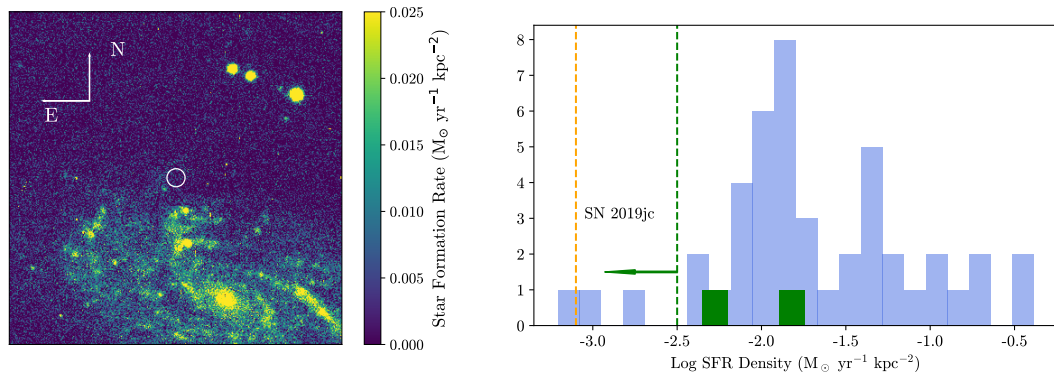


Figure 5.10: Left: u' -band stacked CFHT image of the host galaxy of SN 2019jc. The SN location is marked by a 1.5 kpc diameter aperture. Right: a histogram comparing the estimated SFR density at the location of SN 2019jc (orange) with SFR densities at the locations of SESNe from Galbany et al. (2018, blue) and USSNe (green). The value we measure at the location of iPTF14gqr is an upper limit, marked by a dashed green line and left-pointing arrow. SN 2019jc lies at the very lower edge of the SESN distribution.

studying their host properties at the explosion site difficult. Instead, only the global properties of their host galaxies have been estimated. These objects exploded at low projected offsets from their star-forming host centers (Gal-Yam et al. 2022; Perley et al. 2022). SN 2019jc, on the other hand, exploded on the outskirts of the nearby ($z = 0.0195$), face-on spiral galaxy UGC 11849, at a projected distance of 11.2 kpc from the galaxy center. Several high-quality, deep pre-explosion images exist of this field, affording us the opportunity to study the location of this SN Icn in greater detail.

We use archival u' -band images from the MegaCam imager on the Canada-France-Hawaii Telescope (CFHT) to estimate the SFR density at the SN location. With a typical seeing FWHM of $0''.7$ and an angular pixel scale of $0''.185 \text{ px}^{-1}$, these images allow us to probe the local environment of the SN progenitor. Following the procedure of Hosseinzadeh et al. (2019), we use MegaCam u' -band images of the host galaxy to estimate the SFR density at the SN location. First, we stack the preprocessed images, obtained from the Canadian Astronomy Data Centre, after correcting their astrometry.

To subtract the background flux, we mask the center of the host galaxy and use SEP (Barbary 2016) to model the background using a $64 \text{ pixel} \times 64 \text{ pixel}$ box and $3 \text{ pixel} \times 3 \text{ pixel}$ filter. We use this stacked, background-subtracted image to find the flux within a 1.5 kpc diameter aperture centered on the SN location. This yields a 3σ detection of $23.76 \pm 0.31 \text{ mag}$. After correcting for Galactic reddening, this magnitude gives an SFR density $\Sigma_{\text{SFR}} = -7.9 (\pm 2.5) \times 10^{-4}$ (Kennicutt 1998).

In Figure 5.10 we compare this SFR density limit to values in the literature for a sample of SESNe (Galbany et al. 2018). In order to ensure that the host galaxy of SN 2019jc is representative of those in the Galbany et al. (2018) sample, we compare the stellar mass of the host of SN 2019jc with the sample mean and find that they are in good agreement ($\log(M_{\text{host},19\text{jc}}) = 10.32 \pm 0.20 M_{\odot}$, Durbala et al. (2020); $\log(\langle M_{\text{host,sample}} \rangle) = 10.37 M_{\odot}$). We also estimate the SFR densities at the locations of USSNe (Drout et al. 2013; De et al. 2018; Yao et al. 2020) using archival SDSS u' -band images in the same way as for SN 2019jc. In all these cases the values we estimate roughly agree with those in the literature. SN 2019jc lies at the very lowest end of the SESN distribution. However, the SFR density at the SN location is more consistent with values we measure for the USSNe. These low SFR densities have been used to argue against progenitors with high zero-age main-sequence masses for USSNe.

Interestingly, a similar analysis by Hosseinzadeh et al. (2019) placed strict constraints on the nature of the progenitor of the Type Ibn PS1-12sk. PS1-12sk exploded at a projected separation of 28 kpc from its apparent host (Sanders et al. 2013), in a region devoid of star formation. No excess UV flux was detected at the explosion site in Hubble Space Telescope images, leading to a strong upper limit on the SFR density at the explosion site that is at odds with a massive star progenitor. Although a Kolmogorov-Smirnov test finds no statistically significant difference between the cumulative distribution functions of the SFR densities of SNe Ibn from Hosseinzadeh et al. (2019), including SN 2019jc, and

SNe Ibc (from [Galbany et al. 2018](#) $p=0.24$), it is intriguing that two out of only tens of discovered interacting SESNe exploded in regions of low star formation, compared with $\lesssim 1\%$ of all core-collapse SNe ([Schulze et al. 2021](#); [Irani et al. 2022](#)). This tension is heightened if one assumes that the progenitors of all SNe Icn are W-R stars, in which case the zero-age main-sequence masses of these objects would be more massive than the average progenitor mass of a core-collapse SN. Instead, SN 2019jc may be the result of a different progenitor channel than other SNe Icn.

Studying the field distribution of O- and B-type stars in the local universe reveals that in situ formation is rare for these populations (e.g., [Dorigo Jones et al. 2020](#); [Vargas-Salazar et al. 2020](#)). Instead, these stars are hypothesized to travel from their places of birth to their explosion sites owing to either SN kicks from a binary companion or dynamical interactions within a stellar cluster. We consider whether these scenarios are consistent with a high-mass star at the location of SN 2019jc. We estimate that the nearest region of high SFR density lies approximately 2.7 kpc from SN 2019jc (Figure 5.10). Conservatively estimating the time from formation to core collapse as ≈ 10 Myr, a massive star progenitor would need a runaway velocity of $\approx 250 \text{ km s}^{-1}$ to reach the SN location in its lifetime. It is unlikely that a W-R star could be ejected from its binary system with this velocity by a companion SN, as typical kick velocities from companion SNe are an order of magnitude below this estimated velocity ([Renzo et al. 2019](#)), and most massive stars only travel tens or hundreds of parsecs before core collapse ([Cantiello et al. 2007](#); [Eldridge et al. 2011](#); [Renzo et al. 2019](#)). On the other hand, it is possible to achieve this runaway velocity through dynamical interaction in stellar clusters ([Perets & Šubr 2012](#); [Andersson et al. 2021](#)), although it still lies on the higher end of the simulated runaway velocity distribution ([Oh & Kroupa 2016](#)).

If, instead, the progenitor of SN 2019jc were less massive than a W-R star and in a close binary, the lifetime of the primary star could be longer, which would either lower

the high runaway velocity needed to reach the SN location to a more reasonable value or reduce the tension in allowing the progenitor to be formed in situ. In such a case the large amounts of CSM around the SN progenitor would be formed owing to binary stripping rather than stellar winds occurring toward the end of a massive star’s lifetime, which have mass-loss rates that are orders of magnitude lower than those estimated for SNe Ibn and SNe Icn (Chevalier & Fransson 2006; Crowther 2007; Gal-Yam et al. 2022; Maeda & Moriya 2022), but are more similar to those observed for SN Ibc progenitors (Wellons et al. 2012). The M_{ej} and M_{Ni} values inferred from our bolometric modeling permit a progenitor with a lower mass than a W-R star while also ruling out traditional thermonuclear explosions of white dwarfs.

In the future, deeper images in the UV may be used to more accurately measure the SFR density at the location of SN 2019jc. Despite capturing more of the UV flux, Swift UVOT images have a shallower depth than the CFHT images and would therefore not significantly improve our results. Hubble Space Telescope WFC3 UVIS images, on the other hand, would be beneficial owing to their smaller angular pixel scale and deeper limiting magnitudes. Even so, our reported SFR density value, along with the low ejecta and ^{56}Ni mass estimates inferred from SN Icn light-curve modeling, leads us to question the assumption of a W-R progenitor of SN 2019jc.

5.6 Discussion

Observations of their photometric and spectral evolution reveal that SNe Icn are interesting objects at the cross section of SESNe, SNe Ibn, and fast transients. Their rapid light-curve evolution, diverse peak luminosities, and narrow spectral lines at early times resemble the interaction-powered early phases of SNe Ibn and other fast transients, but their spectra 2 weeks after maximum can also resemble other SESNe. Additionally, the

ejecta and ^{56}Ni masses inferred from modeling their light curves are often an order of magnitude smaller than those of typical SESNe. In this section we search for progenitor systems and explosion mechanisms that can explain the combination of these characteristics.

5.6.1 Possible Progenitor Channels

A W-R Star Progenitor?

The defining characteristic of SNe Icn is their interaction with H- and He-poor CSM. This is most similar to SNe Ibn, which have early-time light curves and spectra that are dominated by interaction with H-poor CSM. Based on these CSM environments, we explore whether SNe Ibn and SNe Icn could share a progenitor channel. Although our sample is small, most of the SNe Icn we study have $g-r$ colors (Figure 5.3), blackbody properties (Figure 5.4), and rise times and peak luminosities (Figure 5.9) that are consistent with those of SNe Ibn. SNe Ibn are also a rare class of SNe; although not as rare as SNe Icn, only tens of SNe Ibn have been discovered to date (Hosseinzadeh et al. 2017b).

W-R stars are commonly thought to be the progenitors of SNe Ibn (Foley et al. 2007; Pastorello et al. 2007; Hosseinzadeh et al. 2017b). Several observational pieces of evidence support this. Perhaps the strongest such piece of evidence is the Type Ibn SN 2006jc, the archetype of its class, for which a pre-explosion outburst was noted roughly 2 years before the terminal explosion (Pastorello et al. 2007). Only late-stage massive stars have been observed to undergo such explosive outbursts during LBV stages (Smith & Owocki 2006), before transitioning into W-R stars. This, along with the CSM composition and velocity inferred from the narrow features in the spectra of SN 2006jc (Foley et al. 2007), supports the notion that these progenitors are massive stars. Additionally, SNe Ibn

are almost exclusively found in star-forming galaxies (Pastorello et al. 2015 but see also Sanders et al. 2013) and at locations with high SFR densities (Hosseinzadeh et al. 2019), implying a younger stellar population.

Both SNe Ibn and SNe Icn have spectral features consistent with a W-R stellar wind (Gal-Yam et al. 2022), specifically with highly ionized species of He, N, C, and O. Gal-Yam et al. (2022) propose that the differences between SNe Ibn and SNe Icn spectral features—mainly the lack of He and N in SNe Icn—mirror the differences in WN and WC subtypes of W-R stars. The lack of H, He, and N and the presence of Ne, in the CSM around SN 2019hgp match the chemical composition of WC stars (Gal-Yam et al. 2022) and the yields expected from the triple-alpha process (Perley et al. 2022), indicating that the composition of the material stripped from the progenitor must be similar to that of a W-R star.

W-R stars have also been theoretically predicted to be the progenitors of at least some normal SESNe as well (Sukhbold et al. 2016). Some early-time observations of SESNe support this (e.g., Cao et al. 2013; Gal-Yam et al. 2014b), but other studies have found that SESNe are unlikely to originate exclusively from W-R stars (Eldridge et al. 2013; Smith 2014; Taddia et al. 2018). Gal-Yam et al. (2022) notice similarities between the late-time spectra of SN 2019hgp and the Type Ic SN 2007gr, possibly showing that the explosion of SN 2019hgp is similar to that of SN 2007gr but is concealed by a dense CSM. However, Mazzali et al. (2010) find $M_{\text{Ni}} = 0.076 M_{\odot}$ for SN 2007gr, which is incompatible with the upper limits on the ^{56}Ni mass derived by Gal-Yam et al. (2022) and this study. We also find that the explosion energies and ejecta and ^{56}Ni masses of the SNe Icn in our sample are broadly inconsistent with estimates for SESNe from the literature. Therefore, it seems unlikely that the explosion mechanism of normal SESNe—possibly the successful core-collapse of a W-R star—can reproduce both SESN and SN Icn observables, as previously noted by Perley et al. (2022).

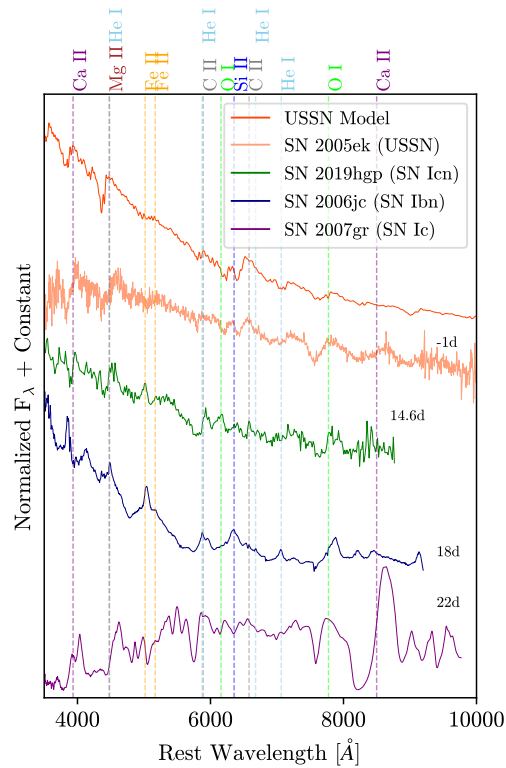


Figure 5.11: A spectrum of SN 2019hgp compared with the USSN model spectrum at maximum light from [Moriya et al. \(2017\)](#), the USSN SN 2005ek ([Drouot et al. 2013](#)), the prototypical Type Ibn SN 2006jc, and the normal Type Ic SN 2007gr. Spectra of SN 2006jc, SN 2005ek, and SN 2007gr were obtained from WiseRep ([Yaron & Gal-Yam 2012](#)). Phases are denoted to the right of each spectrum. Possible spectral features are marked with dashed lines. SN 2019hgp shares several features with the USSNe at these phases.

A New Type of Ultra-stripped-envelope Supernovae?

Based on the similar spectral features between SNe Ibn and SNe Icn, [Gal-Yam et al. \(2022\)](#) and [Perley et al. \(2022\)](#) suggest that the distinction between SNe Ibn and SNe Icn follows the differences in WN and WC subtypes of W-R stars. However, several problems exist with assuming W-R stars as the progenitors to all SNe Ibn. Estimates of the rates of W-R explosions ([Smith 2014](#); [Perley et al. 2022](#)) are often orders of magnitude higher than the rates of SNe Ibn ([Maeda & Moriya 2022](#)). Furthermore, observations of Galactic

W-R stars have not found evidence for high mass-loss rates necessary to produce the large amounts of CSM estimated from SN Ibn light-curve modeling (Crowther 2007). These discrepancies may be resolved if not one but several progenitor systems lead to H-poor interaction-powered SNe. There is evidence that a W-R or other high-mass progenitor is in tension with observations of the Type Ibn PS1-12sk. Hosseinzadeh et al. (2019) showed that PS1-12sk was unusual in that the SN exploded in a region devoid of star formation. Deep Hubble Space Telescope upper limits placed strong constraints on the SFR density at the SN location, all but ruling out a massive star progenitor of this SN.

Similarly, we find that the location of SN 2019jc has relatively little ongoing star formation. Estimating the SFR density at the SN location places SN 2019jc at the lower edge of the SESN host environment distribution, at odds with a W-R progenitor of this object. Interestingly, SN 2019jc has a relatively similar host galaxy offset and SFR density to several USSNe, including iPTF14gqr (De et al. 2018) and SN 2005ek (Drout et al. 2013). De et al. (2018) and Drout et al. (2013) both favor a binary system consisting of a low-mass evolved star and a compact degenerate object, such as a neutron star, for these SNe largely because of the SFRs of their local environments. Assuming a lower-mass star in a close binary system for SN 2019jc would alleviate the problem of finding unlikely methods for a W-R star to travel far from regions of higher star formation.

In addition, the ejecta and ^{56}Ni masses inferred from our SN Icn light-curve modeling are strongly at odds with those of typical SESNe. Our upper limit on the ^{56}Ni mass for SN 2021csp agrees with the value from Perley et al. (2022), which places strong limits on the type of explosion that could power these objects. The discrepancy in ejecta parameters is most extreme between the SNe Icn and samples of SNe Ic-BL. SNe Ic-BL have been suggested to be related to SNe Icn (Fraser et al. 2021), yet Figure 5.8 shows that the SN Icn ejecta and ^{56}Ni masses differ from those of SNe Ic-BL by up to an order of magnitude. However, they are similar to those of USSNe in the literature (Drout et al.

2013; De et al. 2018; Yao et al. 2020). The combination of low ($\lesssim 1 M_{\odot}$) ejecta mass and ^{56}Ni mass is found in observations and theoretical models (Tauris et al. 2013; Moriya et al. 2017) of these objects.

We compare spectra of SNe Icn, models and observations of USSNe, and prototypical SESNe in Figure 5.11. SN Icn spectra are dominated by signatures of CSI at early times, masking the underlying ejecta features. Unfortunately, spectra of SN 2019jc were only obtained during this time. However, our spectrum of SN 2019jc at maximum appears most similar to SN 2019hgp (Figure 5.5), for which there is ample spectroscopic coverage at later phases. Therefore, we include a spectrum of SN 2019hgp 15 days after maximum instead of SN 2019jc, assuming that they have similar late-time evolution despite differences in peak brightness and decline rates.

The spectrum of SN 2019hgp appears to match that of SN 2006jc at first glance, but on closer inspection we find that the dominant He I $\lambda\lambda 4472$ and 5876 features in the latter are instead replaced by Mg II $\lambda 4481$ and C II $\lambda 5890$ lines in the former. We notice more qualitative similarities between SN 2019hgp and the USSNe than any of the other objects, particularly blueward of 5000 \AA where we identify Mg II and Ca II absorption features not seen in the other objects, as well as similar O I absorption features around 7775 \AA . SN 2005ek quickly transitioned to its optically thin phase roughly 10 days after maximum. However, this transition does not occur until weeks later in the case of the SNe Icn. It is possible that the sustained CSI we see in the SNe Icn maintains a higher opacity until later times, leading to better agreement between the late-time spectrum of SN 2019hgp and the USSN spectra at maximum light. The spectrum of the normal Type Ic SN 2007gr has a different continuum shape and absorption features than SN 2019hgp at a similar phase, again providing evidence that SNe Icn are not normal SESN explosions.

We find some discrepancies between theoretical models of USSNe (Moriya et al. 2017) and SN 2019jc, especially in terms of peak luminosity and early-time spectral features.

However, these differences can easily be explained by the addition of CSI, which masks the spectral signatures of the underlying ejecta at early times and provides an additional power source that can increase the peak luminosity by several orders of magnitude. For several of the USSNe (De et al. 2018; Yao et al. 2020) shock cooling was instead modeled as an additional mechanism powering the early-time light curves. We suggest that SN 2019jc could be an USSN that has completely lost its outer layers owing to extreme binary stripping, whereas others studied in the literature have still retained an extended envelope. This could explain how both shock breakout and CSI are observed in objects of this class.

5.6.2 Possible Explosion Mechanisms

If SNe Icn have a diverse set of progenitor systems, then their explosion mechanisms may vary as well. Differing explosion mechanisms between these objects can explain some of the observed diversity in light-curve and spectral properties. Any proposed explosion scenario must reproduce the ejecta velocities, ejecta masses, and ^{56}Ni masses estimated from light-curve fits. A normal SESN explosion interacting with CSM is ruled out by our ^{56}Ni upper limits; therefore, we search for more exotic scenarios.

SN 2019jc is unique in having a light curve that is both faster evolving and fainter than those of the other SNe Icn (Figure 5.9). Our light-curve modeling shows that SN 2019jc has a low explosion energy ($\approx 4 \times 10^{50}$ erg) and ejecta mass ($\approx 0.7 M_{\odot}$), both of which are lower than those of more normal SESNe but are consistent with theoretical models and observations of USSNe. The core collapse of an ultra-stripped, lower-mass progenitor to SN 2019jc is also consistent with its location far from regions of active star formation.

Interestingly, the explosion energy, ejecta and ^{56}Ni masses, rapid light-curve evolution, and explosion site properties of SN 2019jc are also consistent with theoretical models

of stripped-envelope electron-capture (EC) SNe (Moriya & Eldridge 2016). Stars with initial masses $\approx 8 M_{\odot}$ are predicted to explode when their O-Ne-Mg degenerate cores undergo EC, triggering core collapse (e.g., Miyaji et al. 1980; Nomoto 1984, 1987). Normally in single star evolutionary models the EC SN progenitor retains its H envelope and is observed as a Type II SN. However, if the progenitor is stripped of its outer layers through binary interaction (Moriya & Eldridge 2016) or enhanced mass loss due to episodic burning (Woosley & Heger 2015), a H-poor EC SN would be observed. Some theoretical models of ultra-stripped He stars also explode as EC SNe (Tauris et al. 2015). While an EC explosion mechanism has been proposed for the Type II SN 2018zd (Hiramatsu et al. 2021b), to date the possibility of an EC origin of interaction-powered SESNe has not been explored.

On the other hand, modeling the light curve of SN 2021csp gives ejecta masses and explosion energies that are higher than those predicted for and observed in USSNe. This object may have an explosion mechanism that is different from that of SN 2019jc. SN 2021csp could be similar to other SNe Ibc that interact with dense CSM (Whitesides et al. 2017; Ho et al. 2019b; Pritchard et al. 2021), as noted by Fraser et al. (2021). The ejecta masses inferred from modeling this CSI could be underestimated if only a fraction of the ejecta interacts with the CSM. However, stringent limits on the amount of ^{56}Ni produced in the explosion of SN 2021csp are strongly at odds with the amounts estimated for normal SNe Ibc and SNe Ic-BL (Figure 5.8), which can be up to an order of magnitude larger (Perley et al. 2022). Therefore, the explosion of SN 2021csp must eject more mass at higher velocities than USSNe but produce less ^{56}Ni than normal SESNe.

Perley et al. (2022) proposed that a jet launched during the partial or failed explosion of a massive star could meet these criteria (Woosley 1993; Moriya et al. 2010). The high ejecta velocities observed for SN 2021csp could be due to a small amount of material being launched by a jet. Jets have been suggested as the powering mechanism behind

long GRBs (Khokhlov et al. 1999; MacFadyen & Woosley 1999; MacFadyen et al. 2001), some of which are associated with SNe Ic-BL (e.g., Reichart 1999; Stanek et al. 2003). Indeed, Fraser et al. (2021) notice spectral similarities between SN 2021csp and SNe Ic-BL at later phases, when signatures of the CSI have faded. However, the ejecta parameters (in particular, the ^{56}Ni masses) we infer from our light-curve fits rule out normal SN Ic-BL explosions, and Perley et al. (2022) note that the late-time SN Icn spectral features are more similar to those of SNe Ibn.

To explain both the low amount of ^{56}Ni produced during the explosion and the presence of a jet, a substantial amount of the inner ejecta must have remained gravitationally bound and collapsed after the explosion. These so-called fallback SNe are predicted to occur when the core collapse of a stripped massive star is not energetic enough to unbind the entire star. As a result, only the outermost material is ejected and the rest falls back onto the central remnant. The amount of ^{56}Ni that remains unbound after the fallback is variable and subject to the explosion parameters, such as the amount of mixing during the explosion, but is orders of magnitude smaller than in normal SESNe. Although fallback SNe have been used to explain the faintest SNe (e.g., Valenti et al. 2009; Moriya et al. 2010), some models reproduce the range of explosion energies and ejecta masses we estimate for SN 2021csp and the other SNe Icn (see Table 1 of Moriya et al. 2010). These models originate from massive (25–40 M_{\odot}) main-sequence stars, which are at odds with the progenitor masses inferred from our host galaxy analysis of SN 2019jc but are potentially allowed for the locations of the other objects in our sample. The presence of a jet launched during a fallback SN has been used to explain long GRBs not associated with visible SNe (Della Valle et al. 2006; Gal-Yam et al. 2006; Fynbo et al. 2006). If a jet was launched during the explosion of SN 2021csp, it could explain the large ejecta velocities measured and possibly mix some of the ^{56}Ni out into the ejecta that becomes unbound.

Recently, Metzger (2022) proposed an alternate scenario in which the rapid evolution, multiband emission, and spectral features of SNe Ibn, SNe Icn, and AT 2018cow-like fast transients can all be reproduced by the merger of a W-R star and a compact object. The differences in observed spectral features and luminosities between these classes are primarily due to the timescales on which the W-R star and its compact companion merge. This scenario has the benefit of explaining the similar ejecta velocities, peak luminosities, and rise times of AT 2018cow and SN 2021csp (Fraser et al. 2021). Although any explosion mechanism involving a high-mass star appears unlikely for SN 2019jc, we cannot rule out this scenario for the other objects in our sample. More detailed comparisons between observations of SNe Icn and other rapidly evolving objects are needed to test this model.

Therefore, it is possible that different underlying explosions and progenitors are responsible for the diversity in SN Icn light-curve properties, late-time spectral features, and host environments we observe. A higher-mass progenitor star is compatible with the location of SN 2021csp, but a normal SESN explosion within a dense CSM is ruled out based on the M_{ej} and M_{Ni} values inferred from its light curve. Instead, a more exotic explosion mechanism, such as a partially successful or fallback explosion, is needed to explain its high ejecta velocities, low ^{56}Ni mass, and bright light curve. On the other hand, models of USSNe, which necessarily involve lower explosion energies and ejecta masses, match the photometric properties, spectral features, and explosion site of SN 2019jc. In both cases, the observable photometric and spectroscopic signatures of these different explosions are masked by the dominant CSI at early times, making all SNe Icn appear similar at first glance.

5.7 Conclusions

We have analyzed the photometric and spectral properties of the largest sample of SNe Icn to date. Photometrically the SNe Icn all display rapid evolution, blue colors, and heterogeneous peak magnitudes. Their spectra, which are all dominated by narrow emission lines of highly ionized C at early times, are evidence for the SN ejecta interacting with a H- and He-poor CSM. At later phases diverse spectral features are observed, with some objects resembling SNe Ibc or SNe Ibn and at least one showing similarities to USSNe.

In order to better understand their progenitor systems and explosion mechanisms, we model the bolometric light curves of the well-observed objects in our sample with luminosity inputs from CSI and ^{56}Ni decay. We find that their rapid evolution and peak luminosities can all be explained by $\lesssim 2 M_{\odot}$ of ejecta interacting with $\lesssim 0.5 M_{\odot}$ of CSM, with very little ($\leq 0.04 M_{\odot}$) ^{56}Ni permitted by our observations. These values are in tension with the ejecta and ^{56}Ni masses inferred from the light curves of normal SNe Ibc and SNe Ic-BL but are similar to those of USSNe (Drout et al. 2013; De et al. 2018; Yao et al. 2020). Additionally, the lowest-redshift SN Icn in our sample (SN 2019jc) exploded in the outskirts of its host galaxy, with an SFR density at the SN location that is on the extreme low end of the SN Ibc distribution but is similar to the SFR densities at the locations of USSNe in the literature (Drout et al. 2013; De et al. 2018).

Based on the low estimated ejecta and ^{56}Ni masses, late-time spectral features, and local SFR densities, we conclude that the explosion of an ultra-stripped low-mass star can explain the observed properties of at least one SN Icn. In particular, the spectra, inferred ejecta parameters, and explosion site properties of SN 2019jc favor an ultra-stripped progenitor of this object. On the other hand, at least two other objects in our sample—SN 2021ckj and SN 2021csp—may have a different progenitor system. An SN

explosion with substantial fallback onto a compact remnant formed by the collapse of a W-R star could produce these objects, which have slightly higher peak luminosities and smaller host galaxy separations and show different late-time spectral evolution. In addition, a jet launched during the fallback explosion may be necessary to reproduce the ejecta velocities we measure and could connect these objects with peculiar SNe Ic-BL (e.g., [Whitesides et al. 2017](#); [Pritchard et al. 2021](#)).

In terms of their light-curve properties and spectral features, SNe Icn most resemble SNe Ibn, which are also powered by ejecta interacting with H-poor CSM. Therefore, it is natural to wonder whether SNe Ibn and SNe Icn may be a continuum of objects with the same (or similar) progenitors. This could be the case if both SNe Ibn and SNe Icn are the core collapse of W-R stars, or He stars that have been stripped of their outer layers by close binary interaction ([Tauris et al. 2013](#)), with SNe Icn undergoing more stripping than SNe Ibn. The latter has been suggested as the progenitor of the fast-evolving Type Ic SN 1994I ([Nomoto et al. 1994](#)). Although a W-R progenitor of SNe Ibn has been suggested ([Foley et al. 2007](#)), it is difficult to reconcile a high-mass progenitor with the location of at least one SN Ibn ([Hosseinzadeh et al. 2019](#)). It may be that any explosion within a H-poor (and He-poor) CSM produces properties that are consistent with SNe Ibn (and SNe Icn), in which case multiple progenitor channels are possible for these objects. More systematic studies of the locations of SNe Ibn, as well as their ejecta and CSM properties, are necessary to better constrain their possible progenitors.

If a fraction of SNe Icn are the explosions of low-mass stars stripped by interaction with a compact binary companion, these objects may have important implications for the formation of binary neutron star and neutron star-black hole systems. USSNe have been proposed as the origins of possibly all merging binary neutron stars ([Tauris et al. 2015](#)). If this is the case, then better understanding the rates and host galaxy environments of these objects would have important implications for gravitational wave and multimessenger

astrophysics.

Chapter 6

SN 2020bio: Diversity in the Class of Double-peaked Type IIb Supernovae

This chapter now turns to the other half of fast transient phase space—the less-luminous ($M \gtrsim -17$), rapidly-evolving objects. In many ways these objects are harder to discover and observe than the objects discussed in Chapters 4 and 5 due to their intrinsic faintness. As a result, we must rely on discovering nearby fast-evolving objects to study in greater detail their explosion mechanisms, powering sources, and progenitor stars.

Surveys such as the ZTF BTS have revealed that many of the supernovae in this region of phase space are spectroscopically classified as hydrogen-rich Type II supernovae. In particular, [Ho et al. \(2021\)](#) show that many are Type IIb supernovae with strong early-time shock-cooling emission. Type IIb supernovae are thought to be relatively well-understood. The prototype of this class, SN 1993J, exploded nearby at 3.3 Mpc ([Woosley et al. 1994](#)). As a result, it is one of the best-studied supernovae of the past 30 years. Observations covering the electromagnetic spectrum for ≈ 1000 days after the explosion, as well as a progenitor detection in pre-explosion images, revealed it to be the explosion of a red supergiant star with a binary companion. Its double-peaked light curve has been extensively studied and modeled numerically and analytically, assuming shock cooling as its early-time powering source.

However, the fact that many Type IIb supernovae are classified as fast transients is unexpected given the observed photometric evolution of SN 1993J, which had a secondary light curve peak equally, if not more, luminous to its first. This suggests greater diversity in the properties of Type IIb supernovae, and therefore their progenitors, than previously thought. In particular, the much stronger early-time emission relative to the later-time radioactive decay emission needed to power such rapidly-evolving early-time light curves calls into question the structure of their progenitor stars, the amount of ^{56}Ni produced in their explosions, and shock cooling as the only mechanism powering their light curves. This chapter discusses how observations of the nearby Type IIb SN 2020bio address these three questions.

This chapter was reproduced from the revised version of [Pellegrino et al. \(2023b\)](#) with only minor changes to fit the formatting of this dissertation. I'd like to thank my coauthors, without whom this work would not have been possible: D. Hiramatsu, I. Arcavi, D. A. Howell, K. A. Bostroem, P. J. Brown, J. Burke, N. Elias-Rosa, K. Itagaki, H. Kaneda, C. McCully, M. Modjaz, E. Padilla Gonzalez, and T. A. Pritchard.

6.1 Introduction

While the majority of stars with initial masses $\gtrsim 8 M_{\odot}$ end their lives as H-rich core-collapse supernovae (SNe; e.g., [Janka 2012](#)), some massive stars lose their outer H and even He envelopes and explode as stripped-envelope SNe (SESNe; e.g., [Filippenko 1997](#); [Gal-Yam 2017b](#)). A small but growing number of SNe have been observed with spectra that show similarities to both these classes ([Smith et al. 2011](#)). Classified as Type IIb SNe (SNe IIb), their spectra have H features at early times that gradually give way to He features, indicating that their progenitors were partially stripped of their outer envelopes before exploding ([Woosley et al. 1994](#)).

It is unclear what mechanisms are responsible for this mass loss. Common hypotheses include stellar winds, binary interaction, or late-stage stellar instabilities (see e.g., [Smith & Arnett 2014](#) for a review). Recent studies have shown that mass loss is common during the late stages of massive star evolution, as inferred from early-time observations of core-collapse SNe (e.g., [Ofek et al. 2014](#); [Bruch et al. 2021](#); [Strotjohann et al. 2021](#)). A significant fraction of core-collapse SNe show signatures of pre-existing circumstellar material (CSM) in their early-time spectra, obtained days after their estimated explosion epochs. This CSM is the material shed by the progenitor star in the months to years before core-collapse. As the SN shock breaks out of the expanding ejecta the resulting X-ray and ultraviolet (UV) flash may ionize the surrounding CSM, producing narrow spectral features as the CSM cools and recombines (e.g., [Fassia et al. 2001](#); [Yaron et al. 2017](#)). Interaction between the SN ejecta and CSM can also influence the early-time light-curve evolution ([Morozova et al. 2018](#)).

Some SNe IIb are observed to have double-peaked light curves, with rapidly-fading luminosities during the first several days after explosion before the radioactive decay of ^{56}Ni synthesized during the explosion causes a re-brightening that lasts for several weeks. The early-time emission is thought to be the cooling of the extended envelope of the progenitor star that is heated by the SN shock ([Soderberg et al. 2012](#)). This shock-cooling emission (SCE) has only been extensively observed in a handful of cases, including SN 1993J (e.g., [Woosley et al. 1994](#); [Richmond et al. 1994](#)), SN 2011dh (e.g., [Arcavi et al. 2011](#); [Ergon et al. 2014](#)), SN2013 df (e.g., [Morales-Garoffolo et al. 2014](#); [Van Dyk et al. 2014](#)), SN 2016gkg ([Arcavi et al. 2017](#)), SN 2017jgh ([Armstrong et al. 2021](#)), and ZTF18aalrxas ([Fremling et al. 2019](#)), among others. Most of these objects are nearby and had follow-up observations scheduled hours after explosion, which proved crucial to observing the rapidly-evolving SCE. These studies have found that SNe IIb are consistent with the explosions of stars with extended outer envelopes, with the duration

of the SCE dependent on the extent of this envelope (Soderberg et al. 2012).

Numerical and analytical models of SCE can complement pre-explosion imaging in determining the progenitors of these objects. Several models have been successful in reproducing the observed early-time evolution across all wavelengths. Piro (2015 hereafter P15) is one of the first to present a one-zone analytical description of the cooling of an extended low-mass envelope shock-heated by the explosion of a compact massive core. Piro et al. (2021 hereafter P21) extend this to a two-zone model in order to better capture the emission from the outermost material in extended envelopes. Sapir & Waxman (2017 hereafter SW17) calibrate earlier models by Rabinak & Waxman (2011)—that depend on the precise density structure of the outer material—to numerical simulations for several days after explosion.

Comparing observed SCE to analytical and numerical models is one of the only ways of directly measuring the radii and stellar structure of core-collapse progenitors from SN observations. This has been done for a handful of SNe IIb as well as SNe of other subtypes, including stripped-envelope Type Ib SNe (e.g., Modjaz et al. 2009; Yao et al. 2020), short-plateau Type II SNe (Hiramatsu et al. 2021a), and exotic Ca-rich transients (e.g., Jacobson-Galán et al. 2020, 2022b). Analytical and numerical modeling of double-peaked SNe IIb generally yield large radii progenitors ($\approx 100\text{--}500 R_{\odot}$) with low-mass ($\approx 10^{-2}\text{--}10^{-1} M_{\odot}$) extended envelopes (Piro et al. 2021 and references therein). These properties are usually in agreement with those of SNe IIb progenitors from pre-explosion *Hubble Space Telescope* images, which have revealed them to be supergiants (Aldering et al. 1994; Maund et al. 2011; Van Dyk et al. 2014). In some cases, however, the progenitor radii estimated from SCE modeling are in tension with those measured from direct imaging (e.g., Arcavi et al. 2017; Tartaglia et al. 2017 in the case of SN 2016gkg). Potential binary companions to the progenitor, which have been observed or inferred in a handful of cases (e.g., Maund et al. 2004; Benvenuto et al. 2013) can further complicate

direct imaging estimates when the individual binary members are unresolvable.

Here we present photometric and spectroscopic observations of SN 2020bio, an SN IIb showing remarkably strong SCE, obtained by Las Cumbres Observatory (LCO) through the Global Supernova Project (GSP). LCO extensively observed SN 2020bio from hours to ≈ 160 days after explosion, providing a detailed look into the full evolution of a double-peaked SN IIb. In this work, we analyze its light curve evolution, spectral features, and fit analytic models to its full light-curve evolution to estimate the radius, mass, and structure of its progenitor star. We also compare its bolometric light curve and spectra to numerical models in order to infer its progenitor mass and the properties of its circumstellar environment.

This paper is organized as follows. In Section 6.2 we describe the discovery and follow-up observations of SN 2020bio. We present its full light curve and spectral time series in Section 6.3 and compare observations to analytical and numerical models in Section 6.4. Finally, in Section 6.5 we discuss the potential progenitor properties of SN 2020bio given the presented evidence.

6.2 Discovery and Data Description

SN 2020bio was discovered by Koichi Itagaki on UT 2020 January 29.77 at the Itagaki Astronomical Observatory at an unfiltered Vega magnitude of 16.7. Stacking images of the same field obtained by the Asteroid Terrestrial-impact Last Alert System (ATLAS) survey on the previous night yields a nondetection down to c -band magnitude 20.6. Soon after discovery rapid photometric and spectroscopic follow-up observations were requested by the GSP through the Las Cumbres global network of telescopes. The GSP also triggered its Swift Key Project (1518618: PI Howell) to obtain daily UV and optical photometry. A classification spectrum obtained on the 2.0m Liverpool Telescope

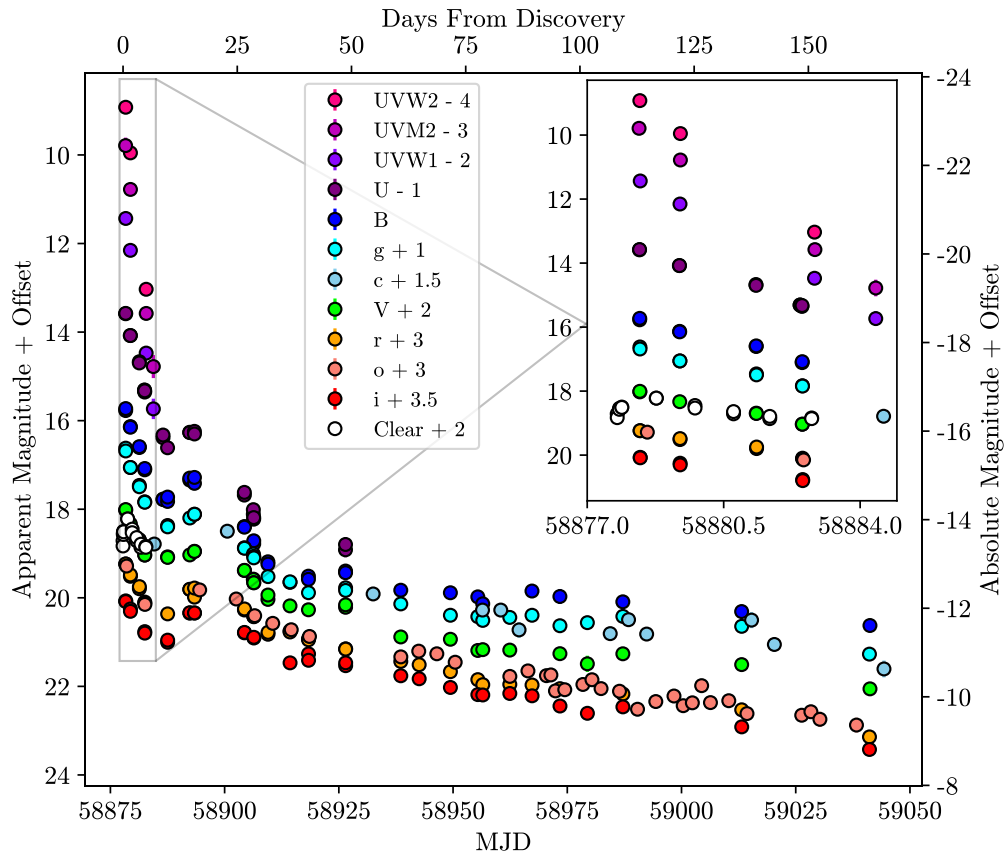


Figure 6.1: The full extinction-corrected light curves of SN 2020bio. Photometry in different filters have been offset for clarity. Unfiltered photometry from the Itagaki Astronomical Observatory is included as clear points and calibrated to the V -band. The inset focuses on the rapidly-evolving shock-cooling emission.

on 2020 January 31.19—approximately 1.5 days after the first detection—shows a blue continuum superimposed with a narrow $H\alpha$ emission feature and a broad possible He I λ 5876Å feature, consistent with a young core-collapse SN (Srivastav et al. 2020).

SN 2020bio exploded at right ascension $13^{\text{h}}55^{\text{m}}37^{\text{s}}.69$ and declination $+40^{\circ}28'39''.1$ in the spiral galaxy NGC 5371 at redshift $z = 0.008533$ (Springob et al. 2005). The distance to NGC 5371 is uncertain due to its low redshift. We adopt the mean of several distances measured using the method of Tully & Fisher (1977), which gives $d =$

29.9 ± 5.1 Mpc (values from the NASA Extragalactic Database¹). Using the [Schlafly & Finkbeiner \(2011\)](#) dust map calibrations, we estimate a Galactic line-of-sight extinction to SN 2020bio $E_{MW}(B - V) = 0.008$ mag. Given the location of SN 2020bio with respect to its host galaxy, we also estimate host extinction using the Na I D equivalent widths measured in a high-resolution spectrum of the SN. From the conversions presented in [Poznanski et al. \(2012\)](#), we estimate $E_{host}(B - V) = 0.068 \pm 0.038$ mag for a total extinction $E(B - V) = 0.076 \pm 0.038$ mag. The photometry of SN 2020bio presented throughout this work is corrected for this mean total extinction.

LCO photometric follow-up commenced less than a day after discovery. *UBgVri*-band images were obtained by the Sinistro and Spectral cameras mounted on LCO 1.0m and 2.0m telescopes, respectively, located at McDonald Observatory, Teide Observatory, and Haleakala Observatory. Data were reduced using `lcogtsnpipe` ([Valenti et al. 2016](#)) which extracts point-spread function magnitudes after calculating zero-points and color terms ([Stetson 1987](#)). *UBV*-band photometry was calibrated to Vega magnitudes using Landolt standard fields ([Landolt 1992](#)) while *gri*-band photometry was calibrated to AB magnitudes ([Smith et al. 2002](#)) using Sloan Digital Sky Survey (SDSS) catalogs. As SN 2020bio exploded coincident with its host galaxy, to remove host galaxy light we performed template subtraction using the HOTPANTS ([Becker 2015](#)) algorithm and template images obtained after the SN had faded. Unfiltered images were obtained with the Itagaki Astronomical Observatory (Okayama and Kochi, Japan) 0.35 m telescopes + KAF-1001E (CCD). Using our custom software, the photometry was extracted after host subtraction and calibrated to the V-band magnitudes of 45 field stars from the Fourth US Naval Observatory CCD Astrograph Catalog ([Zacharias et al. 2013](#)).

We also obtained ATLAS ([Tonry et al. 2018](#); [Smith et al. 2020](#)) forced photometry from the forced photometry server ([Shingles et al. 2021](#)). Images obtained on the same

¹<https://ned.ipac.caltech.edu/>

night were averaged for higher signal-to-noise. Magnitudes in the c - and o -bands were calibrated to AB magnitudes.

UV and optical photometry were obtained with the Ultraviolet and Optical Telescope (UVOT; [Romig et al. 2005](#)) on the Neil Gehrels Swift observatory ([Gehrels et al. 2004](#)). Swift data were reduced using a custom adaptation of the Swift Optical/Ultraviolet Supernova Archive ([Brown et al. 2014](#)) pipeline with the most recent calibration files and the zeropoints of [Breeveld et al. \(2011\)](#). Images from the final epoch, obtained after the SN had sufficiently faded, were used as templates to subtract the host galaxy light. All Swift photometry is calibrated to Vega magnitudes.

LCO spectra were obtained by the FLOYDS spectrograph on the 2.0m Faulkes Telescope North at Haleakala Observatory. Spectra cover a wavelength range of 3500–10,000 Å at a resolution $R \approx 300$ -600. Data were reduced using the `floydsspec` pipeline², a custom pipeline which performs cosmic ray removal, spectrum extraction, and wavelength and flux calibration. We also present one spectrum obtained by the B&C spectrograph on the 2.3m Bok Telescope at Steward Observatory, two spectra obtained by the Blue Channel Spectrograph on the 6.5m MMT at the Fred Lawrence Whipple Observatory, and one spectrum obtained by the Optical System for Imaging and low-Intermediate-Resolution Integrated Spectroscopy spectrograph on the 10.4m Gran Telescopio Canarias.

6.3 Photometric and Spectral Analysis

6.3.1 Spectroscopic Classification

Given the unusual features of SN 2020bio compared to SNe IIb in literature (see Sections [6.3](#), [6.4](#)), as well as the lack of a public classification, here we attempt to accurately

²https://github.com/svalenti/FLOYDS_pipeline/

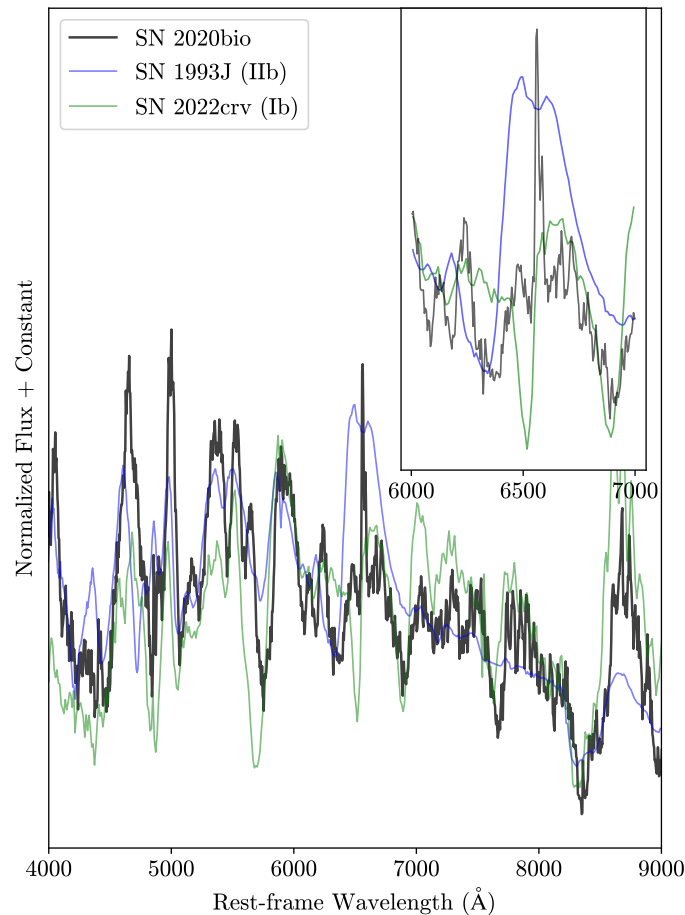


Figure 6.2: The spectrum of SN 2020bio compared with spectra of the Type IIb SN 1993J and the Type Ib SN 2022crv at the same phase. SN 2020bio has spectral features in common with both these classes. The inset shows the region surrounding the $H\alpha$ line. SN 2020bio has a weak and broad $H\alpha$ emission feature that is weaker than that in the spectrum of SN 1993J. However, this feature is much different than seen in SN 2022crv. This may indicate that the progenitor of SN 2020bio was stripped almost entirely of its H-rich envelope.

classify SN 2020bio. Analyzing the spectrum of SN 2020bio 25 days after discovery using SN classification software (Howell et al. 2005; Blondin & Tonry 2007) gives matches to both SNe IIb and SNe Ib at the correct phase and redshift. This spectrum of SN 2020bio compared with spectra at the same phase from the prototypical Type IIb SN 1993J (Barbon et al. 1995) as well as the normal Type Ib SN 2022crv (Y. Dong et al., in prep.) are

shown in Figure 6.2. SN 2020bio has spectral features that match both objects. For example, the strong Ca II near-infrared P-Cygni feature matches the SN Ib, but the features blueward of 5000 Å more closely resemble SN 1993J. We focus on the region surrounding the H α feature in the inset. SN 2020bio lacks the strong, broad emission feature that is commonplace in most SNe IIb spectra. However, it also does not match the strong He I λ 6678 feature that is seen in the SN Ib.

We consider two possibilities to explain the observed features in this region of the spectrum. First, it may consist mainly of broad but weak H α emission with a superimposed narrow host emission line. An absorption feature just blueward of that host line may be He λ 6678 absorption, as seen in other “flat-topped” H α features in SNe IIb. Assuming this absorption is from He, we measure an ejecta velocity of ≈ 7500 km s $^{-1}$. This velocity also corresponds to other absorption features seen in the spectrum corresponding to He I λ 5876 and He I λ 7065.

The second possibility is that the broad feature is composed entirely of He I emission. In this case, the He absorption from this P-Cygni feature gives an ejecta velocity of $\approx 14,000$ km s $^{-1}$. The narrow absorption just blueward of the narrow H α is more difficult to explain. One potential source is absorption by circumstellar H. The velocity of the absorption minimum relative to H α is ≈ 1000 km s $^{-1}$ —faster than typical red supergiant or yellow supergiant winds (Smith & Arnett 2014) but not unreasonable if the CSM is accelerated by interaction with the SN ejecta. Circumstellar interaction may also contribute to the narrow H α emission feature. While inspecting the 2D FLOYDS spectrum reveals residual H α contamination from the host galaxy, analyzing the full-width at half-maximum of this line over the first three weeks after explosion reveals a decreasing trend. Therefore, we cannot rule out circumstellar interaction as a contribution to the narrow H P-Cygni feature.

In summary, the classification of SN 2020bio is difficult to determine with high con-

vidence. The spectra reveal that this object is unique—emission from H-rich ejecta is very weak or nonexistent at all, and circumstellar interaction may be contributing to the peculiar spectral features. If there is weak but broad H emission, then the outer layers of the progenitor may have been almost entirely stripped of the H-rich material, placing SN 2020bio in a transitional region between SNe IIb and SNe Ib. On the other hand, if the ejecta is H-free then SN 2020bio is a very rare example of an SN Ib with a double-peaked light curve. However, based on the emission centered around $\approx 6550 \text{ \AA}$ that is broader than seen in typical SN Ib spectra, as well as the consistent ejecta velocity measurements of $\approx 7500 \text{ km s}^{-1}$, we favor the former interpretation. Therefore, for the sake of classification, the presence of weak H allows us to classify this object as a SN of Type IIb.

6.3.2 Light Curve and Color Evolution

In Figure 6.1 we show the full LCO, ATLAS, and Swift extinction-corrected light curve of SN 2020bio, from detection to ≈ 160 days after explosion. The discovery and subsequent follow-up photometry from Itagaki are included as “Clear” data points. The inset shows in greater detail the early-time evolution of the SCE, focusing on the first week after discovery. The most distinctive feature of the light curve is the luminous and rapidly-declining SCE at early times. The peak SCE luminosity exceeds that of the secondary peak ≈ 15 days later, but SCE only dominates the light curve during the first several days. Over this time the light curve falls by ≈ 4 mag in the first week, making this phase difficult to observe without rapid multi-wavelength follow-up.

After ≈ 4 days from discovery the slope of the light curve decline changes as the luminosity from ^{56}Ni decay begins to dominate the light curve. After about a week the light curve re-brightens and reaches a secondary maximum ≈ 15 days after discovery.

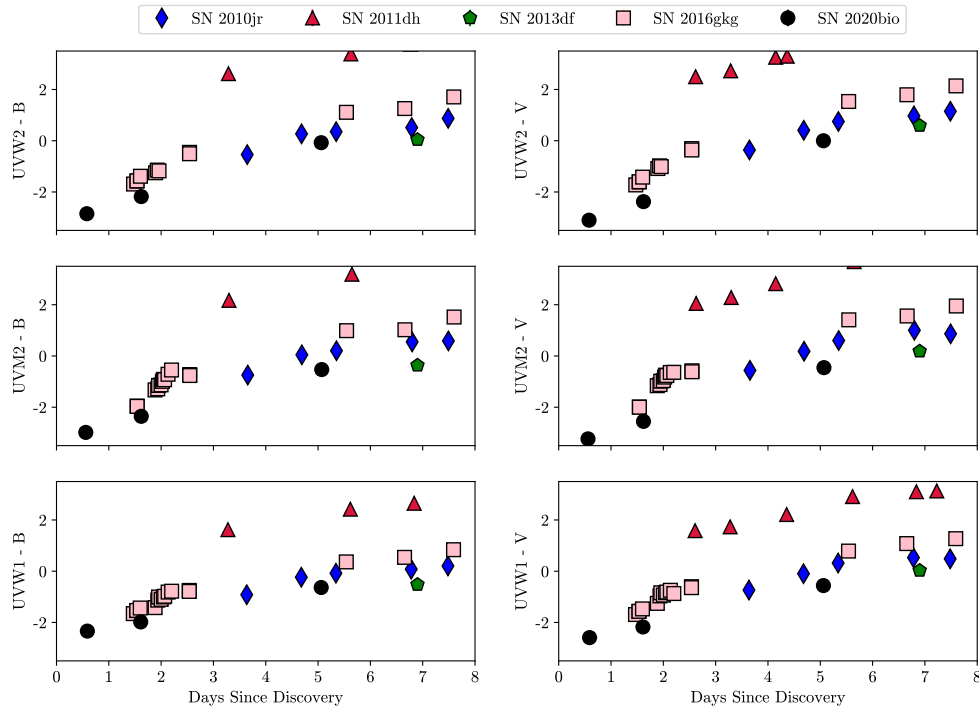


Figure 6.3: UV - optical colors of SN 2020bio compared with those of other SNe IIb with early-time Swift observations. SN 2020bio was bluer at earlier phases than the other SNe IIb. Data for these comparison SNe were obtained from the following sources: [Arcavi et al. \(2011\)](#) (SN 2011dh); [Morales-Garoffolo et al. \(2014\)](#) (SN 2013df); [Arcavi et al. \(2017\)](#) (SN 2016gkg); [Pritchard et al. \(2014\)](#) and Open Astronomy Catalog (SN 2010jr); this work (SN 2020bio).

From this point the emission settles onto the radioactive decay tail, powered by ^{56}Co decay, for the remainder of the observations. The secondary peak and overall late-time light curve is relatively dim, peaking at $M \approx -14$ mag in the V -band, hinting at a small amount of ^{56}Ni synthesized in the explosion.

In Figure 6.3 we compare the early-time UV-optical colors of SN 2020bio to those of other SNe IIb with observed SCE in the UV. The B - and V -band data for all the objects, with the exception of SN 2010jr, are ground-based photometry to avoid uncertain subtractions and calibrations in Swift optical bands. All dates are given with respect to the time of discovery and corrected for extinction according to the published values

for each object. SN 2020bio has both the earliest observations relative to discovery and the bluest colors throughout its evolution compared to the other objects. While objects such as SN 2010jr and SN 2016gkg have more densely-sampled light curves, their observations began later and their colors evolved redward faster compared to SN 2020bio. Of the 6 colors plotted, SN 2020bio is exceptionally blue in the $UVM2-B$ and $UVM2-V$ colors, particularly in the earliest epochs. This may be evidence for another luminosity contribution besides SCE, as we discuss in Section 6.5.

6.3.3 Spectral Comparison

Spectral coverage of SN 2020bio began fewer than 2 days after the first detection—approximately 3 days since the estimated explosion time (Section 6.4.2)—and continued for 201 days. We plot the full spectral series in Figure 6.4. The earliest spectrum of SN 2020bio, reported to the Transient Name Server (Srivastav et al. 2020), shows a hot blue continuum superimposed with weak emission features. We identify a potential weak, broad feature of He I $\lambda 5876 \text{ \AA}$ blueshifted by $\approx 11000 \text{ km s}^{-1}$. We also note potential narrow lines of $H\alpha$ and $H\beta$; however, these features are consistent with host galaxy contamination at the resolution of the spectrum.

After about a week post explosion, absorption features begin to develop in the spectra. We identify lines of He, O, and Ca. The absorption feature blueward of the rest-frame $H\alpha$ line matches He I $\lambda 6678 \text{ \AA}$ absorption blueshifted by $\approx 7500 \text{ km s}^{-1}$, which is commonly noted to cause “flat-topped” $H\alpha$ emission profiles in other SNe IIb (e.g., Filippenko et al. 1993). In general, the absorption features in the SN 2020bio spectra are shallower than those of the other SNe IIb, particularly SN 2011dh. Interaction with CSM can produce absorption features that are weaker and shallower than expected, which has been noted in the spectra of SN 1993J and SN 2013df (Fremming et al. 2019).

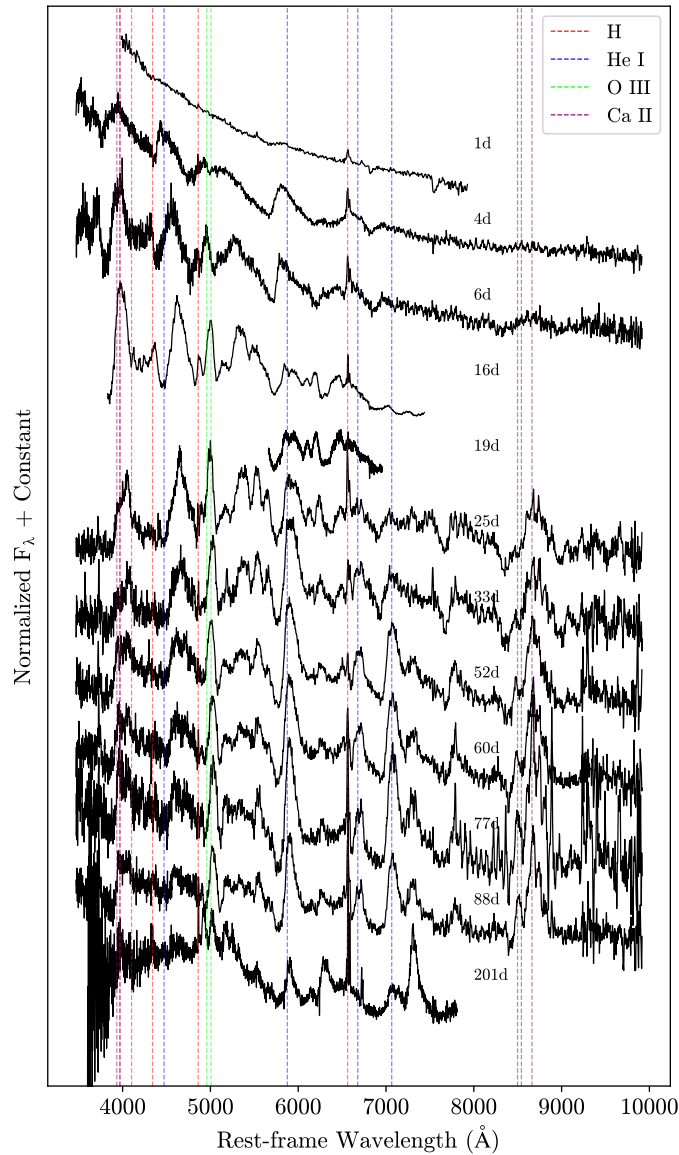


Figure 6.4: The full spectral time series of SN 2020bio. Phases with respect to the detection epoch are given above each spectrum. Notable spectral features are identified with dashed lines. The first spectrum is the publicly-available classification spectrum retrieved from the Transient Name Server.

To further investigate the differences between SN 2020bio and other SNe IIb, we plot comparison spectra just after explosion (top), after two weeks (middle), and three weeks (bottom) after explosion in Figure 6.5. Among this sample, many of the other SNe IIb

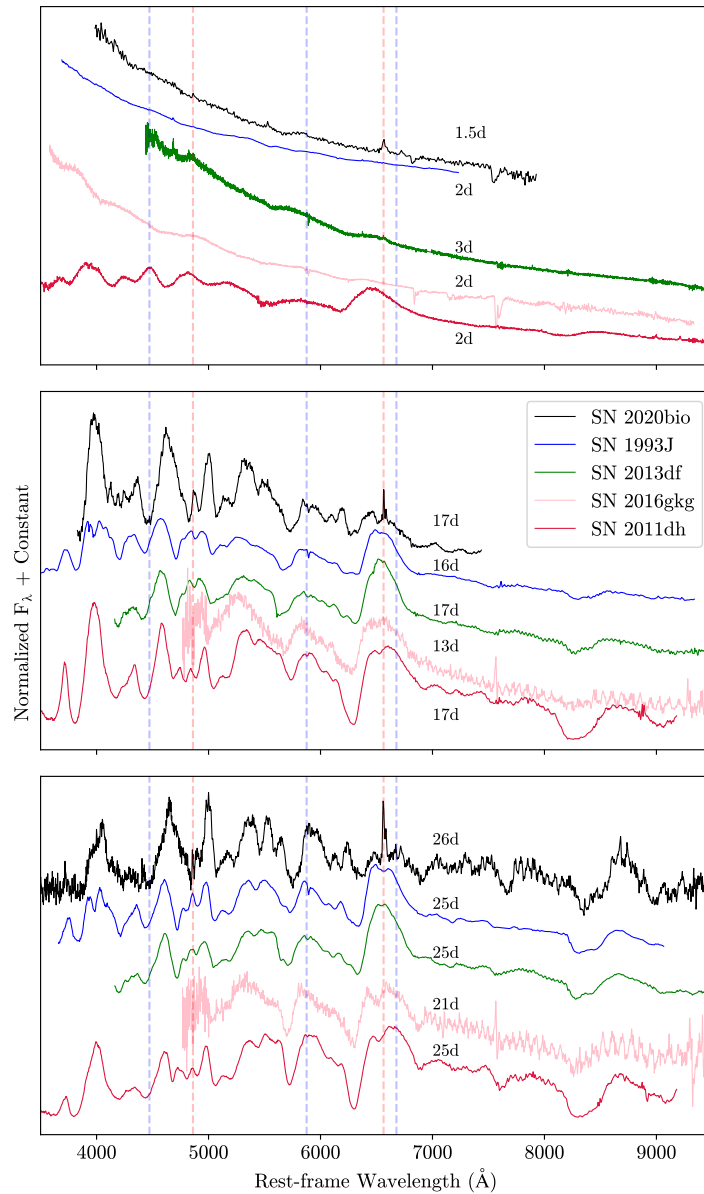


Figure 6.5: Spectra of SN 2020bio compared with spectra of other SNe IIb at similar phases. Phases with respect to the estimated explosion time are given above each spectrum and notable spectral features are identified with red (H) and blue (He) vertical lines at their rest-frame wavelengths. The spectra of SN 2016gkg are unpublished spectra obtained by LCO while the other comparison spectra were retrieved from WiseRep (Yaron & Gal-Yam 2012).

show broadened, high-velocity H and He features at early times. However, the spectrum of SN 2020bio at this same phase shows only a blue continuum with possible weak He I

emission. This difference suggests that the photosphere has not yet receded within the outermost ejecta. One explanation for this is if the SN ejecta is surrounded by low-density CSM. At this phase any narrow lines caused by photoionization or collisional excitation may have vanished but the photosphere could still lie within this shock-heated material, obscuring the ejecta features within. By the time of our next spectrum (4 days after discovery) the photosphere has receded into the SN ejecta, revealing broad SN features. Narrow lines also persist in the spectra of SN 2020bio; however, these are at least partially due to galaxy contamination, as `floydsspec` does not remove host galaxy contamination during the reduction.

Differences persist weeks after the estimated explosion times. While the other SNe IIb have developed broad $H\alpha$ and $H\beta$ emission features, these same lines are weaker in SN 2020bio. This could be partly caused by He I λ 6678Å absorption, which has an absorption trough coincident with the $H\alpha$ flux when blueshifted by ≈ 7500 km s⁻¹. Another possibility, as mentioned in Section 6.3.1, is that the H emission from SN 2020bio is inherently weaker than in other SNe IIb, which may be the case if the progenitor lost more of its outer H envelope than the progenitors of the other SNe IIb did. Weak H emission, along with potential CSM, point to a scenario in which the progenitor of SN 2020bio underwent enhanced mass-loss, shedding almost all of its outer H layer before exploding. If this is the case, such a progenitor scenario to SN 2020bio is unique among other well-studied SNe IIb.

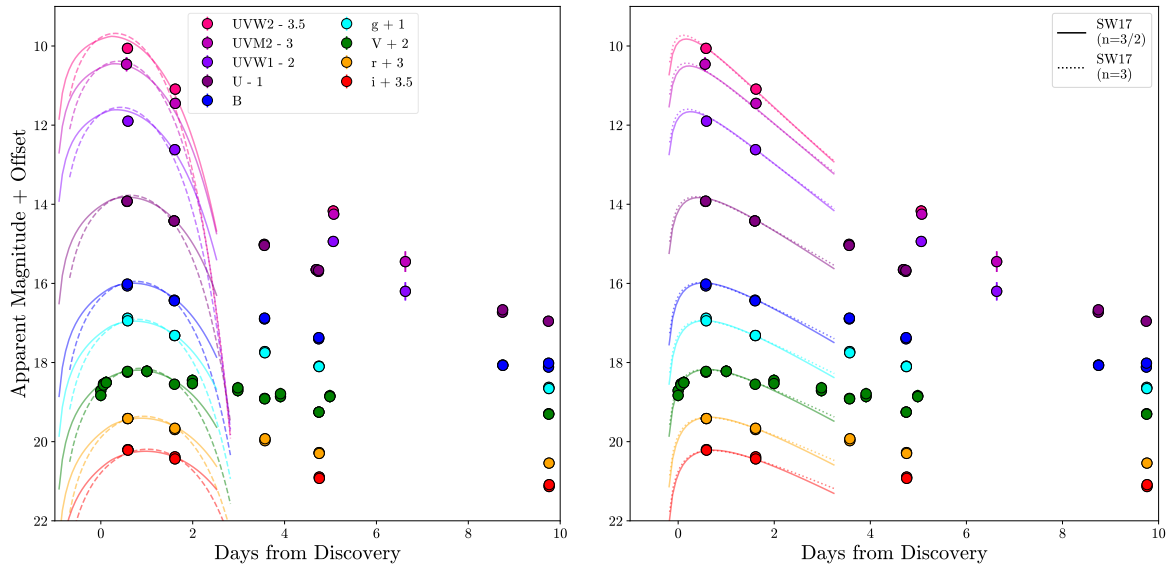


Figure 6.6: Shock-cooling fits to the early-time photometry of SN 2020bio using the models of (left) P15 and P21; and (right) SW17, assuming a constant optical opacity appropriate for solar-composition material. Photometry in each band has been offset for clarity. Itagaki discovery photometry has been included in the V -band fits.

6.4 Light-curve Modeling and Progenitor Inference

6.4.1 Shock-cooling Model Descriptions

A variety of analytical and numerical models of SCE have been developed in recent years. Here we consider 3 analytical models that are commonly used to fit the early-time emission of core-collapse SNe. The P15 model extends the formalism of [Nakar & Piro \(2014\)](#) to reproduce the full shock-cooling peak. It assumes a lower mass extended envelope without assuming its specific density structure. On the other hand, SW17 calibrates to the numerical models of [Rabinak & Waxman \(2011\)](#) and assumes specific polytropic indices for the extended envelope. The methodology used to fit these models to the data and derive resulting blackbody properties are presented in [Arcavi et al. \(2017\)](#).

More recently, [Piro et al. \(2021\)](#) developed another analytical model to better reproduce the early SCE observed in a variety of transients (e.g., [Arcavi et al. 2017](#); [Yao et al.](#)

2020). They assume a two-zone extended envelope in homologous expansion and calculate the emission from this shocked material. This method begins by assuming extended material in homologous expansion separated into two regions—an outer density profile described by $\rho \propto r^{-n}$, where $n \approx 10$, and an inner region with $\rho \propto r^{-\delta}$, where $\delta \approx 1.1$. Assuming a transitional velocity v_t between the inner and outer regions of the extended material, the time for the diffusion front to reach this transition is given by

$$t_d = \left(\frac{3\kappa K M_e}{(n-1)v_t c} \right)^{1/2} \quad (6.1)$$

where $K = \frac{(n-3)(3-\delta)}{4\pi(n-\delta)}$, κ is the optical opacity, and M_e is the mass of the extended material. The luminosity from the cooling of the extended material is then defined piecewise for times before and after this diffusion time:

$$L(t) \approx \frac{\pi(n-1)}{3(n-5)} \frac{cR_e v_t^2}{\kappa} \left(\frac{t_d}{t} \right)^{4/(n-2)}, t \leq t_d \quad (6.2)$$

and

$$L(t) \approx \frac{\pi(n-1)}{3(n-5)} \frac{cR_e v_t^2}{\kappa} \exp \left[-\frac{1}{2} \left(\frac{t^2}{t_d^2} - 1 \right) \right], t \geq t_d \quad (6.3)$$

To fit the photometry in each band, we assume that the material radiates as a blackbody at some photospheric radius r_{ph} . The photosphere reaches the transition between the two regions at a time

$$t_{ph} = \left[\frac{3\kappa K M_e}{2(n-1)v_t^2} \right]^{1/2} \quad (6.4)$$

and the time evolution of the photospheric radius is given relative to this characteristic time:

$$r_{ph}(t) = \left(\frac{t_{ph}}{t} \right)^{2/(n-1)} v_t t, t \leq t_{ph} \quad (6.5)$$

and

$$r_{ph}(t) = \left[\frac{\delta-1}{n-1} \left(\frac{t^2}{t_{ph}^2} - 1 \right) + 1 \right]^{-1/(\delta-1)} v_t t, t \geq t_{ph} \quad (6.6)$$

In addition, we attempt to fit the analytical models of [Shussman et al. \(2016\)](#), which are calibrated to numerical simulations from shock breakout to recombination. However, these model fits are unable to reproduce the rapidly-declining shock-cooling emission in all filters during the week after explosion. It is possible this shortcoming is due to an unphysical application of the model—which is calibrated to numerical simulations of red supergiants—to the early light curve of SN 2020bio, which likely had a different progenitor structure. Detailed comparisons between numerical models of SNe IIb and the [Shussman et al. \(2016\)](#) models are beyond the scope of this work.

6.4.2 Best-fit Analytic Models

We fit each model to the early-time photometry of SN 2020bio. For the SW17 model we consider two polytropic indices ($n = 3/2$ and $n = 3$), appropriate for convective and radiative envelopes, respectively. Only data taken up to 3.5 days after discovery are fit, as this is the time when SCE dominates the luminosity over radioactive decay (see Section 6.4.3 for a quantitative treatment of the ^{56}Ni light curve). Additionally, we ensure that the phases we fit fall within the validity range of each model. In each case we fit for the progenitor extended envelope radius, R_{env} , the envelope mass, M_{env} , either the characteristic velocity or the shock velocity v of the outer material, and the offset time since explosion t_0 . We use the `emcee` package ([Foreman-Mackey et al. 2013](#)) to perform Markov Chain Monte Carlo fitting of each model, initializing 100 walkers with 1000 burn-in steps and running for an additional 1000 steps after burn-in. For each step, the total luminosity is computed using the analytical model formalism, and the luminosity within each filter is compared to the observed photometry assuming a blackbody spectral energy distribution (SED). We fit each model assuming an optical opacity $\kappa = 0.34 \text{ cm}^2 \text{ g}^{-1}$, consistent with solar composition material.

The best-fit models to the multi-band SCE light curves are shown in Figure 6.6. The Itagaki discovery data that capture the rise are calibrated to the V -band. We find that all the models fit the early-time data well, reproducing the rapid rise, luminous peak, and subsequent decline in all filters. Quantitatively the SW17 model for convective envelopes ($n = 3/2$) has the lowest reduced χ^2 value, indicating the model most closely matches the observations. On the other hand, the best-fit envelope mass for the SW17 model with a radiative ($n = 3$) envelope is larger than the total ejecta mass, estimated in Section 6.4.3. Therefore, we do not consider this model representative of the progenitor of SN 2020bio.

Based on the unusual properties of SN 2020bio compared to other SNe IIb, including its weak H spectral features and faint secondary light-curve peak, we test whether a lower-opacity envelope better reproduces the observed SCE. This could be the case if the progenitor star was almost completely stripped of its outer H envelope. We perform the same fitting routine but fix the opacity $\kappa = 0.20 \text{ cm}^2 \text{ g}^{-1}$ for H-poor material. We find no differences in goodness of fits for each model between the two chosen opacities—both the H-rich and H-poor envelopes produce similarly good fits. However, there are differences in the fitted parameters between the best-fit models. In the H-rich case, the envelope radii and masses from the best-fit SW17 model are consistent with those estimated for other SNe IIb (i.e. radii of $\approx 1 \times 10^{13} \text{ cm}$ and masses of 10^{-3} – $10^{-2} M_{\odot}$). In the H-poor case, however, the radii are smaller ($\approx 100 R_{\odot}$) and the envelope masses are larger ($\approx 0.5 M_{\odot}$). These values are more consistent with those estimated for Type Ib and Ca-rich transients with observed SCE (e.g., Yao et al. 2020; Jacobson-Galán et al. 2022b).

6.4.3 Bolometric Luminosities and Numerical Modeling

SCE dominates the total luminosity only for several days after explosion. The rest of the light curve is powered by the radioactive decay of ^{56}Ni and its children isotopes.

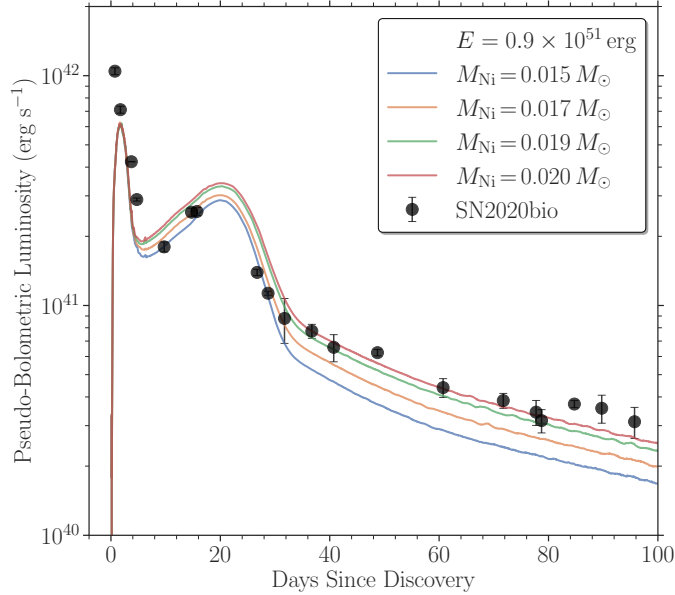


Figure 6.7: Numerical MESA and STELLA model light curves of SN 2020bio for varying M_{Ni} . Both the secondary light-curve peak and late-time light-curve slope are best reproduced with $\approx 0.02 M_{\odot}$ of ^{56}Ni synthesized in the explosion.

Using our multi-band coverage of SN 2020bio for ≈ 160 days after explosion, we construct a pseudo-bolometric light curve to fit for the amount of ^{56}Ni produced in the explosion. For epochs with observations in more than 3 filters, we extrapolate the SED out to the blue and red edges of the U - and i -band filters, respectively, using a univariate spline. We choose to extrapolate the (extinction-corrected) photometry rather than fit a blackbody SED because the spectra are not representative of a blackbody throughout the object’s evolution.

To infer the properties of the pre-explosion progenitor as well as the explosion itself, we compare numerical MESA (Paxton et al. 2011, 2013, 2015, 2018, 2019) and STELLA (Blinnikov et al. 1998, 2000, 2006) model explosions to our pseudo-bolometric light curve. As no model from the grid of Hiramatsu et al. (2021a) reproduces the weak secondary peak of SN 2020bio, we attempt to construct our own best-fit model. We begin with a MESA progenitor with $M_{\text{ZAMS}} = 15 M_{\odot}$ and evolve it to a final mass of $4.8 M_{\odot}$. At

explosion the progenitor has a H-rich envelope radius of $280 R_{\odot}$ and mass of $0.10 M_{\odot}$, in agreement with values we find from our best-fit H-rich SCE models. The explosion energy and ejecta mass are fixed at 0.9×10^{51} erg and $2.9 M_{\odot}$, respectively, and the mass of ^{56}Ni (M_{Ni}) is varied between 0.015 and $0.020 M_{\odot}$. These explosion models are then run through STELLA in order to reproduce the bolometric luminosity evolution. For more information, see [Hiramatsu et al. \(2021a\)](#).

The resulting model light curves are shown in Figure 6.7, compared with the pseudo-bolometric light curve of SN 2020bio. We find decent qualitative agreement between the numerical models and the observed light-curve evolution, particularly at later times. The secondary light-curve peak and late-time light-curve slope are well reproduced by an explosion which synthesizes $\approx 0.02 M_{\odot}$ of ^{56}Ni . The secondary light-curve peak may be overproduced, but the exact peak luminosity and time of peak are uncertain given the gap in our observational coverage.

Interestingly, however, the peak luminosity of the SCE is not reproduced by these models. It may be that the treatment of the SN shock and the subsequent cooling of the outer envelope is too complex to fully simulate within these models. On the other hand, it is possible that an additional powering mechanism contributes to the early-time evolution. To test this, we explore how the addition of different mass-loss rates and timescales to the models affects the early-time light curve through short-lived circumstellar interaction. To the best-fit MESA model we attach a wind density profile $\rho_{\text{CSM}}(r) = \dot{M}_{\text{wind}}/4\pi r^2 v_{\text{wind}}$, where $v_{\text{wind}} = 10 \text{ km s}^{-1}$. These CSM models are shown in Figure 6.8. We find that the best-fit models have a confined CSM with masses of $1 \times 10^{-3} - 1 \times 10^{-2} M_{\odot}$ lost by the progenitor within the last several months before explosion. This hints that circumstellar interaction may contribute to the rapidly-fading early-time emission of SN 2020bio and possibly other SNe IIb. If this is the case, then the information estimated through SCE model fits may not be truly representative of the true nature of their progenitors.

The values inferred from this numerical modelling, particularly the ^{56}Ni mass, are on the low end of the distribution of values estimated for other well-studied SNe IIb. SNe IIb with double-peaked light curves typically display secondary radioactive decay-powered peaks equally or more luminous than the peak of the SCE, implying a greater amount of ^{56}Ni synthesized. Studies using samples of these objects have found average ^{56}Ni masses of $\approx 0.10 - 0.15 M_{\odot}$ and average ejecta masses of $\approx 2.2 - 4.5 M_{\odot}$ (Lyman et al. 2016; Prentice et al. 2016; Taddia et al. 2018), in better agreement with ejecta parameters of other stripped-envelope and H-rich core-collapse SNe. However, rare cases of underluminous SNe IIb with low inferred M_{Ni} have been discovered (e.g., Nakaoka et al. 2019; Maeda et al. 2023). These objects have light curves that appear transitional between standard SNe II-P and SNe IIb, which differ from the observed photometric evolution of SN 2020bio.

On the other hand, in the case of SN 2018ivc, both a low ^{56}Ni mass ($M_{\text{Ni}} \leq 0.015 M_{\odot}$) and progenitor mass ($M_{\text{ZAMS}} \lesssim 12 M_{\odot}$) are inferred (Maeda et al. 2023). It is possible that other SNe IIb with little synthesized ^{56}Ni may be undercounted due to their rapidly-fading or underluminous light curves. Maeda et al. (2023) also concluded that the light curve of SN 2018ivc was powered at least in part by circumstellar interaction. Sustained circumstellar interaction has been inferred for other SNe IIb, either through late-time spectral features (Maeda et al. 2015; Fremling et al. 2019) or through X-ray and radio observations (Fransson et al. 1996). It may be that the mechanism that produced the confined CSM inferred from our numerical models of SN 2020bio, and possibly that seen in the case of SN 2018ivc, points to more extreme mass-loss than found in other SNe IIb.

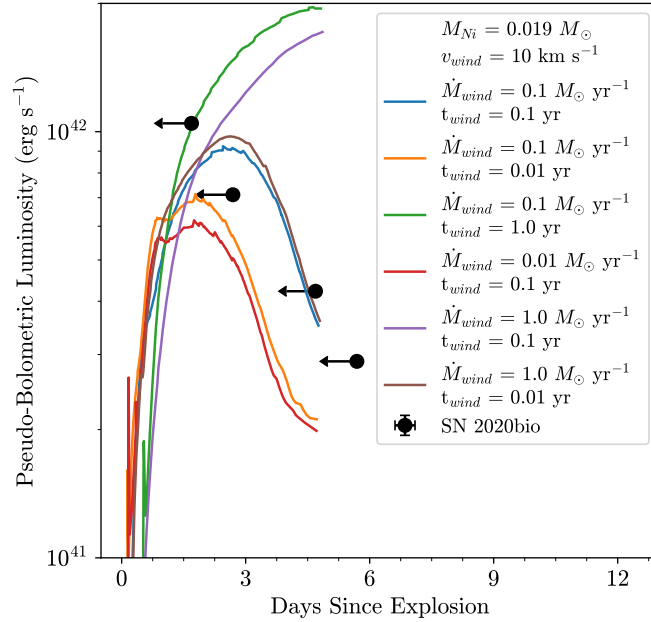


Figure 6.8: Numerical MESA and STELLA circumstellar interaction-powered model light curves of SN 2020bio at early times. Different color curves correspond to models with varying mass-loss rates and timescales. Leftward-facing arrows show the range of possible explosion epochs inferred from our SCE fits. The early-time emission excess is best reproduced with 0.001-0.01 M_{\odot} of CSM.

6.4.4 Comparison to Nebula Spectra Models

A trend between an increasing amount of synthesized O and increasing core-collapse SN progenitor mass has been extensively studied (e.g., [Woosley & Heger 2007](#)). [Jerkstrand et al. \(2015\)](#) use this relationship to calibrate the [O I] $\lambda\lambda$ 6300,6364 luminosity, normalized by the radioactive decay luminosity at the same phase, with numerical models of SNe IIb progenitors (see Eq. 1 of [Jerkstrand et al. 2015](#)). The authors consider models with zero-age main-sequence masses between 12 M_{\odot} and 17 M_{\odot} . Comparing the observed normalized [O I] luminosity for a handful of SNe IIb, such as SN 1993J, SN 2008ax, and SN 2011dh, to these models allows for a direct estimate of their progenitor masses—all of which fall in the range of masses modeled.

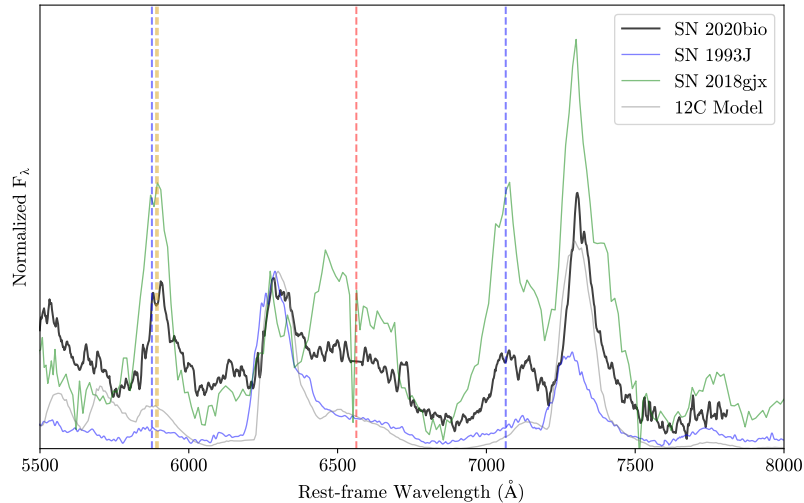


Figure 6.9: The nebular spectrum of SN 2020bio (black) compared to that of SN 1993J (blue), the 12C model of [Jerkstrand et al. \(2015\)](#) (gray), and the transitional Type IIb/Ibn SN 2018gix ([Prentice et al. 2020](#)) at the same phase. Fluxes have been normalized to the [O I] emission feature and galaxy emission lines have been masked for clarity. Notable features in the spectrum of SN 2020bio have been marked with dashed lines—H α (red), He I λ 5876, λ 7065 (blue), and Na ID (gold).

Here we reproduce this analysis using a nebular spectrum of SN 2020bio, obtained 201 days after the estimated explosion, shown in Figure 6.9. We estimate the luminosity from the [O I] $\lambda\lambda$ 6300,6364 emission doublet in the same way as [Jerkstrand et al. \(2015\)](#)—assuming the width of the feature to be 5000 km s^{-1} , we estimate the continuum by finding the minimum flux redward and blueward of this width and calculate the luminosity within the continuum-subtracted feature. We normalize this luminosity using the luminosity of ^{56}Ni decay, assuming the best-fit M_{Ni} from Section 6.4.3.

The normalized luminosity at 201 days is $L_{\text{norm}}(t=201) = 9 \times 10^{-4} \pm 2 \times 10^{-5}$. This value is lower than any of the numerical models analyzed by [Jerkstrand et al. \(2015\)](#), implying a progenitor mass $\leq 12 M_{\odot}$. A low progenitor mass for SN 2020bio can also be inferred from the ratio of the [Ca II] $\lambda\lambda$ 7311, 7324 to [O I] $\lambda\lambda$ 6300, 6364 fluxes. A higher ratio implies a lower-mass progenitor, with SNe IIb from literature having values $\lesssim 1$

throughout their nebular phases (e.g., Fang et al. 2019; Terreran et al. 2019; Hiramatsu et al. 2021a). Using the same procedure as above, we estimate a [Ca II] to [O I] ratio of 1.34 ± 0.03 —again pointing to a low-mass progenitor star.

Nebular spectroscopy has also been used to infer the presence of late-time circumstellar interaction in several SNe IIb, including SN 1993J (Fransson et al. 1996), SN 2013df (Maeda et al. 2015), and ZTF18aalrxas (Fremming et al. 2019). In these objects, interaction with H-rich material lost by the progenitor star was inferred through the presence of a boxy H α profile which strengthened with time. While the origin of this feature at times $\lesssim 300$ days after explosion is debated (e.g., Fang & Maeda 2018), Fremming et al. (2019) show that this feature is visible as early as ≈ 180 days after explosion. To search for signatures of interaction, in Figure 6.9 we compare the nebular spectrum of SN 2020bio with that of SN 1993J from a similar phase, the 12C model from Jerkstrand et al. (2015), and the interacting Type IIb/Ibn SN 2018gjx (Prentice et al. 2020). The host galaxy emission lines have been masked in the spectrum of SN 2020bio and all spectra have been normalized to the strength of the [O I] emission feature. The relative strength of the [O I] and [Ca II] features of SN 2020bio is well-reproduced by this model, again supporting a $\approx 12 M_{\odot}$ zero-age main sequence progenitor.

At this phase SN 2020bio exhibits several unusual features. An excess redward of the [O I] $\lambda\lambda$ 6300,6364 feature relative to the 12C model can be attributed to H α powered by circumstellar interaction (Maeda et al. 2015; Fremming et al. 2019). While this feature may be due to [N II] (Jerkstrand et al. 2015), Fremming et al. (2019) found that ZTF18aalrxas still showed an excess even after subtracting off numerical models of SN IIb nebular spectra at this phase. More intriguing are two additional features centered around the He I λ 5876 and He I λ 7065 lines. These features are not found in the 12C model spectrum; however, they are of comparable width (albeit weaker in intensity) to the He I lines found in the nebular spectrum of SN 2018gjx. Prentice et al. (2020) claim that

these lines are due to persistent interaction with He-rich circumstellar material that is revealed after the SN photosphere has receded sufficiently far. It is interesting to note that SN 2020bio and SN 2018gix share several characteristics, including: H α P Cygni features that are weaker than that of SN 1993J roughly 20 days after explosion; strong shock cooling emission and a weak secondary light curve peak, with similar amounts of ^{56}Ni produced; and weak [O I] compared to [Ca II] in their nebular spectra.

Based on its low synthesized ^{56}Ni mass and nebular spectral features, we conclude that SN 2020bio was likely the core-collapse of a star with a lower mass than the progenitors of most other SNe IIb.

6.5 Discussion and Conclusions

We have presented rapid multi-band photometric and spectroscopic observations of SN 2020bio, a Type IIb SN with luminous and rapidly-evolving SCE, beginning ≤ 1 day after explosion. Compared with other well-observed SNe IIb, SN 2020bio has the bluest colors at early times as well as weak H spectral features throughout its evolution. Fitting analytical models of SCE to the early-time light curve gives progenitor radii on the order of $100 R_{\odot} - 500 R_{\odot}$ and envelope masses of $0.01 M_{\odot} - 0.5 M_{\odot}$ for our best-fit models, which are slightly greater than values derived for other SNe IIb progenitors using the same methods (e.g., SN 2016gkg; [Arcavi et al. 2017](#)). The weak secondary peak powered by radioactive decay is evidence of relatively little ^{56}Ni synthesized, $M_{\text{Ni}} \approx 0.02 M_{\odot}$, which is in tension with average M_{Ni} estimates from samples of other SNe IIb. Numerical modeling of the progenitor explosion within confined circumstellar material is consistent with the observed light curve, showing that circumstellar interaction is likely needed to reproduce the complete pseudo-bolometric light curve. Finally, comparing the nebular spectra to numerical models implies a progenitor mass $\leq 12 M_{\odot}$.

It is difficult to explain all these peculiar features of SN 2020bio in one consistent model. The combination of its blue colors, nebular spectral features, and our numerical modeling points to interaction with confined CSM that was stripped from the progenitor’s outer envelope during the months prior to explosion. The best-fit progenitor parameters, particularly the large envelope radius and low envelope mass, may suggest an inflated progenitor undergoing enhanced mass-loss immediately before exploding. However, the very low ^{56}Ni and ejecta masses inferred from the later-time light curve, as well as the nebular spectroscopy, point to a lower-mass progenitor. It is possible that SN 2020bio was the collapse of an unusually low-mass core within a dense CSM produced from its lost H layers. Such extensive mass-loss likely requires interaction with a binary companion, as inferred for other SNe IIb (e.g., [Maund et al. 2004](#); [Benvenuto et al. 2013](#); [Prentice et al. 2020](#)). Interaction between the SN ejecta and this CSM explains the blue colors and obscured ejecta features at early times while the small ^{56}Ni mass and nebular spectrum indicate a low zero-age main-sequence mass. This interaction can lead to an over-estimated progenitor radius—if the CSM was near enough to the progenitor, we may have observed the shock-cooling of this extended CSM instead of the outer envelope of the progenitor. In the future, more detailed models and multi-wavelength observations, particularly in the radio and X-rays, will be needed to infer SNe IIb progenitor mass-loss rates and CSM masses.

Given the weak H spectral features when compared to spectra of other SNe IIb, SN 2020bio may be an intermediary object between the Type IIb and Ib subclasses, representing a progenitor that was recently stripped almost entirely of its H-rich envelope. Transitional objects between SNe IIb and SNe Ib have been observed ([Prentice & Mazzali 2017](#)) and can be explained by different amounts of H remaining in the outer envelope at the time of explosion. More difficult to explain are the small ^{56}Ni and ejecta masses, which are lower than those measured for both SNe IIb and SNe Ib (e.g., [Taddia et al.](#)

2018). Some objects that exist in the literature with both low ejecta and ^{56}Ni masses and observed SCE are peculiar SNe Ib as well as Ca-rich transients. However, it is difficult to reconcile the photospheric-phase spectra of SN 2020bio, which are most similar to those of other SNe IIb, with the spectra of these objects, which are often used to argue for a degenerate or ultra-stripped progenitor (Yao et al. 2020; Jacobson-Galán et al. 2022b). Instead, it is more likely that SN 2020bio had a massive star progenitor more similar to the progenitors of other SNe IIb based on their similar photospheric-phase spectral features.

Perhaps more interesting are the similarities between SN 2020bio and SN 2018gix. SN 2018gix is a peculiar object; Prentice et al. (2020) found that it showed evidence for CSM shock-cooling at early times before displaying typical SN IIb spectra. Around 30 days after explosion the spectra began showing strong emission features of He I that the authors argued were powered by interaction with He-rich material, revealed by the receding photosphere, that persisted into the nebular phase. Like SN 2020bio, it had a weak secondary light-curve peak that implied a synthesized ^{56}Ni mass of $0.021 M_{\odot}$. A scenario that explains all these observations is an SN IIb explosion with an asymmetric ring or torus of CSM, viewed equatorially. The fact that the interaction signatures are not as prevalent in the spectra of SN 2020bio, both within the first few days of explosion and during the nebular phase, may suggest a viewing angle between equatorial and polar—if this is the case, more of the SN photospheric and nebular features would be visible, rather than blocked by the ongoing interaction. The CSM masses inferred from model fits for both objects are roughly the same ($\approx 0.01 M_{\odot}$). This may reveal that the progenitor of SN 2020bio underwent extensive mass-loss, perhaps losing almost all of its H-rich material before exploding. Even in this extreme case, however, the models used throughout this analysis (e.g., Piro 2015; Sapir & Waxman 2017; Piro et al. 2021) have been applied to both H-rich and H-poor objects. Therefore we are confident our conclusions remains

valid, regardless of the exact amount of H remaining in the progenitor envelope.

This study contributes to the overall diversity in the progenitors of SNe IIb. More systematic studies of SNe with observed SCE will be needed to search for similarities and differences in their progenitor systems. In particular, this work shows the importance of rapid, multi-wavelength follow-up of these objects. It is particularly important to better understand the number of SNe IIb with weak secondary light-curve peaks, such as SN 2020bio. These objects may have later-time (≥ 5 days) luminosity below the detection threshold of current all-sky surveys as well as rapid early-time emission which evolves too quickly to be extensively followed. Therefore we may be under-counting the rates of core-collapse, stripped-envelope SNe with low ^{56}Ni and ejecta masses. A better understanding of their progenitors will be important for exploring the low-mass end of core-collapse SNe.

Chapter 7

Conclusions and Future Outlook

Today, wide-field time-domain surveys are greatly increasing the sample of supernova candidates each year. However, to maximize the scientific impact from these large data sets it is necessary to obtain high-cadence photometric and spectroscopic follow-up observations of potential targets of interest, including objects with poorly-understood properties. This dissertation shows the importance of studying objects discovered on the extreme edges of supernova parameter spaces. In particular, the advances made by the presented works would not have been possible without rapidly-schedulable, multi-wavelength follow-up resources such as Las Cumbres Observatory.

The presented works have emphasized the importance of early-time observations of supernovae in multiple ways. Rapidly-triggered spectroscopic follow-up has revealed significant diversity in the ejecta velocities of otherwise homogeneous Type Ia supernovae; Chapter 2 studies the origin of some of the fastest-moving ejecta ever observed for a Type Ia supernova, and the constraints these observations can place on its otherwise poorly-understood progenitor system and explosion mechanism.

This dissertation is also one of the first works to probe the extremes of supernova phase space, using multi-wavelength data sets from the ultraviolet to the infrared, in order to study the group of rapidly-evolving supernovae in greater detail. As a result, this research question has led to several discoveries at the forefront of the field today. Comparisons

between spectroscopically-classified and unclassified objects points to circumstellar interaction as a powering mechanism that can reproduce the light curves of many luminous fast transients, connecting these objects to poorly-understood mass loss at the endpoints of stellar evolution (Chapter 4). Furthermore, the search for fast-evolving supernovae led to the discovery of Type Icn supernovae, a new class showing evidence for extreme mass loss. Remarkably, studying the first sample of these rare objects revealed strong evidence for diversity in their progenitor channels, including low-mass, ultra-stripped stars as potential progenitors for interacting, stripped-envelope supernovae (Chapter 5). Finally, studying a peculiar example of a relatively well-understood class (Type IIb) revealed surprising diversity in their progenitor stars and circumstellar environments, elucidating the origins of faint, fast-evolving supernovae (Chapter 6).

These research advances are just a few of the many that have been spurred by early-time detections and observations of supernovae. Indeed this deluge of discoveries and data have paved the way for new areas of research and revealed new tensions between theory and observation. For example, advances in theoretical simulations have renewed the community's interest in double detonations as the potential explosion mechanism for some, if not all, Type Ia supernovae (e.g., [Shen & Bildsten 2009](#); [Polin et al. 2019](#)). On the observational side, a growing number of Type Ia supernovae show early-time light-curve excesses (e.g., [Hosseinzadeh et al. 2017a](#); [Burke et al. 2021](#); [Hosseinzadeh et al. 2022](#)). These excesses may be evidence of a double detonation explosion, a nondegenerate companion ([Kasen 2010](#)), or significant ^{56}Ni mixing ([Magee & Maguire 2020](#)), among other scenarios. Along with their ejecta velocities, Type Ia supernovae show greater diversity at early times than expected, and understanding the causes of this diversity will be essential for understanding their explosion mechanisms and progenitor channels.

For core-collapse supernovae, early-time observations have shown surprising diversity in their circumstellar environments. Along with new classes of transients with unique

circumstellar compositions, such as Type Icn supernovae, there is a renewed interest in interaction with circumstellar material in otherwise normal supernovae. For example, large fractions of Type II supernovae show evidence for pre-existing circumstellar material in their early-time “flash” spectroscopy (e.g., [Bruch et al. 2022](#)). This supports recent findings that even “normal” red supergiants undergo greatly-enhanced mass-loss in the final years of their lives, perhaps due to unstable nuclear burning ([Jacobson-Galán et al. 2022a](#)). Furthermore, several recent studies find that late-time interaction may be more common than previously thought, particularly in stripped-envelope supernovae ([Kuncarayakti et al. 2022](#)). Evidence that interaction with circumstellar material is commonplace has already begun to reshape the field’s understanding of early- and late-time powering mechanisms as well as theories of stellar evolution.

In the future, to continue maximizing the science from early-time discoveries it will be essential to obtain rapidly-triggered multi-wavelength observations. This dissertation has shown the scientific impact of ground-based optical observations working in tandem with complementary-wavelength observations, such as ultraviolet photometry from *Swift*. As we continue to explore the extremes of supernova physics it will be necessary to expand our data sets across the electromagnetic spectrum. In particular, observations in the X-ray and radio have the potential to probe the full range of circumstellar environments and interaction-powered transients in ways that optical observations cannot, with greater sensitivity to mass-loss rates, circumstellar geometries, and ongoing interaction well after the optical emission has faded (e.g., [Ofek et al. 2013](#)).

Future satellites and observatories will break new ground in these regards in the 2020s and beyond. For example, the Ultraviolet Transient Astronomy Satellite (ULTRASAT) will revolutionize time-domain science in the ultraviolet by observing shock breakout from tens of core-collapse supernovae and measuring full ultraviolet light curves for hundreds more, increasing the current sample sizes by over an order of magnitude ([Ben-Ami et al.](#)

2022). These data sets will reveal the progenitor structure and circumstellar environments of multiple classes of supernovae. From the ground, the advent of LSST at the Rubin Observatory will vastly increase the number of supernovae discovered in the optical each year. LSST will detect transients out to high redshifts, even observing the rest-frame ultraviolet light curves of the most distant and ultraviolet-bright objects. However, these exponentially-growing data sets will require programmatic methods for searching for supernovae at the extremes of parameter space.

Despite (or perhaps because of) this oncoming influx of data, dedicated follow-up resources such as Las Cumbres Observatory will still be vital to obtaining high-cadence, multi-band observations at early times. This work has shown that even small samples of extreme objects with extensive data sets can provide groundbreaking results. As the 2020s progress, a growing emphasis is being placed on time-domain astronomy. New research advances in the next decade will build on those presented in this dissertation, revealing rare and extreme objects that challenge our notion of supernova physics and providing evidence for new theories of stellar evolution.

Bibliography

- Abbott, D. C. 1982, [ApJ](#), **259**, 282
- Adelman-McCarthy, J. K., Agüeros, M. A., Allam, S. S., et al. 2007, [ApJS](#), **172**, 634
- Albareti, F. D., Allende Prieto, C., Almeida, A., et al. 2017, [ApJS](#), **233**, 25
- Aldering, G., Humphreys, R. M., & Richmond, M. 1994, [AJ](#), **107**, 662
- Altavilla, G., Stehle, M., Ruiz-Lapuente, P., et al. 2007, [A&A](#), **475**, 585
- Anderson, J. P., Habergham, S. M., James, P. A., & Hamuy, M. 2012, [MNRAS](#), **424**, 1372
- Anderson, L., Aubourg, É., Bailey, S., et al. 2014, [MNRAS](#), **441**, 24
- Andersson, E. P., Renaud, F., & Agertz, O. 2021, [MNRAS](#), **502**, L29
- Andrews, J. E., & Smith, N. 2018, [MNRAS](#), **477**, 74
- Arcavi, I., Gal-Yam, A., Yaron, O., et al. 2011, [ApJL](#), **742**, L18
- Arcavi, I., Wolf, W. M., Howell, D. A., et al. 2016, [ApJ](#), **819**, 35
- Arcavi, I., Hosseinzadeh, G., Brown, P. J., et al. 2017, [ApJL](#), **837**, L2
- Armstrong, P., Tucker, B. E., Rest, A., et al. 2021, [MNRAS](#), **507**, 3125
- Arnett, W. D. 1979, [ApJL](#), **230**, L37
- . 1982, [ApJ](#), **253**, 785
- Barbary, K. 2016, [The Journal of Open Source Software](#), **1**, 58
- Barbon, R., Benetti, S., Cappellaro, E., et al. 1995, [A&AS](#), **110**, 513
- Becker, A. 2015, HOTPANTS: High Order Transform of PSF ANd Template Subtraction, Astrophysics Source Code Library, record ascl:1504.004, ascl:[1504.004](#)
- Beers, T. C., Kriessler, J. R., Bird, C. M., & Huchra, J. P. 1995, [AJ](#), **109**, 874

- Bellm, E. C., Kulkarni, S. R., Graham, M. J., et al. 2019, [PASP](#), **131**, 018002
- Ben-Ami, S., Shvartzvald, Y., Waxman, E., et al. 2022, in Society of Photo-Optical Instrumentation Engineers (SPIE) Conference Series, Vol. 12181, Space Telescopes and Instrumentation 2022: Ultraviolet to Gamma Ray, ed. J.-W. A. den Herder, S. Nikzad, & K. Nakazawa, 1218105
- Benetti, S., Pastorello, A., Cappellaro, E., et al. 2018, *The Astronomer's Telegram*, **11836**, 1
- Benetti, S., Meikle, P., Stehle, M., et al. 2004, [MNRAS](#), **348**, 261
- Benetti, S., Cappellaro, E., Mazzali, P. A., et al. 2005, [ApJ](#), **623**, 1011
- Benvenuto, O. G., Bersten, M. C., & Nomoto, K. 2013, [ApJ](#), **762**, 74
- Bersten, M. C., Benvenuto, O. G., Folatelli, G., et al. 2014, [AJ](#), **148**, 68
- Betoule, M., Kessler, R., Guy, J., et al. 2014, [A&A](#), **568**, A22
- Bianco, F. B., Modjaz, M., Hicken, M., et al. 2014, [ApJS](#), **213**, 19
- Blinnikov, S., Lundqvist, P., Bartunov, O., Nomoto, K., & Iwamoto, K. 2000, [ApJ](#), **532**, 1132
- Blinnikov, S. I., Eastman, R., Bartunov, O. S., Popolitov, V. A., & Woosley, S. E. 1998, [ApJ](#), **496**, 454
- Blinnikov, S. I., Röpkke, F. K., Sorokina, E. I., et al. 2006, [A&A](#), **453**, 229
- Blondin, S., Dessart, L., & Hillier, D. J. 2015, [MNRAS](#), **448**, 2766
- Blondin, S., & Tonry, J. L. 2007, [ApJ](#), **666**, 1024
- Blondin, S., Dessart, L., Leibundgut, B., et al. 2006, [AJ](#), **131**, 1648
- Blondin, S., Matheson, T., Kirshner, R. P., et al. 2012, [AJ](#), **143**, 126
- Bloom, J. S., Kasen, D., Shen, K. J., et al. 2012, [ApJL](#), **744**, L17
- Branch, D., Dang, L. C., Hall, N., et al. 2006, [PASP](#), **118**, 560
- Branch, D., Troxel, M. A., Jeffery, D. J., et al. 2007, [PASP](#), **119**, 709
- Breeveld, A. A., Landsman, W., Holland, S. T., et al. 2011, in American Institute of Physics Conference Series, Vol. 1358, Gamma Ray Bursts 2010, ed. J. E. McEnery, J. L. Racusin, & N. Gehrels, 373–376

- Brown, P. J., Breeveld, A. A., Holland, S., Kuin, P., & Pritchard, T. 2014, *Ap&SS*, **354**, 89
- Brown, T. M., Baliber, N., Bianco, F. B., et al. 2013, *PASP*, **125**, 1031
- Bruch, R. J., Gal-Yam, A., Schulze, S., et al. 2021, *ApJ*, **912**, 46
- Bruch, R. J., Gal-Yam, A., Yaron, O., et al. 2022, *arXiv e-prints*, , arXiv:2212.03313
- Bulla, M., Sim, S. A., Kromer, M., et al. 2016, *MNRAS*, **462**, 1039
- Burke, J., Arcavi, I., Howell, D. A., et al. 2019, *The Astronomer’s Telegram*, **12719**, 1
- Burke, J., Howell, D. A., Sarbadhicary, S. K., et al. 2021, *ApJ*, **919**, 142
- Burrows, D. N., Hill, J. E., Nousek, J. A., et al. 2005, *SSRv*, **120**, 165
- Cain, C., Baron, E., Phillips, M. M., et al. 2018, *ApJ*, **869**, 162
- Cantiello, M., Yoon, S. C., Langer, N., & Livio, M. 2007, in *American Institute of Physics Conference Series*, Vol. 948, *Unsolved Problems in Stellar Physics: A Conference in Honor of Douglas Gough*, ed. R. J. Stancliffe, G. Houdek, R. G. Martin, & C. A. Tout, 413–418
- Cao, Y., Kasliwal, M. M., Arcavi, I., et al. 2013, *ApJL*, **775**, L7
- Cardelli, J. A., Clayton, G. C., & Mathis, J. S. 1989, *ApJ*, **345**, 245
- Castor, J. I., Abbott, D. C., & Klein, R. I. 1975, *ApJ*, **195**, 157
- Cendes, Y., Drout, M. R., Chomiuk, L., & Sarbadhicary, S. K. 2020, *ApJ*, **894**, 39
- Chang, C.-Z., Zhang, J., Feng, X., et al. 2013, *Science*, **340**, 167
- Chatzopoulos, E., Wheeler, J. C., & Vinko, J. 2012, *ApJ*, **746**, 121
- Chatzopoulos, E., Wheeler, J. C., Vinko, J., Horvath, Z. L., & Nagy, A. 2013, *ApJ*, **773**, 76
- Chen, X., Han, Z., & Tout, C. A. 2011, *ApJL*, **735**, L31
- Chevalier, R. A. 1982, *ApJ*, **259**, 302
- . 1984, *ApJL*, **285**, L63
- . 1989, *ApJ*, **346**, 847
- . 1998, *ApJ*, **499**, 810

- Chevalier, R. A., & Fransson, C. 1994, [ApJ](#), **420**, 268
- . 2006, [ApJ](#), **651**, 381
- . 2008, [ApJL](#), **683**, L135
- Childress, M., Aldering, G., Antilogus, P., et al. 2013, [ApJ](#), **770**, 108
- Childress, M. J., Filippenko, A. V., Ganeshalingam, M., & Schmidt, B. P. 2014, [MNRAS](#), **437**, 338
- Chomiuk, L., Soderberg, A. M., Moe, M., et al. 2012, [ApJ](#), **750**, 164
- Chomiuk, L., Soderberg, A. M., Chevalier, R. A., et al. 2016, [ApJ](#), **821**, 119
- Cikota, A., Patat, F., Wang, L., et al. 2019, [MNRAS](#), **490**, 578
- Clark, P., Maguire, K., Inserra, C., et al. 2020, [MNRAS](#), **492**, 2208
- Clocchiatti, A., & Wheeler, J. C. 1997, [ApJ](#), **491**, 375
- Contreras, C., Phillips, M. M., Burns, C. R., et al. 2018, [ApJ](#), **859**, 24
- Coppejans, D. L., Margutti, R., Terreran, G., et al. 2020, [ApJL](#), **895**, L23
- Cornwell, T. J. 2008, [IEEE Journal of Selected Topics in Signal Processing](#), **2**, 793
- Crowther, P. A. 2007, [ARA&A](#), **45**, 177
- Crowther, P. A., Dessart, L., Hillier, D. J., Abbott, J. B., & Fullerton, A. W. 2002, [A&A](#), **392**, 653
- Davis, K. W., Taggart, K., Tinyanont, S., et al. 2022, [arXiv e-prints](#), , [arXiv:2211.05134](#)
- De, K., Kasliwal, M. M., Ofek, E. O., et al. 2018, [Science](#), **362**, 201
- Della Valle, M., Chincarini, G., Panagia, N., et al. 2006, [Nature](#), **444**, 1050
- Dessart, L., Blondin, S., Hillier, D. J., & Khokhlov, A. 2014, [MNRAS](#), **441**, 532
- Dessart, L., & Hillier, D. J. 2005, [A&A](#), **439**, 671
- . 2011, [MNRAS](#), **415**, 3497
- Dessart, L., Hillier, D. J., & Kuncarayakti, H. 2022, [A&A](#), **658**, A130
- Dexter, J., & Kasen, D. 2013, [ApJ](#), **772**, 30
- Dorigo Jones, J., Oey, M. S., Paggeot, K., Castro, N., & Moe, M. 2020, [ApJ](#), **903**, 43

- Dressler, A., Hare, T., Bigelow, B. C., & Osip, D. J. 2006, in Society of Photo-Optical Instrumentation Engineers (SPIE) Conference Series, Vol. 6269, Ground-based and Airborne Instrumentation for Astronomy, ed. I. S. McLean & M. Iye, 62690F
- Drout, M. R., Soderberg, A. M., Mazzali, P. A., et al. 2013, [ApJ](#), **774**, 58
- Drout, M. R., Chornock, R., Soderberg, A. M., et al. 2014, [ApJ](#), **794**, 23
- Durbala, A., Finn, R. A., Crone Odekon, M., et al. 2020, [AJ](#), **160**, 271
- Eldridge, J. J., Fraser, M., Smartt, S. J., Maund, J. R., & Crockett, R. M. 2013, [MNRAS](#), **436**, 774
- Eldridge, J. J., Langer, N., & Tout, C. A. 2011, [MNRAS](#), **414**, 3501
- Ergon, M., Sollerman, J., Fraser, M., et al. 2014, [A&A](#), **562**, A17
- Fang, Q., & Maeda, K. 2018, [ApJ](#), **864**, 47
- Fang, Q., Maeda, K., Kuncarayakti, H., Sun, F., & Gal-Yam, A. 2019, [Nature Astronomy](#), **3**, 434
- Fassia, A., Meikle, W. P. S., Chugai, N., et al. 2001, [MNRAS](#), **325**, 907
- Filippenko, A. V. 1997, [ARA&A](#), **35**, 309
- Filippenko, A. V., Matheson, T., & Ho, L. C. 1993, [ApJL](#), **415**, L103
- Filippenko, A. V., Richmond, M. W., Matheson, T., et al. 1992a, [ApJL](#), **384**, L15
- Filippenko, A. V., Richmond, M. W., Branch, D., et al. 1992b, [AJ](#), **104**, 1543
- Fink, M., Röpke, F. K., Hillebrandt, W., et al. 2010, [A&A](#), **514**, A53
- Flaugher, B. 2005, [International Journal of Modern Physics A](#), **20**, 3121
- Folatelli, G., Phillips, M. M., Morrell, N., et al. 2012, [ApJ](#), **745**, 74
- Foley, R. J., & Kasen, D. 2011, [ApJ](#), **729**, 55
- Foley, R. J., Smith, N., Ganeshalingam, M., et al. 2007, [ApJL](#), **657**, L105
- Foley, R. J., Challis, P. J., Chornock, R., et al. 2013, [ApJ](#), **767**, 57
- Foreman-Mackey, D., Hogg, D. W., Lang, D., & Goodman, J. 2013, [PASP](#), **125**, 306
- Forster, F., Bauer, F. E., Munoz-Arancibia, A., et al. 2021, Transient Name Server Discovery Report, [2021-395](#), 1

- Fox, O. D., & Smith, N. 2019, [MNRAS](#), **488**, 3772
- Fransson, C., Lundqvist, P., & Chevalier, R. A. 1996, [ApJ](#), **461**, 993
- Fraser, M., Stritzinger, M. D., Brennan, S. J., et al. 2021, [arXiv e-prints](#), ,
[arXiv:2108.07278](#)
- Fremling, C., Ko, H., Dugas, A., et al. 2019, [ApJL](#), **878**, L5
- Fremling, C., Miller, A. A., Sharma, Y., et al. 2020, [ApJ](#), **895**, 32
- Fynbo, J. P. U., Watson, D., Thöne, C. C., et al. 2006, [Nature](#), **444**, 1047
- Gal-Yam, A. 2017a, in *Handbook of Supernovae*, ed. A. W. Alsabti & P. Murdin, 195
- Gal-Yam, A. 2017b, in *Handbook of Supernovae*, ed. A. W. Alsabti & P. Murdin, 195
- Gal-Yam, A. 2019, [ApJ](#), **882**, 102
- Gal-Yam, A., Yaron, O., Pastorello, A., et al. 2021, *Transient Name Server AstroNote*,
76, 1
- Gal-Yam, A., Fox, D. B., Price, P. A., et al. 2006, [Nature](#), **444**, 1053
- Gal-Yam, A., Arcavi, I., Ofek, E. O., et al. 2014a, [Nature](#), **509**, 471
- . 2014b, [Nature](#), **509**, 471
- Gal-Yam, A., Bruch, R., Schulze, S., et al. 2022, [Nature](#), **601**, 201
- Galbany, L., Anderson, J. P., Sánchez, S. F., et al. 2018, [ApJ](#), **855**, 107
- Gall, C., Hjorth, J., Watson, D., et al. 2014, [Nature](#), **511**, 326
- Ganeshalingam, M., Li, W., & Filippenko, A. V. 2011, [MNRAS](#), **416**, 2607
- Gangopadhyay, A., Misra, K., Hiramatsu, D., et al. 2020, [ApJ](#), **889**, 170
- Gangopadhyay, A., Misra, K., Hosseinzadeh, G., et al. 2022, [ApJ](#), **930**, 127
- Garavini, G., Folatelli, G., Nobili, S., et al. 2007, [A&A](#), **470**, 411
- Gehrels, N., Chincarini, G., Giommi, P., et al. 2004, [ApJ](#), **611**, 1005
- Gerardy, C. L., Höflich, P., Fesen, R. A., et al. 2004, [ApJ](#), **607**, 391
- Graham, M. J., Kulkarni, S. R., Bellm, E. C., et al. 2019, [PASP](#), **131**, 078001
- Guevel, D., & Hosseinzadeh, G. 2017, *Dguevel/Pyzogy: Initial Release*, Zenodo,
vv0.0.1, Zenodo, doi:[10.5281/zenodo.1043973](#)

- Gutiérrez, C. P., González-Gaitán, S., Folatelli, G., et al. 2016, [A&A](#), **590**, A5
- Guy, J., Astier, P., Baumont, S., et al. 2007, [A&A](#), **466**, 11
- Guy, J., Sullivan, M., Conley, A., et al. 2010, [A&A](#), **523**, A7
- Hachisu, I., Kato, M., & Nomoto, K. 1999, [ApJ](#), **522**, 487
- Hamuy, M. 2003, [ApJ](#), **582**, 905
- Hamuy, M., Phillips, M. M., Suntzeff, N. B., et al. 1996, [AJ](#), **112**, 2391
- Heinze, A., Denneau, L., Tonry, J., Flewelling, H., & Weiland, H. 2019, in EPSC-DPS Joint Meeting 2019, Vol. 2019, EPSC–DPS2019–1169
- Hillier, D. J., & Miller, D. L. 1998, [ApJ](#), **496**, 407
- Hiramatsu, D., Howell, D. A., Moriya, T. J., et al. 2021a, [ApJ](#), **913**, 55
- Hiramatsu, D., Howell, D. A., Van Dyk, S. D., et al. 2021b, [Nature Astronomy](#), **5**, 903
- Ho, A. Y. Q., Phinney, E. S., Ravi, V., et al. 2019a, [ApJ](#), **871**, 73
- Ho, A. Y. Q., Goldstein, D. A., Schulze, S., et al. 2019b, [ApJ](#), **887**, 169
- Ho, A. Y. Q., Perley, D. A., Kulkarni, S. R., et al. 2020, [ApJ](#), **895**, 49
- Ho, A. Y. Q., Perley, D. A., Gal-Yam, A., et al. 2021, [arXiv e-prints](#), , [arXiv:2105.08811](#)
- Hogg, D. W., Baldry, I. K., Blanton, M. R., & Eisenstein, D. J. 2002, [arXiv e-prints](#), , [astro](#)
- Hook, I. M., Jørgensen, I., Allington-Smith, J. R., et al. 2004, [PASP](#), **116**, 425
- Horesh, A., Kulkarni, S. R., Fox, D. B., et al. 2012, [ApJ](#), **746**, 21
- Hosseinzadeh, G., McCully, C., Zabludoff, A. I., et al. 2019, [ApJL](#), **871**, L9
- Hosseinzadeh, G., Sand, D. J., Valenti, S., et al. 2017a, [ApJL](#), **845**, L11
- Hosseinzadeh, G., Arcavi, I., Valenti, S., et al. 2017b, [ApJ](#), **836**, 158
- Hosseinzadeh, G., Sand, D. J., Lundqvist, P., et al. 2022, [ApJL](#), **933**, L45
- Howell, D. A. 2017, in Handbook of Supernovae, ed. A. W. Alsabti & P. Murdin, 431
- Howell, D. A., Sullivan, M., Perrett, K., et al. 2005, [ApJ](#), **634**, 1190
- Howell, D. A., Sullivan, M., Brown, E. F., et al. 2009, [ApJ](#), **691**, 661

- Hsiao, E. Y., Marion, G. H., Phillips, M. M., et al. 2013, [ApJ](#), **766**, 72
- Hsiao, E. Y., Burns, C. R., Contreras, C., et al. 2015, [A&A](#), **578**, A9
- Hsiao, E. Y., Phillips, M. M., Marion, G. H., et al. 2019, [PASP](#), **131**, 014002
- Huang, F., Li, J.-Z., Wang, X.-F., et al. 2012, [Research in Astronomy and Astrophysics](#), **12**, 1585
- Iben, I., J., & Tutukov, A. V. 1984, [ApJS](#), **54**, 335
- Immler, S., Modjaz, M., Landsman, W., et al. 2008, [ApJL](#), **674**, L85
- Irani, I., Prentice, S. J., Schulze, S., et al. 2022, [ApJ](#), **927**, 10
- Ivezić, Ž., Kahn, S. M., Tyson, J. A., et al. 2019, [ApJ](#), **873**, 111
- Iwamoto, K., Brachwitz, F., Nomoto, K., et al. 1999, [ApJS](#), **125**, 439
- Jacobson-Galán, W. V., Margutti, R., Kilpatrick, C. D., et al. 2020, [ApJ](#), **898**, 166
- Jacobson-Galán, W. V., Dessart, L., Jones, D. O., et al. 2022a, [ApJ](#), **924**, 15
- Jacobson-Galán, W. V., Venkatraman, P., Margutti, R., et al. 2022b, [ApJ](#), **932**, 58
- Janka, H.-T. 2012, [Annual Review of Nuclear and Particle Science](#), **62**, 407
- Jerkstrand, A. 2017, in *Handbook of Supernovae*, ed. A. W. Alsabti & P. Murdin, 795
- Jerkstrand, A., Ergon, M., Smartt, S. J., et al. 2015, [A&A](#), **573**, A12
- Jiang, B., Jiang, S., & Ashley Villar, V. 2020, [Research Notes of the American Astronomical Society](#), **4**, 16
- Kaiser, N., Burgett, W., Chambers, K., et al. 2010, in *Society of Photo-Optical Instrumentation Engineers (SPIE) Conference Series*, Vol. 7733, *Ground-based and Airborne Telescopes III*, ed. L. M. Stepp, R. Gilmozzi, & H. J. Hall, 77330E
- Karamahmetoglu, E., Fransson, C., Sollerman, J., et al. 2021, [A&A](#), **649**, A163
- Kasen, D. 2010, [ApJ](#), **708**, 1025
- Kawabata, M., Maeda, K., Yamanaka, M., et al. 2020, [ApJ](#), **893**, 143
- Kennicutt, Robert C., J. 1998, [ARA&A](#), **36**, 189
- Khatami, D., & Kasen, D. 2023, [arXiv e-prints](#), , [arXiv:2304.03360](#)
- Khokhlov, A. M. 1991, [A&A](#), **245**, 114

Khokhlov, A. M., Höflich, P. A., Oran, E. S., et al. 1999, [ApJL](#), 524, L107

Kilpatrick, C. D., Drout, M. R., Auchettl, K., et al. 2021, [MNRAS](#), 504, 2073

Kleiser, I. K. W., & Kasen, D. 2014, [MNRAS](#), 438, 318

Kleiser, I. K. W., Kasen, D., & Duffell, P. C. 2018, [MNRAS](#), 475, 3152

Könyves-Tóth, R., Vinkó, J., Ordasi, A., et al. 2020, [ApJ](#), 892, 121

Kromer, M., Sim, S. A., Fink, M., et al. 2010, [ApJ](#), 719, 1067

Kuncarayakti, H., Maeda, K., Dessart, L., et al. 2022, [ApJL](#), 941, L32

Landolt, A. U. 1992, [AJ](#), 104, 340

Law, N. M., Kulkarni, S. R., Dekany, R. G., et al. 2009, [PASP](#), 121, 1395

Leung, S.-C., Fuller, J., & Nomoto, K. 2021, [ApJ](#), 915, 80

Loyd, R. O. P., France, K., Youngblood, A., et al. 2018, [ApJ](#), 867, 71

Lusso, E., Comastri, A., Simmons, B. D., et al. 2012, [MNRAS](#), 425, 623

Lyman, J. D., Bersier, D., James, P. A., et al. 2016, [MNRAS](#), 457, 328

Lyman, J. D., Galbany, L., Sánchez, S. F., et al. 2020, [MNRAS](#), 495, 992

Macaulay, E., Nichol, R. C., Bacon, D., et al. 2019, [MNRAS](#), 486, 2184

MacFadyen, A. I., & Woosley, S. E. 1999, [ApJ](#), 524, 262

MacFadyen, A. I., Woosley, S. E., & Heger, A. 2001, [ApJ](#), 550, 410

Maeda, K., & Moriya, T. J. 2022, [ApJ](#), 927, 25

Maeda, K., Benetti, S., Stritzinger, M., et al. 2010, [Nature](#), 466, 82

Maeda, K., Hattori, T., Milisavljevic, D., et al. 2015, [ApJ](#), 807, 35

Maeda, K., Chandra, P., Moriya, T. J., et al. 2023, [ApJ](#), 942, 17

Magee, M. R., & Maguire, K. 2020, [A&A](#), 642, A189

Maguire, K., Sullivan, M., Pan, Y. C., et al. 2014, [MNRAS](#), 444, 3258

Maoz, D., Mannucci, F., & Nelemans, G. 2014, [ARA&A](#), 52, 107

Margutti, R., Metzger, B. D., Chornock, R., et al. 2019, [ApJ](#), 872, 18

- Maund, J. R., Smartt, S. J., Kudritzki, R. P., Podsiadlowski, P., & Gilmore, G. F. 2004, [Nature](#), **427**, 129
- Maund, J. R., Höflich, P., Patat, F., et al. 2010, [ApJL](#), **725**, L167
- Maund, J. R., Fraser, M., Ergon, M., et al. 2011, [ApJL](#), **739**, L37
- Maund, J. R., Spyromilio, J., Höflich, P. A., et al. 2013, [MNRAS](#), **433**, L20
- Mazzali, P. A., Benetti, S., Stehle, M., et al. 2005, [MNRAS](#), **357**, 200
- Mazzali, P. A., Maurer, I., Valenti, S., Kotak, R., & Hunter, D. 2010, [MNRAS](#), **408**, 87
- Metzger, B. D. 2022, [ApJ](#), **932**, 84
- Metzger, B. D., & Pejcha, O. 2017, [MNRAS](#), **471**, 3200
- Miller, A. A., Yao, Y., Bulla, M., et al. 2020, [ApJ](#), **902**, 47
- Milne, P. A., Brown, P. J., Roming, P. W. A., Bufano, F., & Gehrels, N. 2013, [ApJ](#), **779**, 23
- Miyaji, S., Nomoto, K., Yokoi, K., & Sugimoto, D. 1980, [PASJ](#), **32**, 303
- Modjaz, M., Liu, Y. Q., Bianco, F. B., & Graur, O. 2016, [ApJ](#), **832**, 108
- Modjaz, M., Li, W., Butler, N., et al. 2009, [ApJ](#), **702**, 226
- Morales-Garoffolo, A., Elias-Rosa, N., Benetti, S., et al. 2014, [MNRAS](#), **445**, 1647
- Moriya, T., Tominaga, N., Tanaka, M., et al. 2010, [ApJ](#), **719**, 1445
- Moriya, T. J., & Eldridge, J. J. 2016, [MNRAS](#), **461**, 2155
- Moriya, T. J., Mazzali, P. A., Tominaga, N., et al. 2017, [MNRAS](#), **466**, 2085
- Morozova, V., Piro, A. L., & Valenti, S. 2018, [ApJ](#), **858**, 15
- Mulligan, B. W., & Wheeler, J. C. 2017, [MNRAS](#), **467**, 778
- . 2018, [MNRAS](#), **476**, 1299
- Nagao, T., Cikota, A., Patat, F., et al. 2019, [MNRAS](#), **489**, L69
- Nakaoka, T., Moriya, T. J., Tanaka, M., et al. 2019, [ApJ](#), **875**, 76
- Nakar, E., & Piro, A. L. 2014, [ApJ](#), **788**, 193
- Nakar, E., & Sari, R. 2010, [ApJ](#), **725**, 904

- Nayyeri, H., Keele, M., Cooray, A., et al. 2016, *ApJ*, 823, 17
- Nicholl, M. 2018, *Research Notes of the American Astronomical Society*, 2, 230
- Nomoto, K. 1984, *ApJ*, 277, 791
- . 1987, *ApJ*, 322, 206
- Nomoto, K., Kamiya, Y., & Nakasato, N. 2013, in *Binary Paths to Type Ia Supernovae Explosions*, ed. R. Di Stefano, M. Orio, & M. Moe, Vol. 281, 253–260
- Nomoto, K., Yamaoka, H., Pols, O. R., et al. 1994, *Nature*, 371, 227
- Ofek, E. O., Fox, D., Cenko, S. B., et al. 2013, *ApJ*, 763, 42
- Ofek, E. O., Sullivan, M., Shaviv, N. J., et al. 2014, *ApJ*, 789, 104
- Oh, S., & Kroupa, P. 2016, *A&A*, 590, A107
- Oke, J. B., Cohen, J. G., Carr, M., et al. 1995, *PASP*, 107, 375
- Panagia, N., Van Dyk, S. D., Weiler, K. W., et al. 2006, *ApJ*, 646, 369
- Parrent, J., Friesen, B., & Parthasarathy, M. 2014, *Ap&SS*, 351, 1
- Parrent, J. T., Thomas, R. C., Fesen, R. A., et al. 2011, *ApJ*, 732, 30
- Parrent, J. T., Howell, D. A., Friesen, B., et al. 2012, *ApJL*, 752, L26
- Pastorello, A., Smartt, S. J., Mattila, S., et al. 2007, *Nature*, 447, 829
- Pastorello, A., Mattila, S., Zampieri, L., et al. 2008, *MNRAS*, 389, 113
- Pastorello, A., Hadjiyska, E., Rabinowitz, D., et al. 2015, *MNRAS*, 449, 1954
- Pastorello, A., Vogl, C., Taubenberger, S., et al. 2021, *Transient Name Server AstroNote*, 71, 1
- Patat, F., Chugai, N. N., Podsiadlowski, P., et al. 2011, *A&A*, 530, A63
- Paxton, B., Bildsten, L., Dotter, A., et al. 2011, *ApJS*, 192, 3
- Paxton, B., Cantiello, M., Arras, P., et al. 2013, *ApJS*, 208, 4
- Paxton, B., Marchant, P., Schwab, J., et al. 2015, *ApJS*, 220, 15
- Paxton, B., Schwab, J., Bauer, E. B., et al. 2018, *ApJS*, 234, 34
- Paxton, B., Smolec, R., Schwab, J., et al. 2019, *ApJS*, 243, 10

- Pellegrino, C., Burke, J., Hiramatsu, D., et al. 2022a, Transient Name Server Classification Report, [2022-1233](#), [1](#)
- Pellegrino, C., Gonzalez, E. P., Farah, J., et al. 2023a, Transient Name Server AstroNote, [75](#), [1](#)
- Pellegrino, C., Terreran, G., Burke, J., et al. 2022b, Transient Name Server Classification Report, [2022-712](#), [1](#)
- Pellegrino, C., Howell, D. A., Sarbadhicary, S. K., et al. 2020, [ApJ](#), [897](#), [159](#)
- Pellegrino, C., Howell, D. A., Vinkó, J., et al. 2022c, [ApJ](#), [926](#), [125](#)
- Pellegrino, C., Howell, D. A., Terreran, G., et al. 2022d, [ApJ](#), [938](#), [73](#)
- Pellegrino, C., Hiramatsu, D., Arcavi, I., et al. 2023b, [arXiv e-prints](#), , [arXiv:2301.04662](#)
- Pereira, R., Thomas, R. C., Aldering, G., et al. 2013, [A&A](#), [554](#), [A27](#)
- Perets, H. B., & Šubr, L. 2012, [ApJ](#), [751](#), [133](#)
- Pérez-Torres, M. A., Lundqvist, P., Beswick, R. J., et al. 2014, [ApJ](#), [792](#), [38](#)
- Perley, D. A. 2019, [PASP](#), [131](#), [084503](#)
- Perley, D. A., Mazzali, P. A., Yan, L., et al. 2019, [MNRAS](#), [484](#), [1031](#)
- Perley, D. A., Fremling, C., Sollerman, J., et al. 2020, [ApJ](#), [904](#), [35](#)
- Perley, D. A., Ho, A. Y. Q., Yao, Y., et al. 2021, [MNRAS](#), [508](#), [5138](#)
- Perley, D. A., Sollerman, J., Schulze, S., et al. 2022, [ApJ](#), [927](#), [180](#)
- Perlmutter, S., Aldering, G., Goldhaber, G., et al. 1999, [ApJ](#), [517](#), [565](#)
- Phillips, M. M. 1993, [ApJL](#), [413](#), [L105](#)
- Phillips, M. M., Wells, L. A., Suntzeff, N. B., et al. 1992, [AJ](#), [103](#), [1632](#)
- Piro, A. L. 2015, [ApJL](#), [808](#), [L51](#)
- Piro, A. L., Haynie, A., & Yao, Y. 2021, [ApJ](#), [909](#), [209](#)
- Podsiadlowski, P., Joss, P. C., & Hsu, J. J. L. 1992, [ApJ](#), [391](#), [246](#)
- Polin, A., Nugent, P., & Kasen, D. 2019, [ApJ](#), [873](#), [84](#)
- Poznanski, D., Prochaska, J. X., & Bloom, J. S. 2012, [MNRAS](#), [426](#), [1465](#)
- Prentice, S. J., & Mazzali, P. A. 2017, [MNRAS](#), [469](#), [2672](#)

Prentice, S. J., Mazzali, P. A., Pian, E., et al. 2016, [MNRAS](#), **458**, 2973

Prentice, S. J., Maguire, K., Smartt, S. J., et al. 2018, [ApJL](#), **865**, L3

Prentice, S. J., Maguire, K., Boian, I., et al. 2020, [MNRAS](#), **499**, 1450

Pritchard, T. A., Roming, P. W. A., Brown, P. J., Bayless, A. J., & Frey, L. H. 2014, [ApJ](#), **787**, 157

Pritchard, T. A., Bensch, K., Modjaz, M., et al. 2021, [ApJ](#), **915**, 121

Pursiainen, M., Childress, M., Smith, M., et al. 2018, [MNRAS](#), **481**, 894

Rabinak, I., & Waxman, E. 2011, [ApJ](#), **728**, 63

Rau, U., & Cornwell, T. J. 2011, [A&A](#), **532**, A71

Rayner, J. T., Toomey, D. W., Onaka, P. M., et al. 2003, [PASP](#), **115**, 362

Reichart, D. E. 1999, [ApJL](#), **521**, L111

Renzo, M., Zapartas, E., de Mink, S. E., et al. 2019, [A&A](#), **624**, A66

Rest, A., Garnavich, P. M., Khatami, D., et al. 2018, [Nature Astronomy](#), **2**, 307

Richmond, M. W., Treffers, R. R., Filippenko, A. V., et al. 1994, [AJ](#), **107**, 1022

Riess, A. G., Casertano, S., Yuan, W., Macri, L. M., & Scolnic, D. 2019, [ApJ](#), **876**, 85

Riess, A. G., Filippenko, A. V., Challis, P., et al. 1998, [AJ](#), **116**, 1009

Rivera Sandoval, L. E., Maccarone, T. J., Corsi, A., et al. 2018, [MNRAS](#), **480**, L146

Roming, P. W. A., Kennedy, T. E., Mason, K. O., et al. 2005, [SSRv](#), **120**, 95

Ryder, S. D., Sadler, E. M., Subrahmanyam, R., et al. 2004, [MNRAS](#), **349**, 1093

Sako, M., Bassett, B., Becker, A. C., et al. 2018, [PASP](#), **130**, 064002

Salas, P., Bauer, F. E., Stockdale, C., & Prieto, J. L. 2013, [MNRAS](#), **428**, 1207

Sana, H., de Mink, S. E., de Koter, A., et al. 2012, [Science](#), **337**, 444

Sander, A. A. C., Hamann, W. R., Todt, H., et al. 2019, [A&A](#), **621**, A92

Sanders, N. E., Soderberg, A. M., Foley, R. J., et al. 2013, [ApJ](#), **769**, 39

Sapir, N., & Waxman, E. 2017, [ApJ](#), **838**, 130

Schlaflty, E. F., & Finkbeiner, D. P. 2011, [ApJ](#), **737**, 103

Schmidt, B. P., Suntzeff, N. B., Phillips, M. M., et al. 1998, [ApJ](#), 507, 46

Schulze, S., Yaron, O., Sollerman, J., et al. 2021, [ApJS](#), 255, 29

Seaquist, E. R., Krogulec, M., & Taylor, A. R. 1993, [ApJ](#), 410, 260

Seaquist, E. R., & Taylor, A. R. 1990, [ApJ](#), 349, 313

Seitzzahl, I. R., Ciaraldi-Schoolmann, F., Röpke, F. K., et al. 2013, [MNRAS](#), 429, 1156

Shappee, B. J., Prieto, J. L., Grupe, D., et al. 2014, [ApJ](#), 788, 48

Shen, K. J., & Bildsten, L. 2007, [ApJ](#), 660, 1444

—. 2009, [ApJ](#), 699, 1365

Shingles, L., Smith, K. W., Young, D. R., et al. 2021, Transient Name Server
AstroNote, 7, 1

Shiode, J. H., & Quataert, E. 2014, [ApJ](#), 780, 96

Shussman, T., Waldman, R., & Nakar, E. 2016, [arXiv e-prints](#), , [arXiv:1610.05323](#)

Sironi, L., & Spitkovsky, A. 2011, [ApJ](#), 726, 75

Skrutskie, M. F., Cutri, R. M., Stiening, R., et al. 2006, [AJ](#), 131, 1163

Smartt, S. J. 2009, [ARA&A](#), 47, 63

—. 2015, [PASA](#), 32, e016

Smartt, S. J., Clark, P., Smith, K. W., et al. 2018, The Astronomer’s Telegram, 11727, 1

Smith, J. A., Tucker, D. L., Kent, S., et al. 2002, [AJ](#), 123, 2121

Smith, K. W., Smartt, S. J., Young, D. R., et al. 2020, [PASP](#), 132, 085002

Smith, N. 2014, [ARA&A](#), 52, 487

Smith, N. 2017, in Handbook of Supernovae, ed. A. W. Alsabti & P. Murdin, 403

Smith, N., & Arnett, W. D. 2014, [ApJ](#), 785, 82

Smith, N., Foley, R. J., & Filippenko, A. V. 2008, [ApJ](#), 680, 568

Smith, N., Li, W., Filippenko, A. V., & Chornock, R. 2011, [MNRAS](#), 412, 1522

Smith, N., Mauerhan, J. C., Silverman, J. M., et al. 2012, [MNRAS](#), 426, 1905

Smith, N., & Owocki, S. P. 2006, [ApJL](#), 645, L45

Soderberg, A. M., Chevalier, R. A., Kulkarni, S. R., & Frail, D. A. 2006, [ApJ](#), **651**, 1005

Soderberg, A. M., Margutti, R., Zauderer, B. A., et al. 2012, [ApJ](#), **752**, 78

Sollerman, J., Cumming, R. J., & Lundqvist, P. 1998, [ApJ](#), **493**, 933

Soumagnac, M. T., Ofek, E. O., Liang, J., et al. 2020, [ApJ](#), **899**, 51

Springob, C. M., Haynes, M. P., Giovanelli, R., & Kent, B. R. 2005, [ApJS](#), **160**, 149

Srivastav, S., Smartt, S. J., McBrien, O., Smith, K. W., & Young, D. R. 2020, [Transient Name Server AstroNote](#), **32**, 1

Stanek, K. Z., Matheson, T., Garnavich, P. M., et al. 2003, [ApJL](#), **591**, L17

Stetson, P. B. 1987, [PASP](#), **99**, 191

Stritzinger, M., Mazzali, P. A., Sollerman, J., & Benetti, S. 2006, [A&A](#), **460**, 793

Stritzinger, M. D., Shappee, B. J., Piro, A. L., et al. 2018, [ApJL](#), **864**, L35

Strotjohann, N. L., Ofek, E. O., Gal-Yam, A., et al. 2021, [ApJ](#), **907**, 99

Sukhbold, T., Ertl, T., Woosley, S. E., Brown, J. M., & Janka, H. T. 2016, [ApJ](#), **821**, 38

Sun, N.-C., Maund, J. R., & Crowther, P. A. 2023, [MNRAS](#), **521**, 2860

Taddia, F., Stritzinger, M. D., Sollerman, J., et al. 2013, [A&A](#), **555**, A10

Taddia, F., Sollerman, J., Leloudas, G., et al. 2015, [A&A](#), **574**, A60

Taddia, F., Stritzinger, M. D., Bersten, M., et al. 2018, [A&A](#), **609**, A136

Taddia, F., Sollerman, J., Fremling, C., et al. 2019, [A&A](#), **621**, A71

Tartaglia, L., Fraser, M., Sand, D. J., et al. 2017, [ApJL](#), **836**, L12

Taubenberger, S. 2017, in *Handbook of Supernovae*, ed. A. W. Alsabti & P. Murdin, 317

Taubenberger, S., Csoernyei, G., Vogl, C., et al. 2021, [Transient Name Server AstroNote](#), **125**, 1

Tauris, T. M., Langer, N., Moriya, T. J., et al. 2013, [ApJL](#), **778**, L23

Tauris, T. M., Langer, N., & Podsiadlowski, P. 2015, [MNRAS](#), **451**, 2123

Terreran, G., Margutti, R., Bersier, D., et al. 2019, [ApJ](#), **883**, 147

Thomas, R. C., Nugent, P. E., & Meza, J. C. 2011, [PASP](#), **123**, 237

Todini, P., & Ferrara, A. 2001, [MNRAS](#), **325**, 726

Tonry, J. L., Denneau, L., Heinze, A. N., et al. 2018, [PASP](#), **130**, 064505

Tully, R. B., & Fisher, J. R. 1977, [A&A](#), **54**, 661

Valenti, S., Pastorello, A., Cappellaro, E., et al. 2009, [Nature](#), **459**, 674

Valenti, S., Howell, D. A., Stritzinger, M. D., et al. 2016, [MNRAS](#), **459**, 3939

Van Dyk, S. D. 2017, [Philosophical Transactions of the Royal Society of London Series A](#), **375**, 20160277

Van Dyk, S. D., Li, W., & Filippenko, A. V. 2003, [PASP](#), **115**, 1

Van Dyk, S. D., Zheng, W., Fox, O. D., et al. 2014, [AJ](#), **147**, 37

Vargas-Salazar, I., Oey, M. S., Barnes, J. R., et al. 2020, [ApJ](#), **903**, 42

Vink, J. S. 2017, [A&A](#), **607**, L8

Vink, J. S., de Koter, A., & Lamers, H. J. G. L. M. 2000, [A&A](#), **362**, 295

Wang, L., & Wheeler, J. C. 2008, [ARA&A](#), **46**, 433

Wang, S.-Q., & Li, L. 2020, [ApJ](#), **900**, 83

Wang, X., Filippenko, A. V., Ganeshalingam, M., et al. 2009, [ApJL](#), **699**, L139

Wang, X., Lin, W., Zhang, J., et al. 2021, [ApJ](#), **917**, 97

Weiler, K. W., Williams, C. L., Panagia, N., et al. 2007, [ApJ](#), **671**, 1959

Wellons, S., Soderberg, A. M., & Chevalier, R. A. 2012, [ApJ](#), **752**, 17

Whelan, J., & Iben, Icko, J. 1973, [ApJ](#), **186**, 1007

Whitesides, L., Lunnan, R., Kasliwal, M. M., et al. 2017, [ApJ](#), **851**, 107

Wiseman, P., Pursiainen, M., Childress, M., et al. 2020, [MNRAS](#), **498**, 2575

Wood-Vasey, W. M., & Sokoloski, J. L. 2006, [ApJL](#), **645**, L53

Woosley, S. E. 1993, [ApJ](#), **405**, 273

—. 2017, [ApJ](#), **836**, 244

Woosley, S. E., Eastman, R. G., Weaver, T. A., & Pinto, P. A. 1994, [ApJ](#), **429**, 300

Woosley, S. E., & Heger, A. 2007, [PhR](#), **442**, 269

- . 2015, [ApJ](#), 810, 34
- Woosley, S. E., & Kasen, D. 2011, [ApJ](#), 734, 38
- Woosley, S. E., Kasen, D., Blinnikov, S., & Sorokina, E. 2007, [ApJ](#), 662, 487
- Wu, S. C., & Fuller, J. 2022, [ApJL](#), 940, L27
- Xiang, D., Wang, X., Lin, W., et al. 2021, [ApJ](#), 910, 42
- Yao, Y., Miller, A. A., Kulkarni, S. R., et al. 2019, [ApJ](#), 886, 152
- Yao, Y., De, K., Kasliwal, M. M., et al. 2020, [ApJ](#), 900, 46
- Yaron, O., & Gal-Yam, A. 2012, [PASP](#), 124, 668
- Yaron, O., Perley, D. A., Gal-Yam, A., et al. 2017, [Nature Physics](#), 13, 510
- Yoon, S. C., Woosley, S. E., & Langer, N. 2010, [ApJ](#), 725, 940
- Zacharias, N., Finch, C. T., Girard, T. M., et al. 2013, [AJ](#), 145, 44
- Zackay, B., Ofek, E. O., & Gal-Yam, A. 2016, [ApJ](#), 830, 27
- Zheng, W., Kelly, P. L., & Filippenko, A. V. 2018, [ApJ](#), 858, 104